

Neutron Scattering Investigations of Zero- and One-dimensional Quantum Magnets

vorgelegt von
Diplom-Physiker Oliver Pieper
geb. am 17. April 1979 in Rodewisch

Von der Fakultät II - Mathematik und Naturwissenschaften
der Technischen Universität Berlin
zur Erlangung des akademischen Grades
Doktor der Naturwissenschaften
Dr. rer. nat.

g e n e h m i g t e D i s s e r t a t i o n

Promotionsausschuss:

Vorsitzender: Prof. Dr. M. Dähne
Berichter/Gutachter: Prof. Dr. B. Lake
Berichter/Gutachter: Prof. Dr. D. A. Tennant
Berichter/Gutachter: Prof. Dr. J. Schnack

Tag der wissenschaftlichen Aussprache: 09. Juni 2010

Berlin 2010

D 83

Abstract

This thesis deals with the investigation of two different types of low-dimensional quantum magnets using the technique of neutron scattering.

In the first part, the magnetic properties of three Mn_6 -based single molecule magnets are explored by means of inelastic neutron scattering. The experimental data reveal that small structural distortions of the molecular geometry produce a significant effect on the energy level diagram and therefore on the magnetic properties of the molecule. It will be shown that the giant spin model completely fails to describe the spin level structure of the ground spin multiplets. The data enabled the determination of the parameters of the microscopic spin Hamiltonian and based on this it is shown that the excited S -multiplets play a key role in determining the effective energy barrier for the magnetization reversal.

The second part of this thesis presents an in-depth study of the nuclear and magnetic properties of the quasi-one-dimensional Heisenberg antiferromagnet CaV_2O_4 . The magnetism in this system arises from the partially filled t_{2g} -levels of the V^{3+} -ions, which in addition give an orbital degree of freedom to the system. The crystal structure consists of weakly coupled double-chains of edge-sharing VO_6 -octahedra, where the particular octahedral staggering creates a zigzag-like arrangement of the vanadium ions. This in return gives rise to strong magnetic direct exchange interactions between nearest and next nearest neighbour vanadium ions and to geometrical frustration. However, the strength of the exchange interactions is strongly influenced by the particular occupation of the t_{2g} -orbitals.

Single crystal and powder neutron diffraction as well as neutron spectroscopy are used to determine the nuclear and magnetic structure as well as the complex excitation spectrum of CaV_2O_4 . The results are analysed theoretically and from this the leading exchange paths are deduced and discussed in terms of orbital ordering.

Zusammenfassung

Die vorliegende Arbeit beschäftigt sich mit der Untersuchung von zwei unterschiedlichen Arten von niedrigdimensionalen Quantenmagneten unter Verwendung der Methode der Neutronenstreuung.

Im ersten Teil der Arbeit werden die magnetischen Eigenschaften von drei Mn_6 -basierenden Einzelmolekülmagneten mit Hilfe der inelastischen Neutronenstreuung erforscht. Die experimentellen Daten verdeutlichen, dass geringe strukturelle Verformungen der Molekülgeometrie einen erheblichen Einfluss auf das Energieleveldiagramm und demzufolge auf die magnetischen Eigenschaften der Moleküle haben. Es wird gezeigt, dass das Giant-Spin Modell nicht in der Lage ist, die Spinlevelstruktur des Grundmultipletts zu beschreiben. Die gewonnenen Daten erlauben die Bestimmung der relevanten Parameter des mikroskopischen Spin-Hamiltonoperators und basierend auf diesen Erkenntnissen wird gezeigt, dass die angeregten S -Multipletts eine Schlüsselrolle bei der Bestimmung der effektiven Energiebarriere für die Umkehrung der Magnetisierung spielen.

Der zweite Teil dieser Arbeit präsentiert eine detaillierte Untersuchung der nuklearen und magnetischen Eigenschaften des quasi-eindimensionalen Heisenberg-Antiferromagneten CaV_2O_4 . Der Magnetismus dieses Systems resultiert von den teilweise gefüllten t_{2g} -Orbitalen der V^{3+} -Ionen, welche dem System noch einen zusätzlichen orbitalen Freiheitsgrad zu Verfügung stellen. Die Kristallstruktur besteht aus schwach gekoppelten Doppelketten von eckteilenden VO_6 -Oktaedern, wobei die spezielle Staffelung der Oktaeder zu einer zigzagartigen Anordnung der Vanadiumionen führt. Dies gibt wiederum Anlass zu starken magnetischen Wechselwirkungen zwischen nächsten und übernächsten Vanadiumnachbarn und impliziert geometrische Frustration. Allerdings wird die Stärke der Wechselwirkungen stark von der speziellen Besetzung der t_{2g} -Orbitale beeinflusst.

Zur Bestimmung der nuklearen und magnetischen Struktur, sowie des komplexen Anregungsspektrums wurde sowohl die Methode der Einzelkristall- und Pulverdiffraktion, als auch die der Neutronenspektroskopie verwendet. Die experimentellen Resultate werden theoretisch analysiert und auf Grundlage dessen werden die dominanten Austauschpfade bestimmt und bezüglich orbitaler Ordnung diskutiert.

Acknowledgements

I would like to use the following lines to thank all those people who helped me with both the preparation of this thesis and also with the work that is described in it. First and foremost, I would like to thank my supervisor Bella Lake for all her great support and encouragement, for the many inspiring conversations and for her tireless availability. Without her this thesis would have never been possible. Thank you Bella!

Further, I am especially grateful to my ‘quasi-supervisor’ Tatiana Guidi, who not only introduced me to the fascinating world of molecular magnetism, but has always been an incredibly helpful, encouraging and very special friend to me. Thank you Tati!

I would like to thank all members of the MN-1 group, who always provided a very pleasant working atmosphere. Whenever I got stuck with things like programming, sample preparation or any other physical or non-physical issues, you were the ones who always helped me out. Furthermore, I very much enjoyed the culinary delicacies that you brought from all over the world to share them. Those always were my ‘gleam of hope’ after I had one of those interesting canteen dishes. Thank you Elisa, Diana, Nazmul and Sándor!

The most essential need for an experimentalist are the samples to measure and a special thanks goes to all the people who supplied me with their crystals and powders during the last years. In particular, I thank Jiaqiang Yan who did an amazing job in growing large quantities of high quality CaV_2O_4 single crystals. Further, I thank Constantinos Miliotis, who prepared most of the Mn_6 samples measured for this thesis. Additionally, I also thank David C. Johnston, Azad Niazi, Euan Brechin, Jan Tejada and Anna Julia and Joris van Slageren for their great help.

The neutron experiments have been performed at various institutions and it was the excellent expertise and support of all the instrument scientists that made a great contribution to the success of the experiments. In particular, I would like to thank: Manfred Reehuis, Mechthild Enderle, Toby Perring, Aziz Daoud-Aladine, Hannu Mutka, Marek Koza, Klaus Habicht, Klaus Kiefer, Bastian Klemke, Kirrily Rule, Margarita Russina, Karel Prokeš, Konrad Siemensmeyer, Andreas Schnegg, Oksana Zaharko, Phil Pattison, Herman Emerich and Andreas Kreyssig. Aziz deserves a special thanks for all his patience while teaching me the secrets of FULLPROF.

I had the great opportunity to collaborate with various theoreticians, with whom I had very fruitful discussions and who helped me a lot to understand the experimental data. In particular, I thank Stefano Carretta, Paolo Santini and Giuseppe Amoretti for their invaluable help with the single molecule magnets. Further, my thanks go to Andreas Honecker, Natalia Perkins and Volker Eyert who provided me important insights into the physics of CaV_2O_4 .

I would also like to express gratitude to Alan Tennant and Jürgen Schnack for agreeing

to examine this thesis.

A big thanks goes to John, Marko and Simon for proof-reading the manuscript.

I am extremely grateful to my family. I thank my parents for all their support, not only during the time of this thesis. In particular, I would like to thank my mother, who is always there for me.

Finally, I would like to thank Antje for all her love, patience and belief in me.

Contents

1. Introduction	1
2. Low-dimensional quantum magnetism	5
2.1. Spins, orbitals and exchange interactions	5
2.1.1. Orbital physics	6
2.1.2. Orbital order and magnetic exchange	9
2.2. Molecular magnetism	11
2.2.1. Slow relaxation of magnetization	12
2.2.2. Quantum tunnelling of the magnetization	15
2.2.3. Spin Hamiltonian	17
2.2.4. Spin states	22
2.2.5. Strong exchange limit - Giant Spin Approximation	24
2.2.6. Beyond the Giant Spin Approximation - <i>S</i> -mixing	25
2.2.7. Criterion for the anisotropy barrier in SMM	26
2.3. One-dimensional magnetism	27
2.3.1. Magnetic ordering	27
2.3.2. Excitations	30
2.3.3. Effects of anisotropy	34
2.3.4. Effects of 3D coupling	34
2.3.5. Frustration	35
3. Experimental techniques	37
3.1. Neutron scattering	37
3.1.1. Neutron scattering cross section	38
3.1.2. Neutron Diffraction	44
3.1.3. Neutron spectroscopy	58
3.2. Other techniques	63
3.2.1. X-ray diffraction	63
3.2.2. Magnetic susceptibility	66
4. The hexanuclear single molecule magnets Mn₆	71
4.1. Introduction	71
4.2. Experimental method	73
4.3. Theoretical modeling and experimental results	74
4.3.1. Mn ₆ (1) (S=4) $U_{\text{eff}} \approx 28$ K	75
4.3.2. Mn ₆ (2) $U_{\text{eff}} \approx 53$ K vs. Mn ₆ (3) $U_{\text{eff}} \approx 86.4$ K; (S=12)	83
4.4. Discussion	94

4.5. Conclusions	98
5. Nuclear and magnetic structure of CaV_2O_4	99
5.1. Nuclear structure	99
5.1.1. Introduction	99
5.1.2. Experimental details	101
5.1.3. Experimental results and analysis	103
5.1.4. Discussion	117
5.1.5. Conclusions	126
5.2. Magnetic susceptibility	128
5.2.1. Introduction	128
5.2.2. Experimental details	128
5.2.3. Experimental results	129
5.2.4. Data analysis and discussion	131
5.3. Magnetic structure	144
5.3.1. Introduction	144
5.3.2. The problem of twinning	145
5.3.3. Theoretical analysis - representation theory	146
5.3.4. Experimental details	150
5.3.5. Experimental results	153
5.3.6. Discussion	167
5.3.7. Conclusions	175
6. Magnetic excitations in CaV_2O_4	177
6.1. Introduction	177
6.2. Experimental details	178
6.2.1. MAPS experiment	178
6.2.2. IN20 set-up	179
6.2.3. V2 experiment	180
6.3. Theoretical model, spin wave calculations	181
6.4. Experimental results and data analysis	187
6.4.1. Low energy excitations	195
6.4.2. Spin wave analysis	198
6.4.3. Resolution effects	211
6.5. Discussion	215
6.6. Conclusions	221
7. Conclusions and perspectives	223
A. Exact diagonalization	227
B. Additional details about the nuclear structure of CaV_2O_4	231
B.1. $T = 160\text{K}$ synchrotron data	231
B.2. High temperature single crystal diffraction data	233

C. Linear spin wave theory for the CaV_2O_4 lattice	235
C.1. The four sublattice case	235
C.2. The 32 sublattice case	246
D. Neutron scattering instruments	253
D.1. IN5	253
D.2. IN6	253
D.3. NEAT, V3	255
D.4. MAPS	256

1. Introduction

Low dimensional magnetism appears in materials, where magnetic ions are arranged within the crystal lattice in such a way, that strong interactions only appear along certain directions, giving rise to well separated clusters, chains or planes. The reduction of dimensionality strongly enhances quantum effects resulting in exotic magnetic properties that differ significantly from those of conventional bulk magnets.

An important class of low dimensional materials are the Single Molecule Magnets (SMM). These are (quasi-zero-dimensional) clusters of exchange coupled magnetic ions, which are embedded in a large organic molecule and arranged on a crystal lattice. The clusters are usually characterized by a large spin ground state S and an easy-axis anisotropy which determines the Zero-Field Splitting (ZFS) of the S state sublevels. The resulting magnetic bistability makes them interesting for magnetic storage applications due to their potential to shrink the magnetic bit down to the size of one single molecule.

One dimension ‘above’ the SMM reside the one-dimensional chain magnets, which represent another class of low dimensional materials that attract a great deal of interest among scientists. These materials consist of well separated chains of magnetically interacting ions. In particular, if interactions between neighbouring ions are antiferromagnetic and if the ions possess a low spin moment, quantum fluctuations persist down to lowest temperatures and prevent the system from establishing long range magnetic order. As a result the magnetic ground states and excitations show peculiar features, such as fractional excitations, bound modes, gapped spectra and multi-particle continua. One-dimensional structures can arise naturally in crystalline materials, either because of bulky non-magnetic ions which are located between the chains and thus preventing the mediation of spin-spin interactions, or because of orbital ordering phenomena leading to spatially anisotropic electronic interactions. However, in real materials the chains are not entirely isolated, since small (but finite) interchain interaction persist. As a consequence cooperative ordering phenomena arise below a critical temperature T_c , where thermal fluctuations become weak. But even in the ordered phase, those weakly coupled systems retain their low-dimensional character, which is particularly true for systems with antiferromagnetic spin coupling. Here the quasi-low dimensionality gives rise to

zero point fluctuations of the spins, leading to a considerable reduction of the ordered moment value per spin (if compared to the saturation value). While at low energies the magnetic excitation spectrum is dominated by semi-classical transverse spin waves (Goldstone modes), the quantum fluctuations have a strong effect on the magnetic excitation spectra at energies that are high compared to the magnetic ordering temperature. In this thesis representative materials of both above mentioned classes have been investigated, predominantly by means of neutron scattering. The unique properties of neutrons make this experimental technique ideal to study both the nuclear and magnetic structure of materials as well as their elementary excitations.

Concerning the SMMs, a comprehensive inelastic neutron scattering study of three members of the recently discovered Mn_6 -SMM family has been performed. The Mn_6 -SMMs have become a subject of intense research, since for one member of this family a new record barrier for the reversal of the magnetization was discovered [1]. The molecules investigated here, only show tiny structural differences, which however, produce a significant effect on the energy level diagram and therefore on their magnetic properties.

The second system that was studied in the framework of this thesis is the quasi-one-dimensional spin-1 antiferromagnet CaV_2O_4 . This material consists of weakly coupled zigzag chains of V^{3+} -ions. The particular lattice geometry gives rise to strong antiferromagnetic direct exchange interactions between nearest and next nearest neighbour vanadium ions and to geometrical frustration. However, in addition the vanadium ions possess an orbital degree of freedom and the strength of the exchange interactions is strongly influenced by the particular d -orbital occupation. Furthermore, a weak inter-chain coupling leads to antiferromagnetic long range order at low temperatures. Neutron scattering as well as complementary experimental techniques have been used to determine the nuclear and magnetic structure of CaV_2O_4 and to explore the magnetic excitation spectrum in the ordered phase. This combined study has shed light on the complex interplay between lattice, spin and orbital degrees of freedom in this system.

In order to explain the experimental data, theoretical models have been employed. In most cases the complexity of many-body systems prevents an exact solution of the given model and one has to find appropriate approximations that simplifies the model without adulterating the underlining physics. In the case of SMMs, a well established approximation is the Giant Spin Approximation (GSA), where one assumes that the ground state multiplet of spin S is well separated from higher lying spin multiplets, such that the coupling to higher states can be neglected. However, the spectroscopic data for the three Mn_6 molecules reveal that the GSA completely fails to describe the spin level structure and the relaxation dynamics of those molecules and other more sophisticated

techniques had to be used to describe the experimental data.

The magnetic excitation spectra of CaV_2O_4 could be successfully reproduced by means of linear spin wave theory. Nevertheless, some discrepancies between theory and experiment have been observed for the high energy part of the spin wave spectrum and which were attributed to quantum fluctuations of the ordered spin moment.

The thesis is structured as follows. Chapter 2 provides an introduction to the theory of low dimensional magnetism. The basic concept of magnetic exchange interactions will be discussed, where particular emphasis is placed on the physics relevant for the materials presented in this thesis. In Chapter 3 the theory of neutron scattering is outlined, along with a description of the basic instrumentation and concepts of data analysis. The chapter is completed by a brief explanation of complementary techniques which have been used, including magnetic susceptibility measurements and X-ray diffraction.

The results of the inelastic neutron scattering experiments on the Mn_6 molecular magnets are presented in Chapter 4. The experimental data are compared to those obtained by Frequency Domain Magnetic Resonance (FDMR) measurements and the data are analysed theoretically using the concepts introduced in Chapter 2.

In Chapter 5, a detailed study of the nuclear and magnetic structure of CaV_2O_4 will be presented. The structural data are used to interpret the observed nuclear and magnetic phase transitions and to draw conclusions about the orbital physics in the material. Additionally, high temperature susceptibility data will be discussed and theoretically analysed using a frustrated Heisenberg model for finite spin-1 chains. The structural data served as a basis for the spin wave model, which was employed to interpret the magnetic excitation spectrum of CaV_2O_4 . The magnetic excitations are the topic of Chapter 6.

Finally, the main results of the work on both, the Mn_6 -SMMs and CaV_2O_4 are reviewed in Chapter 7 and some suggestions for possible future experimental and theoretical work are given.

2. Low-dimensional quantum magnetism

This chapter gives an introduction to the field of low dimensional quantum magnetism, where particular emphasis is placed on two classes of systems, namely the (zero-dimensional) single molecule magnets and the one-dimensional antiferromagnetic Heisenberg chains. Both classes have been the subject of intensive research activities for many decades, due to their fascinating quantum effects that give rise to exotic and highly non-trivial magnetic ground states and excitations.

Members of both classes will be presented in the framework of this thesis. Chapter 4 deals with the magnetic properties of three Mn-based single molecule magnets and in Chapters 5 and 6 the physics of the quasi-one-dimensional Heisenberg chain system CaV_2O_4 will be explored.

Before the basic properties of those low dimensional systems will be introduced in the second and third section of this chapter, the first section will provide a summary about the origin of localized magnetic moments, the coupling between them and how crystal field effects can influence the electronic and magnetic structures of those systems.

2.1. Spins, orbitals and exchange interactions

The magnetic moment of an ion arises from the orbital motion of unpaired electrons, which are bound to the atomic nucleus via Coulomb forces, and from the spin angular momentum of these electrons. Due to the famous Pauli exclusion principle the electrons cannot all possess the same energy, but are forced to occupy electronic ‘shells’, with well defined angular momentum and energy. The vector sum of all individual electron spins \mathbf{s}_i and orbital angular momenta \mathbf{l}_i defines the total spin $\mathbf{S} = \sum_i \mathbf{s}_i$ and total angular momentum $\mathbf{L} = \sum_i \mathbf{l}_i$ of the ion. Due to their spherical symmetry the vector sum for completely filled shells is zero and therefore those do not contribute to the magnetic moment of the ion. Generally, due to spin-orbit coupling $\mathcal{H}_{\text{so}} = \lambda \mathbf{S} \cdot \mathbf{L}$ (where λ is a constant which depends on the particular ion), the quantities \mathbf{S} and \mathbf{L} are not separately conserved and only the total angular momentum $\mathbf{J} = \mathbf{L} + \mathbf{S}$ is a good quantum number. The way in which the spin and orbital angular momenta combine in order to give the

energetically most favourable state is given by Hund's rules. According to these rules, the ground state of an isolated ion is that which maximizes the total spin \mathbf{S} and the total orbital angular momentum \mathbf{L} (in agreement with the Pauli principle). Further, the total angular momentum is $J = |L - S|$ for less-than-half-filled shells, and $J = L + S$ for more-than-half-filled shells. It follows that the total magnetic moment of the ion is given by:

$$\mu_{\text{eff}} = g_J \mu_B \sqrt{J(J+1)}, \quad (2.1)$$

where μ_B is the Bohr magneton and g_J is the Landé factor, which is defined as:

$$g_J = \frac{3}{2} + \frac{S(S+1) + L(L+1)}{2J(J+1)}. \quad (2.2)$$

For spin-only systems with $L = 0$ the Landé factor is $g \simeq 2$.

So far the discussion has only focused on the properties of single isolated ions. However, in condensed matter physics one is interested in bulk properties of materials and consequently one has to deal with ions which are embedded in solids. Those ions are certainly not isolated, but subject to the crystal field of the surrounding atoms. If the energy scale of the crystal field becomes similar to the energy of the spin-orbit coupling, Hund's third rule is no longer valid. This is the case for many $3d$ -transition metal ions. For even stronger crystal fields (which can be found in $4d$ and $5d$ transition metal compounds), even Hund's first two rules are set out of action.

2.1.1. Orbital physics

The electronic wave functions in the field of a nucleus are termed orbitals and they consist of an angular and a radial part. As a result of the spherical symmetry of the atomic potential, the corresponding eigenstates coincide with the eigenstates of the angular momentum operator. The corresponding eigenfunctions are the well known spherical harmonics (see e.g. [2]) and they express the angular dependence of the electron density. The orbitals of the s -electrons are spherical symmetric, while all other orbitals have a pronounced angular dependence. This is a crucial fact, since in most cases the local atomic environment is also not spherically symmetric, such that different orbitals will behave in different ways. The magnetic and electronic properties of the materials presented in this thesis are governed by the unpaired $3d$ -electrons of transition metal ions and the corresponding d -orbitals are depicted in Fig. 2.1. The five orbitals can be

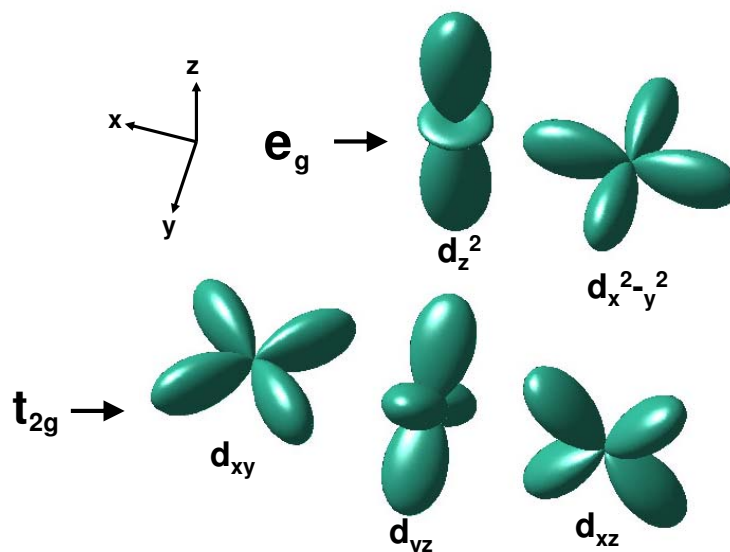


Figure 2.1.: The angular distribution of the d -orbitals. The d_{xy} , d_{xz} and d_{yz} orbitals are grouped together and called t_{2g} -orbitals and the $d_{x^2-y^2}$ and d_{z^2} orbitals are grouped together and called e_g -orbitals.

grouped into two classes, the t_{2g} - and the e_g -orbitals. The lobes of the three t_{2g} -orbitals point *between* the x , y and z axes of the local coordinate system, while the lobes of the two e_g -orbitals point *along* these axes.

On the ionic level the five d -orbitals are fully degenerate and, (when neglecting spin-orbit coupling) a single d -electron can occupy all orbitals with equal probability. This changes, if the ion is embedded in a solid. In many transition metal compounds the metal ions are in an octahedral environment, meaning that they are surrounded by six nearest neighbour anions (e.g. O^{2-}), which are located at the corners of an octahedron. This scenario is visualized on the left site of Fig. 2.2, where only the octahedron is shown and the surrounding ions are omitted for clarity. If considering an ideal octahedron with cubic symmetry¹, it becomes immediately clear that the d -orbital degeneracy will be partially lifted. The two e_g -states have a charge maximum near to the negatively charged ions at the octahedron's corners giving rise to strong Coulomb repulsion, while the lobes of the three t_{2g} -orbitals point along the octahedron's edges and are therefore less effected by the anions. Hence, the t_{2g} -levels are lowered in energy, while the e_g -orbitals are raised

¹The crystal field of the octahedron is conventionally termed cubic field, which arises from the fact that the symmetry of the crystal field produced by eight ions located at the corners of a cube is identical to those produced by the ions of the octahedron.

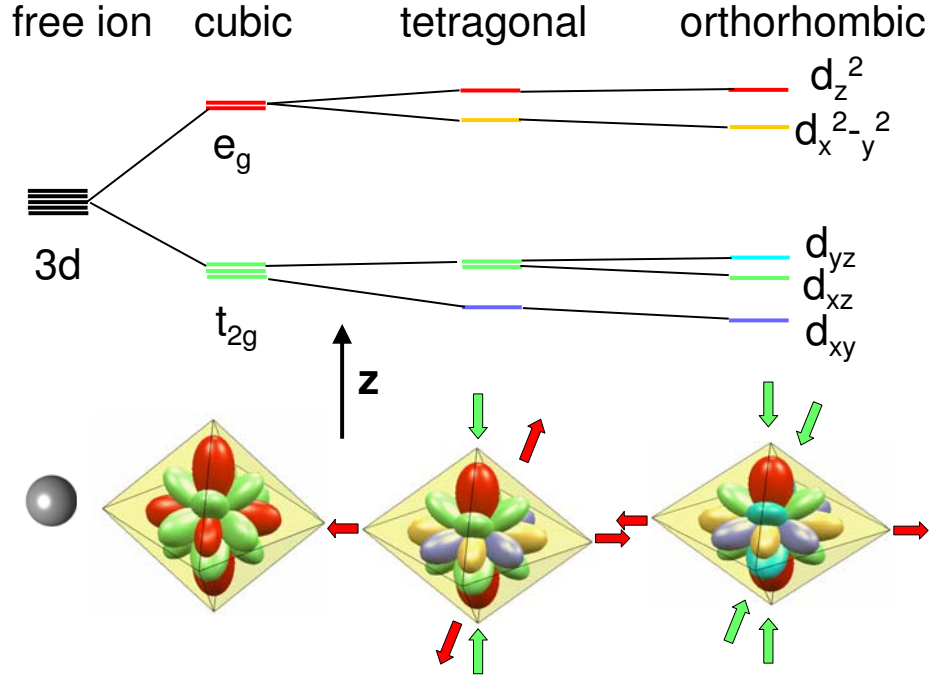


Figure 2.2.: Energy level diagram of d -orbitals in an octahedral field. The cubic crystal field of the octahedron splits the d -states into a t_{2g} -triplet and an e_g -doublet. If the octahedron experiences a tetragonal compression along the z -axis, the degeneracy is further lifted and only the d_{xz} - and d_{yz} -orbitals remain degenerate. In case of an orthorhombic distortion, the degeneracy is completely lifted. The colour of the energy levels corresponds to the colour of the orbitals.

in energy.

Often, the ideal octahedral environment is not given due to distortions in the crystal lattice. In such cases the reduction of symmetry leads to a further lifting of d -level degeneracy. A commonly encountered distortion is the tetragonal one, where the octahedron is either compressed or elongated along one of its main axes. Assuming a compression along the z -direction (see Fig. 2.2), the orbitals which are extended in the plane parallel to the compression axis will be less effected by the repulsing forces of the two negatively charged ions along the z -axis. As a result, the two e_g -levels split, with the $d_{x^2-y^2}$ -level being lowered in energy. On the other hand, the t_{2g} degeneracy is only partially lifted, since the d_{yz} - and d_{xz} -orbitals are equally effected by the tetragonal compression. The d_{xy} -orbital is the energetically most favourable one since its orientation within the octahedron is the most ideal to avoid the repelling charges. Similar effects occur if the tetragonal distortion is an elongation, however, in this case the order of the split e_g - and

t_{2g} -levels is reversed.

Finally, if the distortion is such that the distances between the three opposite lying anion-pairs are all different (orthorhombic distortion), the d -level degeneracy will be completely lifted and the corresponding energy level diagram is shown in the very right side of Fig. 2.2.

2.1.2. Orbital order and magnetic exchange

Interesting orbital physics arises in transition metal compounds that have an orbitally degenerate ground state. For instance, in the high temperature phase of LaMnO_3 the MnO_6 octahedra are in cubic symmetry. Since manganese is in the Mn^{3+} -state it contains four d -electrons, where three of them occupy the low-lying t_{2g} -orbitals. The remaining fourth electron can choose to occupy one of the two degenerate e_g -orbitals, thus the system is said to possess an orbital degree of freedom. However, the cubic phase of LaMnO_3 is only stable at high temperatures and at $T \approx 800$ K a cubic-to-tetragonal phase-transition occurs [3]. As a consequence of this transition the e_g -orbital degeneracy is lifted and the fourth electron now solely occupies the d_{z^2} -orbital. This phase-transition was interpreted to be a direct consequence of the famous *Jahn-Teller-theorem*. It says that if the ground state of an ion in a crystal field is orbitally degenerate, then it will be energetically preferable for the crystal to distort in such a way that the orbital degeneracy is lifted [4]. The reason for this behaviour is simple: the electronic energy gained by the lowering of the d_{z^2} -level is larger than the loss of elastic energy necessary to distort the crystal. In order to minimize the total energy of the crystal the octahedral distortions do not occur randomly, but they form a well defined pattern. This phenomenon is called the cooperative Jahn-Teller effect and is the most prominent example of *orbital order*. The cooperative Jahn-Teller effect is not the only mechanism which causes orbital order, another one is the kinetic exchange between electrons of neighbouring orbitals (see below).

Magnetic exchange interactions

Many materials with localized magnetic moments show long range magnetic order below a certain critical temperature $T = T_c$. The magnetic order is a result of electrostatic interactions between electrons of neighbouring magnetic ions. Those interactions arise from the requirement of antisymmetric wavefunctions, being a consequence of Pauli's exclusion principle. It was first pointed out by Dirac, that the Hamiltonian which

describes the electrostatic interactions can be replaced by an effective spin Hamiltonian [5], which for the simplest case of two interacting electrons with spins \mathbf{S}_1 and \mathbf{S}_2 is given by:

$$\mathcal{H}_{1,2} = E_0 + 2J\mathbf{S}_1\mathbf{S}_2. \quad (2.3)$$

In the above expression, E_0 is a constant energy term and J is the exchange integral performed over the electrostatic interaction. Depending on whether J is positive or negative, the spins prefer an antiparallel or parallel alignment, respectively. The generalization of Eq. 2.3 for many body systems is far from trivial, however, it turned out that in most cases the effect of electron-electron interactions can be approximated by the simple sum over all spin-pair interactions. The resulting exchange Hamiltonian is the Heisenberg model and it is discussed in detail in Sec. (2.3.1)².

The exchange interactions that occur due to the direct overlap of orbitals of neighbouring magnetic ions are referred to as *direct exchange* interactions. However, there exist many magnetic materials, whose crystallographic geometry prevents a sufficient direct overlap between neighbouring magnetic orbitals³. A prominent example is the antiferromagnetic perovskite-type manganite LaMnO_3 , which was briefly introduced in the previous section. Its structure consists of corner sharing MnO_6 octahedra, with the La^{3+} ions incorporated in between. Recalling that the magnetism in this system arises from the four d -electrons of the Mn^{3+} cations, a look at Fig. 2.2 reveals that a direct overlap between neighbouring d -orbitals is not possible due to the corner sharing geometry. In this case the exchange interactions are *indirect* and occur via the p -orbitals of the non-magnetic oxygen anions placed at the corners of the octahedra. This type of interaction which involves an intermediate anion was first proposed by Anderson and is called *superexchange* [7]. The overlap between p - and d -orbitals gives rise to covalent mixing, thus allowing the nominal p -electrons to partially reoccupy the cations (one speaks about a virtual electron transfer), leading to fractional charges. Since this rearrangement depends on the relative orientation of the d -spins of the cations, the process transmits a d - d interaction [8].

Whether the dominant interactions of a particular material are direct or indirect in nature depends strongly on the underlying lattice geometry. Goodenough has pointed out, that in systems where the magnetic cation occupies an octahedral site, direct exchange

²A more general form of the spin Hamiltonian will be introduced in Sec. 2.2.3.

³The direct exchange interaction does strongly depend on the orbital overlap. For example, the exchange energy between neighbouring d -orbitals was calculated to be $J \propto R^{-10}$ (!), where R is the interionic distance [6].

interactions are dominant if the outer electron configuration is $3d^m$ ($m \leq 5$) and if the occupied octahedra share either a common edge or a common face [9]. In this case the lobes of neighbouring t_{2g} -orbitals point directly towards each other. On the other hand, if the cation-occupied octahedra share a common corner, there can be no direct overlap between neighbouring cation orbitals and the cation coupling occurs via superexchange interactions mediated by an anion.

The sign and the relative strength of spin-spin interactions between any pair of cation in octahedral geometry depends on two factors: the relative orientation within the anion octahedra and the number of electrons in the d -shell. Anderson has pointed out that superexchange interactions are maximized if the cation-anion-cation angle is 180° , while the interactions are weak in case of a 90° arrangement [7]. The latter also contributes to the fact that edge- and face-sharing geometries prefer direct exchange interactions, since in this case the superexchange angle is 90° . Anderson's preliminary findings were extended by Goodenough and Kanamori, who formulated general rules for the sign of superexchange interactions. Those rules state, that superexchange interactions are antiferromagnetic if the virtual electron transfer occurs between orbitals that are each half-filled (ferro-orbital order), while the interactions are ferromagnetic, if the virtual electron transfer occurs between an empty and a half-filled, or an filled and a half-filled orbital (antiferro-orbital order) [3, 10]. Apart from a few exceptions [11], those rules are also valid for direct exchange processes. The Goodenough-Kanamori rules reveal an interesting aspect, which is characteristic for many transition-metal compounds. They imply that spin order is accompanied by a certain orbital order. In contrast to the cooperative Jahn-Teller effect, this orbital order mechanism is purely electronic and results from kinetic exchange processes.

Finally, it has to be mentioned that the superexchange is not the only indirect exchange mechanism. The *double exchange* interaction occurs between ions with mixed valency states and results from the hopping of electrons between neighbouring (mixed valency) ions. In metallic systems, the exchange interaction between localized magnetic moments can be mediated via conduction electrons and it is termed *RKKY interaction* (Ruderman, Kittel, Kasuya, Yosida).

2.2. Molecular magnetism

The subject of molecular magnetism deals with magnetic materials that are based on organic matter. Among those materials the so called single molecule magnets (SMMs) have in particular attracted a great deal of interest in the scientific world, since it was dis-

covered that they show a slow relaxation of the magnetization at low temperatures and thus behave as tiny nano-sized magnets [12]. Similar to conventional bulk ferromagnets, SMMs exhibit a pronounced magnetic hysteresis, however, in contrast to the classical ‘bulk’ case, this cannot be ascribed as a cooperative effect, but has a pure molecular origin. Due to the resulting magnetic bistability, SMMs are considered as promising candidates for ultra-high density data storage devices.

Another key feature of SMMs is, that they allow a direct observation of pure quantum effects, such as quantum tunnelling of the magnetization and quantum coherence [13, 14]. In terms of data storage, quantum tunnelling is a negative effect, since it provides a short-cut for the relaxation of the magnetization and thus leads to a loss of information. On the other hand, the control of tunnelling effects could provide an effective way for ultra-fast switching of the magnetization, a key parameter for data processing.

In detail, SMM consist of clusters of (super)-exchange coupled magnetic ions (mostly transition metals), which are embedded in a crystal matrix of non-magnetic organic ligands [15, 16, 17, 18, 19, 20]. These ligands isolate neighbouring clusters from each other, such that magnetic inter-cluster interactions are negligible. Therefore, each molecule can be seen as a single magnetic unit of zero dimension, carrying a total ‘giant’ spin S . This spin S is derived from the individual spins s of the interacting ions within the cluster by considering the particular magnetic exchange interactions between them. The main requirement for a molecular cluster to show what is called ‘SMM behaviour’, is an energy barrier to magnetization reorientation. This energy barrier is mainly provided by two factors, a strong (negative) single ion axial anisotropy D and a high spin ground state S . The anisotropy causes a zero field splitting of the S levels into a $2S+1$ -fold multiplet, ranging from $-M_S \leq S \leq M_S$, where M_S is the spin projection quantum number belonging to the z component of the spin operator S_z (the easy axis of the molecule is assumed to point along the z direction). In the absence of any further perturbations, the levels $+M_S$ and $-M_S$ are energetically degenerate, but are separated from each other by an energy barrier $U = |D|S_z^2$ (Fig. 2.3).

2.2.1. Slow relaxation of magnetization

At sufficiently low temperatures, only the two ground state levels $|\pm M_S\rangle$ are (equally) occupied, so that in a macroscopic sample $\langle S_z \rangle = 0$. However, if a magnetic field H_z is applied parallel to the easy axis of the molecule, the ground state degeneracy is lifted and one of the two states in Fig. 2.3 becomes energetically favourable. Thus, in a sufficiently high field and at sufficiently low temperatures the system will be completely magnetized

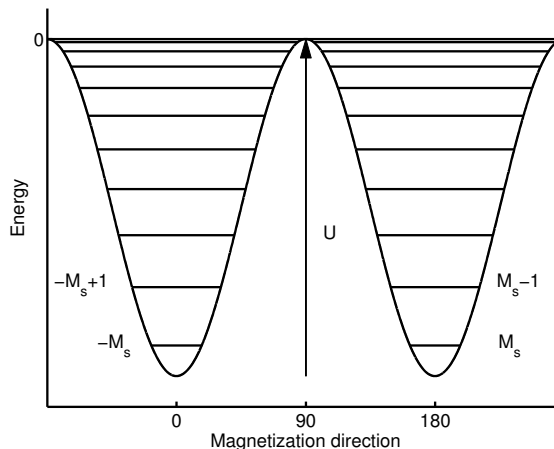


Figure 2.3.: Double well potential seen by the ‘giant’ spin of a single molecule magnet due to an uniaxial anisotropy. The classical anisotropy potential energy is given by $E(\Theta) = DS_z^2$, where $S_z = S \cos \Theta$. U denotes the height of the energy barrier and $-M_S \leq S \leq M_S$ are the spin projection quantum numbers. The abscissa gives the projection angle Θ between the magnetic moment and the easy axis of the molecule.

and behaves like a (super)paramagnet⁴. Once the field is switched off again, the system starts to relax in order to return back to its thermal equilibrium ($\langle S_z \rangle = 0$). One of the key features of SMM is that the corresponding time that characterizes the relaxation process, becomes very long at low temperatures.

The spectacular relaxation behaviour of SMM was first discovered by Sessoli *et al.* in 1993 for a dodecanuclear manganese complex of formula $[\text{Mn}_{12}\text{O}_{12}(\text{O}_2\text{CCH}_3)_{16}(\text{H}_2\text{O})_4] \cdot 2\text{CH}_3\text{COOH} \cdot 4\text{H}_2\text{O}$ (briefly $\text{Mn}_{12}\text{-ac}$) [12]. This molecule contains four ferromagnetically coupled Mn^{4+} ($s = 3/2$) ions placed in a central tetrahedron. Those ions are surrounded by eight Mn^{3+} ($s = 2$) ions, which are also ferromagnetically coupled to each other, but antiferromagnetically aligned with respect to the four central ions (see Figure 2.4(a)). Thus, the total giant spin of the molecule at low temperatures is $S = 8 \times 2 - 4 \times 3/2 = 10$. Since the molecule further possesses a strong uniaxial anisotropy, a spin ground state with $M_S = \pm 10$ is stabilized and an energy barrier for the reversal of the magnetization is generated.

Sessoli *et al.* discovered the onset of an out-of-phase component (χ'') of the ac-susceptibility below $T = 7$ K. This indicates, that the magnetization does not relax sufficiently fast in order to keep up with the applied oscillating field. Therefore, this was a clear sig-

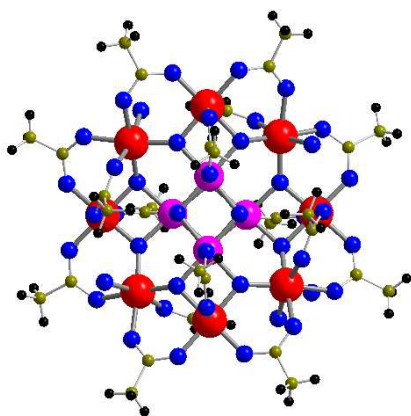
⁴The word ‘super’ refers to the fact, that the magnetic response to the external perturbation comes from all the individual magnetic centres and is therefore large.

nature, that the material experiences a barrier for the reorientation of the magnetization. Further, below the blocking temperature $T_B \approx 3.0$ K, no changes of the magnetization due to relaxation processes could be detected anymore, because the time scale of the relaxation exceeded the time scale of this experimental technique.

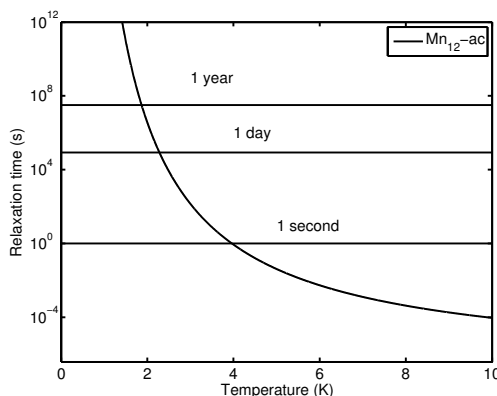
The experiment revealed, that the relaxation time τ of the magnetization follows an exponential behaviour, expressed by the Arrhenius law [12]:

$$\tau = \tau_0 \exp \frac{U}{k_B T}. \quad (2.4)$$

In the above equation, τ_0 is a system specific constant, U corresponds to the height of the barrier which has to be overcome and k_B is Boltzmann's constant. Villain *et al.* have shown, that the 'over the barrier' relaxation process is mainly driven by the coupling of the spin system to the lattice. The spin-phonon coupling allows transitions from states $|M_s\rangle$ to $|M_s \pm 1\rangle$ and $|M_s \pm 2\rangle$, which means that the reversal of the magnetization occurs through many steps, involving a sequence of energy levels (multi-step Orbach process) [21]. The fitted values of Eq. 2.4 for data from Mn₁₂-ac are $U/k_B = 61$ K and $\tau_0 = 2.1 \cdot 10^{-7}$ s [12] and the corresponding temperature dependence of the relaxation is shown in Fig. 2.4(b). Towards low temperatures the relaxation time of the magnetization becomes very long, since the thermal population of the levels is small and



(a) Mn₁₂-ac molecule



(b) Relaxation time vs. temperature

Figure 2.4.: (a) Sketch of the Mn₁₂-ac molecule. Ions are coloured as follows: Mn³⁺: red, Mn⁴⁺: pink, oxygen: blue, carbon: yellow and hydrogen: black. Reprinted (Fig. 1) with permission from Chaboussant *et al.*, Phys. Rev. B **70**, 104422 (2004). Copyright (2004) by the American Physical Society. (b) Characteristic relaxation time vs. temperature for Mn₁₂-ac. The displayed graph was obtained by plotting the Arrhenius law (Eq. 2.4) using the experimentally obtained values: $U/k_B = 61$ K and $\tau_0 = 2.1 \cdot 10^{-7}$ s [12].

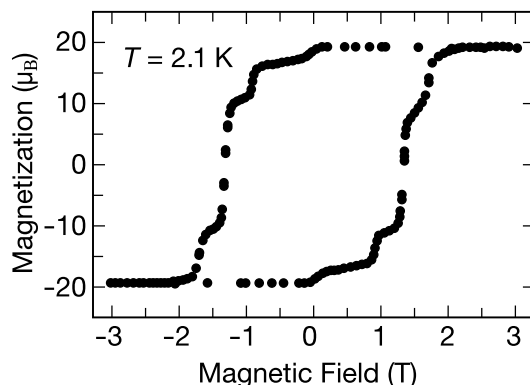


Figure 2.5.: Magnetization hysteresis loop observed for an oriented crystal of $\text{Mn}_{12}\text{-ac}$ [18]. Reproduced by permission of the *MRS Bulletin*.

the transition probability due to spin lattice coupling becomes marginal. In a system with truly axial anisotropy, the height of the energy barrier is approximately given by $U \approx |D|S^2$. Thus, the Arrhenius fit provides an indirect quantitative estimate on the magnitude of the single ion anisotropy.

However, as will be shown later in this thesis, the appearance of additional higher order anisotropy terms strongly affects the relaxation dynamics of the molecule and in this case the barrier height obtained from the Arrhenius law takes an effective value U_{eff} , which can differ significantly from the U derived by assuming only axial anisotropy.

2.2.2. Quantum tunnelling of the magnetization

At sufficiently low temperatures ($T < T_B$), single molecule magnets show a characteristic hysteresis behaviour of the magnetization. Figure 2.5 displays a typical magnetic hysteresis loop measured in $\text{Mn}_{12}\text{-ac}$ at $T = 2.1$ K. The measurements were performed with a dc-magnetometer on single crystals of $\text{Mn}_{12}\text{-ac}$ with the easy axis parallel to the applied field [18]. The hysteresis is a direct consequence of the slow relaxation dynamics of the system. More interestingly, a closer look at the data reveals that the magnetization does not change smoothly with the applied field, but undergoes several steps. At those steps, the relaxation rate is significantly increased, indicating that a further relaxation mechanism is involved in the process. This mechanism has been identified as field tuned quantum tunnelling of the magnetization between different states [13, 22]. When a field is applied along the easy axis of the SMM, the spin states of both sides of the double well potential are no longer degenerate. However, for certain regular values

of the magnetic field H_z , the energy levels on different sites of the barrier do coincide and tunnelling between those levels is allowed (see Fig. 2.6). In systems with pure axial symmetry (and considering only second order anisotropy terms), quantum tunnelling between states $M_S^{-m} = -m$ and $M_S^{-m+n} = -m + n$ can occur if the following condition is fulfilled [15]:

$$-Dm^2 + g\mu_B m H_z = -D(m-n)^2 - g\mu_B(m-n)H_z, \quad (2.5)$$

which gives:

$$H_z(n) = n \frac{D}{g\mu_B}, \quad (2.6)$$

with $n = 0, 1, 2, \dots$. Therefore, this method also allows the axial anisotropy parameter D to be estimated.

The coincidence between two energy levels at both sites of the barrier is a necessary, but not a sufficient criteria for quantum tunnelling of the magnetization. Tunnelling can only occur, if the corresponding wave functions of the two involved states are mixed and thus a transverse interaction is required. Sources for transverse interactions are low symmetry elements of the crystal field (e.g. the second order transverse anisotropy $E(S_x^2 - S_y^2)$) or internal magnetic fields, provided either by magnetic nuclei or by neighbouring molecules [18]. The mixing of states gives rise to the so called tunnel-splitting,

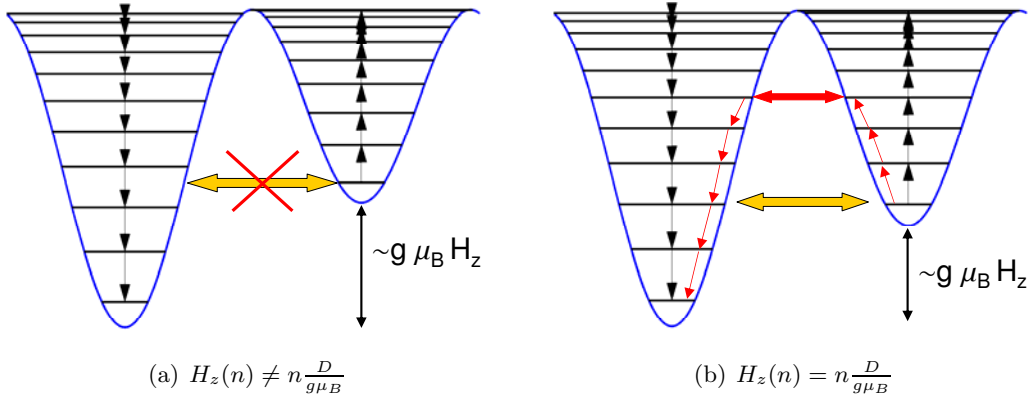


Figure 2.6.: Relaxation dynamics of a SMM for different values of the axial magnetic field. (a) Condition 2.6 is not fulfilled and the relaxation only occurs via spin-phonon coupling involving all energy levels. The process is indicated by black arrows. (b) Condition 2.6 is fulfilled and the magnetization can short cut its reversal via quantum tunnelling. Red arrows indicate the process of phonon assistant quantum tunnelling.

where the size of the splitting (Δ) determines the tunnelling rate and in general it is larger for mixed states which are at the top of the energy barrier [16]. Therefore, most of the tunnelling processes occur in the thermally activated regime and are phonon assisted. This process is indicated by the red arrows in Fig. 2.6(b). A direct result of that effect is, that the actual measured energy-barrier U_{eff} is always smaller than the one estimated by the formula $U = |D|S_z^2$.

Resonant quantum tunnelling and quantum phase interference

Pure resonant quantum tunnelling, that is tunnelling between the ground state levels only, was first observed by Sangregorio *et al.* in the octanuclear Fe(III) cluster $[\text{Fe}_8\text{O}_2(\text{OH})_{12}(\text{tacn})_6]^{8+}$ (briefly Fe_8)[23]. The Fe_8 , like $\text{Mn}_{12}\text{-ac}$, possesses an $S = 10$ ground state, which is further split due to a negative single ion anisotropy, leading to an energy barrier for magnetization reorientation of $U = 22.2$ K [24]. However, in contrast to $\text{Mn}_{12}\text{-ac}$, the Fe_8 cluster exhibits a noticeable transverse (in plane) anisotropy ($E(S_x^2 - S_y^2)$), caused by the low symmetry of the molecule. Due to this, S_z is no longer a good quantum number of the system and therefore states $+M_S$ and $-M_S$ are mixed and the corresponding wavefunctions are partially delocalized on both wells, giving rise to tunnelling. In Fig. 2.7 the relaxation times for the reversal of the magnetization as a function of temperature obtained by ac- and dc-susceptibility measurements on Fe_8 powder are displayed [25]. Down to $T_c \approx 400$ mK, the $(\ln(\tau)$ vs. $1/T$)-plot shows a straight line, indicating that the relaxation follows the exponential law given in Eq. 2.4. However, below T_c the relaxation becomes temperature independent, which means that no thermally activated levels are involved in the relaxation process and thus the pure quantum tunnelling regime is attained.

2.2.3. Spin Hamiltonian

The most common theoretical approach to describe the physics of molecular nanomagnets is the spin Hamiltonian approach. This approach is generally based on the assumption that the orbital angular momentum of the magnetic ions is quenched and thus it can be treated in a perturbative way. The corresponding Hamiltonian contains only spin-, but no orbital- coordinates, since those can be replaced by spin coordinates under consideration of the symmetry of the system. The assumption of a quenched orbital angular moment is justified for most SMM, in particular for clusters containing Mn^{3+} -ions, which

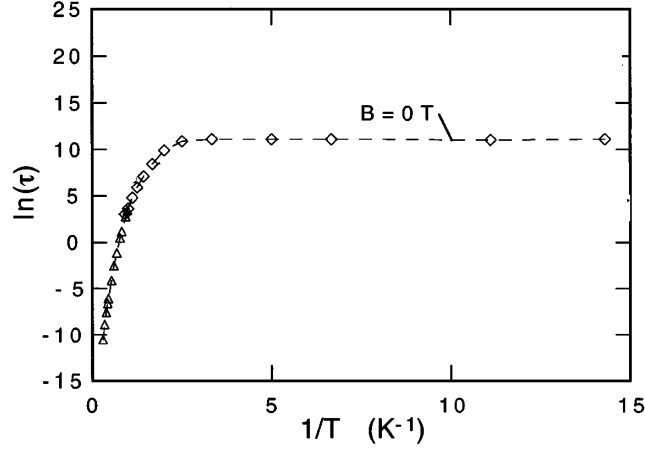


Figure 2.7.: Relaxation of magnetization measured on a powdered sample of Fe_8 in zero field. Reprinted from [25], Copyright (1998), with permission from Elsevier.

will be focused on throughout this thesis. This has been recently proved experimentally by Ghigna and co-workers, who showed by means of X-ray magnetic-circular-dichroism measurements on Mn_{12} -ac clusters, that the z -component of the orbital angular momentum $\langle L_z \rangle \approx 0$ for this material [26].

The spin Hamiltonian for a finite cluster of interacting magnetic ions reads:

$$\begin{aligned}
 \mathcal{H} &= \mathcal{H}_{\text{exc}} + \mathcal{H}_{\text{dip}} + \mathcal{H}_{\text{cf}} + \mathcal{H}_{\text{B}} \\
 &= \sum_{i>j} \mathbf{s}_i \cdot \mathbf{E} \cdot \mathbf{s}_j + \sum_{i>j} \mathbf{s}_i \cdot \mathbf{D}_{ij}^{\text{dip}} \cdot \mathbf{s}_j + \sum_i \sum_{k=0,|q|\leq k} B_k^q(i) O_k^q(\mathbf{s}_i) \\
 &+ \mu_B \sum_i g_i \mathbf{B}_i \cdot \mathbf{s}_i,
 \end{aligned} \tag{2.7}$$

where \mathbf{s}_i denotes the spin operator of the i th magnetic ion of the molecule. The first summand in Eq. 2.7 represents the exchange interactions between the magnetic ions, while the second and third term describe the dipole-dipole- and the local crystal field interaction, respectively. In the presence of a magnetic field, a fourth term describing the so called Zeeman interaction has to be considered. In the following the different terms of \mathcal{H} will be explained in detail.

Exchange interaction

The term describing the pairwise linear exchange interactions between the magnetic ions is:

$$\mathcal{H}_{\text{exc}} = \sum_{i>j} \mathbf{s}_i \cdot \mathbf{E} \cdot \mathbf{s}_j, \quad (2.8)$$

where \mathbf{E} is a cartesian spin-spin interaction tensor of rank 2. Using group theory, this tensor can be further decomposed into three irreducible independent components:

$$\begin{aligned} E^{ab} &= \frac{1}{3}(E^{xx} + E^{yy} + E^{zz})\delta_{ab} + \frac{1}{2}(E^{ab} - E^{ba}) + \\ &+ \left(\frac{1}{2}(E^{ab} + E^{ba}) - \frac{1}{3}(E^{xx} + E^{yy} + E^{zz})\delta_{ab} \right), \quad (a, b = x, y, z). \end{aligned} \quad (2.9)$$

With the expression above, Eq. 2.8 can be rewritten:

$$\mathcal{H}_{\text{exc}} = \sum_{i>j} J_{ij} \mathbf{s}_i \cdot \mathbf{s}_j + \sum_{i>j} \mathbf{d}_{ij} \cdot (\mathbf{s}_i \times \mathbf{s}_j) + \sum_{i>j} \mathbf{s}_i \cdot \mathbf{D}_{ij}^0 \cdot \mathbf{s}_j \quad (2.10)$$

where the following abbreviations were used:

$$J = \frac{1}{3}(E^{xx} + E^{yy} + E^{zz}) \quad (2.11)$$

$$\mathbf{d}_{ij} = (d_{ij}^{yz}, d_{ij}^{zx}, d_{ij}^{xz}), \quad \text{with} \quad d_{ij}^{ab} = \frac{1}{2}(E_{ij}^{ab} - E_{ij}^{ba}) = -d_{ij}^{ba} \quad (2.12)$$

$$D_{ij}^{0,ab} = \frac{1}{2}(E_{ij}^{ab} + E_{ij}^{ba} - J_{ij}\delta_{ab}) = D_{ij}^{0,ba} \quad (2.13)$$

The first term in Eq. 2.10 represents the isotropic Heisenberg interaction, the second term denotes the antisymmetric (Dzyaloshinsky-Moriya) exchange interaction and the last term represents the asymmetric anisotropic exchange interaction. In general, the isotropic Heisenberg interaction dominates the physics of the SMM and often (but not always) the other contributions can be neglected. In fact, it was recently shown, that the Dzyaloshinsky-Moriya interaction can play an important role for the tunnelling between different spin multiplets [27].

An even more general form of expression 2.10 would also include non-linear spin-spin interaction terms, such as the biquadratic exchange interaction ($\sum_{i>j} J'_{ij}(\mathbf{s}_i \cdot \mathbf{s}_j)^2$). However, contributions from those terms are usually tiny and will not be considered within this thesis [28].

Dipole-dipole interaction

The second term in Eq. 2.7 describes the magnetic intra-cluster dipole-dipole interaction. It can be derived by assuming a simple point dipole model, where the individual magnetic moments can be represented by point dipoles, whose separation from each other has to be much larger than their individual spatial extension [15]. In detail, the dipole-dipole interaction is given by:

$$\mathcal{H}_{\text{dip}} = \sum_i \sum_{i < j} \left(\frac{\mu_0}{4\pi} \right) \left(\frac{4\mu_B^2}{R_{ij}^3} \right) \left[\mathbf{s}_i \cdot \mathbf{s}_j - \frac{3}{R_{ij}^2} (\mathbf{s}_i \cdot \mathbf{R}_{ij})(\mathbf{s}_j \cdot \mathbf{R}_{ij}) \right], \quad (2.14)$$

where \mathbf{R}_{ij} is the vector joining the two dipoles at position i and j . Since \mathcal{H}_{dip} formally has the same structure as the asymmetric anisotropic exchange interaction (see Eqs. 2.10 and 2.13), both terms can be combined within an unique expression, which reads:

$$\mathcal{H}_{\text{comb}} = \sum_{i > j} \mathbf{s}_i \cdot \mathbf{D}'_{ij} \cdot \mathbf{s}_j = \sum_{i > j} \sum_a^{x,y,z} J_{ij}^a s_i^a s_j^a, \quad (2.15)$$

where the anisotropic exchange coupling parameter J_{ij}^a contains contributions from both, the dipole-dipole interaction and pure asymmetric exchange.

Crystal field interactions and Stevens operator equivalent

The interaction of the magnetic ions with the crystal field can be expressed in a symbolic way by the following Hamiltonian:

$$\mathcal{H}_{cf} = \sum_i \sum_{k=0, q \leq k}^{k_{\text{max}}} B_k^q(i) O_k^q(\mathbf{s}_i), \quad (2.16)$$

where $O_k^q(\mathbf{s}_i)$ are the so called Stevens operator equivalents for the i th ion and $B_k^q(i)$ are crystal field parameter [15, 29]. The index k can only take even integer values and depends on the single ion spin, while q is equal to a multiple of the order of rotational symmetry around the z -axis. The value of k cannot exceed $k = 4$ for transition metal ions and $k = 6$ for f-electron systems. In particular one finds:

$$s_i = 1, \frac{3}{2} \Rightarrow k = 0, 2 \quad (2.17)$$

$$s_i = 2, \frac{5}{2} \Rightarrow k = 0, 2, 4 \quad (2.18)$$

$$s_i = 3, \frac{7}{2} \Rightarrow k = 0, 2, 4, 6. \quad (2.19)$$

However, generally not all terms of Eq. 2.16 contribute to the final crystal field Hamiltonian, since, depending on the symmetry of the system, certain crystal field coefficients $B_k^q(i)$ vanish. For example in cubic crystal symmetry, with the quantization axis pointing along the fourfold axis, only the fourth- and sixth-order terms of the crystal field Hamiltonian are non-zero.

The Stevens operator equivalents $O_k^q(\mathbf{s}_i)$ are related to the single spin operators \mathbf{s}_i . Up to the fourth order they are defined as follows:

$$O_0^0(\mathbf{s}_i) = s_i(s_i + 1) \quad (2.20)$$

$$O_2^0(\mathbf{s}_i) = 3(s_i^z)^2 - s_i(s_i + 1) \quad (2.21)$$

$$O_2^2(\mathbf{s}_i) = (s_i^x)^2 - (s_i^y)^2 = \frac{1}{2}((s_i^+)^2 + (s_i^-)^2) \quad (2.22)$$

$$O_4^0(\mathbf{s}_i) = 35(s_i^z)^4 - (30s_i(s_i + 1) - 25)(s_i^z)^2 - 6s_i(s_i + 1) + 3s_i^2(s_i + 1)^2 \quad (2.23)$$

$$O_4^2(\mathbf{s}_i) = \frac{1}{4} [7(s_i^z)^2 - s_i(s_i + 1) - 5] ((s_i^+)^2 + (s_i^-)^2) + \frac{1}{4} ((s_i^+)^2 + (s_i^-)^2) [7(s_i^z)^2 - s_i(s_i + 1) - 5] \quad (2.24)$$

$$O_4^3(\mathbf{s}_i) = \frac{1}{4} s_i^z ((s_i^+)^3 + (s_i^-)^3) + \frac{1}{4} ((s_i^+)^3 + (s_i^-)^3) s_i^z \quad (2.25)$$

$$O_4^4(\mathbf{s}_i) = \frac{1}{2} ((s_i^+)^4 + (s_i^-)^4). \quad (2.26)$$

In most single molecule magnets consisting of transition metal ions, the magnetic ions are in a distorted octahedral symmetry. The resulting widely used second order crystal field Hamiltonian reads:

$$\mathcal{H}_{\text{CF}}^{\text{2nd}} = \sum_i B_0^0(i) O_0^0(\mathbf{s}_i) + B_2^0(i) O_2^0(\mathbf{s}_i) + B_2^2(i) O_2^2(\mathbf{s}_i) \quad (2.27)$$

$$= \sum_i B_0^0(i) (s_i(s_i + 1)) + B_2^0(i) [3(s_i^z)^2 - s_i(s_i + 1)] + B_2^2(i) \left[\frac{1}{2} ((s_i^+)^2 + (s_i^-)^2) \right] \quad (2.28)$$

In literature, one often finds a slightly different notation for the crystal field coefficients, being $B_2^0(i) = \frac{1}{3}d(i)$, $B_2^2(i) = e(i)$ and $B_0^0(i) = k(i)$. Using those conversions, Eq. 2.28 becomes:

$$\mathcal{H}_{\text{CF}}^{\text{2nd}} = \sum_i \left\{ d(i) [(s_i^z)^2 - \frac{1}{3} s_i(s_i + 1)] + e(i) [(s_i^x)^2 - (s_i^y)^2] + k(i) (s_i(s_i + 1)) \right\} \quad (2.29)$$

The first term in Eq. 2.29 denotes the single-ion anisotropy, while the second term represents the in-plane or transverse anisotropy. The last term is a constant which uniformly shifts all the energy levels and therefore can be omitted. If expression 2.29 is not sufficient to describe the energy level diagram of the system under investigation, higher order terms (in agreement with the crystal symmetry) can be included. However, the energies associated with the levels obtained with higher order terms (e.g. $k = 4$) of the Hamiltonian 2.16 are typically significantly smaller than the second order ones (approximately one-hundredths of that [15]) and their determination by experimental techniques is difficult.

To summarize, the spin Hamiltonian which will be used to interpret the experimental data of SMM presented in this thesis has the following form:

$$\mathcal{H} = \sum_{i>j} J_{ij} \mathbf{s}_i \cdot \mathbf{s}_j + \sum_i \sum_{k=0, q \leq k} B_k^q(i) O_k^q(\mathbf{s}_i) + \mu_B \sum_i g_i \mathbf{B}_i \cdot \mathbf{s}_i. \quad (2.30)$$

In particular, the dipole-dipole interaction will be neglected, since its contribution compared to the large crystal field anisotropy of the molecules under investigation is small. The dimension of the total Hamiltonian matrix is given by:

$$d = \prod_{i=1}^N (2s_i + 1) \quad (2.31)$$

and it becomes immediately clear, that depending on the values of the single spins and the total number of interacting ions N within the cluster, d exceeds the capability of diagonalization routines on currently available processors. It is therefore useful to find justifiable approximations, which simplify the numerical problem.

2.2.4. Spin states

In order to obtain the energy level diagram for a SMM cluster consisting of N magnetic ions, one has to solve the equation:

$$\mathcal{H}|\nu\rangle = E|\nu\rangle \quad (2.32)$$

where \mathcal{H} is the Hamiltonian given in Eq. 2.30. The eigenstates $|\nu\rangle$ of the spin Hamiltonian are a superposition of basis vectors, which in their most natural form are given by

the product states:

$$|s_1 m_1\rangle |s_2 m_2\rangle \cdots |s_N m_N\rangle, \quad (2.33)$$

where s_N is the spin of the N th ion and m_N is the corresponding spin projection quantum number belonging to $s_z(N)$. However, since generally the isotropic exchange is the leading term in Eq. 2.30, it is more convenient to choose a basis composed of the eigenstates of the total spin $\mathbf{S} = \sum_i \mathbf{s}_i$ [30]. To do so, one has to adopt a successive spin coupling scheme, where the states must be uniquely identified by a set of intermediate spin coupling quantum numbers. In the case of N magnetic ions, the following coupling scheme can be chosen:

$$\mathbf{s}_1 + \mathbf{s}_2 = \tilde{\mathbf{S}}_2, \quad \tilde{\mathbf{S}}_2 + \mathbf{s}_3 = \tilde{\mathbf{S}}_3, \quad \cdots, \quad \tilde{\mathbf{S}}_{N-1} + \mathbf{s}_N = \mathbf{S}. \quad (2.34)$$

The corresponding basis states read:

$$|s_1 s_2(\tilde{S}_2) s_3(\tilde{S}_3) s_{N-1}(\tilde{S}_{N-1}) s_N M\rangle = |(\tilde{S})SM\rangle, \quad (2.35)$$

where (\tilde{S}) represents the complete set of (\tilde{S}_k) intermediate spin states and M are the eigenvalues of the z component of the total spin operator \mathbf{S} . The coupling procedure given above is not a unique choice and a unitary transformation can be found that relates states belonging to different coupling schemes. With the basis states 2.35 a generic spin state, e.g. an eigenstate of the cluster can be expressed as follows:

$$|\nu\rangle = \sum_{(\tilde{S})SM} \langle(\tilde{S})SM\nu\rangle |(\tilde{S})SM\rangle. \quad (2.36)$$

The coefficients $\langle(\tilde{S})SM\nu\rangle$ can be found by solving the eigenvector problem for the given spin Hamiltonian \mathcal{H} .

An elegant method to simplify numerical as well as analytical calculations when working in the spin basis 2.35, is the irreducible tensor operator (ITO) formalism [31, 32]. In this formalism, which exploits the full spin symmetry of the given system, the spin Hamiltonian 2.30 can be rewritten in terms of ITO's and the corresponding matrix elements of \mathcal{H} in the basis 2.35 can then be easily evaluated by using the Wigner-Eckart theorem and a successive decoupling procedure [15].

2.2.5. Strong exchange limit - Giant Spin Approximation

In many SMM the isotropic exchange interaction ($\mathcal{H}_{\text{iso}} = \sum_{i>j} J_{ij} \mathbf{s}_i \cdot \mathbf{s}_j$) represents the most important contribution to the spin Hamiltonian. The isotropic interaction splits the energy levels of the molecule into distinct multiplets that correspond to a particular total spin value S , where the size of the level separation depends on the exchange coupling J_{ij} . If the influence of the crystal field \mathcal{H}_{CF} and other anisotropy terms $\mathcal{H}_{\text{comb}}$ (including the dipole-dipole interaction) is small compared to \mathcal{H}_{iso} , those terms can be treated as a perturbation in first order. In this so called *strong exchange limit*, one works in a fixed S multiplet and neglects the mixing between states belonging to different S manifolds caused by \mathcal{H}_{CF} and $\mathcal{H}_{\text{comb}}$. The spin Hamiltonian 2.7 can then be replaced by an effective Giant Spin (GS) Hamiltonian $\mathcal{H}_S^{\text{GS}}$, which is written in terms of the total spin operator

$$\mathbf{S} = \sum_i^N \mathbf{s}_i. \quad (2.37)$$

If one only focuses on second order anisotropy terms, one gets:

$$\mathcal{H}_S^{\text{GS}} = D_S(\hat{S}_z^2 - \frac{1}{3}S(S+1)) + E(\hat{S}_x^2 + \hat{S}_y^2) \quad (2.38)$$

In Eq. 2.38 D_S and E_S are global anisotropy parameter which can be derived from the local crystal field and asymmetric anisotropy parameter via the following expressions:

$$D = \sum_i \Gamma_i(S)d(i) + \sum_{i>j} \Gamma_{ij}(S)d'(ij) \quad (2.39)$$

$$E = \sum_i \Gamma_i(S)e(i) + \sum_{i>j} \Gamma_{ij}(S)e'(ij), \quad (2.40)$$

where Γ_i and Γ_{ij} are projection coefficients, which can be evaluated using well-established techniques [30, 31].

The anisotropy term $\mathcal{H}_S^{\text{GS}}$ causes a splitting of the isolated spin S multiplet into $(2S+1)$ components (zero field splitting). One of the great advantages of the Giant Spin Approximation is, that one works in a fixed subspace S and the dimension of the Hamiltonian matrix is therefore drastically reduced, being only $2S+1$.

2.2.6. Beyond the Giant Spin Approximation - S -mixing

The giant spin approach represents an exact solution of the spin system, if the full Hamiltonian commutes with S^2 , as it is the case for isotropically exchange coupled ions in a cluster. As long as other terms in the spin Hamiltonian, such as the magnetic dipole-dipole coupling and the local crystal field are small compared to the isotropic exchange term, the giant spin description is still a valid approximation, which in most cases leads to accurate results. However, there exist some members belonging to the class of SMMs, for which the strong exchange limit is not valid. Three examples of such SMMs will be presented in this thesis. For those molecules, the energy separation between the ground state level and the first excited level is of the same order as the zero field splitting of the ground state multiplet. As a result, S^2 is no longer a good quantum number and spin states of different total S are significantly mixed (S -mixing). In this case, Eq. 2.38 becomes completely inadequate to describe the physics of the spin cluster. It was also shown, that S -mixing tremendously affects the process of quantum tunnelling of the magnetization, since it gives rise to a strong renormalization of the tunnelling gap [33, 34].

The most straightforward way to account for S -mixing effects would be to diagonalize the full Hamiltonian given in Eq. 2.30, however, due to the large Hilbert space of certain SMMs, the evaluation of the full eigenvector spectrum, requires enormous computer power and in particular the use of fitting routines can become very tedious.

Liviotti *et al.* have proposed an alternative approach based on perturbation theory, which accounts for S -mixing by adding some additional terms to the effective Hamiltonian \mathcal{H}_S (Eq. 2.38). These terms can be written as functions of new operators, which depend on the total spin S and which are similar to the well known Stevens operator equivalents [30]. In detail, a transformation is introduced, which changes the original Hamiltonian matrix into a new one, that has very small elements in the off-diagonal blocks. The advantage is that in the new basis, states belonging to different multiplets are practically uncoupled and thus they can again be described by an effective Hamiltonian. However, it has to be mentioned, that the transformation also changes the diagonal elements of the Hamilton matrix, leading to a renormalization of the energy level scheme [30]. In particular, S -mixing has a strong effect on the fourth order anisotropy parameter, e.g. B_4^q . For example, it was shown for Fe_8 that the size of the coefficient for the O_4^0 operator resulting from S -mixing, is similar to the corresponding fourth order ZFS parameter B_4^0 , but has an opposite sign. For this reason, much care is needed when interpreting the experimentally obtained fourth order parameter [30].

2.2.7. Criterion for the anisotropy barrier in SMM

There is a continuously ongoing discussion amongst chemists and physicists about possible strategies for increasing the barrier height of the SMM and thus reaching higher blocking temperatures in order to make those systems more attractive for technical applications [17, 35, 36, 37]. When working in the strong exchange limit (expression 2.38), the barrier height is approximately given by $U \approx |D|S^2$ (the weak transverse anisotropy part will be neglected for the discussion). The strategy for reaching higher barriers seems to be quite simple then: find a SMM with a strong negative single ion anisotropy D and a high ground state spin value S . Since the latter even scales with S^2 , the strategy to increase S seems to be particularly promising. However, even the synthesis of new SMM with a total spin as high as $S = 83/2$ [38] has not brought the expected increase in barrier height and blocking temperature. For more than ten years, the barrier record was held by different variants of clusters from the Mn_{12} -family [12, 39], and it was just recently broken by one of the hexanuclear manganese complexes which will be discussed later in this thesis. However, even in this new Mn_6 compound the blocking temperature does not exceed $T_B = 4.5$ K and thus making it commercially unviable.

The reason why the concept of increasing S did not work out well is, because D and S are not independent from each other, but in fact do intrinsically belong together. This can be easily seen from expression 2.39. The total uniaxial anisotropy D is not simply the sum of the single ion anisotropies d_i of all the magnetic ions within the cluster, but depends on certain projection coefficients, which are directly related to the ground state spin S . In a magnetic cluster where all the individual magnetic ions are ferromagnetically coupled, the single ion contribution to the global D value is given by [15]:

$$D = \frac{2s_i - 1}{2S - 1} d_i. \quad (2.41)$$

From Eq. 2.41 it becomes immediately clear that the energy barrier ($U \approx |D|S^2$) only scales linearly with S . In a recent paper, Waldmann has investigated this issue in detail and extended Eq. 2.41 to the general case of spin clusters in the strong coupling limit [36]. He found out, that the increase of the barrier is even lower than one would expect from Eq. 2.41, being only of the order of unity ($\propto S^0$).

Another important role for the actual size of the energy barrier is played by the excited spin multiplets and their position in energy. In molecules, where the exchange coupling and the crystal field interactions have approximately the same size, the giant spin approximation is not valid any more and the relation $U \approx |D|S^2$ does not hold any longer. It is certainly one of the tasks of this thesis to investigate the role of excited spin multi-

plets and their influence on the barrier height and relaxation dynamics of the molecules under investigation.

2.3. One-dimensional magnetism

One-dimensional magnets present an intermediate class of compounds situated between zero-dimensional clusters of high nuclearity and three-dimensional extended lattices. Such compounds consist of isolated chains of exchange coupled magnetic moments, however, despite their simple geometry the underlining physics is highly complex and their magnetic ground states and spin dynamics differ significantly from those of conventional bulk magnets. A basic introduction will be given in the following paragraphs.

2.3.1. Magnetic ordering

To understand the relation between reduced dimensionality and the quantum nature of systems it is helpful to recall some of the findings for 3D magnets. An array of localized and exchange coupled spins can be described by the isotropic Heisenberg model:

$$\mathcal{H} = J \sum_{i,j} \mathbf{S}_i \cdot \mathbf{S}_j, \quad (2.42)$$

where \mathbf{S}_i is the spin operator of the i th site and J is the exchange interaction between neighbouring spins (only nearest neighbour interactions will be considered). For $J < 0$ the spins gain energy by aligning parallel with respect to their neighbours, leading to a ferromagnetic state, while $J > 0$ denotes an antiferromagnetic spin alignment. The vector dot product at the right side of Eq. 2.42 can be rewritten in terms of spin ladder operators $S_i^\pm = S_i^x \pm S_i^y$ and the resulting expression reads:

$$\mathcal{H} = J \sum_{i,j} \frac{1}{2} (S_i^+ S_j^- + S_i^- S_j^+) + S_i^z S_j^z. \quad (2.43)$$

The last term in Eq. 2.43 can be interpreted as the ‘potential energy’ of the spins, where it is conventional to choose the z -axis as the quantization axis. The term containing the ladder operators S_i^\pm describes fluctuations of the z -component of the spins, such that it can be interpreted as the ‘kinetic energy’ part of the spin system. In case of ferromagnetic interactions between spins ($J < 0$), the true ground state of the system is simply given by a state where all spins point along the same direction and where the

fluctuations are zero. Defining $|S_i^z| = S$, the ground state energy of Eq. 2.42 is given by:

$$\mathcal{E}_{\text{FM}} = -\frac{1}{2}N|J|zS^2, \quad (2.44)$$

where N denotes the number of lattice sites and z is the coordination number. In the ground state the system has maximum polarization along the z -direction and the maximum value of the total spin is simply $S_{\text{tot}}^z = NS$. The expectation value $M_z = \langle S_{\text{tot}}^z \rangle / N$ is the order parameter of the ferromagnetic system. It is essential to note that in the ferromagnetic case the order parameter is a conserved quantity, since the operator S_{tot}^z commutes with the Hamiltonian 2.42.

The situation becomes less simple for antiferromagnets. In this case, the ground state is not simply given by an antiparallel alignment of neighbouring spins (Néel state), in fact such an arrangement is not even an eigenstate of the system. For a strict antiparallel alignment, the system only lowers its energy from the z - z -part of the Heisenberg interactions, however, in order to obtain the true ground state energy, one also has to allow the spin z -component to fluctuate, such that the system can account for the spin flip term in Eq. 2.43. Therefore, in contrast to the ferromagnetic case, the ground state of the antiferromagnetic Heisenberg model shows *quantum fluctuations*. No exact solution exists for the ground state of an antiferromagnet in three dimensions⁵, however, it is possible to give an interval in which the real ground state energy has to lie [8]:

$$\left(-1 - \frac{1}{zS}\right)\left(\frac{NzJS^2}{2}\right) < \mathcal{E}_{\text{AFM}} < -\frac{NzJS^2}{2}. \quad (2.45)$$

The upper boundary is simply given by the Néel state, while the lower boundary is given for a scenario where all single bond energies can be minimized simultaneously. However, this is not possible, simply because a spin that has formed a singlet bond with one of its neighbours cannot form another singlet bond with another neighbour. The inequality 2.45 indicates that the largest discrepancy with the Néel state is possible for systems with a low spin value S and a low number of nearest neighbours z . In other words, quantum fluctuations are largest for low-dimensional systems with small S .

The order parameter of the antiferromagnet is the sublattice magnetization:

$$M_{\text{afm}}^z = \frac{1}{N} \left(\sum_{i \in A} S_i^z - \sum_{j \in B} S_j^z \right). \quad (2.46)$$

⁵For the $S = \frac{1}{2}$ antiferromagnetic Heisenberg chain an exact solution was given by Bethe [40].

The antiferromagnet can be divided into two alternating sublattices A and B , with all spins of A pointing up and all spins of B pointing down. This corresponds to the classical Néel state and consequently one would expect that M_{afm}^z is reduced from its saturation value due to quantum fluctuations:

$$M_{\text{afm}}^z = S - \Delta S, \quad (2.47)$$

where ΔS is called the spin reduction and can be calculated by evaluating the expectation value in Eq. 2.46. It is given by [8]:

$$\Delta S = \frac{1}{2} \left(\int \frac{d^D \mathbf{k}}{(2\pi)^D} \frac{1}{\sqrt{1 - \gamma_{\mathbf{k}}^2}} - 1 \right). \quad (2.48)$$

In Eq. 2.48 one integrates over the D -dimensional momentum space, where $\gamma_{\mathbf{k}}^2$ is a geometrical factor which is given by:

$$\gamma_{\mathbf{k}}^2 = \frac{1}{z} \sum_{\delta} e^{i\mathbf{k}\delta}, \quad (2.49)$$

where δ is a vector pointing to the nearest neighbour site. In the three-dimensional case ($D = 3$), the integral in Eq. 2.48 gives a negligible contribution and the spin reduction is found to be small (e.g $\Delta S \approx 0.078$ for the simple cubic lattice [8]). This means that quantum fluctuations are weak in a 3D system. Much more interesting, for $D = 1$ the integral in Eq. 2.48 diverges ($\Delta S \rightarrow \infty$), indicating that the assumption of antiferromagnetic long range order made in Eq. 2.46 does not hold for one-dimensional systems. In fact, strong quantum fluctuations destroy the antiferromagnetic long range order in the one-dimensional isotropic Heisenberg model for any value of S . This finding was generalized by Mermin and Wagner in their theorem, which states that the isotropic Heisenberg system does not show long range order in one and two dimensions at finite temperatures⁶ [42].

⁶This theorem is true for both, ferromagnetic and antiferromagnetic systems. In the ferromagnetic case quantum fluctuations are not present and the breakdown of long range order for $T > 0$ is due to a diverging number of low lying excitations, which result in an exponential decay of correlations at arbitrarily small finite temperatures. [8, 41, 42].

2.3.2. Excitations

Next the effect of quantum fluctuations on the excitation spectra of magnetic materials is investigated. For the sake of convenience the basic theoretical concept will be exemplified for the ferromagnet.

Since the ferromagnetic ground state is a state with all spins pointing along the same direction (e.g. the z -direction), the lowest lying excitation is certainly created if one reduces the z -component of the spin by one unit (from $S_i^z = S$ to $S_i^z = S - 1$) and let this disturbance propagate through the crystal. This excited state is called a spin wave and it corresponds to the creation of a (bosonic) quasi particle called a magnon. To explore the resulting excitation spectrum it is convenient to rewrite the spin operators in Eq. 2.43 in terms of magnon creation (a_i^\dagger) and annihilation (a_i) operators. This can be done by applying the transformation proposed by Holstein and Primakoff [43, 44]:

$$S_i^+ = \sqrt{2S} \left(1 - \frac{a_i^\dagger a_i}{2S} \right)^{1/2} a_i, \quad (2.50)$$

$$S_i^- = \sqrt{2S} a_i^\dagger \left(1 - \frac{a_i^\dagger a_i}{2S} \right)^{1/2}, \quad (2.51)$$

$$S_i^z = S - a_i^\dagger a_i, \quad (2.52)$$

where the magnon operators satisfy the fundamental commutator relations for bosonic operators: $[a_i, a_j^\dagger] = \delta_{ij}$ and $[a_i, a_i] = [a_i^\dagger, a_j^\dagger] = 0$. In order to study propagating excitations it is convenient to perform a transformation into wavevector (\mathbf{k})-space:

$$a_i^\dagger = \frac{1}{\sqrt{N}} \sum_{\mathbf{k}} e^{-i\mathbf{k}\mathbf{R}_i} a_{\mathbf{k}}^\dagger; \quad a_i = \frac{1}{\sqrt{N}} \sum_{\mathbf{k}} e^{i\mathbf{k}\mathbf{R}_i} a_{\mathbf{k}}. \quad (2.53)$$

In Eq. 2.53 R_i is the position vector of the spin at site i . In the limit of low temperatures and small numbers of excited spin waves, a suitable approximation is to replace the square-root in Eqs. 2.50 and 2.51 by 1 and only consider terms in the Hamiltonian that are linear in the bosonic operators (thus neglecting magnon-magnon interactions). This approach is called linear spin wave theory and the resulting Hamiltonian in terms of magnon operators is given by [8]:

$$\mathcal{H} = JzS \sum_{\mathbf{k}} (\gamma_{\mathbf{k}} - 1) a_{\mathbf{k}}^\dagger a_{\mathbf{k}} = \sum_{\mathbf{k}} \omega_{\mathbf{k}} a_{\mathbf{k}}^\dagger a_{\mathbf{k}}, \quad (2.54)$$

where $\omega_{\mathbf{k}} = JzS(\gamma_{\mathbf{k}} - 1)$ is the ferromagnetic dispersion relation. For the one-dimensional chain this expression simplifies to $\omega_{\mathbf{k}} = 2SJ(\cos ak - 1)$, with a being the lattice spacing. It can be noted that the dispersion of the ferromagnetic chain approaches zero for $k \rightarrow 0$, which is a consequence of the fundamental Goldstone theorem⁷ [45].

A similar approach can be used to explore the excitation spectrum of the antiferromagnet, e.g. assuming the Néel state to be the ground state and investigate the propagating properties of a flipped spin (or a created magnon, respectively). However, as has been mentioned before, the Néel-state is not the true ground state and one has to expect strong discrepancies between the real excitations of the antiferromagnet and those obtained with linear spin wave theory. Those discrepancies should be small for the 3D case, while they should be tremendous for the one-dimensional case, simply because the starting assumption of long range spin order in the ground state is not given for the latter case.

From the analytical point of view linear spin wave theory for the antiferromagnet is quite similar to the ferromagnetic case. The only main difference is that one has to introduce a pair of Bose operators for each sublattice. In Appendix C the derivation of the energy dispersion relation for the four sublattice spin wave model is described in full detail. For the simple two sublattice case, the dispersion relation is given by:

$$\omega_{\mathbf{k}} = JzS\sqrt{1 - \gamma_{\mathbf{k}}^2}. \quad (2.55)$$

As for the ferromagnet case, the gapless energy spectrum is a consequence of the Goldstone theorem. For the simple antiferromagnetic chain with each spin having two nearest neighbours, relation 2.55 simplifies to:

$$\omega_{\mathbf{k}} = JzS|\sin ka|. \quad (2.56)$$

As previously mentioned this result should differ significantly from the exact solution, due to the strong quantum fluctuations that are present in the one-dimensional case. For the $S = 1/2$ antiferromagnetic Heisenberg chain Cloizeaux and Pearson have derived the exact dispersion law, which is given by [46]:

$$\omega_{\mathbf{k}} = \frac{\pi}{2}J|\sin ka|. \quad (2.57)$$

⁷ The Goldstone theorem states that in the case of a spontaneous symmetry breaking in the ground state (e.g. the rotational symmetry in the current case) there must exist a branch of excitations for which: $\omega(\mathbf{k} \rightarrow 0) = 0$ is valid.

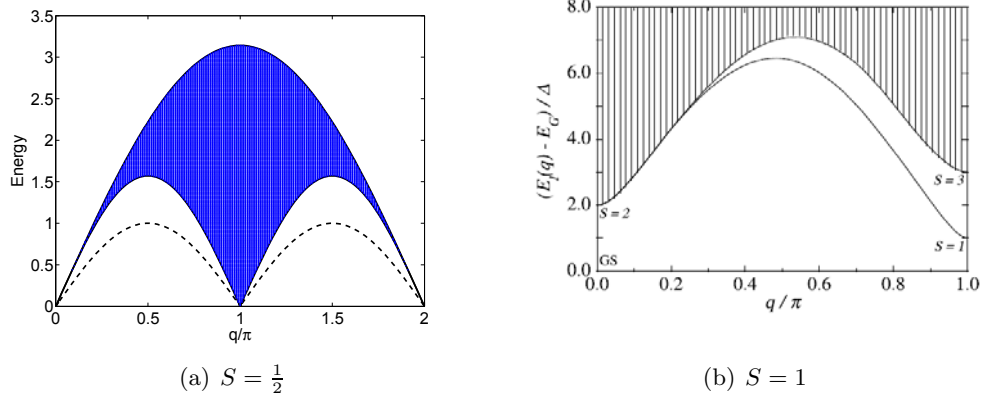


Figure 2.8.: The magnetic excitation spectra of an isotropic antiferromagnetic chain with (a) $S = \frac{1}{2}$ and (b) $S = 1$ (Reprinted from [47, 41], Copyright (1997), with permission from Elsevier. The blue region in (a) indicates the two-spinon continuum with the boundaries given by the Cloizeaux and Pearson relation [46]. The dashed line is the dispersion obtained with classical spin wave theory. The striped area in (b) indicates the multi-magnon continuum of the $S = 1$ chain.

Expression 2.57 differs from the spin wave result by a factor of $\frac{\pi}{2}$ (assuming $S = 1/2$) implying that quantum fluctuations lead to a renormalization of the excitation spectra (see Fig. 2.8(a)). Surprisingly, despite the renormalization factor, there is no further difference between Eqs. 2.57 and 2.56, suggesting that linear spin wave theory is an acceptable approximation also in the 1D case. However, this result is misleading, because there are essential differences regarding the nature of the two expressions. The dispersion 2.56 describes twofold degenerate magnon excitations from the symmetry breaking two-sublattice Néel state. As a consequence, this expression only holds for the reduced Brillouin-zone, because the magnetic unit cell is doubled. In contrast, Eq. 2.57 describes a threefold degenerate excited state, which results from a non-symmetry breaking ground state. Due to this, Eq. 2.57 holds for the entire Brillouin zone. The fundamental excitations of the antiferromagnetic $S = 1/2$ Heisenberg chain are spin- $\frac{1}{2}$ fractional fermionic particles, which are called spinons. Since in quantum mechanics changes in angular momentum are restricted to integer units, spinons can only be created in pairs [48]. As a consequence of this, the excitation spectrum shows a two-spinon continuum, where the lower boundary is given by Eq. 2.57 and the upper one is given by: $\omega_k^u = \pi J |\sin \frac{ka}{2}|$. The continuum is indicated by the blue area in Fig. 2.8(a).

There is another misleading aspect of spin wave theory for one-dimensional antiferromagnets. The result in Eq. 2.55 suggests qualitatively similar behaviour for systems with different spin values S . In fact, this is far from true and there is a fundamental difference

between antiferromagnetic chains with integer and half-integer spin values. While half-integer spin chains have a gapless spectra, with Goldstone-like modes ($\omega(k \rightarrow 0) = 0$), the integer spin chains are gapped. Moreover, the spin-spin correlation function $\langle S_i^z S_{i+j}^z \rangle$ decays with a power law for the half-integer case, giving rise to *quasi-long range order*, while it decays exponentially for the integer spin chains. This essential difference was first pointed out by Haldane [49]. In contrast to the half-integer case, the excitations of the integer spin chain are magnons and therefore bosons. Thus, the difference in the excitation spectra has a topological origin and is related to the fundamental difference between fermions and bosons under exchange [2]. The most widely studied integer spin chain is the $S = 1$ antiferromagnetic Haldane chain. It is characterized by very short-ranged spin-spin correlations, which follow an exponential law:

$$\langle S_i^z S_{i+j}^z \rangle \propto \frac{(-1)^{|j|}}{\sqrt{|j|}} \exp\left(-\frac{|j|}{\xi}\right), \quad (2.58)$$

where $\xi \approx 6.25$ is the correlation length. The excitation spectrum is depicted in Fig. 2.8(b). The size of the energy gap that separates the ground state (singlet) from the first excited state (triplet) is given by:

$$\Delta_{S=1}(q = \pi) \approx 0.41J. \quad (2.59)$$

In the vicinity of $q = \pi$ the dispersion relation can be described by:

$$\omega_q = \sqrt{\Delta_{S=1}^2 + (2.46J)^2(q - \pi)^2}. \quad (2.60)$$

Interestingly, the spectra at $q = 0$ is dominated by the two-magnon continuum, whose lower boundary starts at $\approx 2\Delta_{S=1}$, which is indicated by the striped area in Fig. 2.8(b) [41].

An important quantity of the Haldane chain, is the so called string order, which defines the order parameter of the system:

$$\mathcal{O}(i, j) = \langle -S_i^\alpha e^{i\pi \sum_{l=i+1}^{j-1} S_l^\alpha} S_j^\alpha \rangle; \quad \alpha = x, y, z. \quad (2.61)$$

The above expression describes an alternating arrangement of spin up $|+1\rangle$ and spin down $|-1\rangle$ -states, which are ‘diluted’ with strings of $|0\rangle$ states of arbitrary length [41]. Due to this, string order is often referred to as *diluted antiferromagnetic order*.

2.3.3. Effects of anisotropy

In many real crystals the assumption of spin rotational symmetry does not hold, since the mechanism of anisotropy forces the spins to point along a certain direction. Anisotropy can either be caused by direction-dependent exchange interactions, or by spin-orbit coupling, where the direction of the spin moment is influenced by the electron orbital motion. The latter type gives rise to single-ion anisotropy and since this type is the one that is relevant for the materials discussed in this thesis, the following discussion will focus on that. Single ion anisotropy has a particular impact for antiferromagnetic materials, which is due to the fact that it helps to stabilize the Néel order, even for low-dimensional systems.

The effects of single ion anisotropy can be expressed by the following term, which has to be added to the Heisenberg Hamiltonian (Eq. 2.439):

$$\mathcal{H}_{\text{ani}} = -D \sum_i (S_i^z)^2, \quad (2.62)$$

where $D > 0$ is the strength of the anisotropy. By performing linear spin wave theory for the two-sublattice antiferromagnet one obtains the following dispersion relation:

$$\omega_{\mathbf{k}} = zJS \sqrt{\left(1 + \frac{2D}{Jz}\right)^2 - \gamma_{\mathbf{k}}^2}. \quad (2.63)$$

The essential difference of Eq. 2.63 compared to Eq. 2.55 is that the excitations are now separated by an energy gap from the ground state. The size of the gap at $k = 0$ is given by:

$$\Delta_{\text{ani}} = \omega(k = 0) = zJS \sqrt{\left(1 + \frac{2D}{Jz}\right)^2 - 1}. \quad (2.64)$$

The gap size depends on both, the anisotropy parameter D and the exchange interaction J and is related to the fact, that the anisotropy forces the spins to point along a certain direction, such that any deviation from this direction requires a finite energy.

2.3.4. Effects of 3D coupling

Often, materials which are considered as one-dimensional systems, consist of chains that are *not entirely* isolated, but experience a weak coupling J_{int} perpendicular to the chain direction. Interchain coupling increases the dimensionality of the system and there-

fore it can suppress diverging fluctuations, thus enabling the system to establish long range magnetic order below a critical temperature T_c . However, even in the ordered phase, those weakly coupled systems retain their low-dimensional character, which is particularly true for systems with antiferromagnetic spin coupling. Here the quasi-low dimensionality gives rise to zero point fluctuations of the spins and the ordered moment per spin is considerably reduced. While at low energies the magnetic excitation spectra is dominated by classical transverse spin waves (Goldstone modes), the quantum fluctuations have a strong effect on the magnetic excitation spectra at energies that are high compared to the magnetic ordering temperature. A very typical feature, which appears in the crossover region between the low energy spin wave spectra and the high energy part, is the appearance of an additional longitudinal mode. This mode, which is absent in linear spin wave theory arises due to fluctuations of the spin amplitude. Longitudinal modes have been confirmed experimentally for several systems and the most prominent examples are the $S = 1/2$ chain system KCuF_3 [50, 51] and the $S = 1$ chain material CsNiCl_3 [52].

A further interesting aspect is that interchain coupling has a different effect on antiferromagnetic integer- and half-integer-chains, which is a direct consequence of Haldane's conjecture [49]. For half-integer spin chains, any finite coupling J_{inter} is sufficient to lead to 3D order at a finite Néel temperature T_N , this is because the excitation spectrum is gapless with a power law decay of the spin-spin correlation functions. A rough approximation for the critical temperature (omitting logarithmic factors) is given by: $T_N \sim |J_{\text{int}}|$ [53]. In contrast, a finite value of J_{int} is necessary to overcome the Haldane gap for integer spin systems and thus to induce 3D order below T_N . However, even for systems with sufficiently large J_{int} the 3D ordering is a weak effect and the Haldane gap reestablishes for $T > T_N$ [8, 54].

2.3.5. Frustration

Summarizing the previous findings, the recipe for strong quantum fluctuations is based on three ingredients: low-dimensionality, antiferromagnetic spin coupling and low spin values. However, there is an additional factor that can enhance quantum fluctuations and can even prevent materials with strong 3D interactions from establishing long range magnetic order. This phenomena is called geometrical frustration.

Geometrical frustration denotes the inability of a system to minimize all magnetic interactions simultaneously in the ground state. This issue is exemplified in Fig. 2.9. The three magnetic sites located at the corner of an equilateral triangle have two nearest neighbours (NN) each. If there are only NN interactions which are all equal and

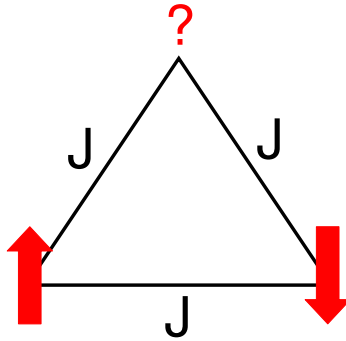


Figure 2.9.: Antiferromagnetic interactions on a triangle. All interactions have the same coupling strength J and therefore give rise to geometrical frustration.

antiferromagnetic, it is not possible to orient the spin on the third site such that it satisfies the bond interactions with its two neighbours. Generally, frustration occurs in systems composed of triangular plaquettes, such as the zigzag-chain (see Fig. 5.15), the triangular lattice, the kagomé lattice or the pyrochlore structure (lattice of corner sharing tetrahedra) [55]. The ground state of frustrated quantum materials is highly degenerate, since despite the fact that no state exists for which all interactions can be satisfied, there exist several states which are equally energetic compromises. As a result, frustrated magnets are characterized by a strongly reduced Néel temperature, or even by a complete suppression of 3D ordering.

For frustrated triangular-based systems with classical spins ($S \gg 1/2$), the best compromise between competing interactions can give rise to a non-collinear spin ordering. For example in the classical 2D triangular lattice the ground state consists of spins which are arranged in a 120° structure. However, the resulting ordering pattern is not unique and the ground state shows a discrete two-fold degeneracy that is associated with the permutation of the (three) sublattices of the triangular lattice [8]. The quantity that characterizes this is the chirality, which is defined as the sign of spin rotation along the three sides of each elementary triangle. Interestingly, for one- and two-dimensional quantum spin systems, where long range order is suppressed due to quantum fluctuations, cases exist, where the chiral symmetry is broken, meaning that there is an imbalance between left- and right- rotating spins [41]. A prominent example of chiral ordering is the $S = 1$ Haldane chain with frustrated nearest and next nearest neighbour interactions [56].

3. Experimental techniques

This chapter provides an insight into the experimental techniques that have been used in the framework of this thesis together with the corresponding basic theoretical concepts. First and foremost the technique of neutron scattering has been employed in all its variety. On the one hand, neutron diffraction measurements have been performed, which allowed a detailed analysis of the nuclear and magnetic structure of the samples under investigation, while on the other hand neutron spectroscopy served as a key tool for the study of magnetic excitations.

The experimental investigations were completed by synchrotron powder diffraction and DC-susceptibility measurements, the former being a complementary technique to neutron powder diffraction, and thus particular helpful for the investigation of elements, which are less sensitive to neutron radiation.

3.1. Neutron scattering

The interaction between neutrons and condensed matter provides unique information about the spatial and temporal correlations as well as the magnetic properties (magnetic order, magnetization density, magnetic excitations) of materials. There are several reasons why neutrons are so well suited for exploring those properties. First of all, the mass of the neutron is such ($m_n = 1.675 \times 10^{-24}$ g), that the corresponding de Broglie wavelength λ is of the same order than the interatomic distances in solids (typically a few Ångström). This leads to interference effects, that yield information on the structure of the scattering system. Secondly, the energy of neutrons produced by research sources matches that of motions in condensed matter and therefore enables the study of excitations.

Another important property of the neutron is, that it possesses a zero net charge. Due to this, it only interacts very weakly with matter and penetrates deeply into the sample, thus revealing important information about the bulk properties. Furthermore, it does not experience Coulomb forces created by the electronic charge cloud and therefore it interacts directly with the nuclei of the atoms.

Even though, the neutron has no charge, it *does* have a magnetic moment and thus it interacts with the orbital and spin angular momenta of unpaired electrons via the dipole-dipole interaction. For this reason, neutrons are a very powerful probe of magnetic properties of solids.

There are two types of modern research sources, which provide neutron radiation for scattering experiments. Either, the neutrons are ‘produced’ in a nuclear reactor, where they arise from the spontaneous fission of ^{235}U , or they are created in a spallation source by bombarding heavy targets (e.g., W, Ta, Pb, or Hg) with high-energy protons. While in the former case, the neutrons are produced continuously in time, they typically appear in pulses in the latter case.

In the next subsections the basic theoretical concepts of a neutron scattering experiment will be summarized. In detail, the neutron-scattering cross section for both, nuclear and magnetic scattering will be presented. Further, an introduction to the various types of neutron scattering techniques and instruments, which have been used in the framework of this thesis, will be given.

The following summary is mainly based on some of the many excellent textbooks on neutron scattering that are available in literature (e.g. [57, 58, 59, 60, 61]). Those books are recommended for more detailed reading.

3.1.1. Neutron scattering cross section

In a typical neutron scattering experiment, a collimated beam of neutrons with well defined momentum $\hbar\mathbf{k}_i$ and energy E_i scatters from a sample under a certain angle 2Θ and changes its momentum and energy during the scattering process into $\hbar\mathbf{k}_f$ and E_f . Since the total energy and momentum are conserved quantities, the scattering event can be expressed by the following equations:

$$\mathbf{Q} = \mathbf{k}_i - \mathbf{k}_f, \quad |\mathbf{Q}|^2 = k_i^2 + k_f^2 - 2k_i k_f \cos 2\Theta, \quad (3.1)$$

$$\hbar\omega = E_i - E_f = \frac{\hbar^2(k_i^2 - k_f^2)}{2m}, \quad (3.2)$$

where \mathbf{Q} is called the wave vector transfer (Fig. 3.1) and $\hbar\omega$ denotes the energy transferred to the sample. Generally, one differs between two types of scattering, namely elastic and inelastic. In the elastic case, no energy is transferred from the neutron to the sample and it holds that $|\mathbf{k}_i| = |\mathbf{k}_f|$. In contrast, in an inelastic scattering process the neutron either loses or gains energy throughout the scattering process ($\hbar\omega \gtrless 0$) and therefore $|\mathbf{k}_i| \neq |\mathbf{k}_f|$.

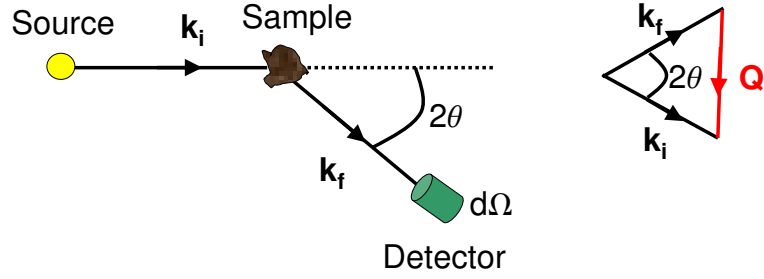


Figure 3.1.: Schematic picture of a neutron scattering event. Neutrons with a certain wavevector \mathbf{k}_i scatter at the sample under an angle 2θ . The scattered neutrons with wave-vector \mathbf{k}_f are detected within a solid angle $d\Omega$. The right picture shows the scattering triangle, which defines the scattering wavevector $\mathbf{Q} = \mathbf{k}_i - \mathbf{k}_f$.

In order to detect the neutrons which are scattered by the sample, a detector subtending the solid angle $d\Omega$ is arranged at a large distance from the sample position (see Fig. 3.1). The count-rate of the detector for neutrons having an energy between E_f and $E_f + dE_f$ is then given by:

$$I = \eta \Phi_0 \frac{d^2\sigma}{d\Omega dE_f} d\Omega dE_f. \quad (3.3)$$

In this equation, η denotes the efficiency of the detector and Φ_0 represents the incident neutron flux. The quantity $d^2\sigma/d\Omega dE_f$ is called the partial differential cross section and it is the basic quantity that is measured throughout a neutron scattering experiment and which can be related to theoretical models.

For what concerns the probing of condensed matter, the neutron interaction with the sample is generally weak and thus the corresponding interacting potential V can be treated as a perturbation. In this case, Fermi's Golden rule can be applied to calculate the transition probability W between the initial and final states (λ_i and λ_f) of the sample:

$$W_{|\lambda_i \mathbf{k}_i \sigma_i\rangle \rightarrow |\lambda_f \mathbf{k}_f \sigma_f\rangle} = \frac{2\pi}{\hbar} |\langle \lambda_i \mathbf{k}_i \sigma_i | V | \lambda_f \mathbf{k}_f \sigma_f \rangle|^2 \rho_{\mathbf{k}_f}, \quad (3.4)$$

where \mathbf{k}_i, σ_i and \mathbf{k}_f, σ_f denote the initial and final wavevector and spin of the neutron. The quantity $\rho_{\mathbf{k}_f}$ represents the number of momentum states in the solid angle $d\Omega$ per unit energy range for neutrons in the state \mathbf{k}_f .

By summing in Eq. 3.4 over all final states and averaging over all incident states (as it is generally the case in an (unpolarized) scattering experiment), one obtains the following

expression for the partial differential cross section [57]:

$$\frac{d^2\sigma}{d\Omega dE_f} = \frac{k_f}{k_i} \left(\frac{m}{2\pi\hbar^2} \right)^2 \sum_{\lambda_i, \lambda_f} p_\lambda \sum_{\sigma_i, \sigma_f} p_\sigma |\langle \lambda_f \sigma_f | V(\mathbf{Q}) | \lambda_i \sigma_i \rangle|^2 \delta(\hbar\omega + E_i - E_f), \quad (3.5)$$

where m is the neutron mass and p_λ, p_σ are statistical weight factors (assuming Boltzmann distribution) for the initial states $|\lambda_i \sigma_i\rangle$ and the δ -function ensures the conservation of energy. For the derivation of Eq. 3.5 the neutron wave-functions were approximated as plane waves and the density of states was calculated using ‘box normalization’. Further, $V(\mathbf{Q})$ describes the Fourier transform of the interaction potential at the scattering wave vector $\mathbf{Q} = \mathbf{k}_i - \mathbf{k}_f$:

$$V(\mathbf{Q}) = \int d\mathbf{r} V(\mathbf{r}) e^{i\mathbf{Q}\cdot\mathbf{r}}. \quad (3.6)$$

The integration in Eq. 3.6 runs over the neutron coordinate \mathbf{r} .

The next step is to find an explicit expression for the interaction potential V . The neutron can interact with a given sample in two ways, either via nuclear or magnetic scattering. In the first case the neutron interacts with the atomic nuclei via the strong nuclear force, while in the second case, the interaction is due to magnetic dipole forces between the magnetic moment of the neutron and the spin and orbital angular momenta present in the sample.

Nuclear scattering

The interaction between an incident neutron at position \mathbf{r} and the j th atomic nucleus positioned at \mathbf{R}_j can be described by a Fermi pseudo potential [57]:

$$V_j(\mathbf{r}) = \frac{2\pi\hbar^2}{m} b_j \delta(\mathbf{r} - \mathbf{R}_j). \quad (3.7)$$

The δ -function arises from the fact, that the strong nuclear force has a very short range (e.g. $\sim 10^5$ times smaller than the de Broglie wave-length of the neutron), such that the scattering by the nucleus is approximately spherically symmetric. In expression 3.7, b_j is the scattering length of the j th nucleus and depends on the type of the nucleus, the isotope and the relative orientation of the nuclear and neutron spin.

By inserting 3.7 into 3.5 and summing over all nuclei, one obtains an expression for the (unpolarized) neutron scattering cross section, which can be split into a coherent and

an incoherent term. Using Fourier transforms, one gets:

$$\frac{d^2\sigma}{d\Omega dE_f} = \frac{d^2\sigma_{\text{coh}}}{d\Omega dE_f} + \frac{d^2\sigma_{\text{inc}}}{d\Omega dE_f} = \frac{k_f}{k_i} \frac{1}{4\pi} [\sigma_{\text{coh}} S_{\text{coh}}(\mathbf{Q}, \omega) + \sigma_{\text{inc}} S_{\text{inc}}(\mathbf{Q}, \omega)], \quad (3.8)$$

where the total cross-sections σ_{coh} , σ_{inc} for a mono atomic system are:

$$\sigma_{\text{coh}} = 4\pi(\bar{b})^2; \quad \sigma_{\text{inc}} = 4\pi[\bar{b}^2 - (\bar{b})^2], \quad (3.9)$$

and the dynamic correlation functions $S_{\text{coh}}(\mathbf{Q}, \omega)$ and $S_{\text{inc}}(\mathbf{Q}, \omega)$ are given by:

$$S_{\text{coh}}(\mathbf{Q}, \omega) = \frac{1}{2\pi\hbar} \int_{-\infty}^{+\infty} dt e^{-i\omega t} \sum_{j,j'} \langle e^{-i\mathbf{Q}\cdot\mathbf{R}_{j'}(0)} e^{i\mathbf{Q}\cdot\mathbf{R}_j(t)} \rangle \quad (3.10)$$

$$S_{\text{inc}}(\mathbf{Q}, \omega) = \frac{1}{2\pi\hbar} \int_{-\infty}^{+\infty} dt e^{-i\omega t} \sum_j \langle e^{-i\mathbf{Q}\cdot\mathbf{R}_j(0)} e^{i\mathbf{Q}\cdot\mathbf{R}_j(t)} \rangle. \quad (3.11)$$

The bars in Eq. 3.9 denote the average over all nuclei in the system.

The above expressions clarify the different origins of the coherent and incoherent contributions to the partial differential cross-section. Coherent scattering, which manifests in the principal correlation function $S_{\text{coh}}(\mathbf{Q}, \omega)$, arises from interference between the same nucleus at different times, as well as from interference between different nuclei at different times. Therefore, coherent scattering provides information about the crystal structure (Bragg peaks) and lattice excitations. In contrast, incoherent scattering arises only from interference effects of the same nucleus at different times. It is proportional to the variance in the neutron scattering lengths and causes an isotropic background in neutron experiments. For single isotopes with zero nuclear spin, the incoherent cross section is zero.

For neutron scattering on crystalline materials, the major contribution to the coherent neutron scattering cross-section arises from elastic Bragg scattering. Due to the periodic arrangement of atoms in the crystal lattice, the scattered neutrons interfere constructively, if the Bragg condition $\mathbf{k}_i - \mathbf{k}_f = \boldsymbol{\tau}$ is fulfilled, where $\boldsymbol{\tau}$ is a reciprocal-lattice vector. In this case, peaks in intensity can be observed in the scattering pattern. The corresponding scattering cross-section for elastic scattering is given by:

$$\left(\frac{d^2\sigma}{d\Omega dE_f} \right)_{\text{nuc. elast.}} = \frac{N(2\pi)^3}{V_0} |F_N(\mathbf{Q})|^2 \delta(\mathbf{Q} - \boldsymbol{\tau}) \delta(\hbar\omega), \quad (3.12)$$

where $\delta(\mathbf{Q} - \boldsymbol{\tau})$ reflects the periodicity of the crystal lattice and N is the number of unit cells included in the volume V_0 . Further, the nuclear structure factor is defined as:

$$F_N(\mathbf{Q}) = \sum_l b_l \exp(i\mathbf{Q} \cdot \mathbf{r}_l) \exp(-W_l(\mathbf{Q}, T)). \quad (3.13)$$

The sum in Eq. 3.13 runs over all l nuclei of the unit cell, located at positions \mathbf{r}_l . b_l is the scattering length of each atom and $\exp(-W_l(\mathbf{Q}, T))$ is the (temperature dependent) Debye-Waller factor, which occurs due to thermal fluctuations of the atoms about their equilibrium positions. To determine a nuclear structure by means of single crystal diffraction, one has to measure the structure factors for a large number of Bragg reflections. This allows to set-up a model for the crystal structure and to refine the corresponding atomic parameters by comparing the calculated and measured structure factors. The same concept also holds for powder diffraction measurements, however, in this case the obtained intensity pattern represents an average of structure factors over all crystallite orientations.

Magnetic scattering

Since the neutron possesses a magnetic dipole moment, it can scatter from the magnetic moment of an atom via the dipole-dipole interaction. The size of the neutron magnetic moment is given by:

$$\boldsymbol{\mu}_N = -\gamma\mu_{\text{nuc}}\boldsymbol{\sigma}, \quad (3.14)$$

where $\gamma = 1.913$ is the gyromagnetic ratio, μ_{nuc} is the nuclear magneton and $\boldsymbol{\sigma}$ is the Pauli spin operator with eigenvalues ± 1 . The neutron moment interacts with the internal magnetic fields of the sample, which are caused by the spin and orbital angular momenta of unpaired electrons. The field produced by the i th electron of the sample being at a distance \mathbf{R} away, is given by:

$$\mathbf{B}_i = -\frac{\mu_0}{4\pi}2\mu_B \left(\nabla \times \left(\frac{\mathbf{s}_i \times \mathbf{R}}{R^3} \right) + \frac{\mathbf{l}_i \times \mathbf{R}}{R^3} \right). \quad (3.15)$$

\mathbf{s}_i and \mathbf{l}_i represent the spin and angular orbital momenta respectively of the i th electron and μ_B is the Bohr magneton. The first term in the brackets of Eq. 3.15 represents the field arising from the spin angular momentum, while the second term is the field arising from the orbital angular momentum. In many systems consisting of transition metal ions (e.g. transition metal oxides), the orbital angular momentum is quenched

as a result of the crystal field, which lifts the degeneracy of the d -orbitals. For such cases, the magnetic cross-section is purely due to spin scattering. This is e.g. the case for Mn^{3+} -ions, which are responsible for the magnetism in the single molecule magnets presented in this thesis (see Chapter 4). However, the assumption of orbital quenching is not generally valid, and especially for systems with partially filled t_{2g} -orbitals, the orbital angular momentum has a strong effect. An example for such a system is CaV_2O_4 , the second sample which has been investigated in the framework of this thesis (Chapter 5). In order to obtain an expression for the magnetic differential cross section, one needs to define the magnetic interaction potential for a neutron with the i th magnetic ion. This is given by:

$$V = -\boldsymbol{\mu}_N \cdot \mathbf{B}_i. \quad (3.16)$$

By inserting Eq. 3.14 and 3.15 into 3.16 and further inserting Eq. 3.16 into 3.5, one obtains (after a non-trivial amount of algebra [57]) the following expression for the partial differential cross-section for magnetic scattering, where for the sake of simplicity only one type of magnetic ions, with spin angular momentum only, was assumed:

$$\left(\frac{d^2\sigma}{d\Omega dE_f} \right)_{\text{mag}} = (\gamma r_0)^2 \frac{k_f}{k_i} \left(\frac{g}{2} f(\mathbf{Q}) \right)^2 \exp(-2W(\mathbf{Q}, T)) \sum_{\alpha\beta}^{x,y,z} \left(\delta_{\alpha\beta} - \frac{Q_\alpha Q_\beta}{Q^2} \right) S^{\alpha\beta}(\mathbf{Q}, \omega) \quad (3.17)$$

In this expression, $r_0 = 2.818 \cdot 10^{-15}$ m is the classical electron radius, g is the Landé splitting-factor, which equals 2 for spin only scattering and $f(\mathbf{Q})$ is the magnetic form-factor. The form-factor arises, because of the finite spatial extension of the scattering object (electron cloud of unpaired electrons), which cannot be approximated by a δ -function, as it is the case for nuclear scattering. Since $f(\mathbf{Q})$ decreases rapidly with \mathbf{Q} , it limits the range in which magnetic scattering can be observed to the low- \mathbf{Q} region.

The factor $\exp(-2W(\mathbf{Q}, T))$ in Eq. 3.17 is the Debye-Waller factor and the term $(\delta_{\alpha\beta} - \frac{Q_\alpha Q_\beta}{Q^2})$ ensures, that only spin components perpendicular to \mathbf{Q} contribute to the cross-section. Finally, the dynamic spin correlation function $S^{\alpha\beta}(\mathbf{Q}, \omega)$, which is the space and time Fourier transform of the time-dependent spin-spin correlation function, is defined as:

$$S^{\alpha\beta}(\mathbf{Q}, \omega) = \sum_{i,j} \exp(i\mathbf{Q} \cdot (\mathbf{R}_j - \mathbf{R}_i)) \int_{-\infty}^{\infty} dt \exp(i\omega t) \langle S_i^\alpha(0) S_j^\beta(t) \rangle, \quad (3.18)$$

where $S_j^\beta(t)$ is the time dependent operator for the β -component of the spin of the j th magnetic ion. $S^{\alpha\beta}(\mathbf{Q}, \omega)$ is a very important property, since it contains all the information about the magnetic structure and dynamics of the system under investigation.

The generalization to the case of magnetic ions with unquenched orbital angular momentum is straightforward. In this case, the generalized g -factor of Eq. 2.2 accounts for the effects of spin-orbit coupling and the operator S in Eq. 3.18 has to be replaced by an effective total angular momentum operator.

If long range magnetic order occurs in a crystal, meaning that the spins are periodically arranged throughout the lattice, then the magnetic scattering displays interference elastic peaks, similar to the nuclear Bragg scattering. Magnetic Bragg peaks can be detected, if the neutron wave vector transfer \mathbf{Q} equals a magnetic reciprocal lattice vector $\boldsymbol{\tau}_M = \boldsymbol{\tau} + \mathbf{k}$ and if further \mathbf{Q} has a component, which is perpendicular to the direction of the ordered spins. The quantity \mathbf{k} is called the magnetic propagation vector. The partial differential cross-section in the case of magnetic coherent scattering reads:

$$\left(\frac{d^2\sigma}{d\Omega dE_f} \right)_{\text{mag. coh. elast.}} = \frac{(2\pi)^3 N_m}{V_0} \left(\frac{\gamma r_0}{2} \right)^2 \sum_{\alpha\beta}^{x,y,z} \left(\delta_{\alpha\beta} - \frac{Q_\alpha Q_\beta}{Q^2} \right) \times F_M^\alpha(\mathbf{Q}) F_M^\beta(\mathbf{Q}) \delta(\mathbf{Q} - \boldsymbol{\tau}_m) \delta(\hbar\omega), \quad (3.19)$$

where N_M is the number of magnetic unit cells contained in the volume V_0 . Further, the magnetic structure factor $F_M^\alpha(\mathbf{Q})$ is defined as:

$$F_M^\alpha(\mathbf{Q}) = f(\mathbf{Q}) \exp(-W(\mathbf{Q}, T)) \sum_l \mu_l^\alpha \exp(i\mathbf{Q} \cdot \mathbf{r}_l). \quad (3.20)$$

Here, μ_l^α is the component α of the magnetic moment of the l th atom located at position \mathbf{r}_l in the magnetic unit cell. A collection of a suitable set of magnetic Bragg intensities and the comparison to the theoretical expression 3.20 enables a precise determination of the magnetic structure of a given system.

3.1.2. Neutron Diffraction

The aim of a (neutron) diffraction experiment is to gain insights into the nuclear and/or magnetic structure of a given sample. In detail, one measures the partial differential nuclear and/or magnetic coherent elastic cross section (Eq. 3.12 and 3.19) for a broad range of wave vector-transfer \mathbf{Q} . By doing so, peaks in intensity appear in the detector,

if the condition for elastic Bragg scattering is fulfilled:

$$\mathbf{Q} = \mathbf{k}_i - \mathbf{k}_f = \boldsymbol{\tau}, \quad (3.21)$$

$$|\mathbf{Q}| = |\boldsymbol{\tau}| = 2|\mathbf{k}_i| \sin \theta = \frac{4\pi}{\lambda} \sin \theta. \quad (3.22)$$

In the above expression, $\boldsymbol{\tau}$ is a reciprocal lattice vector and 2θ is the angle between the incident and final beam. Under the Bragg condition, constructive interference occurs between the neutrons that are scattered on a set of parallel lattice planes, where the inter-planar spacing is defined as $d = \frac{2\pi}{|\boldsymbol{\tau}|}$. Inserting this expression into Eq. 3.22 leads to the well known Bragg law:

$$n\lambda = 2d \sin \theta, \quad (3.23)$$

with $\lambda = \frac{2\pi}{|\mathbf{k}_i|}$ being the wavelength of the incoming neutrons.

The integrated intensity of the observed Bragg peaks is directly proportional to the square of the nuclear (or magnetic) structure factor $|F(\mathbf{Q})|^2$, which contains detailed information about the structural parameter, such as the atomic positions and (in the case of magnetic scattering) the size and direction of the magnetic moments (Eq. 3.12, 3.13 and 3.19, 3.20). Thus, if a sufficient amount of Bragg intensities has been collected, one can set up a structural model and compare the calculated structure factors F_C^2 with the observed ones F_O^2 . The next step is then, to apply a refinement method and optimize the values of the structural parameters by minimizing the differences $|F_O^2 - F_C^2|$.

In the following subsections, details about the experimental technique of neutron diffraction will be given, where it will be differentiated between single crystal diffraction and powder diffraction. Particular emphasis will be placed on the procedure of data analysis and model refinement, which becomes especially highly non-trivial in the case of powder diffraction. In a powder, reflections belonging to different lattice planes, which have similar lattice spacings, give rise to strong peak overlap and therefore hamper the extraction of exact Bragg intensities.

Even though, the title of this section implies, that the techniques and methods presented here are especially dedicated to neutron radiation, they do also apply for synchrotron radiation, as long as one accounts for the differently defined scattering lengths (for more details on X-rays see Sec. 3.2.1).

Single crystal diffraction

If high quality single crystalline samples of sufficient size are available for a given material, then single crystal diffraction (SCD) is the 'first-choice method' for determining its crystal structure with high accuracy. SCD allows precise information about the crystal symmetry to be obtained, the particular atomic positions, interatomic bond distances and angles and also the thermal atomic displacement factors. Further, neutron SCD is a unique tool to solve the magnetic structure of materials.

Four-circle diffractometer

From Eq. 3.22 it can be seen, that in the case of monochromatic radiation ($\lambda = \text{const.}$), the magnitude of the scattering vector $|\mathbf{Q}|$ is solely controlled by the scattering angle 2θ . The geometry of a conventional single crystal diffractometer is such that the incident beam, the sample and the detector all lie on the same equatorial plane. That means, 2θ can simply be changed by rotating the detector in this plane on a circle around the sample position. Further, the orientation of \mathbf{Q} can be modified by rotating the crystal around one of its axes. Therefore, by an appropriate choice of sample orientation and detector position it is possible in equatorial geometry to measure any point in reciprocal space that lies within the limit $(-\frac{4\pi}{\lambda} \leq |\mathbf{Q}| \leq \frac{4\pi}{\lambda})$.

The most commonly used single crystal diffraction instrument with equatorial geometry is the four-circle diffractometer. Instruments of this type are mostly located at neutron reactor sources, where a steady neutron flux is provided. The main parts of the four-circle diffractometer are:

- the monochromator, which selects a certain neutron wavelength,
- the Eulerian cradle (with the crystal mounted on it), which allows the crystal to rotate all over the three dimensional space,
- and the detector, which can be either a single point or an area detector.

Figure 3.2(a) shows a sketch of such an instrument. The instrumental main axis lies normal to the equatorial plane (and therefore to the incident and diffracted beam) and passes through the crystal. The *four circles* of the diffractometer are described by the angles χ , ϕ , ω and 2θ . The latter two circles are coaxial, both describing a rotation around the main axis, where one moves the cradle (ω) and the other moves the detector (2θ). The cradle is constituted by the χ circle that carries the goniometer head with the

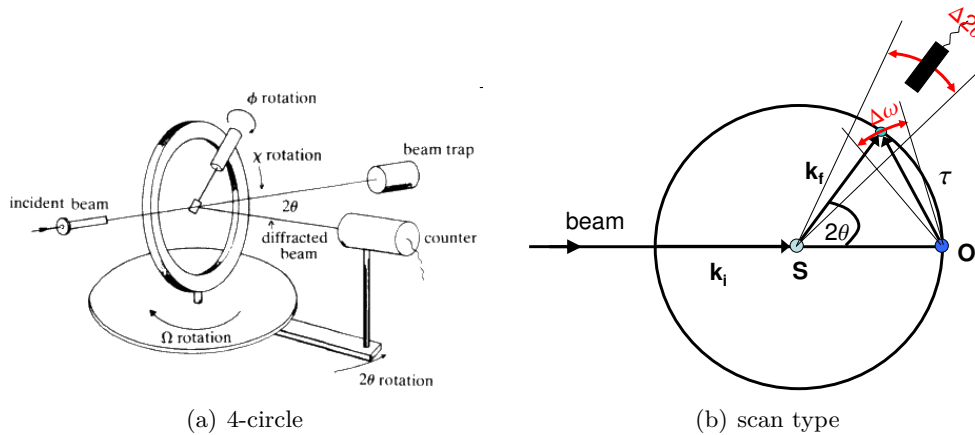


Figure 3.2.: The method of single crystal diffraction. (a) Sketch of a four circle diffractometer (taken from [62]), (b) Relation between the position of the sample S and the detector in real space and the reciprocal lattice of the crystal. \mathbf{k}_i and \mathbf{k}_f are the incident and final lattice vectors, where $|\mathbf{k}_i| = \frac{2\pi}{\lambda}$ denotes the radius of the circle (Ewald construction). The reciprocal lattice vector $\boldsymbol{\tau}$ points from the origin O of the reciprocal lattice towards the reciprocal lattice point, for which the Bragg condition is fulfilled and therefore which lies on the circle. The red arrows show the different scan types.

mounted crystal on top. This circle is vertically arranged with respect to the equatorial plane and the angle χ is defined by the main axis and the spindle of the goniometer head. Finally, the ϕ circle is coaxial to the goniometer and the crystal. For bringing a reciprocal lattice point in diffraction condition on the equatorial plane, it is only necessary to move the angles ω and χ . However, in some cases, the scattered beam might be shadowed by mechanical parts of the diffractometer, such that the rotation around ϕ can be helpful.

The actual data collection on a four-circle diffractometer follows a straightforward procedure. First, one has to find an orientation matrix (UB-matrix), which transforms between the three reciprocal crystal axes and the axes of the goniometer. The UB matrix can be found using standard methods (see e.g. [63]) and once this has been achieved, it is possible to calculate the position of each reciprocal lattice point and thus move the four circles to the calculated positions and measure the Bragg intensity.

The scattered intensity in the case of Bragg reflection does not arise from a single point in reciprocal space only, but from a small three-dimensional volume around the actual Bragg position. This spread of intensity is caused by a combination of small incident beam angular and energy divergence, as well as the mosaic spread within the crystal. Therefore, in order to collect accurate values of integrated Bragg intensities, a scan through the entire reciprocal space volume of each reflection has to be performed. Ba-

sically, there are two different scanning modes which are widely used for this issue. The first one is a pure ω -scan. For this scan type, the detector remains stationary at the ideal diffraction angle 2θ , while the ω -circle is used to move the peak through the diffracting position. The section that is sampled with this type of scan lies on an arc which is centered at the origin of the reciprocal lattice. In the ω - 2θ scan mode, the ω -rotation is performed in the same way than before, but the detector on the 2θ circle moves simultaneously with ω , while having twice the speed. This scene is depicted in Fig. 3.2(b). The section of reciprocal space, which is sampled in this way, lies in the direction of the reciprocal lattice vector $\boldsymbol{\tau}$. Both scan types have certain advantages and disadvantages and their choice depends on the particular experiment [63].

For the single crystal diffraction measurements presented in this thesis the thermal neutron four-circle diffractometer E5 located at Helmholtz-Zentrum Berlin was used (see Chapter 5 and [64]).

In some cases, the extended size of the sample environment, which is necessary to study samples under extreme conditions (low temperatures, high magnetic fields) prevents the use of a four circle diffractometer, since the Euler cradle does not provide much space for additional attachments. In this cases, a simplified two-circle diffractometer can be used, with the two circles defining the rotation of the sample (ω) and of the detector arm (2θ). However, the disadvantage of such an instrument is the limited accessible reciprocal space of the sample, since within one orientation one is only able to access the Bragg reflections of one certain scattering plane. In the framework of this thesis, the two-circle diffractometer E4 at HZB Berlin has been used to study the low temperature magnetic phase of CaV_2O_4 (see Chapter 5 and [64]).

Time-of-flight Laue diffractometer

A different diffraction geometry is used, if the provided neutrons appear in well defined pulses of varying wavelengths, as it is the case in a spallation neutron source. The technique usually utilized in this case is the neutron time-of-flight Laue method. For this method, the diffraction angle is experimentally fixed by the (fixed) position of the detector. The pulsed structure of the beam allows the time-of-flight for each neutron to be investigated and from this, the corresponding wavelengths can be derived:

$$\lambda = \frac{h}{mv} = \frac{ht}{m(L_1 + L_2)} = 2d \sin \theta. \quad (3.24)$$

In this expression, t is the neutron time-of-flight, ($L = L_1 + L_2$) is the total flight path, where L_1 represents the distance from the neutron source to the sample and L_2 is the

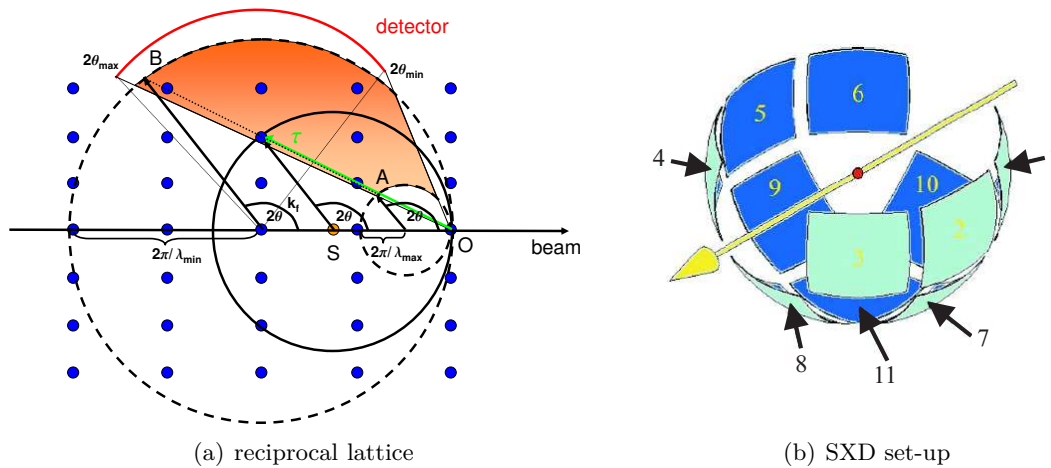


Figure 3.3.: (a) Real space position of detector (red) and sample S and their relation to the available reciprocal space. The minimum and maximum magnitude of the incident neutron wave vector are indicated by the dashed circles. (b) Sketch of the Neutron Laue single crystal diffractometer SXD. The yellow arrow shows the direction of the incoming neutron pulse and the sample position is indicated by the red sphere. From Keen *et al.* [65]. Copyright (2006) by the International Union of Crystallography.

sample detector distance. Further, m is the neutron mass and θ is half the scattering angle.

If the polychromatic neutron pulses cover a wavelength interval between λ_{\min} and λ_{\max} , then a detector positioned at a certain diffraction angle $2\theta_{\text{fix}}$ detects neutrons in the wavevector range $\frac{4\pi}{\lambda_{\max}} \sin \theta_{\text{fix}} \leq |Q| \leq \frac{4\pi}{\lambda_{\min}} \sin \theta_{\text{fix}}$. Therefore, the time-of-flight Laue technique enables it to measure the scattering intensity from a reciprocal lattice point as a function of wavelength. The corresponding structure factors hence can be obtained by integrating the intensity over wavelength, (rather than over scattering angle). This scenario is depicted in Fig. 3.3(a). The reciprocal space volume that is ‘scanned’ by the instrument is defined by the available neutron wavelengths-range (dashed circles) and by the position of the sample and the detector. For instance, a point detector positioned at B (see Fig. 3.3(a)) measures (as a function of time), the line in reciprocal space which connects the points A and B . By placing many detectors around the sample, it is possible to cover a huge area of reciprocal space. An instrument, where the Laue method is utilized is the single crystal diffractometer SXD at the ISIS spallation neutron source. Due to the subtle arrangement of eleven position sensitive ZnS detectors around the sample space (see Fig. 3.3(b)), SXD picks up a huge volume of reciprocal space in one single measurement.

Data integration and correction

Once a suitable set of data is collected, the next step in the process of nuclear (or magnetic) structure determination is the integration and correction of the collected Bragg intensities. The integration of Bragg intensities is usually a straightforward procedure and based on conventional methods [63]. In most cases, it can be done automatically by using special peak integration software for single- or multi-detector data. However, a special case where conventional methods failed to extract correct Bragg intensities will be presented in Chapter 5. In this chapter the nuclear and magnetic structure of CaV_2O_4 is discussed. Due to the low crystal symmetry of this material, twinning of Bragg reflections occurs and leads to significant overlap of certain reflections.

The final list of integrated intensities has to be corrected for the so called *Lorentz factor*. This factor corrects for the fact, that during a scan through the reciprocal lattice, different lattice planes remain for different times in reflection position, thus causing disproportionalities in the integrated Bragg intensities. In its simplest possible form the Lorentz factor is given by $L = (\sin 2\theta)^{-1}$ [63]. Finally, the observed intensities are related to the square of the structure factor in the following way:

$$I_O = SL|F_O|^2 = S(\sin 2\theta)^{-1}|F_O|^2. \quad (3.25)$$

Here S is an overall scale factor, which depends on the particular instrumental setup, the incident flux and some universal constants. In some cases, one has to include additional factors, which account for absorption and extinction effects (for more details see [63, 66]).

Refinement

The final set of corrected integrated Bragg intensities can be used for the actual refinement of the crystal structure. The refinement is based on the least square method, and consists of minimizing the following equation:

$$\sum_{hkl} \omega (F_O^2 - F_C^2)^2 = \min, \quad (3.26)$$

where F_O and F_C are the observed and calculated structure factors for the Bragg reflection with Miller indices (hkl) , respectively, and $\omega = 1/\sigma^2$ is a weight factor that accounts for the standard deviation of the observed reflections. In the case of nuclear

neutron scattering, the static structure factor for the N th Bragg reflection is given by:

$$F_N(\boldsymbol{\tau}) = \sum_j \bar{b}_j e^{i\boldsymbol{\tau}\mathbf{d}_j} e^{-W_j}, \quad (3.27)$$

where $\mathbf{d}_j = (x_j, y_j, z_j)$ are the positions of the j th atom in the unit cell, \bar{b}_j is the coherent scattering length and e^{-W_j} is the Debye-Waller factor, which describes the mean displacement of the j th atom¹. In the case of isotropic displacement $W_j = B_j \sin^2 \theta / \lambda$ can be used.

If the number N of observed structure factors is greater than the number of (unknown) structural parameters (\mathbf{d}_j, B_j) , the parameter are said to be overdetermined. In this case it is possible to evaluate the structural parameters in terms of the measured structure factors and an iterative method can be used to find the minimum of Eq. 3.26. Since the calculated structure factor F_C does depend on (\mathbf{d}_j, B_j) in a complicated, nonlinear fashion, it is important to use suitable structural starting values for the refinement, which lie already in the vicinity of the final ones [66].

Finally, in order to indicate how well a structural model actually conforms to ‘reality’, so called agreement factors are given for each refinement. The three most common ones are listed below:

$$R_F = \frac{\sum_{hkl} ||F_O| - |F_C||}{\sum_{hkl} |F_O|}, \quad (3.28)$$

$$R_F^2 = \frac{\sum_{hkl} |F_O^2 - F_C^2|}{\sum_{hkl} |F_O^2|}, \quad (3.29)$$

$$R_{\omega F}^2 = \sqrt{\frac{\sum_{hkl} \omega (F_O^2 - F_C^2)^2}{\sum_{hkl} \omega (F_O^2)^2}}. \quad (3.30)$$

The first quantity is simply called (conventional) R-factor and it is the one which is most often given in publications. This factor simply depends on the differences of the observed and calculated structure factors and (if multiplied by 100) gives the relative deviation between both values in percent. However, the quantity which is actually observed in a diffraction experiment is the square of the structure factor. This is taken into account by R_F^2 . At last, the weighted $R_{\omega F}^2$ -factor is another helpful quantity, since it accounts for the precision of the measured parameter. For the nuclear and magnetic structural refinements presented in this thesis, all three agreement factors are given.

¹A similar expression is given for the magnetic structure factor, where the scattering length is replaced by the magnetic form factor (see Eq. 3.20).

Powder diffraction

It seems to be an irony of nature, that many of the materials that attract great interest among solid state chemists and physicists are only available as powders. Compared to single crystals, the diffraction from a powder leads to a significant loss of information, because the three-dimensional space is compressed into an one-dimensional powder pattern. This in turn leads to a systematic and/or accidental overlap of diffraction peaks, making it difficult to determine the particular integrated intensities of each Bragg reflection and therefore the structure factor.

However, the development of modern sources for x-ray and neutron radiation with high quality beam and high resolution instruments, in combination with sophisticated data analysing software narrowed the gap between single crystal and powder diffraction. Nowadays, powder diffraction is a very powerful and unique tool for characterizing materials in terms of the types and quantities of phases present in them, the crystal structure and unit cell, crystalline size, macro-stress and micro-strain. In addition, neutron powder diffraction is successfully used to solve magnetic structures of materials.

One of the key-points for a successful powder diffraction experiment is the quality of the powder. The ideal powder consists of a large number of small randomly oriented crystallites. By the large number it is guaranteed, that there are enough crystallites in any diffracting orientation in order to provide reproducible diffraction patterns. On the other hand, those crystallites have to be small [$O(10\mu\text{m})$], since only in this case the intensity of the diffracted rays can be measured accurately. If the randomness of the powder is not given, ‘preferred orientation effects’ arise and show up in the data as disproportionally strong intensities of some reflections.

Figure 3.4 gives a schematic view of an incident beam scattered by a powder. The

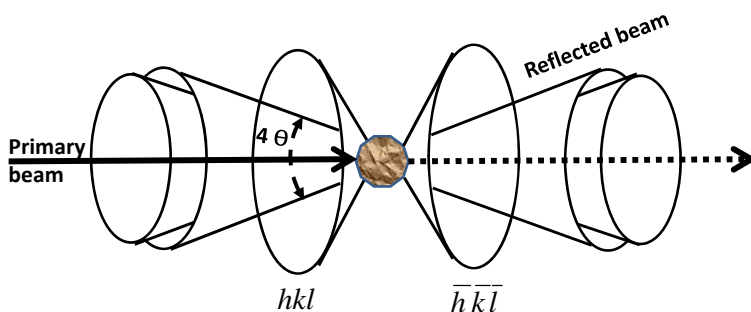


Figure 3.4.: Scattering from a powder sample, for details see text (Own illustration based on [67]).

forward- as well as the back-scattered rays form coaxial cones (Debye-Scherrer cones) with the direction of the incident beam being the cone axis. Each cone results from scattering of a set of lattice planes, having the same d -spacing, but not necessarily the same lattice vector. If a two dimensional detector is placed perpendicular to the direct beam, the cones appear on it as concentric circles. Since each circle represents a different scattering angle 2Θ and therefore a different set of lattice planes, it is possible to draw conclusions on the lattice of the scattered crystallites. In addition, the intensity of each ring provides essential information about the type and position of the atoms within the crystal. Consequently, the main task of a diffraction experiment is the detection and recording of the scattered beam over a broad range of 2Θ . Since the intensity around each ring is isotropic (at least if an ‘ideal’ powder is assumed), conventional powder diffraction experiments only take one-dimensional cuts through the rings. In most experiments using monochromatic radiation, the final powder pattern is obtained by step scanning a detector on a circle around the sample with small increments $\Delta(2\Theta)$. The detector can either be a single point-, a one-dimensional- or a two-dimensional detector. In the latter case it is possible to detect large fractions of the Debye-Scherrer rings and an integration around them can not only improve statistics, but also minimize ‘preferred orientation effects’. An example of an instrument which uses the Debye-Scherrer geometry is the high resolution synchrotron powder diffractometer located at the BM01B beamline at ESRF. The set-up of this instrument is described in Sec. 3.2.1.

A different technique is used when dealing with polychromatic radiation. In this case the energy dispersion of the scattered neutrons or x-rays at a fixed angle 2Θ is measured. This technique is mostly applied at neutron spallation facilities, since the pulsed structure of the neutron beam at these sources provides the possibility to use the ‘energy-selective’ time-of-flight method. By recording the arrival time of each neutron of a particular pulse in the detector, it is possible to determine the neutron wavelength and further the d -spacing of the diffracting lattice planes via:

$$\lambda = \frac{h}{mv} = \frac{ht}{mL} = 2d \sin \Theta. \quad (3.31)$$

In this equation m and v are the mass and velocity of the neutron, respectively, t is the time of flight and L is the length of the flight path. In Fig. 3.5 the schematic of the Special Environment Powder Diffractometer (SEPD), located at IPNS, Argonne is depicted. In contrast to angle-selective diffractometers, SEPD has fixed detectors, which is a great advantage if special sample environments are required (e.g. pressure cells with fixed windows). In detail, the instrument consists of (two times) four detector banks

located at different 2Θ angles around the sample ($2\Theta = \pm 22^\circ, \pm 44^\circ, \pm 90^\circ, \pm 145^\circ$). For a precise crystal structure determination, usually the data recorded at the high angle backscattering detectors are chosen, since those provide the best resolution in d -space². In contrast, the low angle detectors have a lower resolution, but ‘see’ a larger d -range. Those detectors are particularly helpful for the investigation of magnetic scattering, which appears strongest in the low Q - and therefore large d region.

The resulting powder pattern obtained with both, the ‘energy dispersive technique’ and the ‘angular dispersive technique’ look very similar, except that one measures the time-of-flight in one case and 2Θ in the other. However, the analysis of the various patterns does not depend on the underlying diffraction technique and the refinement procedure, which will be described in the next subsection is generally valid.

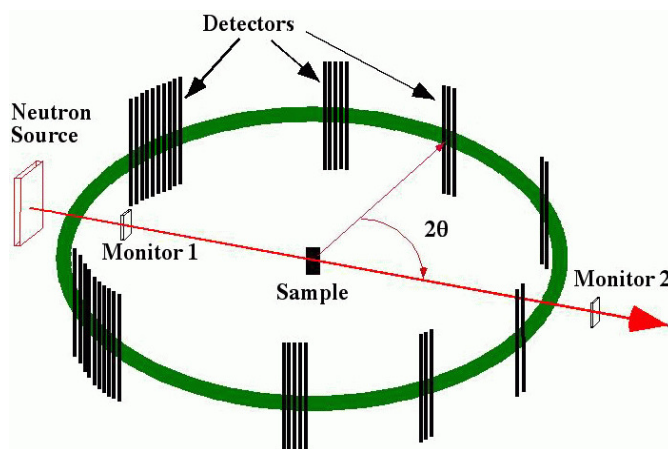


Figure 3.5.: Schematic picture of the time of flight neutron diffractometer SEPD at IPNS (picture taken from [68]).

Rietveld refinement

A very powerful and successful method of extracting structural information from a powder pattern was developed by Rietveld [69]. His method is based on a least-squares refinement of the entire powder pattern until the best fit between a calculated and the measured data set is reached. The calculated pattern is obtained from simultaneously refined models for the crystal structure(s), instrumental factors, diffraction optics effects and other characteristics of the investigated specimen.

²The d -spacing resolution for a time-of-flight powder diffractometer is given by $(\delta d/d)^2 = (\delta t/t)^2 + (\delta L/L)^2 + (\cot \Theta \delta \Theta)^2$ [67]. Therefore, for high 2Θ angles, $\cot \Theta$ approaches zero, which leads to a very good resolution.

The key quantity which is minimized in the least square refinement is the residual S_y :

$$S_y = \sum_i w_i (y_i - y_{ci})^2. \quad (3.32)$$

Here y_i is the observed intensity at the i th data point, y_{ci} is the corresponding calculated value and $w_i = 1/\sigma^2(y_i)$ is a weight. It is one of the great insights of this method, that each individual data point (no matter if it is a strong reflection or background) contributes equally to the refinement. The calculated intensities y_{ci} can be obtained via the following equation:

$$y_{ci} = s \sum_{hkl} L_{hkl} |F_{hkl}|^2 \phi(2\Theta_i - 2\Theta_{hkl}) P_{hkl} A + y_{bi}. \quad (3.33)$$

The sum in Eq. 3.33 runs over a certain range of neighbouring Bragg reflections (h,k,l) which can contribute to the intensity of the powder pattern at position i . Further, s is an overall scale factor, L_{hkl} contains the Lorentz-, polarization-, and multiplicity-factors, ϕ is the peak profile function, P_{hkl} a function which corrects for preferred orientation, A is an absorption factor and y_{bi} is the background intensity at position i . Finally, F_{hkl} is the structure factor for Bragg reflection (h,k,l). Each of those quantities has to be described by a certain case specific model, which then all together provide the final set of refinable parameters [70].

A quantity which is very important for getting a high quality fit of a powder pattern is the peak profile function ϕ . The profile shapes of Bragg reflections are influenced by both, the used instrumentation (beam properties and diffractometer) and the special characteristics of the investigated specimen (e.g. structure, size, shape and strain). The final profile function of a powder pattern is therefore a convolution of various independent symmetric and/or asymmetric angular-dependent functions. However, in most cases it is not necessary to actually perform the convolution, since the profile shape can be approximated by analytical functions. For angle dispersive data, a widely used function is the (modified) pseudo-Voigt function:

$$\phi_{pV}(\Theta) = \eta L(\Theta, \Gamma_L) + (1 - \eta) G(\Theta, \Gamma_G). \quad (3.34)$$

This function consists of a combination of a Lorentzian L and a Gaussian G with profile widths Γ_L and Γ_G , and where $\eta = \eta(\Gamma_L, \Gamma_G)$ is a mixing parameter. The widths are

functions of the scattering angle Θ and can be modelled as:

$$\Gamma_G^2 = U \tan^2 \Theta + V \tan \Theta + W \quad (3.35)$$

$$\Gamma_L = X \tan \Theta + Y / \cos \Theta \quad (3.36)$$

where U , V , W , X and Y are refinable parameters (Thomson-Cox-Hastings pseudo-Voigt [70, 71]).

Some of the powder samples which have been investigated within this thesis showed an anisotropic peak broadening, which could not be modelled with Eqs. 3.34, 3.35 and 3.36. The reason for this broadening could be dedicated to microscopical strain in the crystallites. In order to account for this effect a phenomenological model proposed by Stephens was used [72]. The microscopic strain causes a distribution of the metric parameters $\{A, \dots, F\}$. With those parameters the d -spacing between lattice planes of any given reflection can be expressed as:

$$1/d_{hkl}^2 = M_{hkl} = Ah^2 + Bk^2 + Cl^2 + Dkl + Ehl + Fhk. \quad (3.37)$$

If one further assumes that the distribution of $\{A, \dots, F\}$ is Gaussian, then the variance can be written as [72]:

$$\sigma^2(M_{hkl}) = \sum_{HKL} S_{HKL} h^H k^K l^L. \quad (3.38)$$

S_{HKL} are anisotropic strain parameters, which are defined for $H+K+L=4$. Depending on the crystal symmetry, the number of independent S_{HKL} varies, where in the most general (triclinic) case there are 15.

The anisotropic broadening contribution to the peak width is finally given by:

$$\Gamma_A = \frac{\sqrt{\sigma^2(M_{HKL})}}{M_{HKL}} \tan \Theta, \quad (3.39)$$

and the overall width of the Gaussian and Lorentzian profiles can be expressed by a modified version of Eq. 3.35 and 3.36:

$$\Gamma_G^2 = U \tan^2 \Theta + V \tan \Theta + W + (1 - \xi)^2 \Gamma_A^2(hkl), \quad (3.40)$$

$$\Gamma_L = X \tan \Theta + Y / \cos \Theta + \xi \Gamma_A(hkl). \quad (3.41)$$

ξ is another mixing parameter, which can also be refined [72].

Another important aspect of the refinement is to have a measurable value for the ad-

equacy of the applied model, so that one is able to judge about the quality of the fit. Several agreement factors have been proposed in literature and some of the most important ones will be introduced here. Similar to the refinement of single crystal data a Bragg factor R_B and a structure factor R_F can be defined:

$$R_F = \frac{\sum |(I_{hkl}^{\text{obs}})^{1/2} - (I_{hkl}^{\text{calc}})^{1/2}|}{\sum (I_{hkl}^{\text{obs}})^{1/2}}, \quad (3.42)$$

$$R_B = \frac{\sum |I_{hkl}^{\text{obs}} - I_{hkl}^{\text{calc}}|}{\sum I_{hkl}^{\text{obs}}}. \quad (3.43)$$

Here I_{hkl}^{obs} and I_{hkl}^{calc} denote the ‘observed’ and calculated Bragg intensities of a reflection (hkl). The reason why ‘observed’ is written in quotation marks is that the Bragg intensities are not directly observed (in contrast to single crystal diffraction), but they are deduced with the help of the underlying model.

From a pure statistical point of view, the most straightforward measure of the fit quality is the weighted pattern factor R_{wp} , which gives the square root of the quantity being minimized (see Eq. 3.32), scaled by the weighted intensities:

$$R_{wp} = \left\{ \frac{\sum w_i (y_i - y_{ci})^2}{\sum w_i y_i^2} \right\}^{1/2}. \quad (3.44)$$

This factor describes the fit quality of the whole pattern and is therefore also the most suitable to follow the progress of the refinement. Assuming the case of an ideal model, which would perfectly fit the data, one can define a ‘best possible R_{wp} ’ value, which is sometimes also called expected R -factor:

$$R_{\text{exp}} = \left\{ \frac{N - P}{\sum_i w_i y_i^2} \right\}^{1/2}, \quad (3.45)$$

where N is the total number of data points and P is the number of refined parameters. The final solution should give a ratio $R_{wp}/R_{\text{exp}} \approx 1$.

All the above mentioned goodness factors, allow to make statements about the quality of the underlying model, however, one should never trust those calculated quantities blindly. It may occur that one reaches a local minimum with an excellent fit quality, but with absolutely unphysical atomic parameters (e.g. very short bond lengths). To obtain a meaningful result, it is therefore important to begin with a good starting model, which lies already in the vicinity of the global minimum. Further, it is very important to use graphical criteria of fit and visualize the observed and calculated data, as well as the

difference of them.

More detailed explanations and further insights into the Rietveld method can be found in references [67, 70, 73].

3.1.3. Neutron spectroscopy

Knowing the static properties of a material, e.g. its nuclear and magnetic structure, already allows a detailed understanding of its nature. However, if one wants to gain a deeper insight into the underlying physics, e.g. the driving mechanisms for nuclear and magnetic phase transitions, one has to include dynamic processes into the study. This can be done by performing inelastic neutron scattering (INS) measurements and monitoring the lost or gained energy of the scattered neutron as a function of wavevector transfer. By doing so it is possible to study the collective motion in the material, such as spin waves and phonons excitations, as well as (zero-field split) energy levels of single molecule magnets and crystal field excitations.

INS measurements are mainly carried out on two type of instruments, the triple-axis spectrometer and the time-of-flight spectrometer. Both will be introduced in the following.

The triple axes spectrometer

The triple-axes spectrometer is the most widely used neutron spectrometer at steady-state neutron sources (reactor or long pulsed spallation source). Its ingenious concept of monochromator, sample and analyser sitting each on a rotatable axis enables the highest possible degree of versatility and allows to probe nearly any coordinate in energy and momentum space [58]. A draft of a typical TAS is depicted in Fig. 3.6. The polychromatic neutron beam is guided to the instrument³, where it hits a monochromator crystal (usually pyrolytic graphite (002) or silicium (111)) selecting neutrons with a particular direction and magnitude of the momentum by Bragg reflection. After scattering at the sample the beam is analysed using the Bragg reflection of an analyser crystal, which is usually made of the same material as the monochromator. Often one uses vertically and/or horizontally bent monochromator and analyser crystals. The former is to increase the neutron flux at the sample position by focusing the neutron beam, while the latter is helpful to increase the detected signal and to decrease the background noise, since the

³Within the guide the neutrons are transported via total reflection on the smooth inside walls of the guide tube.

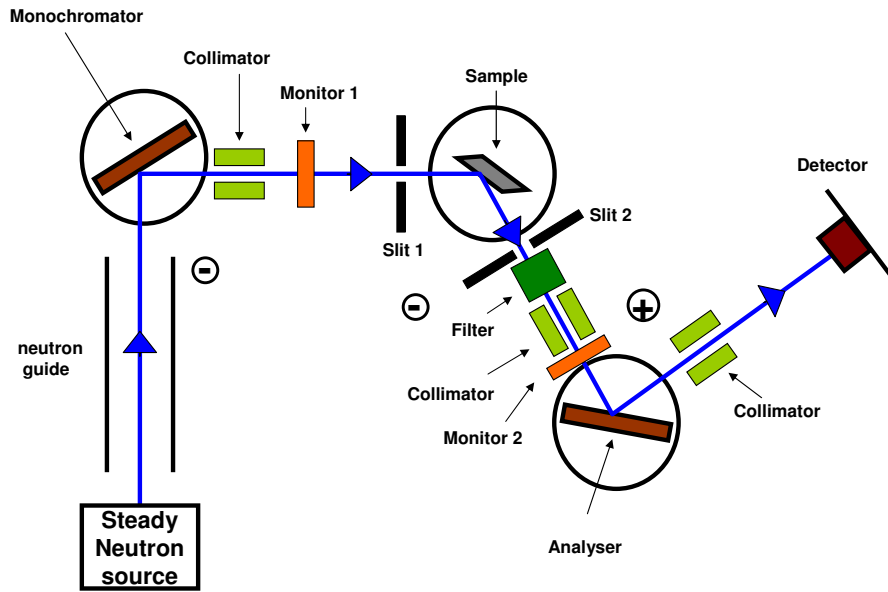


Figure 3.6.: Typical set-up of a triple axes spectrometer.

focused beam requires smaller detectors, thus giving rise to less parasitic signal. On the other hand, focusing deteriorates the instrumental resolution and depending on the aim of the particular experiment the best balance has to be found. The neutron detector itself is most often made of a tube filled with ^3He -gas. When hit by the neutrons, the ^3He atom decays under exothermic conditions into a proton, thus causing a ^3H nucleus and a γ -particle. Those products ionize their surrounding gas particles, causing a detectable electron cascade.

Several collimators are placed along the beam path in order to reduce beam divergence. They consist of parallel arranged plates which are coated with neutron absorbing material. In order to avoid higher order contributions of neutrons scattered from the monochromator, which arise in addition to the main component of wavelength λ as higher order components with λ/n ($n = 2, 3, \dots$), filter elements are placed before or after the sample. Depending on whether cold ($\sim 0.1 - 10$ meV) or thermal ($\sim 5 - 100$ meV) neutrons are used, a nitrogen-cooled beryllium filter or a pyrolytic graphite filter is used. The sample-to-background noise can be improved by positioning variable slits before and after the sample and adjusting the beam width with respect to the size of the sample and detector window, respectively.

In order to account for variations in neutron flux produced by the source, the detected neutrons are normalized to the count rate of a monitor detector that is placed in the incident beam in front of the sample. Additionally, one sometimes finds a second moni-

tor located in front of the analyser. This monitor helps to identify spurious signal from higher order Bragg scattering.

The most commonly encountered way of performing TAS measurements is with the final neutron energy and momentum fixed (so called fixed k_f -mode). In this way only the magnitude of the momentum of the *incoming* neutrons is varied. The advantage of this scan mode is that it provides a larger dynamic range compared to what is available with a fixed incident wavevector. Further, the incident beam monitor efficiency is inversely proportional to the incident wavevector k_i , such that in fixed k_f mode the count rate normalized to the number of monitor counts is directly proportional to the dynamic correlation function $S(\mathbf{Q}, \omega)$, e.g. it automatically corrects for the factor k_f/k_i in Eqs. 3.8 and 3.17.

In a typical TAS experiment one usually explores the interesting (\mathbf{Q}, ω) space with two types of scans, namely constant- \mathbf{Q} and constant energy scans. For the former the energy is varied at a fixed wavevector transfer, while for the latter \mathbf{Q} is scanned at a fixed energy transfer. Both type of scans are used for the inelastic neutron scattering measurements of CaV_2O_4 , which are presented in Chapter 6.

As a result of the divergence of the neutron beam as well as the mosaic spread of the monochromator crystals, the analyser crystals and the sample itself, the TAS has a finite resolution. Therefore, the measured neutron scattering cross section for a particular point in (\mathbf{Q}, ω) -space contains contributions from a finite volume around this point. Knowing the particular instrumental parameter the resolution function of the spectrometer can be calculated according to published methods [74, 75]. Additionally, given that the resolution function is defined in the four-dimensional (\mathbf{Q}, ω) -space, the intensity which is detected while scanning through an energy dispersive mode (e.g. spin waves) also depends on the particular shape of this mode. In order to simulate TAS scans the resolution function has to be convoluted with the defined dispersion and lineshape of the measured feature. In Chapter 6 this was done by using the program `rescal` [76]. Within the framework of this thesis, two triple-axes spectrometers have been utilized, the thermal neutron TAS IN20 located at the Institute Laue-Langevin in Grenoble and the cold neutron TAS FLEX located at the Helmholtz-Zentrum Berlin. The particular set-ups of both instruments are explained Sec. 6.2.

The time-of-flight spectrometer

Time-of-flight (TOF) spectrometers make use of the pulsed time-structured neutron beam that is provided by neutron spallation sources or by a steady state reactor source employing neutron choppers. Similar to TOF diffractometers introduced in Sec. 3.1.2,

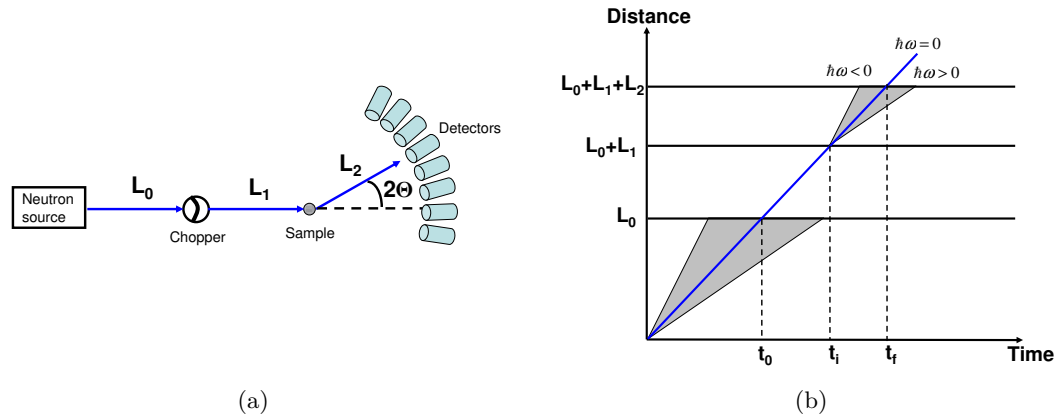


Figure 3.7.: (a) Sketch of a typical time-of-flight set-up. (b) Distance vs time plot for a direct geometry TOF spectrometer. The grey regions represent the neutron velocity distribution before the white neutron beam gets monochromatized by the Fermi chopper and after the neutrons have scattered from the sample, respectively.

energy analysis of the neutrons scattered at a sample is done by measuring the neutron time of flight over a known distance, e.g. from the sample to the detector.

There are two different kind of scattering geometries which can be employed, namely the direct and the indirect geometry. In the case of the former, monochromatic neutrons with a fixed incident energy E_i scatter at the sample position and their final energy is recorded by a time-resolved detector. In contrary, for indirect geometries a white pulsed beam illuminates the sample and a particular final energy E_f is selected by Bragg scattering from an analyser crystal. All experiments presented in this thesis have been performed on instruments with a direct geometry and therefore the following discussion will focus on this type only.

Figure 3.7(a) displays a typical set-up of a direct geometry TOF spectrometer located at a spallation source. After being guided to the instrument, the pulsed neutron beam is monochromatized by a so called Fermi chopper⁴. This is a rotating device, which consists of curved alternating layers of aluminium and boron. The former material is transparent to neutrons, while the latter is a neutron absorber. By choosing the appropriate chopper phase with respect to the incoming beam pulse as well as the correct frequency, only those neutrons which have the desired incident energy (and accordingly a particular incident velocity) are allowed to pass the chopper, while the other neutrons are blocked

⁴At steady state reactor sources, beam monochromatization can be also done using the Bragg reflection of monochromator single crystals. In this cases the pulsed structure is created after the beam is monochromatized using a Fermi chopper or a pair of counter rotating disc choppers. An example for such an instrumental design is the IN6 spectrometer (See Appendix D).

by the absorbing material. Therefore, both the energy range and width are determined by the phase and frequency of the chopper rotation.

The neutrons scattered by the sample are detected by an array of counters covering a large solid angle. The detectors are either single ^3He tube detectors or (in the case of latest generation TOF spectrometers) position sensitive ^3He detectors. The detectors record both, the position of the scattered neutron as well as the time at which they are counted. In detail, the use of detector tubes allows to record the neutrons as a function of scattering angle 2θ , but it provides a poor Q resolution along the direction perpendicular to the scattering plane. For this reason instruments equipped with tube detectors are mostly used for powder measurements. On the other hand, if position sensitive detectors are available, also out-of-plane components of the scattering vector can be measured, thus enabling to access a huge volume of (\mathbf{Q}, ω) -space within a single measurement and therefore being ideal for studying single crystals.

Each detector records the scattering intensity as a function of time and scattering angle 2θ . The conversion to (\mathbf{Q}, ω) -space can be done using the equations for energy and momentum conservation (Eq. 3.2). This yields to:

$$\hbar\omega = E_i - E_f = E_i - \frac{1}{2}m_N \frac{L_2^2}{(t_f - t_i)^2}, \quad (3.46)$$

$$\mathbf{Q}^2 = \frac{2m_N}{\hbar^2} \left(2E_i - \hbar\omega - 2 \cos 2\theta \sqrt{E_i(E_i - \hbar\omega)} \right), \quad (3.47)$$

where m_N is the neutron mass, $(t_f - t_i)$ is time of the neutron from the sample to the detector and L_2 is the corresponding distance. The fixed incident energy is also given by $E_i = \frac{1}{2}m_N \left(\frac{L_1}{t_i - t_0}\right)^2$, with L_1 defining the chopper-sample distance and $(t_i - t_0)$ being the neutron flight time from the chopper to the sample. This scenario is visualized in the phase-space diagram in Fig. 3.7(b).

In most time-of-flight instruments one or more additional background choppers are positioned along the neutron guide prior to the Fermi chopper. They rotate in phase with the Fermi chopper, but at lower speed and are used to eliminate fast neutrons and to prevent frame overlap, which arises when the slowest neutrons of one pulse are overtaken by the fast neutrons of the following pulse.

The resolution in energy transfer of a direct geometry TOF spectrometer is determined by the source and chopper pulse widths (Δt_s and Δt_c) and can be expressed by the following formula [77]:

$$\frac{\Delta\hbar\omega}{E_i} = \frac{2\delta_0}{L_0} \left[\left(1 + \left(\frac{E_f}{E_i} \right)^{3/2} \frac{L_1}{L_2} \right)^2 + \left(\frac{\Delta t_c}{\Delta t_s} \right)^2 \left(1 + \left(\frac{E_f}{E_i} \right)^{3/2} \frac{L_0}{L_2} \left(1 + \frac{L_1}{L_0} \right) \right)^2 \right]^{1/2} \quad (3.48)$$

In the above expression L_0, L_1 and L_2 are the distances defined in Fig. 3.7 and δ_s is an equivalent distance representing the time spread from the source. From Eq. 3.48 it can be seen that the energy resolution for fixed E_i improves with increasing energy transfer. The resolution in momentum transfer is a more complicated quantity, which depends on the detector pixel size, the finite sample size as well as the angular divergence of the beam and its finite energy spread. The latter is because neutrons with slightly different energies scatter at different angles, revealing that energy and \mathbf{Q} -resolution are not independent from each other.

In the framework of this thesis, the TOF spectrometers IN5 and IN6 at ILL and V3, NEAT at HZB have been used to study the zero field excitations of the Mn_6 molecule magnets, while the MAPS spectrometer at the ISIS spallation source has been used to investigate the spin wave excitations in CaV_2O_4 . All instruments are briefly introduced in Appendix D.

3.2. Other techniques

The following subsections provide a brief introduction on other techniques that have been used for sample characterization in the framework of this thesis. Those techniques are X-ray diffraction and DC-susceptibility measurements.

3.2.1. X-ray diffraction

Powder and single crystal X-ray diffraction is a widely used technique to study the nuclear structure of materials and serves as a complementary technique to neutron diffraction. The x-rays commonly employed for diffraction experiment are electromagnetic radiation with wavelengths in the range $\sim 0.1 - 5.0 \text{ \AA}$ (125-2.5 keV). In contrast to neutrons the scattering process does not occur directly between the scattering particles (photons) and the nuclei of the atoms, but involves the electrons that surround the atomic nuclei. The x-rays can scatter coherently and incoherently (Compton scattering) from the electron cloud, but only the coherent scattering gives rise to Bragg reflections [67]. The coherently scattered X-rays interfere with each other, such that the overall scattering from the electrons around an atom can be described as:

$$f(\mathbf{Q}) = \int_{-\infty}^{\infty} \rho(\mathbf{r}) e^{2\pi i(\mathbf{r} \cdot \mathbf{Q})}. \quad (3.49)$$

$f(\mathbf{Q})$ is the Fourier transform of the electron density $\rho(\mathbf{r})$ and is also known as the atomic form factor. \mathbf{r} is the radial coordinate from the atomic nucleus and \mathbf{Q} is the

corresponding reciprocal scattering vector. The nuclear structure factor $F(\mathbf{Q})$ measured in a X-ray diffraction experiment is basically the same as the one introduced for neutron scattering, where one simply has to replace the neutron scattering length by the atomic form factor (cf. Eq. 3.13).

Assuming that the charge distribution has spherical symmetry, $f(\mathbf{Q})$ only depends on the magnitude of \mathbf{Q} and can be rewritten as:

$$f(Q) = \int_0^\infty 4\pi r^2 \rho(r) \frac{\sin(Qr)}{Qr} dr, \quad (3.50)$$

with Q being the magnitude of the scattering vector. $f(Q)$ has its maximum at $f(0)$ and falls off rapidly at larger Q . Further, for $Q = 0$, $f(Q)$ corresponds to the number of electrons Z in the atom [78]. The two last mentioned properties reveal the drawback of X-ray diffraction measurements. Since the scattering intensity becomes very weak for light atoms and at high Q (and thus large scattering angle), X-ray scattering is best suited to study the crystal structure of materials consisting of atoms with high Z and with a sufficient number of Bragg reflections at low scattering angle. On the other hand, this makes X-ray diffraction the first-choice method for determining the atomic positions in crystals that consist of elements which have a very small neutron scattering length.

X-ray instrumentation

X-rays can for example be ‘produced’ in the following ways, either with a standard laboratory X-ray high vacuum tube or as the by-product of particle acceleration in a synchrotron. In the former case, a focused beam of electrons generated by a high voltage (30-60 kV) is made to bombard a metal anode in high vacuum. When hit by the electrons, the anode (mostly made of Cu or Mo) emits a continuous energy spectrum of radiation (‘white’ radiation) due to deceleration of the electrons by the field of the metal ions. More importantly however, at well defined energies one observes a series of discrete peaks in X-ray intensity. This so called ‘characteristic’ radiation is used for the study of crystal structures and is due to ejection of an electron from one of the inner electron shells of the metal atom. Electrons that fall back from higher shells thus give rise to the emission of X-ray photons with a well-defined energy.

Conventional X-ray diffractometers based on high vacuum-tube systems are commercially available and belong to the basic equipment of any laboratory for sample preparation and characterization. In Sec. 5.1 data measured on the Rigaku TTRAX rotating anode X-ray diffractometer will be presented.

The second source of X-ray radiation is a so called synchrotron. The basic principle of

a synchrotron is quite simple: A linear accelerator brings a beam of charged particles (in most cases electrons) near to the velocity of light. The accelerated particles are then injected into a storage ring where they are kept along an almost circular path. In detail, this path consists of alternating sections of straight parts and bending magnets. The bending magnets are there to deflect the beam and therefore to guide it into the next straight section [67]. While accelerated along the curved path, the electrons emit synchrotron radiation which can therefore serve as a source for X-rays. Since the emitted X-ray spectrum is continuous, it is possible to access a great range of wavelength (from infrared to hard x-rays), thus making it possible to select the optimized wavelength needed for the experiment. Further, synchrotron radiation has a much higher intensity and much lower divergence compared to a conventional laboratory source, thus, when used for structure determination, enabling to study very tiny crystals or performing high-resolution powder diffractometry.

One out of several synchrotron facilities around the world is the European Synchrotron Radiation Facility (ESRF) in Grenoble France. The high resolution powder diffractometer positioned at the Swiss-Norwegian beamline (SNBL) BM01 has been used in the framework of this thesis to study the nuclear structure of CaV_2O_4 . Its set-up will be explained in the following.

The ESRF delivers a 6 mrad wide fan of synchrotron radiation to SNBL from the bender magnet BM01. This beam is divided into two parts which are guided to two separate instruments (BM01A and BM01B). The beam part which is guided to the high resolution powder diffractometer (BM01B) has a fan widths of 1 mrad. BM01B is equipped with two different instruments, a high resolution powder diffractometer and an EXAFS (extended X-ray absorption fine structure) instrument, however, only the former one is important for measurements presented in this thesis [79]. Figure 3.8 displays the instrumental set-up. After the beam has past a primary slit system, there is a double crystal monochromator which selects the X-ray wavelength for the EXAFS spectrometer. In case the HRPD is used, the white beam is simply guided further to another monochromator. This monochromator is made of Si(111) crystals and has a channel-cut geometry, which is used to provide monochromatized light parallel to the input beam direction, where the available wavelength range is $0.4 \leq \lambda \leq 1.2 \text{ \AA}$. Another pair of slits is installed after the monochromator in order to minimize beam divergence. The actual powder diffractometer consists of an array of 6 Si(111) analyser crystals positioned in front of six scintillation counters, enabling to measure an extended region in scattering angle 2θ in one single step. The analyser/scintillator arrays are mounted on an rotary 2θ table, allowing to access a wide range of scattering angle. Finally, the (powder)

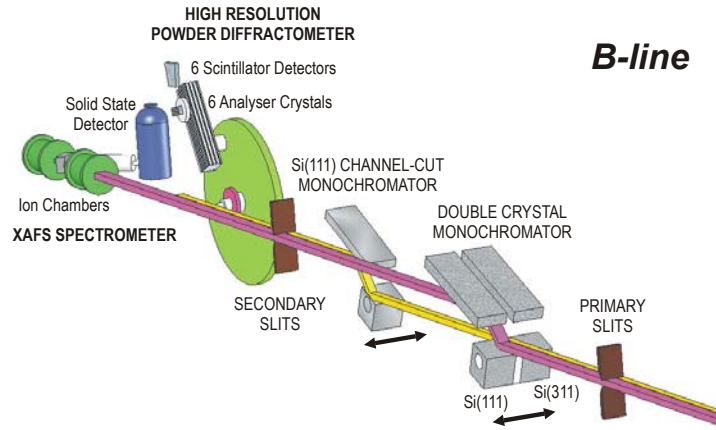


Figure 3.8.: Schematic layout of the BM1B beamline equipped with a two axis high resolution powder diffractometer. Picture taken from [80].

sample itself is located at the centre of this table and is attached to a second inner circle (ω), which allows rotations around the sample axis to be performed. The sample space is constructed such, that the additional sample environment (e.g. a He-flow cryostat to cool the sample down to $T = 4.5$ K) can be used. The data collected at SN01B are presented in Sec. 5.1.

3.2.2. Magnetic susceptibility

One of the elementary problems in condensed matter physics is to understand how a physical system reacts when it experiences a perturbation from outside. The physical quantities dealing with this problem are the so called response functions. Examples for such response functions are the electric conductivity, the heat conductivity and the magnetic susceptibility.

Especially interesting for the investigation of magnetic materials is the magnetic susceptibility, which describes the response to an external magnetic field. In detail, the magnetic susceptibility χ of a sample located in the homogeneous magnetic field H is defined as

$$\chi = \frac{\partial M}{\partial H}. \quad (3.51)$$

In Eq. 3.51 M is a vector and denotes the net-magnetization of the sample, H is an axial vector and χ is a second rank tensor. The form of χ depends on the crystal symmetry of the sample, however, it is always possible to choose the reference axes such, that χ becomes diagonal with respect to these axes. In the case of a magnetically isotropic sample, χ becomes a scalar.

The susceptibility is independent of the applied field, as long as one works in the region of small magnetic fields and not too low temperatures, in general the condition $g\mu_B H \ll k_B T$ has to be fulfilled. If this is the case, Eq. 3.51 simplifies to:

$$\chi = \frac{M}{H}. \quad (3.52)$$

However, there is another aspect that has to be taken into account. The magnetic moments inside the sample cause an inner magnetic field, which points opposite to the applied field direction. Therefore, the measured susceptibility is related to the field:

$$H' = H - dM. \quad (3.53)$$

Here d is the demagnetization factor, which is in general a tensor and depends on the geometry of the sample. For elliptic samples d can be calculated as reported in [81]. The susceptibility measured in an experiment differs from the intrinsic susceptibility of the sample and is defined as:

$$\chi_{\text{exp}} = \frac{M}{H} = \frac{M}{H' + dM} = \frac{\chi_{\text{intr}}}{1 + d\chi_{\text{intr}}}. \quad (3.54)$$

For the sample investigated in the framework for this thesis, the demagnetization factor was assumed to be weak and will therefore be neglected.

Experimental set-up

The standard method for measuring the magnetic moment of a sample is the inductive detection of the magnetic signal, where the sample is magnetized by a homogeneous magnetic field. Following Faraday's law, a time-varying magnetic flux causes a current to flow in a closed circuit. The time-dependent induced voltage can be expressed by the following equation

$$V_{\text{ind}} = \frac{d\Phi}{dt}, \quad (3.55)$$

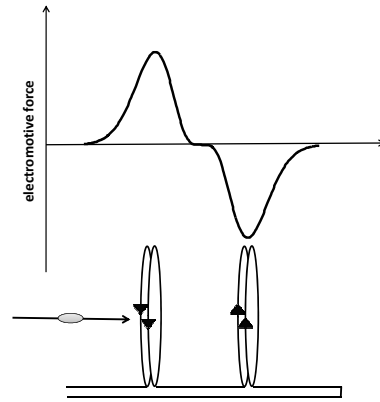


Figure 3.9.: In an inductive measurement of the magnetisation the sample is moved inside pick-up coils (gradiometer). Above the coil, the induced electromotive force on the position of the magnetized sample is shown (own illustration based on [15]).

where Φ denotes the magnetic flux enclosed in the pickup coil. Since the pickup coils are in general sensitive to not only the magnetized sample itself, but also to the magnetic field acting on it, it is necessary to use specially designed coils. Such coils, which are called gradiometers, consist of two or more loops wound in opposite direction, thus making them sensitive only to the gradient of the magnetic field. A first order gradiometer as it is used in a vibrating sample magnetometer (see below) is drafted in Fig. 3.9. The magnetized sample is moved through both of the two loops and the difference between the two voltages measured in each loop is proportional to the magnetization of the sample.

In most of the high sensitive magnetometers available nowadays, the induced current is not directly measured, but the coils are inductively coupled to a Superconducting QUantum Interference Device (SQUID). A SQUID consists of a superconducting ring in which a tunnelling barrier is implemented (Josephson junction). The barrier can be tunnelled by Cooper pairs, thus providing a good way to detect the field-dependent change of the ring current. Due to the laws of quantum mechanics the magnetic flux through the superconducting ring has to be a multiple of the magnetic flux quantum $\Phi_0 = h/2e = 2.07 \times 10^{-15}$ Vs. This effect makes the SQUID the most sensitive detector of magnetic flux.

However, since the SQUID is superconducting, it has to be operated at very low temperatures (usually cooled by liquid Helium) and further due to its sensitivity to magnetic fields, it has to be shielded from them. For this reason the SQUID can not be used for magnetic properties measurements at very high temperatures and fields. In such cases

another set-up called Vibrating Sample Magnetometer (VSM) is used, which will be described below.

Vibrating sample magnetometer

In a VSM the sample is mounted on a stick which is positioned in the middle of a first order gradiometer pick-up coil pair (counter wound). The sample stick is moved in a sinusoidal way within the coils and the time-varying magnetic flux from the sample induces a current, which is amplified and lock-in detected [82]. Starting from Eq. 3.55 the time-dependent induced voltage is given by the following equation:

$$V_{\text{coil}} = 2\pi f C m A \sin(2\pi f t). \quad (3.56)$$

In this equation f is the frequency and A the amplitude of the oscillation, m is the DC magnetic moment of the sample, t is the time and C is a coupling constant. The precise position and amplitude of the oscillation is controlled from the VSM motor module and was set to $f = 40$ Hz and $A = 2$ mm throughout all the measurements reported in this thesis.

In order to increase the signal of the induced voltage, an amplifier is used and in addition a lock-in (phase-sensitive) filter strongly reduces random noise signal and thus a high sensitivity can be achieved (magnetisation changes less than 10^{-6} emu) [82].

4. The hexanuclear single molecule magnets Mn_6

This chapter deals with the investigation of the magnetic properties of three variants of the hexanuclear molecular nano magnet Mn_6 . Inelastic neutron scattering experiments have been performed in order to extract the isotropic exchange coupling and the zero-field splitting parameter. The obtained data have been compared to results from frequency domain magnetic resonance studies in order to identify the character of the obtained transitions (intra- or inter-multiplet). The findings enable quantification of the effect of small structural distortions of the molecular geometry on the magnetic properties. It will be shown, that the giant spin model completely fails to describe the energy level structure of the low energy spin multiplets as well as the relaxation dynamics of the molecules. The obtained model spin Hamiltonian is analysed theoretically and it will be shown that the excited S multiplets play a key role in determining the effective energy barrier for the magnetization reversal for all the three compounds.

4.1. Introduction

Since the discovery of magnetic hysteresis and slow relaxation of the magnetization in the dodecanuclear manganese complex $\text{Mn}_{12}\text{-ac}$ [12], plenty of effort has been devoted in order to tune the key parameter of single molecule magnets (SMM), such as the barrier height U and the corresponding blocking temperature T_B . From this point of view it is rather surprising that it took chemists and physicists almost 14 years until they discovered a complex that broke the long standing barrier record held by the Mn_{12} clusters (being $U \approx 74.4$ K for a high symmetry version of that family [39]).

The new record compound ($U \approx 86.4$ K) belongs to a class of hexanuclear Mn^{3+} clusters (from now on Mn_6) which, despite the generally similar nuclear structure, display a rich variety of spin ground states and anisotropy energy barriers [83, 1, 84, 85, 86, 87].

In the framework of this thesis, three members of this family of Mn_6 clusters have been investigated, with chemical formulas $[\text{Mn}_6\text{O}_2(\text{sao})_6(\text{O}_2\text{CMe})_2(\text{EtOH})_4]\cdot 4\text{EtOH}$ (**1**),

$[Mn_6O_2(Et-sao)_6(O_2CPh)_2(EtOH)_4(H_2O)_2] \cdot 2EtOH$ (**2**) and $[Mn_6O_2(Et-sao)_6(O_2CPh(Me)_2)_2(EtOH)_6]$ (**3**) [88, 83, 1]. All molecules display very similar structures consisting of six Mn^{3+} ions ($s = 2$) arranged in two staggered triangular units (see Fig. 4.1) related by an inversion centre.

The only major structural difference between the three clusters resides in the steric

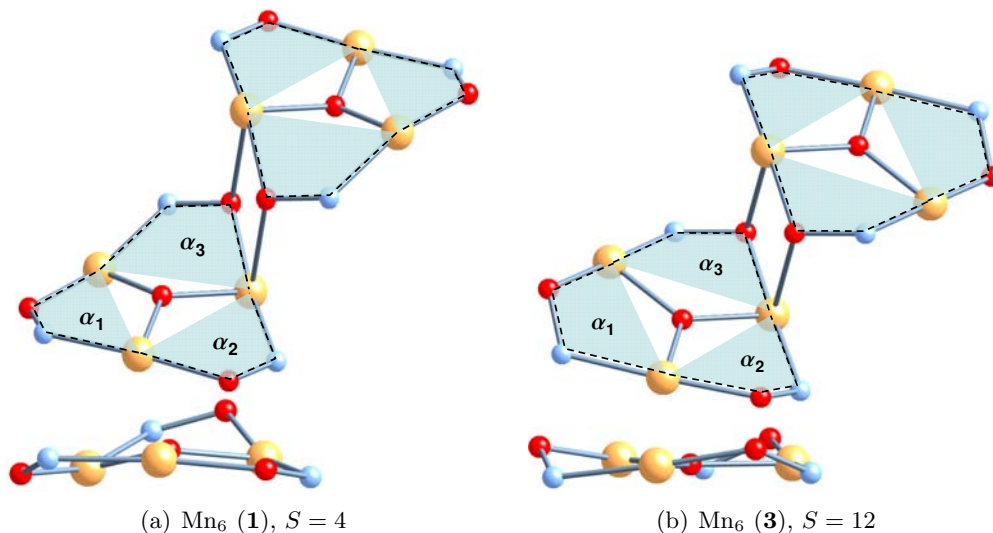


Figure 4.1.: Core of molecules **1** and **3** showing the different torsion angles ($\alpha_1, \alpha_2, \alpha_3$). Colour scheme: Mn, orange, O, red, N, blue. H and C ions are omitted for clarity. Reprinted from [89]. Copyright (2010) by the American Physical Society.

effect of the organic ligands used in proximity to the transition metal ions. However, despite having very similar structures, the three molecules have very different magnetic properties. The coupling between the magnetic ions occurs via superexchange pathways involving oxygen and nitrogen ions and is found to be extremely sensitive to intramolecular bond angles and distances. The particular arrangement of the magnetic ions provides exchange couplings lying in the cross-over region between AFM and FM. For this reason, even small structural distortions have tremendous impact on the magnetic properties of the system. For example, while the coupling between the two triangles is ferromagnetic for all molecules, the intra-triangular coupling changes from antiferromagnetic in (**1**) to ferromagnetic in (**2**) and (**3**) due to a ‘twisting’ of the oximate linkage. This results in a ‘switching’ of the total spin ground state from $S = 4$ to $S = 12$. Systematic synthesis and studies of various members of the Mn_6 family have revealed that the nature of the coupling is extremely sensitive to the intra-triangular Mn-O-N-Mn torsion angles [86, 85] (see Fig. 4.1). There is a critical value for the torsion angle of $30.9(5)^\circ$, above which the pairwise exchange interaction switches from antiferromagnetic to ferromagnetic, while a

further enhancement of the angle increases the strength of the FM interaction.

Molecules **(2)** and **(3)** have the same spin ground state $S = 12$ but very different effective energy barriers ($U_{\text{eff}} \approx 53$ K for **(2)** and $U_{\text{eff}} \approx 86.4$ K for **(3)**). As will be shown later, this difference is closely related to the exchange interactions [90].

In order to understand this rich variety of behaviors, a detailed spectroscopy characterization of the three molecules using inelastic neutron scattering (INS) was performed. Further, the INS data were compared with data from frequency domain magnetic resonance (FDMR) measurements. FDMR is only sensitive to transitions with a predominant intramultiplet character, according to the selection rules $\Delta S = 0, \Delta M_S = \pm 1$. In contrast, in INS both inter- and intramultiplet transitions can be observed ($\Delta S = 0, \pm 1, \Delta M_S = 0, \pm 1$). Thus, the combination of the two techniques allows assignment of all observed excitations [91, 92].

The determination of the model spin Hamiltonian parameters enabled the effective energy barrier to be theoretically estimated. The results on the three different systems show how the presence of low-lying excited spin multiplets plays a crucial role in determining the relaxation of the magnetization.

In conventional systems, the effects of spin-mixing can be effectively modeled by the inclusion of fourth order zero-field splitting parameters in the giant spin Hamiltonian [30, 93]. In the following it will be shown that this Hamiltonian is completely inadequate for the description of the spin state energy level structure of the Mn_6 SMMs.

4.2. Experimental method

The INS measurements were carried out at the time-of-flight instruments IN5 and IN6 at the Institute Laue-Langevin, Grenoble and at NEAT at the Helmholtz-Zentrum Berlin (see Appendix D for a detailed explanation of the instruments). Molecule **(1)** was measured on all three instruments, while **(2)** was investigated on NEAT and IN5 and **(3)** was measured on IN5 only. For each of the three samples ≈ 3 -4 g of non-deuterated polycrystalline powder was filled into hollow cylindrical shaped aluminum container and mounted inside a standard orange cryostat, allowing temperatures in the range $2 \leq T \leq 300$ K to be accessed. A vanadium standard was used for the detector normalization and empty can measurements were used for the background subtraction.

The neutron data were compared to spectra collected with the FDMR technique, where the same samples as for the neutron case (but pressed into pellets) were used. The FDMR measurements were performed by Slageren *et al.* on a quasi-optical spectrometer, which employs backward wave oscillators as monochromatic coherent radiation sources and a

Golay cell as detector (further details can be found in [89]). The analysis of the FDMR data was not part of this thesis, but was done by Slageren *et al.* [89]. However, the results of this analysis will be compared to the INS data, since the complementary use of both techniques helps to identify the particular character of the observed excited energy levels.

4.3. Theoretical modeling and experimental results

Two different theoretical approaches have been employed, to model the observed data and to extract the leading exchange and crystal field parameter. In a first attempt, the giant spin Hamiltonian (GSH) was used, which considers the ZFS of the ground state multiplet only. Including only ZFS terms, the giant spin Hamiltonian for a spin state S reads:

$$H_S = D_S \hat{S}_z^2 + E_S (\hat{S}_x^2 - \hat{S}_y^2) + B_4^0 \hat{O}_4^0 \quad (4.1)$$

where D_S and E_S are second order axial and transverse anisotropy, respectively, and B_4^0 is the fourth order axial anisotropy, with \hat{O}_4^0 the corresponding Stevens operator. If S -mixing becomes apparent, the latter fourth order parameter has to be seen as an effective one, which reflects both, higher order crystal field effects as well as the influence of higher spin multiplets on the ground one. For the actual calculations the <SMMS> software package was utilized [94], which performs exact diagonalization (ED) calculations within a given fixed S multiplet.

In addition, ED calculations of the full microscopic spin Hamiltonian have been performed, where isotropic exchange and single-ion ZFS were treated on equal footings. This allowed a detailed investigation of S -mixing effects and its influence on the relaxation dynamics of the molecule. The microscopic spin Hamiltonian includes an isotropic exchange term for each pairwise interaction and single ion ZFS terms for each ion:

$$H = \sum_{i < j} J_{ij} \mathbf{s}(i) \cdot \mathbf{s}(j) + \sum_i d_i s_z^2(i) + \sum_i e_i (s_x^2(i) - s_y^2(i)) + c_i (35 s_z^4(i) + (25 - 30s(s+1)) s_z^2(i)) \quad (4.2)$$

where $\mathbf{s}(i)$ are spin operators of the i^{th} Mn ion. The first term is the isotropic exchange interaction, while the second, third and fourth terms are the second order axial, second order transverse, and fourth order axial single-ion zero-field splitting, respectively (the z axis is assumed perpendicular to the plane of the triangle). For the calculations it

was assumed, that the magnetic dipole-dipole interaction in the Mn_6 molecules is small compared to the crystal field anisotropy and it was therefore neglected.

The ED calculations for the low spin $S = 4$ molecule (**1**) have been performed with the software packages ALPS [95] and MAGPACK [96] and additional calculations of the neutron scattering cross section and the relaxation dynamics were done by Carretta *et al.* [89]. The numerical investigations for the two high spin $S = 12$ molecules (**2**) and (**3**) have been solely performed by Carretta *et al.* using their own diagonalization routine, where the following strategy was used to obtain the best fit results. In a first step, the molecule was assumed to possess only axial components of the anisotropy. This approximation leads to a block-factorization of the Hamiltonian matrix according to the M_S quantum number. Since the separated M_S -blocks are small, the diagonalization is fast and therefore a fitting of the observed energy levels based on a weighted least square method could be performed. The parameter obtained in this way, served as starting values for an extended ED run, using the full spin Hamiltonian including transverse anisotropy components. To exploit the full symmetry of the spin Hamiltonian, the method of irreducible tensor operators was employed to calculate the full energy level diagram of the systems (see [15, 31]). Finally, for the most promising sets of parameters, the dc-susceptibility has been calculated in order to check for consistency with the experimental data. Once a suitable set of energy levels was found, the inelastic neutron scattering function as well as the relaxation dynamics were calculated according to well known formulas (for details see Section 3.1.1 and [97, 90]).

4.3.1. Mn_6 (**1**) ($S=4$) $U_{\text{eff}} \approx 28$ K

Sample (**1**) was the first reported member of the Mn_6 family [88]. The building block of the molecule is the $[\text{Mn}_3^+ \text{O}]$ triangular unit where Mn_2 pairs, bridged by the NO oxime, form a -Mn-O-N-Mn- moiety (Fig. 4.2). The Mn-O-N-Mn torsion angles (cf. Fig. 4.1) within each triangle are 10.7° , 16.48° and 22.8° , giving rise to a dominant antiferromagnetic exchange coupling [86]. The two triangular units are coupled ferromagnetically, resulting in a total spin ground state of $S = 4$. Four out of the six metal ions (Mn1, Mn2, Mn1', Mn2') are six-coordinate and in distorted octahedral geometry (MnO_5N), with the (elongated) Jahn-Teller axis almost perpendicular to the plane of the triangle, while the two remaining ions (Mn3, Mn3') are five-coordinate and in square pyramidal geometry (see Fig. 4.2). The effective energy barrier was determined from ac-susceptibility measurements to be $U_{\text{eff}} = 28$ K, with $\tau_0 = 3.6 \times 10^{-8}$ s [88]. From the effective energy barrier an estimate of $D \approx -0.15$ meV was derived, which is one of the highest axial anisotropy parameters, that has ever been reported for SMM.

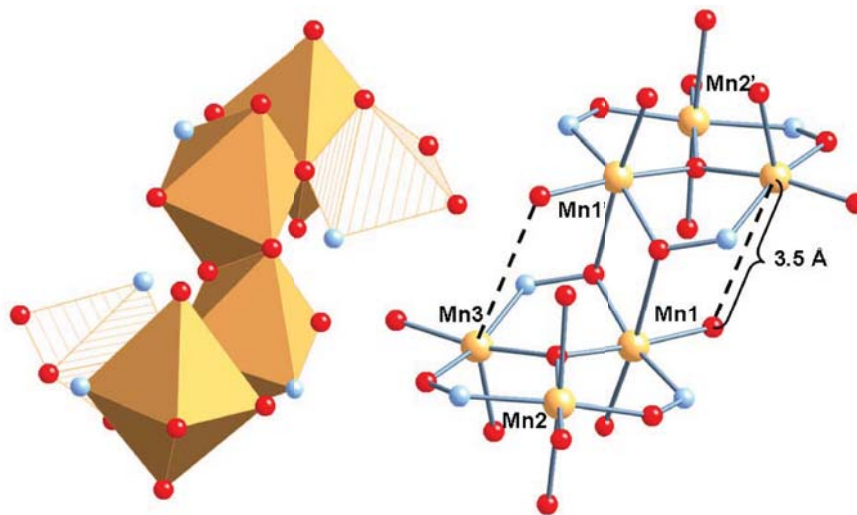


Figure 4.2.: Structure of the Mn_6 (**1**) molecular core. The Mn^{3+} ions are located at the vertices of two oxo-centered triangles. Ions Mn1, Mn2, Mn1' and Mn2' are in octahedral geometry and ions Mn3 and Mn3' in square pyramidal geometry, as highlighted in filled and striped orange (left figure). Color scheme: Mn, orange, O, red, N, blue. H and C ions are omitted for clarity. The distance between the square pyramidal Mn3 (Mn3') ion and the phenolato oxygen is ≈ 3.5 Å (see dashed line) and thus being too large to built a strong bond. Reprinted from [89]. Copyright (2010) by the American Physical Society.

In order to get detailed information about the leading exchange interactions within the molecule and about the zero field splitting parameter, inelastic neutron scattering measurements were performed. By doing so, it was possible to characterize the ground multiplet and to identify the positions of the lowest lying excited states.

The INS measurements were performed on ≈ 4 g of non-deuterated polycrystalline powder of (**1**), which was synthesized as described in [88]. For the measurements, various incident neutron wavelengths were used, ranging from 3.2 Å-6.7 Å with energy resolution between 48 μeV and 360 μeV . Figure 4.3(a) shows the INS spectra for an incident wavelength of 4.6 Å collected on NEAT (172 μeV full width at half maximum (FWHM) resolution at the elastic peak). In order to achieve good statistics, the data have been summed over the scattering angle 2Θ (corresponding Q -range: $0.4 \leq Q \leq 1.5$ Å $^{-1}$). At $T = 2$ K only the ground state is populated and therefore all excitations arise from the ground state level $|S = 4, M_S = \pm 4\rangle$. A strong peak was observed at 1.77(2) meV, while another one was found at 2.53(1) meV. Those peaks can either arise from an intra-multiplet transition to the $|S = 4, M_S = \pm 3\rangle$ level and/or from transitions to other low lying spin multiplets (e.g. $|S = 3, M_S = \pm 3\rangle$). Both observed excitations could be fitted to Gaussian line shapes and the corresponding resolution (FWHM) was found to

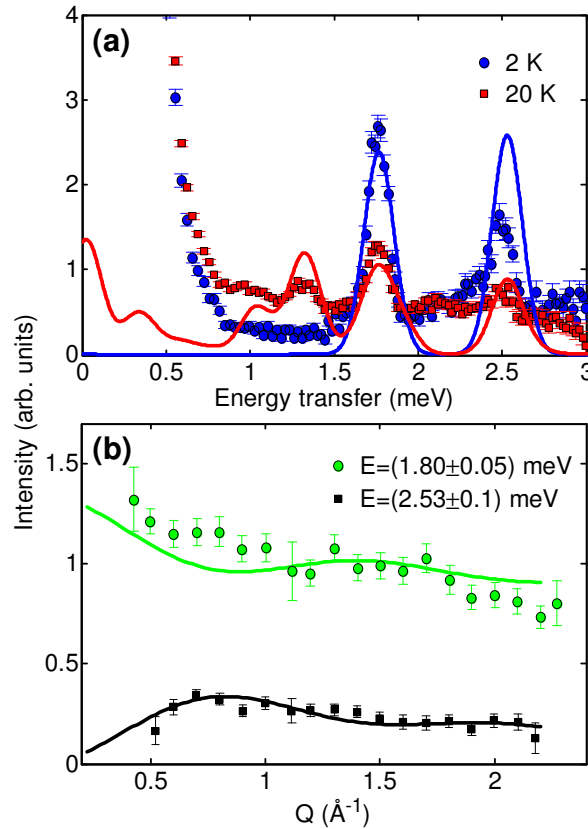


Figure 4.3.: (a) INS spectra of (1) with an incident wavelength of $\lambda = 4.6 \text{ \AA}$ (NEAT) for $T = 2 \text{ K}$ (blue circles) and $T = 20 \text{ K}$ (red squares). The continuous lines represent the spectra calculated assuming a dimer model for the spin Hamiltonian (Eq. 4.3). (b) Q -dependence of first intra- (green circles) and inter-multiplet (black squares) transitions measured on IN6 for $\lambda = 4.1 \text{ \AA}$ and $T = 2 \text{ K}$. Continuous lines represent the calculated Q -dependence using the dimer spin Hamiltonian Eq. 4.3 (assuming a dimer distance of $R = 5.17 \text{ \AA}$, which corresponds to the distance between the centre of the two triangles). Reprinted from [89]. Copyright (2010) by the American Physical Society.

be similar to the instrumental resolution. A closer look to the data reveals, that the peak at higher energy possesses a small shoulder, which (as will be discussed later) can be associated with tiny age depended structural modifications within the polycrystalline sample.

At $T = 20 \text{ K}$, additional excitations were detected, which must be due to transitions from thermally populated excited states. In particular, transitions were found at $1.30(4) \text{ meV}$ and $1.02(8) \text{ meV}$. The corresponding linewidth of the peak at low energy is twice as large as the ones at 1.30 and 1.77 meV , which might be either due to unresolved level splitting caused by second or fourth order transverse anisotropy terms or due to an

overlap of peaks resulting from transitions within different S multiplets.

Some first information concerning the character of the two observed ground state transitions can be gained by investigating the Q -dependence of the corresponding scattering intensity. Figure 4.3 (b) shows this dependence. A characteristic oscillatory behavior has been observed for the Q -dependence of the 2.53 meV transition (black squares), which presents a maximum of intensity at a finite Q value (that is related to the geometry of the molecule), and decreasing intensity as Q goes toward zero. This Q -dependence is typical for intermultiplet-transitions in magnetic clusters and reflects the multi-spin nature of the spin states [98, 99]. By contrast, the excitation at 1.77 meV (green circles) has maximum intensity at $Q = 0$, and thus follows a behaviour which is expected for a transition with $\Delta S = 0$. Furthermore, the intensity decreases with increasing Q , following the magnetic form factor.

Final evidence about the character of the observed excitations can be achieved by comparing the INS data to results from FDMR measurements. With FDMR it is only possible to detect transitions with a predominantly intra-multiplet character, thus the ones which have solely been observed by INS are inter-multiplet transitions. Figure 4.4 shows the FDMR spectra recorded on 350 mg unpressed powder of (1). The most pronounced feature is the resonance line at 1.80 meV, while much weaker features can be observed at 1.328(1) meV and 1.07(1) meV. The intensity of the higher-frequency line is strongest at lowest temperatures, proving that the corresponding transition originates from the ground state level. The lower frequency lines have maximum intensity at around 30 K. All three features agree with the findings from INS and therefore have been unambiguously identified as transitions with a predominant intra-multiplet character. The strong resonance line can be assigned to the transition $|S = 4, M_S = \pm 4\rangle \rightarrow |S = 4, M_S = \pm 3\rangle$, while the exact assignment of the two other intra-multiplet transitions remains the subject of accurate analysis of the corresponding spin Hamiltonian (see next section). The linewidth of the 1.33 meV line is slightly larger than that of the 1.80 meV line (41 μeV compared to 48 μeV), which is similar to what was found with INS. As mentioned above, this can point towards unresolved splitting due to transverse ZFS. No further features were observed with FDMR between 0.5 and 3.0 meV.

The intense resonance line shows two shoulders to lower energies, which are assigned to the lattice solvent loss, as has been also observed in the INS data as asymmetric line broadening (see above). These features are not due to isomers with different orientation of the Jahn-Teller distortion axis, as observed for Mn_{12} [100], because no signature of different isomers is seen in ac-susceptibility. Furthermore, also the possibility of closely spaced transitions due to frustration effects, as observed in the Fe_{13} cluster [101], can

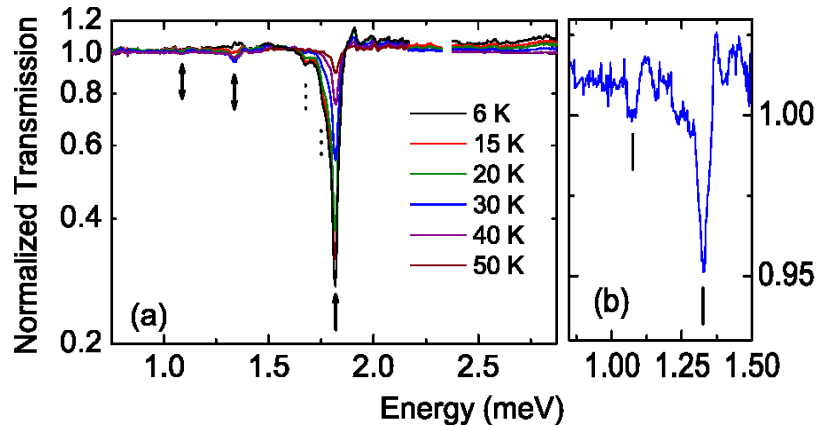


Figure 4.4.: (a) FDMR spectra of unpressed polycrystalline powder of (1) recorded at various temperatures. The intensity of the higher-frequency resonance line decreases with temperature, while that of the lower-frequency lines increases up to 30 K, beyond which it decreases again. Dotted lines indicate resonance lines due to impurities. (b) Expanded view of the low frequency part of the 30 K spectrum. Reprinted from [89]. Copyright (2010) by the American Physical Society.

be excluded, because the three intra-triangle exchange interaction are not equal. Since no further transitions have been observed with FDMR, all additional excitations detected by INS can be assigned to transitions with a predominantly inter-multiplet character. The findings are summarized in Table 4.1. The spectroscopic investigations reveal that at least one excited S multiplet lies very close to the ground state one, such that the strong exchange limit is certainly not a good approximation for this system. In order to interpret the results, ED calculations were performed using both the giant spin Hamiltonian (Eq. 4.1) as well as the full microscopic spin Hamiltonian (Eq. 4.2).

Giant Spin Approximation (GSA)

If one assumes that the three observed intra-multiplet transitions all correspond to transitions within the $S = 4$ ground multiplet, the giant spin Hamiltonian (Eq. 4.1) can be used to model the ground spin energy level diagram. Taking the transition energies from INS, the following crystal field parameters of the GSH gave the best match between theory and experiment: $D_S = -0.258$ meV and $B_4^0 = 1.86 \cdot 10^{-5}$ meV, where the corresponding transition energies are listed in Table 4.1¹. The obtained second or-

¹A similar set of parameters has been found by a fit of the FDMR data, being $D_S = -0.263$ meV and $B_4^0 = 1.86 \cdot 10^{-5}$ meV [89]. The small difference to the INS results is due to the slightly different peak positions in the FDMR spectra. This shift might be due to an age dependent modification of

der axial anisotropy parameter D_S is much larger than other reported spectroscopically determined D_S parameters for SMM, e.g. $D_{S=10} = -0.057$ meV for $\text{Mn}_{12}\text{-ac}$ [102], $D_{S=\frac{17}{2}} = -0.031$ meV for Mn_9 [92] and $D_{S=6} = -0.142$ meV for Mn_3Zn_2 [103]. The main reason for this large D -value is the fact that the projection coefficients for the single ion ZFS onto the cluster ZFS (see Eq. 2.39) are larger for spin states with lower S [31].

With the given set of parameters, the first two intra-multiplet transitions at ≈ 1.77 meV and ≈ 1.30 meV could be reproduced with high accuracy. In contrast, the giant spin model is not able to account for the ≈ 1.02 meV transition (see Table 4.1). A further evidence for the inability of the GSA to explain the INS and FDMR data is given by the calculated energy barrier for magnetisation reversal. The obtained GSA crystal field parameters suggest an energy barrier of $U \approx 48$ K. This value is much higher than the one derived from susceptibility measurements, being $U_{\text{eff}} \approx 28$ K. This indicates that the system is characterized by a more complex relaxation dynamics, involving excited S -multiplets, which are nested within the ground state one. Indeed, the difference in energy between the lowest and the highest energy levels of the anisotropy split $S = 4$ ground state is given, as a first approximation, by $|D|S^2=4.2$ meV. The presence of an inter-multiplet excitation at only 2.53 meV energy transfer, therefore below 4.2 meV, indicates that the first excited S multiplet lies within the energy interval of the anisotropy split $S = 4$ state. This suggests that the observed low energy excitations are possibly not pure intra-multiplet transitions, but are expected to originate from the $S = 4$ ground state and from the first excited S multiplet. Therefore the exact assignment of those excitations requires a more accurate analysis beyond the GSH approximation. Indeed, one fundamental requirement for the validity of the GSH approximation, i.e. an isolated ground state well separated from the excited states, is not fulfilled and S is not a good quantum number to describe the ground state of the molecule. To model the data it is thus necessary to use the full microscopic spin Hamiltonian of Eq. 4.2.

Full Hamiltonian

Given the low symmetry of the triangular units in (1), the number of free parameters in Eq. 4.2 would be too large to obtain unambiguous results, considering the low number of experimentally observed excitations. To account for the limited amount of information, an approximate model was employed that describes the molecule as an exchange-coupled dimer system (see Figure 4.5). More specifically, the two triangular units are described

the sample, caused by a loss of lattice solvent (see text).

Table 4.1.: INS and FDMR peak positions of intra- and inter-multiplet excitations in Mn_6 (**1**). Note that because of S mixing, S is not a good quantum number and the corresponding energy levels are characterized by their leading S component. In addition the calculated positions are given (n.o. = not observed).

	FDMR	Calc. (GSH)	INS	Calc. (GSH)	Calc. (Eq. 4.2)
Intra-multiplet	1.80	1.801	1.77(4)	1.767	1.77
	1.33	1.325	1.30(4)	1.301	1.29
			1.02(8)	0.797	1.02
Inter-multiplet	n.o.		2.53(3)		2.53

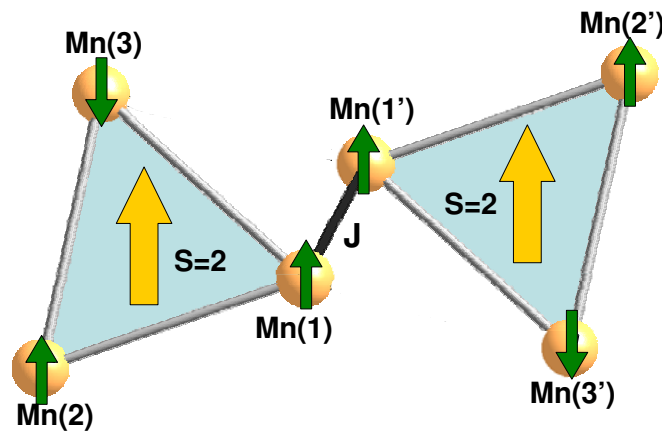


Figure 4.5.: Effective model for the Mn_6 (**1**) molecule. The two Mn-triangles are approximated by a dimer of coupled $S = 2$ spins.

as two ferromagnetically coupled $S = 2$ spins ($S = S_A = S_B$), which also experience an effective uniaxial crystal-field potential:

$$H_{\text{dimer}} = J(\mathbf{S}_A \cdot \mathbf{S}_B) + d(S_{A,z}^2 + S_{B,z}^2). \quad (4.3)$$

The corresponding anisotropy parameter d is equal for the two effective spin sites, since the two Mn-triangles of the molecule are related to each other by an inversion center. This model of course represents a strong simplification of the real problem, e.g. it neglects a huge number of energy levels, since the dimension of the Hamiltonian matrix to be diagonalized decreases from 15625 in the full case down to 25 in the dimer case. However, it can be assumed that this model correctly reproduces the *low energy part* of the spectrum and since the relaxation of the magnetization mainly involves states at low energies, it should provide suitable results concerning this issue. Recently, a similar

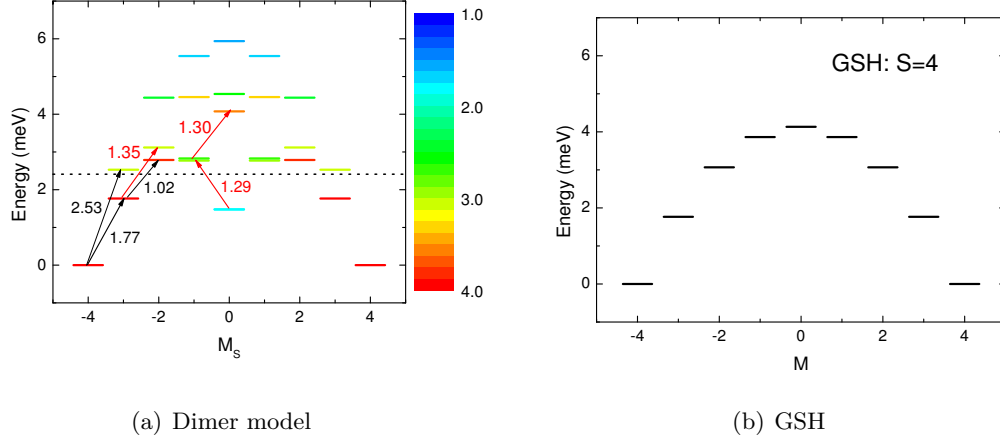


Figure 4.6.: (a) Energy levels as a function of the z -component of the total spin for Mn_6 (**1**). The colour maps S_{eff} , where $\langle S^2 \rangle = S_{\text{eff}}(S_{\text{eff}} + 1)$. The transitions observed by INS and FDMR are highlighted with arrows. The red arrows emphasize transitions that contribute to the peak at ≈ 1.30 meV (cf. Fig. 4.3(a)). The dotted line indicates the experimentally observed energy barrier U_{eff} . (b) Energy level diagram calculated with the GSA. The ground multiplet has $S = 4$.

model was successfully used by Bahr *et al.* to describe the quantum tunneling of the magnetization between different S multiplets in the Mn_6 (**3**) ($S=12$) SMM [104].

The spin Hamiltonian (Eq. 4.3) has been diagonalized numerically and the J and d parameters have been varied to obtain a best fit of the experimental data. The position of the peak at 1.77 meV does not depend on the exchange interaction, therefore its position sets the value of the axial anisotropy d parameter. Given the d parameter, a fit of the position of the peak at 2.53 meV sets the isotropic exchange parameter J .

The best fit of the experimental data is obtained with $J = -0.19$ meV and $d = -0.59$ meV and the calculated energy level scheme is reported in Fig. 4.6(a), where for comparison the energy level diagram in the GSA is also reported (Fig. 4.6(b)). The value of S_{eff} (where $\langle S^2 \rangle := S_{\text{eff}}(S_{\text{eff}} + 1)$) is labeled in colour and shows that the first $S = 3$ excited state is completely nested within the $S = 4$ ground state. From Fig. 4.6 it is also clear that the GSH model does not account for a number of spin states different from the ground state $S = 4$ multiplet at low energies. Furthermore, the assignment of the observed excitations can be misleading if considering the GSA only. For example, using the GSH model, the observed peak at 1.30 meV can only be attributed to a pure intra-multiplet excitation from $|4, \pm 3\rangle$ to $|4, \pm 2\rangle$, while using Eq. 4.3, it is found to be a superposition of several inter-multiplet and intra-multiplet transitions (indicated by red arrows in Fig. 4.6(a)). The GSA fails to describe the low energy level diagram of the

molecule and consequently fails to describe the relaxation of the magnetization. Indeed, the presence of excited states nested within the ground state multiplet has a significant effect on the relaxation dynamics, as will be discussed in Section 4.4.

The extracted axial anisotropy parameter d of the two single sites is considerably larger than the total axial anisotropy D which has been obtained with the GSH. This is because the total D reflects the projection of the single small d 's onto the total spin S . In fact, the projection coefficients according to Eq. 2.39 can be easily evaluated for the spin dimer system [31]. When neglecting the dipole-dipole contributions, one obtains for the case of two coupled $s = 2$ spins:

$$D_{S=4} = \Gamma_1 d_1 + \Gamma_2 d_2 = d(\Gamma_1 + \Gamma_2) = d\left(\frac{3}{14} + \frac{3}{14}\right) \approx -0.253 \text{ meV}. \quad (4.4)$$

This value is indeed very similar to the one obtained with the GSA.

4.3.2. **Mn₆ (2)** $U_{\text{eff}} \approx 53 \text{ K}$ vs. **Mn₆ (3)** $U_{\text{eff}} \approx 86.4 \text{ K}$; (**S=12**)

In a paper published in 2007, Milios and coworkers reported, that the introduction of sterically more demanding oximate ligands for the synthesis of Mn₆-based clusters, results in a twisting of the Mn-N-O-Mn torsion angles [83], which causes a switching of the intra-triangle exchange interactions from antiferromagnetic to ferromagnetic. The result was a large increase of the spin ground state from $S = 4$ to $S = 12$. In the framework of this thesis, two of the many reported derivatives of these $S = 12$ Mn₆ clusters were studied ((**2**) and (**3**), respectively). Compound (**2**) has undergone two structural changes compared to (**1**). First of all, the distance between the phenolato oxygen and the two square pyramidal Mn³⁺ ions has decreased from $\approx 3.5 \text{ \AA}$ to $\approx 2.5 \text{ \AA}$, thus all Mn³⁺ ions are now in six-coordinated distorted octahedral geometry (see Fig. 4.7). Secondly, the torsion angles of the Mn-N-O-Mn moieties have increased strongly with respect to those in **1**, being 38.20° , 39.9° and 31.26° , compared to 10.7° , 16.48° and 22.8° for (**1**). In (**3**), the introduction of two methyl groups on the carboxylate ligand has increased the non-planarity of the Mn-N-O-Mn moieties further, giving torsion angles of 39.08° , 43.07° and 34.88° [1]. The result is that the weakest ferromagnetic coupling is slightly stronger for (**3**) compared to (**2**). This effect has been interpreted in terms of the particular arrangement of the manganese d_{z^2} -orbitals with respect to the p -orbitals of the nitrogen and oxygen ions. A large (small) Mn-O-N-Mn torsion angle results in a small (large) overlap between the magnetic orbitals giving rise to ferromagnetic (antiferromagnetic or weak ferromagnetic) superexchange interactions [105].

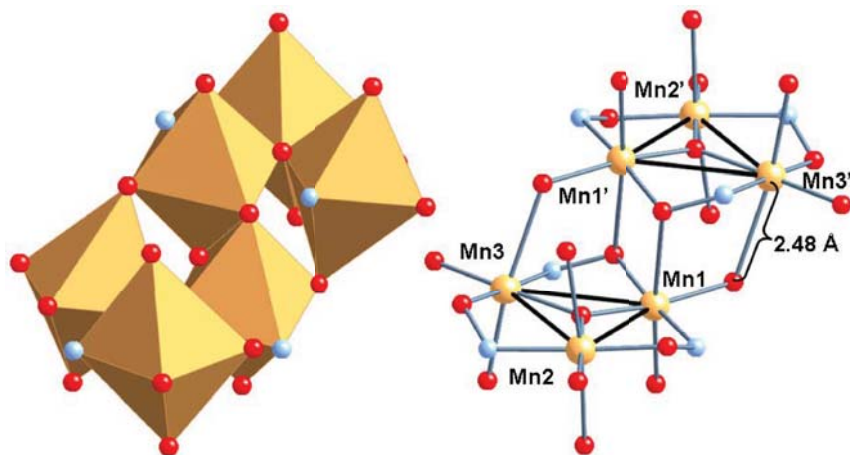


Figure 4.7.: Structure of the Mn_6 (**2**) molecular core. The Mn^{3+} ions are located at the vertices of two oxo-centered triangles. All Mn ions are in octahedral geometry and the octahedra are highlighted in orange (left figure). Color scheme: Mn, orange, O, red, N, blue. H and C ions are omitted for clarity. Reprinted from [89]. Copyright (2010) by the American Physical Society.

Using a single J model (e.g. assuming that the intra- and inter-triangle exchange couplings are equal), Milios *et al.* fitted dc-susceptibility data for molecules (**2**) and (**3**) and obtained: $J(\mathbf{2}) = -0.230$ meV and $J(\mathbf{3}) = -0.404$ meV [87, 85] (in the notation used here).

In spite of the fact that both (**2**) and (**3**) have $S = 12$ ground states and similar geometrical structures, radically different effective energy barriers towards the relaxation of the magnetization were observed, being $U_{\text{eff}} \approx 53$ K for (**2**) and $U_{\text{eff}} \approx 86.4$ K for (**3**). In order to understand this difference, an in-depth study of the energy level structure by means of INS has been performed. In a similar way to the previous section, the results will again be compared to the findings from FDMR measurements. Given that some of the exchange coupling parameters are rather small, and that the symmetry of the complexes is quite low, significant influence from low-lying excited spin multiplets can be expected.

Figures 4.8(a)-(f) present the high resolution INS experimental data for compounds (**2**) and (**3**), respectively, collected on IN5 with an incident wavelength of 6.7 \AA ($53 \mu\text{eV}$ FWHM at the elastic peak). While Figs. 4.8(a)-(d) display the complete energy-wavevector map of the measured spectra, Figs. 4.8(e)-(f) show the Q -integrated data ($0.4 \leq Q \leq 1.6 \text{ \AA}^{-1}$). At the lowest temperature $T = 2$ K only the ground state is populated and, due to the INS selection rules, only transitions with $\Delta S = 0, \pm 1$ and $\Delta M = 0, \pm 1$ can be detected. The excitations lowest in energy can thus be easily at-

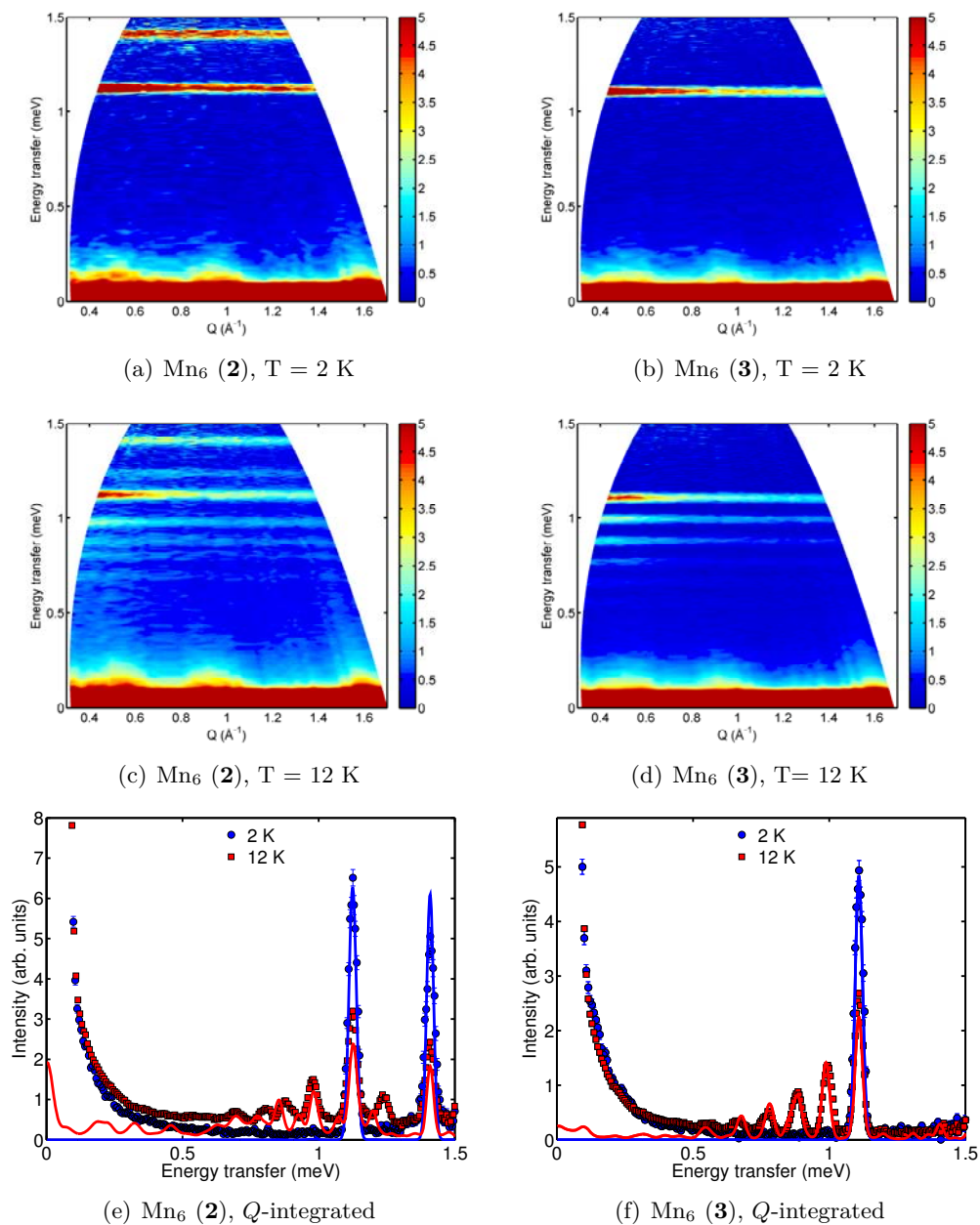


Figure 4.8.: (a)-(d) Energy-wave vector colourmap of the spectra recorded on IN5 for molecules (2) and (3) using an incident wavelength of $\lambda = 6.7 \text{ \AA}$. The colourbar displays the corresponding scattering intensity in arbitrary units. Data were collected at $T = 2 \text{ K}$ and $T = 12 \text{ K}$. (e)-(f) Q -integrated spectra of the two molecules. Continuous lines correspond to the calculated spectra using the parameters listed in Table 4.3. Reprinted from [89]. Copyright (2010) by the American Physical Society.

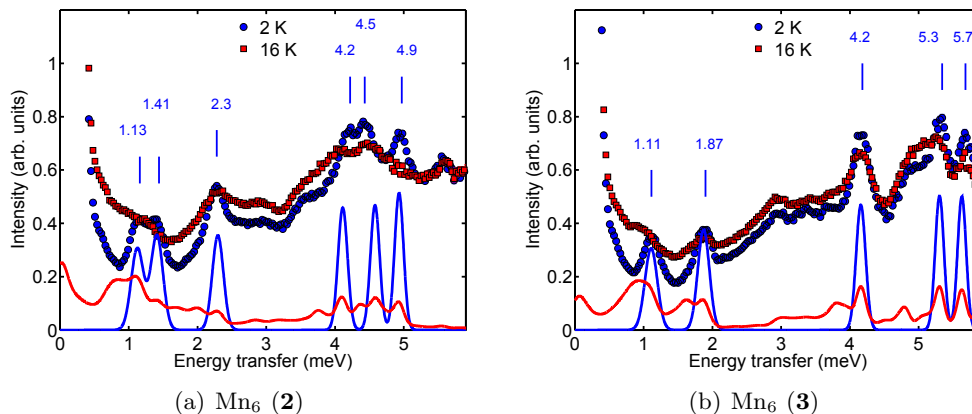


Figure 4.9.: INS spectra collected at IN5 with incident wavelength of 3.4 \AA at $T = 2 \text{ K}$ (blue) and $T = 16 \text{ K}$ (red). Lines represent theoretical calculations using the spin Hamiltonian of Eq. 4.2. Reprinted from [89]. Copyright (2010) by the American Physical Society.

tributed to the intra-multiplet transition from the $|S = 12, M_S = \pm 12\rangle$ ground state to the $|S = 12, M_S = \pm 11\rangle$ first excited level. The position of this intra-multiplet excitation is found to be at about the same energy in both compounds, e.g. $\sim 1.1 \text{ meV}$. The low energy spectra does not display significant differences between the two complexes, indicating only slight changes in the anisotropy of the system. In contrast, the first inter-multiplet $S = 12 \rightarrow S = 11$ excitation at about 1.41 meV in compound **(2)** is not visible in the spectra of compound **(3)** at 6.7 \AA . This can be understood looking at the data at higher energy transfer, collected with an incident wavelength of 3.4 \AA (see Figs. 4.9(a) and 4.9(b)). Indeed, the first inter-multiplet excitation is considerably raised in energy in compound **(3)** with respect to compound **(2)**, from 1.41 meV to 1.87 meV . This gives a direct evidence of an increase of the isotropic exchange parameters, while the anisotropic parameters are approximately the same for both molecules. The INS spectra collected at a base temperature of 2 K , enabled the direct access of a whole set of intra-multiplet and inter-multiplet transitions allowed by the INS selection rules in both compounds. By raising the temperature to 16 K the intensity of the magnetic peaks decreases, thus confirming their magnetic origin². A total of five inter-multiplet excitations for compound **(2)** toward different $S = 11$ excited states can be detected. For compound **(3)** four inter-multiplet excitations have been observed. All the magnetic excitations are marked in Fig. 4.9 with the corresponding transition energies.

In addition, a complete set of excitations from thermally populated levels was collected

²In contrast, the feature at $\sim 3.5 \text{ meV}$, which is present in both samples, is due to phonons and does not decrease upon heating.

at high temperatures, (see spectra at $T = 12$ K in Figure 4.8). Those of the additional peaks, which occur below the most intense $|S = 12, M_S = \pm 11\rangle$ transition at ~ 1.1 meV can be mainly attributed to intra-multiplet transitions within the $S = 12$ ground state multiplet, while additional peaks above this energy (e.g. at ~ 1.24 meV for **(2)**) are due to transitions within and/or between excited S -multiplets. However, a more precise characterization can be given after comparing the INS data to results from FDMR measurements. All peaks of the INS spectra could be fitted to Gaussian line shapes. Down to 0.6 meV, the peak width is in agreement with the instrumental resolution, while peaks below this energy show a slight broadening. This can be either attributed to additional transverse components of the anisotropy which lift the degeneracy of the $|S, \pm M_S\rangle$ doublets, or to transitions within and between excited S -multiplets.

To complete the investigations of the transitions within the $S = 12$ ground-state multiplet, additional high resolution measurements of molecule **(3)** were performed using IN5 with incident wavelengths of 10.5 \AA (FWHM = $13 \mu\text{eV}$ at the elastic line)(see Fig. 4.10). These measurements allowed transitions originating from the top of the anisotropy barrier to be observed.

A further confirmation of the good assignment of the observed excitations is provided by the study of their Q -dependence. As revealed from Fig. 4.11, the intra-multiplet transition ($\Delta S=0$) shows a distinctive Q -dependence, with a pronounced intensity at low Q , that dies out quite rapidly following the Mn^{3+} form factor. In contrast, inter-

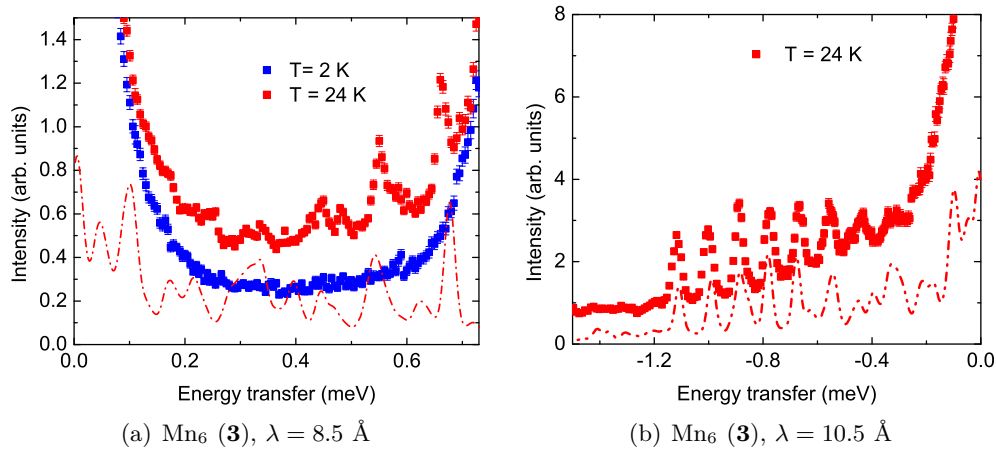


Figure 4.10.: Very high resolution INS spectra of molecule **(3)** collected on IN5 with incident wavelength of 8.5 \AA (a) and 10.5 \AA (b) at $T = 2 \text{ K}$ (blue) and 24 K (red). In (b) the energy gain spectra is displayed and the dotted line represents theoretical calculations using the spin Hamiltonian of Eq. 4.2. Reprinted from [89]. Copyright (2010) by the American Physical Society.

multiplet excitations present a flatter behaviour, with considerably lower intensity at low Q . This Q -dependence is typical for magnetic clusters and reflects the multi-spin nature of the spin states [106].

The FDMR spectra for molecules **(2)** and **(3)**, which have been measured by Slageren *et al.* using pressed **(2)** and unpressed **(3)** powder pellets of the corresponding samples, are depicted in Fig. 4.12. For sample **(2)**, five resonance lines have been observed, which can be attributed to resonance transitions within the $S = 12$ multiplet (Fig. 4.12(a)). Thus, the highest frequency line is assigned to the $|S = 12, M_S = \pm 12\rangle \rightarrow |S = 12, M_S = \pm 11\rangle$ transition, and so on. The magnetic origin of the peaks is further confirmed by their characteristic temperature behaviour. All detected transitions are consistent with the INS measurements and the findings are summarized in Table 4.2. No further transitions have been observed with FDMR between 0.25 meV and 2.2 meV and thus it can be concluded, that all additional peaks observed by INS, are due to transitions with a predominant inter-multiplet character.

Similar observations have been made for sample **(3)**, where the FDMR measurements reveal six sharp resonance lines (Fig. 4.12(b)). Again, the observed features can be attributed to transitions within the $S = 12$ multiplet and perfect agreement with the INS data is given (see Table 4.2). In addition, FDMR shows no further transitions in the measured energy range (0.25 meV-2.2 meV). In particular, none of the low energy peaks from INS below 0.5 meV were observed, even though, those do at least partially originate from intra-multiplet transitions. This indicates that the states at the top of

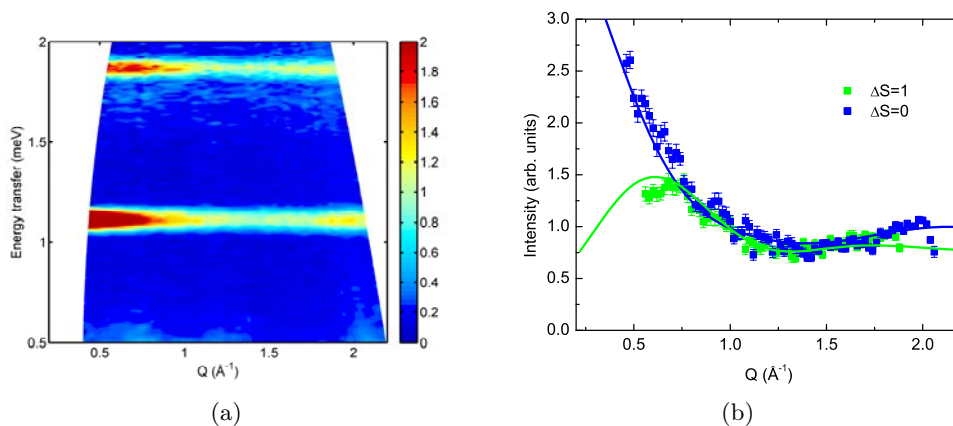


Figure 4.11.: (a) Energy-wavevector colormap of sample **(3)** collected on IN5 with incident wavelength of 5.0 Å. (b) Q dependence of two transitions from the ground state. The blue curve corresponds to the $|S = 12, M_s = \pm 12\rangle \rightarrow \pm 11\rangle$ intramultiplet transition and the green curve displays the $|S = 12\rangle \rightarrow 11, M_s = \pm 12\rangle \rightarrow \pm 11\rangle$. Lines represent the theoretical calculations based on Eq. 4.2. Reprinted from [89]. Copyright (2010) by the American Physical Society.

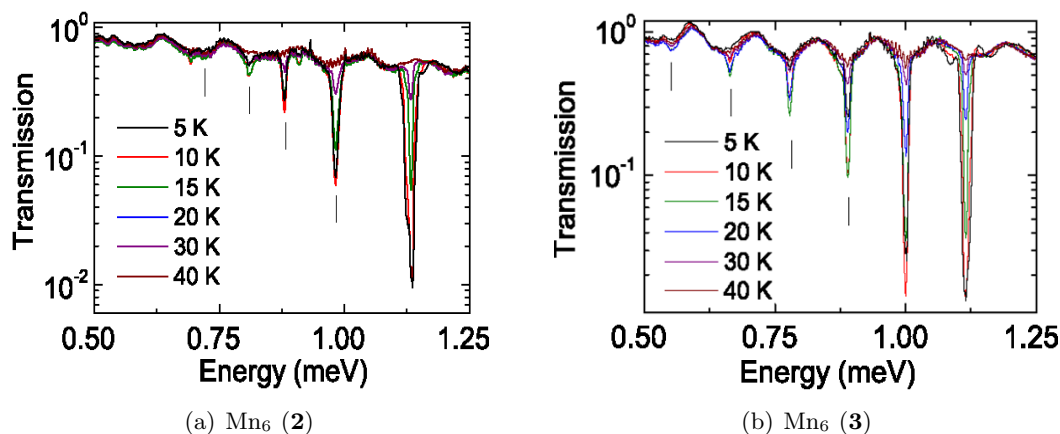


Figure 4.12.: FDMR spectra recorded on (a) a pressed powder pallet of **(2)** and (b) on unpressed polycrystalline powder of **(3)** at various temperatures. All except the strongest transitions are indicated by vertical lines. Reprinted from [89]. Copyright (2010) by the American Physical Society.

the multiplet are not purely assigned to a single S value, but are heavily (S -)mixed, such that with the given resolution of the spectrometer, their observation is not possible.

Giant spin approximation

In a first attempt, the GSA (Eq. 4.1) has been used to model the observed energy levels of the ground state multiplet, where the calculations were done with the <SMMS> software [94]. To do so, the crystal field parameters, as they appear in Eq. 4.1, have been adjusted manually, until the best agreement between measured and calculated data was achieved. For sample **(2)**, the parameters $D = -0.0456$ meV and $B_4^0 = -5 \cdot 10^{-7}$ meV gave the best fit to the data and the corresponding transition energies are listed in Table 4.2. The same results have been obtained by fitting the FDMR spectra [89]. Even though, the energy levels could be reproduced quite well with the extracted giant spin parameters, some discrepancies remain, e.g. it was not possible to find a set of parameters, which could account for the exact positions of the two highest energetic transitions (~ 1.13 meV and ~ 0.98 meV).

The theoretical energy barrier derived from the fitted crystal field parameter is $U = 76.5$ K, which is significantly higher than the one determined from relaxation measurements ($U_{\text{eff}} = 53.1$ K). This indicates, that (as for molecule **(1)**) the energy barrier U is not simply determined by the ground state anisotropy, but is strongly influenced by the mutual interplay between anisotropy and magnetic exchange interactions.

The strong influence of the exchange coupling on the relaxation behaviour can be seen

Table 4.2.: INS and FDMR peak positions of the observed excitations for **(2)** and **(3)** in meV (n.o. = not observed). In addition, the energy levels calculated with the GSA are given, where the ZFS parameter extracted from the INS data were used.

(2)	INS	FDMR	GSA	(3)	INS	FDMR	GSA
	4.9(2)	n.o.			5.7(2)	n.o.	
	4.5(1)	n.o.			5.3(2)	n.o.	
	4.2(2)	n.o.			4.2(2)	n.o.	
	2.3(2)	n.o.			1.87(3)	n.o.	
	1.41(2)	n.o.			1.11(1)	1.107(7)	1.11
	1.24(7)	n.o.			0.99(1)	0.993(6)	0.99
	1.13(2)	1.127(5)	1.10		0.88(2)	0.883(6)	0.87
	0.98(2)	0.975(5)	0.99		0.77(1)	0.772(7)	0.77
	0.88(3)	0.873(6)	0.88		0.66(1)	0.657(7)	0.66
	0.80(2)	0.803(7)	0.78		0.55(2)	0.551(10)	0.56
	0.70(2)	0.687(5)	0.68		0.48(1)	n.o.	0.47
	0.57(4)	n.o.	0.58		0.45(1)	n.o.	0.47
					0.34(1)	n.o.	0.38
					0.31(1)	n.o.	0.38
					0.25(1)	n.o.	0.29
					0.21(3)	n.o.	0.29

by comparing the fitting results from the GSA of molecule **(2)** with the ones of molecule **(3)**. For molecule **(3)**, the best fit of the ground multiplet energy levels was obtained with the crystal field parameter $D = -0.0447$ meV and $B_4^0 = -8.0 \cdot 10^{-7}$ meV and again good agreement with the results from FDMR was found. Furthermore, similar values have been obtained from a ligand field study based on the angular overlap model [107]. In addition, the fine structure of the INS spectra gives rise to a small transverse anisotropy component, for which (according to the data) an upper limit of $E \leq 0.005$ meV could be estimated. The energies of the ground state multiplet, assuming only axial anisotropy, are given in Table 4.2. Apart from the discrepancies at low energy, the GSA provides a good fit of the experimental data for molecule **(3)** and matches the spectroscopic data much more closely than those of molecule **(2)**. The better agreement results from the stronger ferromagnetic exchange interactions in molecule **(3)**, causing a shift of the lowest excited S -multiplet towards higher energies and thus lessens its influence on the ground state multiplet. However, even for molecule **(3)** the GSA is not able to explain the experimentally obtained energy barrier, which is $U_{\text{eff}} = 86.4$ K. The crystal field parameters which have been obtained from INS, suggest a lower barrier of $U = 75.2$ K, e.g. the theoretical value is *smaller* than the experimental one. This unprecedented

finding means that the magnetization relaxation *must* involve states that do not belong to the ground state multiplet.

Another interesting aspect is, that the second order axial anisotropy parameter D , for the systems (2) and (3) is approximately six times smaller than the one for (1), even though the crystal structures of all molecules are very similar. This underlines the fact, that D is directly related to the total spin S , as has been introduced in Eq. 2.2.7. The projection of the individual single ion anisotropies d_i onto S leads to a greater total D for molecules, that have a lower spin ground state S .

The investigations revealed, that the GSA cannot account accurately for the ground multiplet level splitting of both Mn_6 ($S = 12$) molecules. More importantly, it completely fails to describe the relaxation dynamics within the molecule, since it cannot reproduce the correct value of the energy barrier against the reversal of the magnetization. As has been shown above, there is a strong relation between the strength of the isotropic exchange interactions and the effective barrier U_{eff} . In order to understand this relationship, a model is needed, which goes beyond the GSA and treats the crystal field splitting and the Heisenberg exchange interactions on equal footings.

Full Hamiltonian

On a microscopic basis, the Mn_6 molecules can be modeled by the Hamiltonian introduced in Eq. 4.2. This Hamiltonian takes into account both, the individual exchange interactions between the different ions within the cluster and the ZFS interactions at the individual Mn^{3+} sites. The particular structure of Mn_6 allows the number of free parameters in Eq. 4.2 to be constrained, e.g. it can be assumed that the three intra-triangle exchange interactions are equal (see Fig. 4.13). In addition, the ligand cages of sites 1 and 3 are rather similar and thus the corresponding crystal field parameters were set to be equal as well. Since the molecule possesses an inversion center, sites 1 and 1', 2 and 2', 3 and 3' are equivalent, which further reduces the number of parameters (Fig. 4.13). In total, both Mn_6 ($S = 12$) molecules could be described by a set of nine free parameters, including three different exchange constants J_1, J_2, J_3 and two sets of crystal field parameters d_1, c_1, e_1 and d_2, c_2, e_2 . The dominant crystal field terms are the second order axial ones, while the other terms (second order transverse and fourth order axial) are much weaker. Although the INS and FDMR measurements provided a great number of transitions to be observed, the experimental information were not sufficient to fix all four small c and e parameters and therefore it was chosen to constrain the ratios c_1/c_2 and e_1/e_2 to the ratio d_1/d_2 .

With the remaining crystal field and exchange parameter, a successful fit of the observed

INS peak positions could be performed. For the fitting, all free parameter were allowed to vary simultaneously and for each cycle, the eigenvalues of the Hamiltonian matrix were obtained numerically using the exact diagonalization method. The assignment of the observed peaks to intra-multiplet or inter-multiplet transitions has been confirmed by comparison with the FDMR results, where intense transitions only occur between states whose dominant components have the same total spin.

The results for Mn_6 (**2**) are summarized in Table 4.3. As expected from magnetisation measurements, the exchange in (**2**) is predominantly ferromagnetic, where the strongest coupling occurs between the two triangular units (J_1). The ferromagnetic coupling J_2 within the triangles has about half the size of J_1 , while the second inter triangular coupling J_3 is much smaller and antiferromagnetic.

The large axial anisotropy parameters d_i reflect the strong uniaxial distortion of the octahedral cages around the Mn ions. In contrast, the nonaxial contributions to \mathcal{H} appear to be a few percent of the axial ones but too small to be determined precisely with the measured data. Based on the parameters listed in Table 4.3 the INS data could be successfully reproduced, as can be seen by the solid lines in Figs. 4.8(e) and 4.9(a).

The low energy part of the calculated energy level diagram for molecule (**2**) is depict in Fig. 4.14(a), where the colourmap represents the corresponding effective spin associated with the involved spin wave function. The fact, that the ferromagnetic exchange couplings have the same order of magnitude as the axial crystal field parameter, manifests in a nesting of several excited multiplets within the ground $S = 12$ one. For instance, there are four energy levels belonging to $M_S = \pm 11$ states, which lie below the effective energy

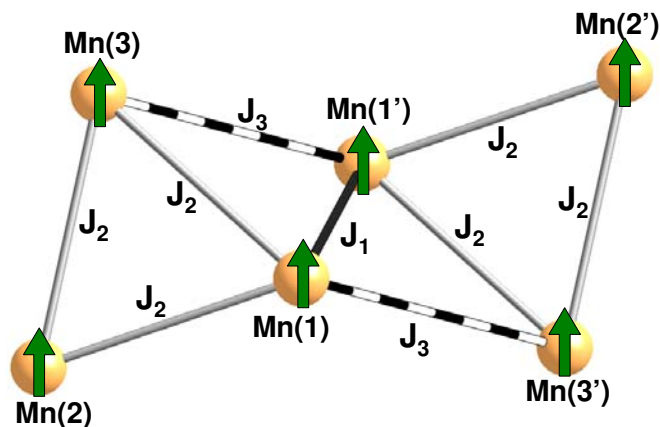


Figure 4.13.: Leading exchange interactions within the Mn_6 molecules (**2**) and (**3**). The single ion spins are highlighted as green arrows. Reprinted from [89]. Copyright (2010) by the American Physical Society.

Table 4.3.: Isotropic exchange and CF parameters for Eq. 4.2 (in meV) deduced by fitting INS and FDMR data for the two Mn_6 $S = 12$ compounds.

	U_{eff} (K)	J_1	J_2	J_3	d_1	d_2	c_1
(2)	53.0	-0.61(5)	-0.31(3)	0.07(1)	-0.23(1)	-0.97(2)	-0.0008(3)
(3)	86.4	-0.84(5)	-0.59(3)	0.01(1)	-0.20(1)	-0.76(2)	-0.0010(3)

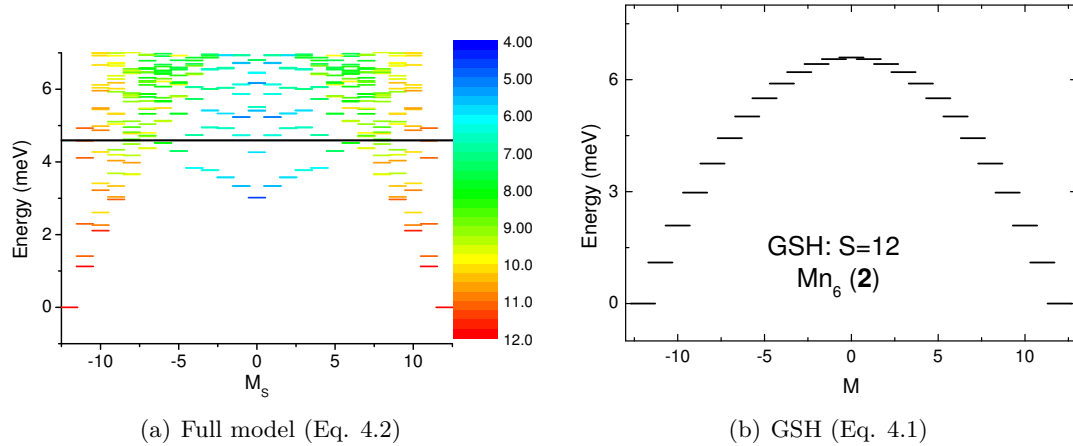


Figure 4.14.: (a) Energy levels as a function of the z -component of the total spin for Mn_6 **(2)**. The colour maps S_{eff} , where $\langle S^2 \rangle = S_{\text{eff}}(S_{\text{eff}} + 1)$. The black dashed line indicates the experimentally observed energy barrier U_{eff} . (b) Energy level diagram calculated with the GSA. The ground multiplet has $S = 12$. Reprinted from [90]. Copyright (2008) by the American Physical Society.

barrier $U_{\text{eff}} \approx 4.6$ meV and which can be associated with different excited S -multiplets. The nesting leads to a very large degree of S -mixing of the spin wave functions and strongly influences the relaxation behaviour.

Similar findings have been made for molecule **(3)**. The best agreement between the theoretical calculations and the data from INS and FDMR could be achieved with the exchange and crystal field parameters listed in Table 4.3, where the corresponding calculations for the INS scattering function are included in Figs. 4.8(f), 4.9(b) and 4.10. In addition, also the characteristic Q -dependence of both, the intra- and the intermultiplet ground state transitions could be reproduced accurately, as can be seen from Figure 4.11(b). Compared to **(2)**, the ferromagnetic exchange interactions increased, which can also be seen in the neutron data from the shift of the $S = 11$ multiplet towards higher energies. On the other hand, the local axial anisotropy parameters remain almost unchanged and thus the remarkable increase of the energy barrier can be directly

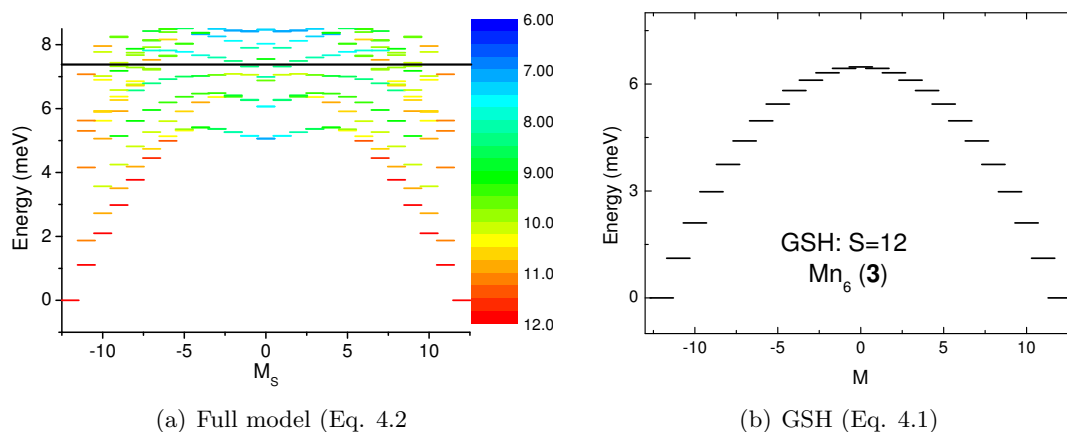


Figure 4.15.: (a) Energy levels as a function of the z -component of the total spin for $\text{Mn}_6(3)$. The colour maps S_{eff} , where $\langle S^2 \rangle = S_{\text{eff}}(S_{\text{eff}} + 1)$. The black dashed line indicates the experimentally observed energy barrier U_{eff} . (b) Energy level diagram calculated with the GSA. The ground multiplet has $S = 12$. Reprinted from [90]. Copyright (2008) by the American Physical Society.

attributed to the different isotropic exchange interactions within the clusters³. Figure 4.15(a) shows the calculated energy level diagram for (3) . Despite the stronger ferromagnetic exchange, the nesting of S multiplets within the ground state one is still strong, e.g. a multiplet with easy-plane effective anisotropy is clearly visible around ~ 5 meV, well below the anisotropy barrier of the $S = 12$ ground state multiplet (~ 6.8 meV).

4.4. Discussion

The experimental data collected on the three variants of Mn_6 SMMs provide direct evidence that a general feature for this class of compounds is the nesting of excited multiplets within the ground state one. This is an unavoidable effect when the isotropic exchange parameters and the single ion anisotropy parameters possess the same energy scale, as it is the case for Mn_6 . By comparing the energy level diagrams of the full microscopic spin Hamiltonian (Figs. 4.6(a) 4.14(a) and 4.15(a)) with the level scheme derived with the GSH (Figs. 4.6(b) 4.15(b) and 4.15(b)), it becomes immediately clear that the giant spin mapping completely breaks down in all three molecules, not only for the large S -mixing in the wave functions, but more fundamentally for failing to account for the number of states located below the barrier.

³ Note that again, the non axial contributions to \mathcal{H} were too small to be determined from a fit of the INS and FDMR data.

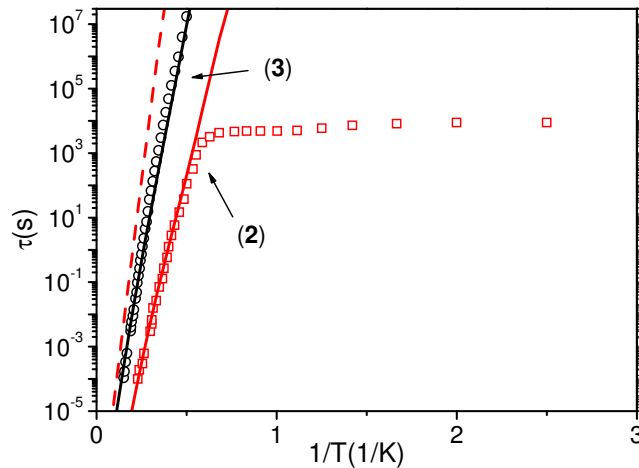


Figure 4.16.: T dependence of the leading relaxation time τ . Black circles and red squares are experimental data of **(3)** [83] and **(2)** [1], respectively. In the thermally activated regime, $\tau \cong \tau_0 \exp(U/k_B T)$ with $U \cong 86.4$ K, $\tau_0 \cong 2 \times 10^{-10}$ sec for **(3)** and $U \cong 53.1$ K, $\tau_0 \cong 8 \times 10^{-10}$ sec for **(2)**. Solid lines are the present theoretical calculations (red for **(2)** and black for **(3)**). The dashed line is the result for **(2)** when excited multiplets are neglected. Reprinted from [90]. Copyright (2008) by the American Physical Society.

Since the main difference between the two high spin Mn_6 molecules **(2)** and **(3)** are the positions of the excited S manifolds, these systems provide the possibility to investigate the role of these manifolds in determining the relaxation behaviour. This issue has been addressed by Carretta *et al.*, who have performed calculations of the relaxation dynamics for the two molecules, based on the findings mentioned in this section [90]. The relaxation dynamics have been studied by modeling the phonon-assisted barrier crossing mechanism, where the main contribution to the magneto elastic coupling comes from the modulation of the electric-quadrupole moment of each Mn^{3+} -ion by Debye acoustic phonons [97]. From the calculation of the corresponding transition rates between pairs of eigenstates of Eq. 4.2 the low temperature relaxation spectrum for the two Mn_6 molecules can be evaluated [90].

Figure 4.16 displays the experimentally obtained relaxation behaviour as a function of temperature for molecules **(2)** [83] and **(3)** [1] together with the theoretical calculations. For both systems, the relaxation spectrum is characterized by a single dominating relaxation time, whose T -dependence displays a nearly Arrhenius behaviour $\tau(T) = \tau_0 \exp(U/k_B T)$, in agreement with the experimental findings. This monoexponential behaviour of τ is not *a priori* obvious, since many different relaxation paths passing through excited S -multiplets can contribute to the decay of the magnetisation.

However, the reason for the presence of a single dominating time is essentially the same as in the conventional giant spin SMM⁴. In spite of multiple nesting, the low energy levels continue to retain a double-well structure (Figs. 4.14(a) and 4.15(a)), which leads to two separated time scales in the relaxation dynamics of the magnetization M . On the one hand, many fast intrawell processes produce an internal equilibrium of each well, while the overall well-occupation probabilities are governed by a single very slow interwell process. In the case of low temperatures and low magnetic fields, thermal fluctuations mainly result in unbalancing the relative population of the two wells and the regression of these fluctuations occurs through the slow process only, resulting in a single-time behaviour. In contrast to the GSA, where the relaxation appears via a multistep process involving only the zero field split ground state multiplet, the process becomes less obvious when many other excited S -multiplets are involved. In this case, the energy barrier U does not simply reflect the anisotropy of the molecule, but has to be seen as an effective value, which results from a nontrivial weighted average of the energies of levels involved in the direct interwell transition path. Thus, U is not simply determined by the ground-multiplet anisotropy alone, but by the mutual interplay of anisotropy and exchange. For example, the significant increase of U in molecule **(3)** with respect to **(2)** results from the substantially larger exchange interactions of the former one. If one artificially isolates the ground spin multiplet of **(2)** by strongly increasing the ferromagnetic exchange interactions, the barrier height reaches a value close to 100 K, which is indicated by the dashed line in Fig. 4.16. It is important to stress, that the value of the effective barrier is not set by the energy of the lowest M_S eigenstate.

Following the same procedure adopted for the two $S = 12$ molecules **(2)** and **(3)**, also the relaxation dynamics of the $S = 4$ molecule **(1)** have been studied and a very similar behaviour has been found. Also in this case the relaxation dynamics of M are characterized by a single dominating relaxation time with a nearly Arrhenius like behaviour, where the corresponding relaxation processes (fast intra-well- and slow inter-well-processes) are the same as described above. As can be observed from the energy level diagram of Fig. 4.6(a) there are several (ground state and excited S -state) levels that can be involved in the inter-well relaxation process, giving rise to an overall effective barrier U_{eff} different from the simple energy difference between the $M = 0$ and $M = \pm 4$ states. The corresponding calculated energy barrier $U_{\text{calc}} = 32$ K reproduces quite well the experimental value, $U_{\text{eff}} = 28$ K. The lowering of the barrier is therefore attributed to the presence of

⁴Since the Hamiltonian is almost axial, the z component of the total spin is conserved, even if S^2 is not. Thus, the selection rule $|\Delta M| \leq 2$ for phonon-induced transitions (see Sec. 2.2.1) remains relevant and the S -mixing in the wave functions does not change the degree of time-scale separation of intra- and inter-well processes.

these extra paths. Indeed, the calculations for artificially isolated $S = 4$ yield $U = 47$ K [89].

Apart from strongly influencing the phonon mediated relaxation processes, the excited S -multiplets that are nested within the ground state one also give rise to quantum tunneling of the magnetization between states belonging to different multiplets. This results in additional steps in the field dependent magnetization, which cannot be explained by conventional intra-multiplet type level crossings [108, 104, 109, 110, 111]. The additional steps result from resonant incoherent tunneling processes between different S -multiplets. Using the parameters given in Table 4.3 one can predict at which values of the applied magnetic field such tunneling occurs and it was shown in Ref. [90] that the calculated level crossings are in good agreement with the experimentally observed ones.

Finally, some further comments can be made regarding the D value for the ground state of each molecule. While no large difference between the local d parameter of the low (**1**) and high (**2**) and (**3**) spin molecules is expected, the overall D value, as determined using the GSH approximation, is much higher for the $S = 4$ molecule ($D \approx -0.26$ meV) than for the high spin molecules ($D \approx -0.046$ meV). However, this observation should not be misinterpreted. The difference arises from the fact that D depends on the projection of the individual single-ion anisotropies of each magnetic ion onto the total spin quantum number S . In the case where the S -mixing is negligible and the spin ground state is a good quantum number, the D parameter for a specific state S can be written as linear combination of the single-ion anisotropy tensors (see Eq. 2.39 and [31]). The projection coefficients of the single ion anisotropy to spin states of different S values can differ significantly, giving rise to considerably different D values. The ligand field study of various members of the Mn_6 family provides experimental evidence for this [107]. Recent theoretical studies proposed that the intrinsic relationship between S and D causes a scaling of U that goes approximately with S^0 (see Ref. [36] and [35]), raising the question whether it is worth trying to increase the value of spin ground state to obtain a larger energy barrier. Indeed, higher spin ground states would correspond to lower D parameters, neutralizing the overall effect on the height of the anisotropy barrier. In recently performed electron paramagnetic resonance studies the authors proposed that the barrier goes roughly with S^1 instead [112]. In the specific case of Mn_6 , because of the very large S -mixing, the projection onto a well defined spin state is no more justified and it is not possible to associate the barrier U to a defined S value. However, if one considers the effective anisotropy barrier for artificially isolated $S = 4$ and $S = 12$ states (i.e. $U = 47$ K for **1**) and $U = 105$ K for **2**), one can confirm that the barrier does not go quadratically with S , as one could naively deduce from the equation $U = |D|S^2$.

Indeed, $U_{S=12}/U_{S=4} = 2.2 \ll 12^2/4^2=9$. This confirms what has been pointed out in Ref. [36], i.e. even though the highest anisotropy barrier is obtained with the molecule with the highest spin ground state, the increase of the total spin is not as efficient as one would expect and alternative routes, like increasing the single ion anisotropy, should be considered.

4.5. Conclusions

In conclusion, by studying three different variants of Mn₆, it could be shown, that the excited S multiplets that overlap with the ground state one, have a tremendous influence on the relaxation processes in the molecules. The giant spin picture, which was successfully used to describe conventional SMM having well separated S multiplets, turned out to be completely inappropriate for the Mn₆ clusters, because the effective energy barrier for the reversal of the magnetization depends crucially on the position of the excited S -multiplets.

5. Nuclear and magnetic structure of CaV_2O_4

This chapter describes (single crystal and powder) neutron and X-ray diffraction measurements done to observe the crystal structure and magnetic order of CaV_2O_4 over range of temperatures. The data reveal a complex double-chain structure of V^{3+} -ions giving rise to quasi-one-dimensional antiferromagnetic exchange interactions and a strongly reduced magnetic ordering temperature. The magnetic structure was found to be non-collinear and the corresponding interactions were interpreted in terms of orbital configurations. Additionally, high temperature dc-susceptibility data are presented, which were analysed by means of exact diagonalization calculations based on a $S = 1$ Heisenberg model with antiferromagnetic nearest and next nearest neighbour exchange interactions.

5.1. Nuclear structure

The following section focuses on the nuclear structure of CaV_2O_4 . A complementary powder diffraction study has been done, using both neutron and X-ray radiation. The data show a structural phase transition from an orthorhombic to a monoclinic structure upon cooling. A combined refinement was used in order to determine the crystal symmetry, the lattice parameters and the atomic positions for both structures. In addition single crystal neutron diffraction was performed, which allowed particular reflections in the region around the phase-transition to be investigated and thus further conclusions to be drawn about the crystal symmetry. The obtained lattice structures were investigated in terms of bond-distances and angles, degree of distortion and bond valences.

5.1.1. Introduction

The room temperature nuclear structure of CaV_2O_4 was first investigated by Bertaut and coworkers in 1955 [113]. By analysing the X-ray powder pattern using the method of Fourier analysis they found out that CaV_2O_4 crystallizes in an orthorhombic structure

with space group Pbnm (D_{2h}^{16}) with a characteristically short b axis ($\approx 3 \text{ \AA}$). In 1956, 8 months after this paper, Hill *et al.* published an article in which they presented a detailed analysis of the crystal structure of CaFe_2O_4 and $\beta\text{-CaCr}_2\text{O}_4$ [114]. Both materials form a structure identical to that of CaV_2O_4 , however, this work attracted a lot more attention, and as a result nowadays this structure is known as the calcium ferrite-type structure. Until today, a great number of other AB_2O_4 -type compounds with CaFe_2O_4 structure was reported, where A and B represent the various number of elements¹.

Throughout this thesis, the equivalent structural representation of [114] will be followed, with the space group being Pnam and the short axis along the c -direction. All atoms in CaV_2O_4 are placed on the Wyckoff position $4c$, with $(x, y, \frac{1}{4})$. In detail, the crystal structure consists of two inequivalent Vanadium(III) sites, both in a distorted octahedral geometry, coordinated by six oxygen ions. The VO_6 octahedra of the same sites are edge-sharing and form double chains running along the crystallographic c -direction. The chains are joined to each other by octahedral corners in such a way, that they form large enough tunnels to accommodate the calcium ions. The Ca^{2+} -ions are eightfold coordinated by oxygen, with six of the oxygen ions forming a trigonal prism, while the two remaining ones lie on the same level as the calcium in staggered bond positions [114]. Materials with the CaFe_2O_4 structure are sometimes also called post-spinels. The reason for this is that some spinel compounds transform into the 6 % denser CaFe_2O_4 structure under high pressure. For example the primal spinel MgAl_2O_4 transforms into a CaFe_2O_4 -type structure at pressures above 25 GPa [116]. Similar discoveries have been made in LiMn_2O_4 [117] and in CuRh_2O_4 [118]. In the case of CaV_2O_4 it's the large eight-coordinated Ca^{2+} -ions that are responsible for the post spinel structure, since they cause chemical pressure which prevents the atoms from ordering in the spinel type fashion.

As part of this thesis, the nuclear structure of CaV_2O_4 was revised using high resolution neutron as well as X-ray diffraction. Those two techniques complement one another, as their scattering cross sections have different sensitiveness to the various elements. In the particular case of CaV_2O_4 the high amount of incoherent neutron scattering and the negative scattering length of vanadium make it impossible to determine the vanadium positions with neutrons, and X-ray diffraction experiments are required. In return oxygen has a very small X-ray scattering cross section, which makes it necessary to determine its positions with neutron scattering. For the interpretation of the magnetic structure, which is crucially influenced by the particular arrangement of the d -orbitals (see Sec. 5.3), it is essential to know the inter-atomic distances and bond-angles with

¹Reported elements are A=Ba, Sr, Ca, Mg, Na, La, and Eu and B=La, Pr, Nd, Sm, Eu, Gd, Tb, Dy, Ho, Yb, Lu, Y, Sc, In, Rh, Ti, Fe, V, Cr, Al, Ru, Mn, Ga and Tl (see references in [115])

very high accuracy, thus making a combined refinement indispensable.

DC-susceptibility as well as specific heat measurements revealed that CaV_2O_4 undergoes a structural phase transition upon cooling ($T_S \approx 141$ K) [119]. In order to find the origin of this phase transition and to solve the low temperature nuclear structure, detailed powder and single crystal diffraction measurements were performed over a broad temperature range from $T = 6 - 300$ K. The low temperature structure was found to be monoclinic, with the monoclinic distortion in the b - c -plane.

5.1.2. Experimental details

The powder diffraction measurements were performed on the Swiss-Norwegian beamline BM01B at ESRF, the neutron time-of-flight powder diffractometer SEPD at IPNS Argonne and on a Rigaku TTRAX rotating anode X-ray powder diffractometer at Ames Laboratory. The synchrotron and the neutron measurements were performed on powders from ground single crystals grown either by the image floating zone technique (synchrotron case) or in the triarc furnace (neutron case), while the lab measurement was performed on a powder made by solid state synthesis [119].

For the synchrotron measurements the ground powder was placed in a quartz capillary with a diameter of 0.5 mm (thickness of the wall: 0.01 mm) and mounted onto a rotating sample stick. Continuous rotation of the sample during the measurement is normally used to minimize ‘preferred orientation effects’, however, due to technical problems most of the measurements were done in static mode. In the rotating mode, the slit size defining the beam width was 1.6118 mm, while for the case of a static measurement it could be reduced to 1.04704 mm. The X-ray wavelength chosen for the experiment was $\lambda = 0.520114$ Å and scans were performed in the range $0.5^\circ \leq 2\theta \leq 46.0^\circ$, with the step-size being $\Delta\theta = 1.5625 \cdot 10^{-3}$ degrees. The diffracted X-rays were detected with an array of six scintillation counters, mounted behind six Si(111) analyser crystals, thus providing a simultaneous measurement of six powder patterns. With this set-up an intrinsic resolution (FWHM) of $\approx 0.015^\circ$ could be achieved. The sample was mounted inside a cryostat under Helium atmosphere and data were collected at $T=10$ K, 160 K and 300 K.

The lab X-ray powder diffraction measurements were carried out by Yan *et al.* on a rotating anode powder diffractometer employing Mo $K\alpha$ radiation [120]. The scattered intensity of the powder was recorded as a function of Bragg angle (2Θ) using a scintillation detector with a step-size of 0.01 degrees and the range of measured Bragg angles was 7° - 51° . The maximum Bragg peak intensity to lowest background intensity ratio was close to 200 with the strongest Bragg peaks registering nearly 5500 counts at their peak

values. The diffractometer was equipped with a continuous flow ^4He cryostat, allowing the temperature of a sample to be controlled between $T = 5 - 300$ K [121].

The neutron time-of-flight powder diffraction measurements were performed by Yan *et al.* [120] at the Special Environment Powder Diffractometer (SEPD). For the nuclear structure refinement, only the data from the high resolution 145° backscattering detector banks ($\Delta d/d=0.0034$) were used (see also Sec. 3.1.2).

Detailed structural information about the high temperature orthorhombic as well as the low temperature monoclinic structure were obtained by refining data with high counting rates from all three sources measured at $T = 300$ K and $T = 10$ K. All powder patterns were refined by the Rietveld method [69] using the program FULLPROF [122]. The neutron atomic scattering lengths and X-ray atomic scattering coefficients provided by the program were used. In order to obtain the structural parameters with the highest possible accuracy, the following strategy was employed: At first, refinements of each individual pattern were performed, where for each pattern the particular instrument dependent resolution function was used. As a starting point for the structural refinement of the room temperature data the orthorhombic space group $Pnam$ was assumed, with the lattice parameters and atomic positions reported in the literature [113]. For each refinement only those atomic parameters, which were found to be sensitive enough to the particular method (neutrons or photons) were allowed to vary. By comparing the results from different methods and transferring particular parameters, the refinement could be optimized. In the final step, a simultaneous refinement of all three patterns was performed, allowing all structural parameters to vary at the same time and thus providing a high level of accuracy that could not be achieved with a single data set. All three patterns were given the same weight, since they all contain equally important information about the crystal structure.

For the refinement of the low temperature structure the same method was applied, where the final high temperature parameters were used as starting values. From symmetry analysis it was found that the highest symmetric subgroup which is in agreement with the obtained data is the monoclinic space group $P2_1/n11$, with the monoclinic angle in the b - c -plane. In this space group the z -coordinate of the atoms is no longer at a fixed position, so that the total number of refinable atomic positions increases from 14 to 21, compared with the high T structure. In addition the monoclinic angle was also refined. Different powder preparation methods potentially influence the powder quality in terms of impurity and micro structural effects (e.g., micro strain). However, it can be assumed that the crystal structure well below and well above the structural phase transition is unique, so that a combined refinement of all patterns will lead to the most accurate re-

sult. The validity of this assumption was confirmed by detailed structural investigations of different growth of CaV_2O_4 by Niazi and co-workers [119].

To complete the structural investigation, single crystal neutron diffraction measurements were performed on the four-circle diffractometer E5 at HZB, Berlin. The investigated single crystal of CaV_2O_4 originated from the same image furnace growth as the one used in the synchrotron experiment. It had a cylindrical shape with dimensions $d = 4$ mm and $h = 6$ mm. For the experiment it was glued on a sample stick and mounted on an Eulian cradle sample holder. A Cu-monochromator in transmission geometry (220 planes) selected neutrons of wave length $\lambda = 0.887$ Å and an Erbium resonance filter was used in order to suppress contribution from $\lambda/2$. Bragg reflections were measured with a two-dimensional position sensitive ^3He detector, being 90×90 mm² in area (32×32 pixel). For the low temperature investigations, the sample was mounted inside a closed cycle Helium refrigerator allowing to access temperatures between 300 K and 6 K.

5.1.3. Experimental results and analysis

The overall refinement of the entire set of three powder patterns included ~ 20000 data points, which were fitted with a total number of 73 parameters in the high T case (300 K) and 80 in the low T case (10 K). 30 (37 for low T) of those parameters were used to describe the crystal structure of CaV_2O_4 , including atomic positions, lattice parameters and isotropic displacement factors. The rest were needed to characterize the details of the powder pattern and included parameters for peak shape, micro strain, preferred orientation, zero offset as well as 4 overall scale factors. In addition, in the neutron case the background was fitted to a polynomial function of seventh order, whereas for the photon pattern the background points were selected manually and interpolated linearly. For the single crystal refinement of the room temperature structure, a large data set with a total of 3128 (988 unique) reflections was collected. The integrated intensity of each reflection was obtained using the multi-detector data-integration program RACER. Further, the data were corrected for absorption and extinction with the program XTAL, and the same program was used for the refinement of the crystal structure. The overall refinement included 42 parameter, where 40 of them were attributed to the crystal structure (atomic positions, occupancies and displacement factors). The remaining two parameters were an overall scale factor and an extinction factor. Due to the high quality of the data, it was possible to refine the components of the tensor describing the elliptical anisotropic displacement parameters for all atoms, except the vanadium.

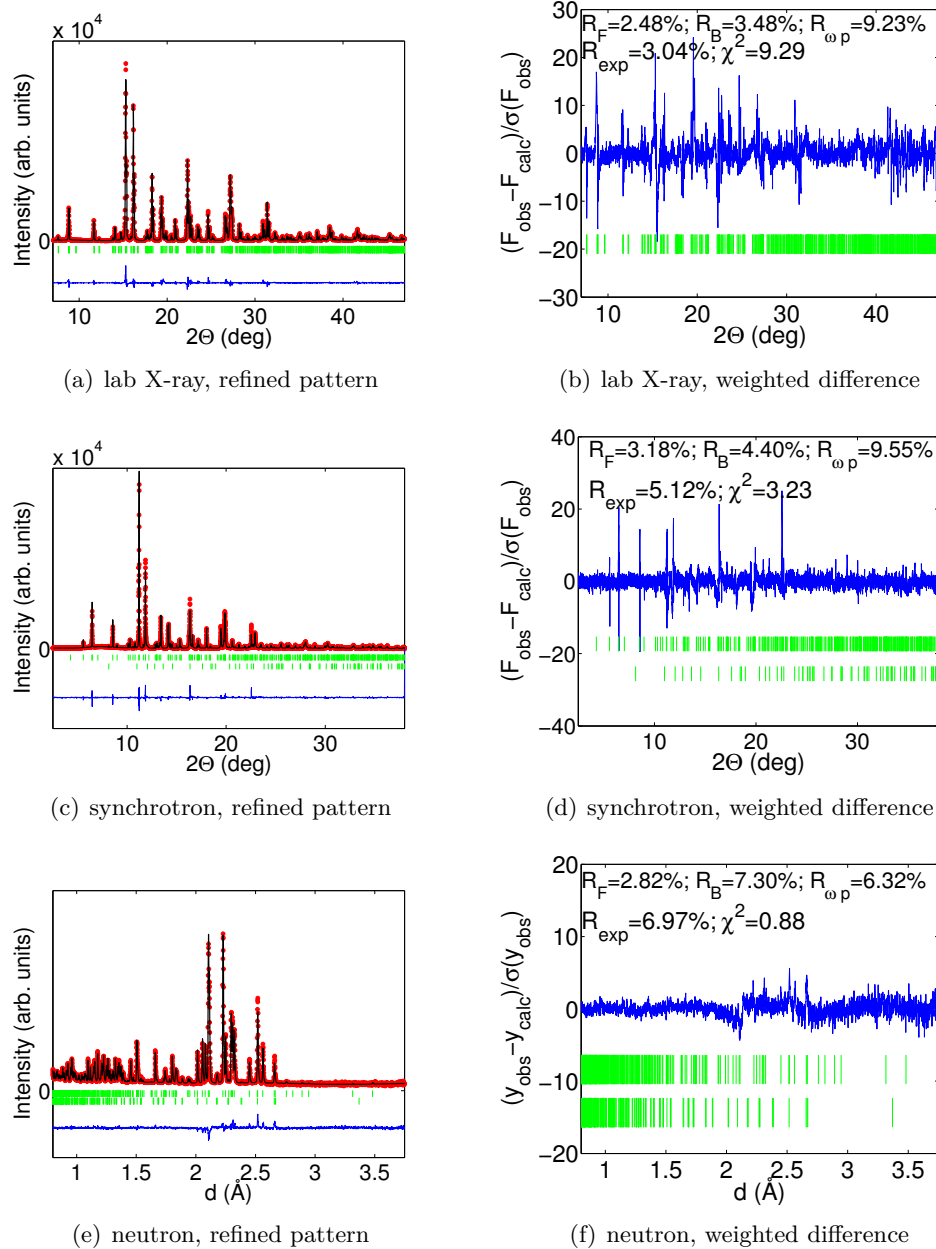


Figure 5.1.: (left) Powder diffraction pattern of CaV_2O_4 samples for different techniques taken at room temperature. The red dots indicate the measured data, the black line indicates the calculated data, the blue line represents the difference of both and the green bars indicate the (hkl) positions. For the synchrotron and neutron case additional impurity phases (V_2O_3 and CaVO_3) were refined. In this case the lower lying green bars stand for the (hkl) positions of the impurity. Note that in Figure (c) the lattice spacing d is displayed on the x -axis (conversion from time-of-flight to d via: $\text{tof} = 7543.71d - 3.41d^2 - 8.7669$). (right) Weighted difference plot for the fit of the corresponding figures on the left side. The inset contains the fit agreement factors.

High temperature phase

In Figs. 5.1(a), 5.1(c) and 5.1(e) the refined powder pattern measured at $T = 300$ K are displayed. By assuming orthorhombic crystal symmetry and space group $Pnam$, it was possible for all patterns to achieve very high agreement between the measured and the calculated data ($R_F \approx 3.0\%$)². For the samples made from crushed pieces of single crystals, additionally trace amounts of an impurity phase were identified. In the case of the synchrotron measurement, where the investigated powder was made from annealed single crystals grown with the optical floating zone technique, we clearly identified the impurity to be V_2O_3 (~ 0.6 mol %). Using the structural parameters of V_2O_3 reported by Rozier *et al.* [123] all additional peaks, not corresponding to the CaV_2O_4 main phase could be indexed. As an example, a selected part of the powder pattern is shown in Figure 5.2(a), where the black arrows indicate the impurity reflections.

On the other hand, the origin of additional peaks apparent in the neutron diffraction pattern, which was obtained from crushed crystals of an annealed triarc growth, could not be attributed to V_2O_3 , but to $CaVO_3$ (~ 1.5 mol %). With the structural data of Fálcon *et al.* [124] it was possible to index all additional reflections, which did not belong to the CaV_2O_4 main phase. A selected part of the refined pattern including characteristic peaks of the $CaVO_3$ impurity phase is displayed in Fig. 5.2(b).

A very helpful graphical tool to identify impurity phases as well as other irregularities between the observed and calculated data is the weighted difference plot ($(y_i - y_{ci})/\sigma_i$ vs. 2Θ or d , respectively) shown for all three pattern in the left side of Fig. 5.1. A closer look at Figs. 5.1(b) and 5.1(d) reveals that the lab X-ray and the synchrotron data show some discrepancies between the observed and calculated points. In the synchrotron case, those discrepancies can be attributed to preferred orientation effects resulting from the very thin and static capillary in which the powder was filled for the experiment. Preferred orientation leads to intensity mismatch of certain Bragg reflections, which either contribute too much or too less to the scattering, compared to the case of a completely randomly distributed powder. The intensity mismatch of Bragg reflections in the low 2Θ region of the lab X-ray pattern is caused by strong asymmetric axial divergence, which could not entirely modelled by the profile function that was used. In the higher 2Θ region again preferred orientation effects might be the reason for the strong deviation from zero of the weighted differences. However, apart from those minor irregularities, all data could be very accurately fitted by the model, as can be also seen by the low agreement factors, displayed in Fig. 5.1.

²For a definition of R_F and further agreement factors see Sec. 3.1.2.

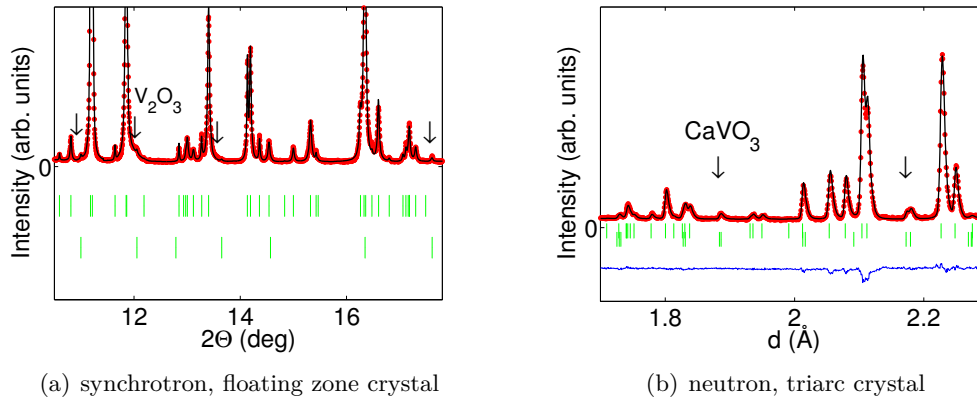


Figure 5.2.: Section of powder diffraction pattern of CaV_2O_4 from (a) synchrotron data and (b) neutron TOF data taken at $T = 300$ K. In (a) the V_2O_3 impurity peaks are indicated by arrows, while in (b) the arrows indicate reflections arising from a CaVO_3 impurity.

To account for the particular peak shape of Bragg reflections in the powder pattern, they were fitted with instrument specific profile functions. In the case of lab X-rays this function is a conventional pseudo-Voigt, while for the synchrotron case a pseudo-Voigt function convoluted with an axial divergence asymmetry function was used. The resolution function of the neutron TOF instrument is a pseudo-Voigt convoluted with a back-to-back exponential function. A remarkable effect was found for the samples made from crushed single crystals. These showed a systematic anisotropic peak broadening, which could not be modelled with the normal resolution function of the spectrometer. The reason for the broadening was found to be microscopic strain within the small grains of the powder. Using a model based on the multidimensional distribution of lattice metrics proposed by Stephens [72], we were able to refine six additional anisotropic strain parameters, in agreement with the orthorhombic lattice (see Figure 5.3). It was found that the strain is especially pronounced along the crystallographic c -direction (chain direction), indicating that the bonds along the chains are stronger than perpendicular to them. In Figure 5.3 this issue is clarified by comparing two sections of the high T synchrotron pattern, where one was refined using the resolution function of the diffractometer, while for the other one a micro-strain model was applied. The improvement of the refinement using the latter model is obvious.

Even though the measured powder pattern are of very high quality and for all of them an excellent fit between the observed and calculated profiles was obtained, the most accurate determination of the atomic positions was reached with the single crystal neutron diffraction experiment. The refinement of the single crystal data was performed in two

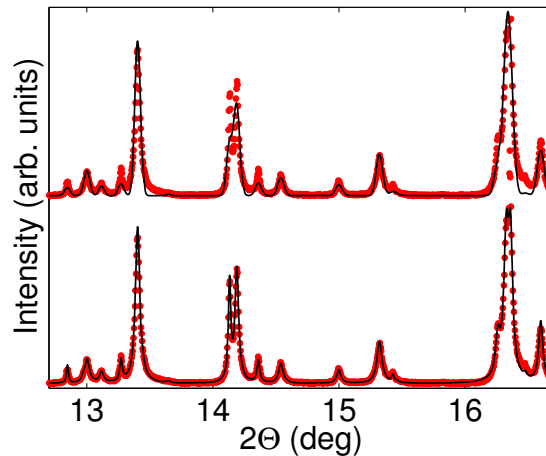


Figure 5.3.: Part of the synchrotron diffraction pattern of the high temperature phase of CaV_2O_4 . (top) Comparison of the observed pattern with the calculated pattern using the resolution function of the diffractometer. (bottom) Observed and calculated pattern using an anisotropic strain model. The following anisotropic strain parameters according to equation (3.38) have been used: $S_{400} = 0.0307(6)$; $S_{040} = 0.0177(3)$; $S_{004} = 5.2(1)$; $S_{220} = 0.009(2)$; $S_{202} = 1.23(4)$; $S_{022} = 2.09(4)$.

steps. At first the atomic positions as well as the anisotropic displacement parameters and a scale factor were refined simultaneously, assuming a totally stoichiometric sample. Secondly, those parameters were all fixed and only the occupancies were allowed to vary. The lattice parameters and the thermal displacement parameters of vanadium were not refined at all, but taken from the Synchrotron powder data. With this procedure an excellent refinement result was obtained with a residual factor $R_F = 0.032$ ($R_w = 0.032$). In Fig. 5.4 the high agreement between observed and calculated structures is visualized in a $F_{obs} - F_{calc}$ -plot.

The final structural and (isotropic) thermal parameters from the powder and single crystal refinement of the high temperature nuclear phase of CaV_2O_4 are summarized in Tables 5.1 and 5.2, while the corresponding unit-cell parameters are given in Tab. 5.3. Additional information about the anisotropic thermal parameters extracted from single crystal diffraction can be found in Appendix B.2. It is noticeable, that there is no appreciable difference between the structural parameters obtained with different methods on different samples, underlining that the powder preparation has very little influence on the crystal structure at this temperature. The most accurate atomic positions could be extracted from the single crystal refinement, with the error bar being almost an order of magnitude smaller than for the powder data. On the other hand, the determination of the unit cell parameters is less precise with the single crystal data. To account for this, it

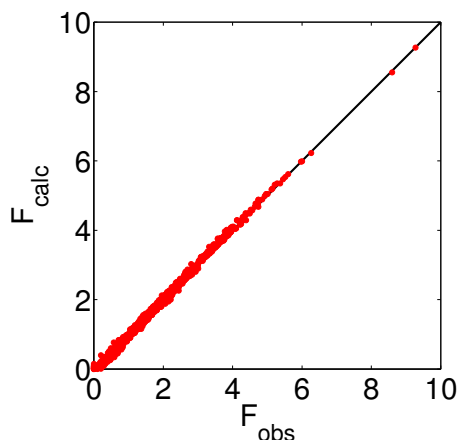


Figure 5.4.: Observed vs. calculated integrated Bragg intensity of CaV_2O_4 nuclear reflections measured on E5 at $T = 300$ K.

was decided to use the parameter obtained with synchrotron powder diffraction as fixed parameter in the single crystal refinement, since the high resolution of the synchrotron powder diffractometer allowed a very accurate determination of Bragg peak positions and thus of the unit cell dimensions as well. It is important to mention that the combination of the neutron single crystal and the synchrotron powder data also provides the most complementary results, since both were performed on pieces of the same floating zone grown crystal.

Low temperature phase

Upon cooling CaV_2O_4 undergoes a structural phase transition from orthorhombic to monoclinic, where the transition temperature T_c varies for different samples between $T_c \approx 110 - 145$ K [119]. This transition is accompanied by a systematic split of Bragg reflections (hkl) with $l \neq 0$. To clarify this behaviour, some selected Bragg peaks from the synchrotron data at high and low T are shown in Fig. 5.5. The reason for the splitting is a monoclinic distortion of the b - c -plane, with an angle $\alpha > 90^\circ$. The distortion leads to a loss of the two screw axes along b and c and therefore reflections with (hkl) and $(h-kl)$ no longer appear at the same 2Θ angle. The highest space group consistent with this reduction of symmetry is space group $P2_1/n11$. In this space group, the atomic z -coordinate is no longer a special position and appears as an additional parameter in the refinement.

Since there is no indication of a further symmetry reduction, space group $P2_1/n11$ was used for the refinement of the low temperature powder pattern. The refined neutron,

Table 5.1.: Atomic coordinates of CaV_2O_4 in orthorhombic space group $Pnam$ as obtained from the nuclear structure refinement. The z coordinate is at fix position $z = 1/4$. The abbreviation (p) and (sc) stand for (powder) and (single crystal), respectively.

x(Pnam)	neutron (p)	lab X-ray	synchrotron	multi	neutron (sc)	ref. [113]
Ca	0.7547(3)	0.7547(2)	0.7543(2)	0.7548(3)	0.75498(7)	0.759
V1	0.4331	0.4334(1)	0.4335(1)	0.4331(2)	0.4315(7)	0.428
V2	0.4194	0.4199(1)	0.4197(1)	0.4194(2)	0.4200(7)	0.428
O1	0.2082(2)	0.2111(4)	0.2114(4)	0.2095(5)	0.20997(5)	0.209
O2	0.1196(2)	0.1157(4)	0.1168(3)	0.1169(5)	0.11715(5)	0.117
O3	0.5225(2)	0.5195(5)	0.5192(4)	0.5202(6)	0.52147(6)	0.530
O4	0.4196(3)	0.4186(4)	0.4200(4)	0.4190(5)	0.41862(5)	0.437
y(Pnam)	neutron (p)	lab X-ray	synchrotron	multi	neutron (sc)	ref. [113]
Ca	0.6541(3)	0.6544(1)	0.6537(1)	0.6544(2)	0.65472(6)	0.654
V1	0.6117	0.6114(1)	0.61177(9)	0.6117(1)	0.6121(7)	0.605
V2	0.1046	0.1046(1)	0.10441(9)	0.1046(1)	0.1037(7)	0.105
O1	0.1616(2)	0.1617(4)	0.1583(3)	0.1608(5)	0.16232(5)	0.145
O2	0.4748(2)	0.4757(4)	0.4757(3)	0.4759(5)	0.47564(5)	0.500
O3	0.7815(2)	0.7815(4)	0.7796(3)	0.7811(5)	0.78144(5)	0.775
O4	0.4278(2)	0.4262(4)	0.4277(3)	0.4269(4)	0.42752(5)	0.413

Table 5.2.: Isotropic displacement parameter for CaV_2O_4 obtained by Rietveld refinement of powder data. (p) stands for powder data.

Pnam B(\AA^2)	neutron (p)	lab X-ray	synchrotron	multi
Ca	0.76(5)	0.77(3)	0.89(3)	0.70(4)
V1	0.48	0.62(2)	0.444(9)	0.48(2)
V2	0.48	0.62(2)	0.444(9)	0.48(2)
O1	0.31(2)	0.75(4)	0.62(4)	0.55(5)
O2	0.31(2)	0.75(4)	0.62(4)	0.55(5)
O3	0.31(2)	0.75(4)	0.62(4)	0.55(5)
O4	0.31(2)	0.75(4)	0.62(4)	0.55(5)

Table 5.3.: Lattice vectors of CaV_2O_4 in orthorhombic space group $Pnam$ as obtained from the nuclear structure refinement. The abbreviation (p) and (sc) stand for (powder) and (single crystal), respectively.

Pnam	a(\AA)	b(\AA)	c(\AA)	$\alpha=\beta=\gamma$	V(\AA^3)
Neutron (p)	9.2081(1)	10.6772(2)	3.00761(4)	90.0	296.567(7)
Lab X-ray	9.2153(2)	10.6841(2)	3.01107(5)	90.0	296.459(8)
Synchrotron	9.20800(5)	10.67866(5)	3.00596(2)	90.0	295.573(3)
Multi	9.2078(1)	10.6772(1)	3.00798(5)	90.0	295.724(7)
Neutron (sc)	9.2015(9)	10.6756(2)	3.0057(1)	90.0	295.254(3)
Ref. [113]	9.20	10.66	3.01	90.0	295.197

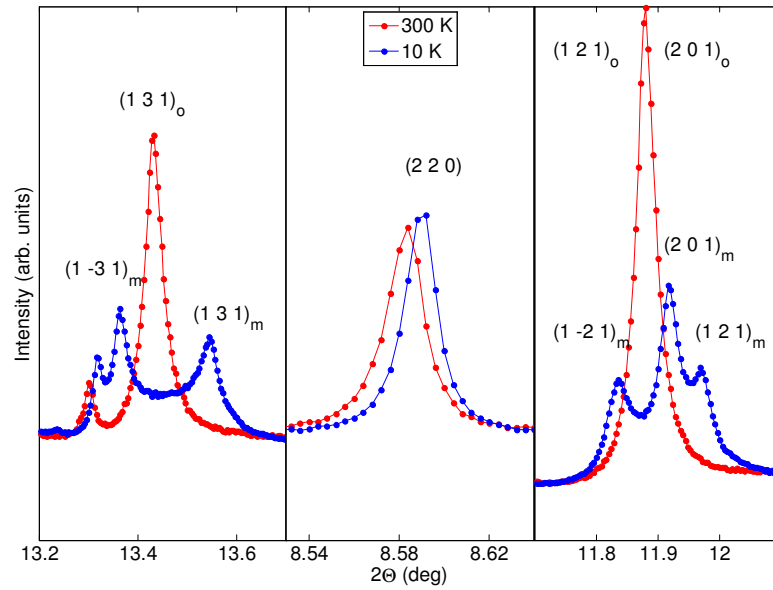


Figure 5.5.: Selected peaks of the high T and low T structure of CaV_2O_4 , obtained with synchrotron powder diffraction.

synchrotron and lab X-ray powder pattern of the $T = 10$ K data are shown at the left side of Fig. 5.6, while the weighted difference plot of these data is displayed at the right side of the same figure. For all pattern a very good agreement between the observed and calculated Bragg intensities was obtained ($2.82 \leq R_F \leq 6.90$). The impurities detected in the high temperature case are of course also apparent in the low temperature data, however, the reduction of symmetry of the main phase causes an increase of total Bragg reflections, which leads to shadowing of peaks coming from the impurity. For this reason it was not possible anymore to refine a scale factor for the V_2O_3 impurity in the synchrotron pattern and therefore the fraction of impurity was fixed to the high T value. Here, one additionally had to take into account that V_2O_3 also undergoes a structural phase transition upon cooling from trigonal to monoclinic, and for this reason the low T structure was used for the refinement [123, 119]. On the other hand, some of the reflections from the CaVO_3 impurity phase apparent in the neutron powder data could be unambiguously identified, such that a two phase refinement was possible in this case. The weighted difference plot in Fig. 5.6(f) underlines the high fit quality of the neutron powder data. The only appreciable irregularity is the one at $d \approx 3.6$ Å. At this position a magnetic Bragg reflection occurs, resulting from the antiferromagnetic ordering at low T . For the final refinement this magnetic peak was removed from the pattern, however, this topic will be picked up again in the next chapter, when the refinement of the mag-

netic structure will be discussed.

A closer look at the weighted difference plots for the synchrotron and lab X-ray data reveals, that the fitting of the observed pattern is slightly worse, than for the high T data. Similar to the high T case, preferred orientation effects lead to an intensity mismatch of some particular reflections and in addition, a small amount of underlying impurity reflections gives rise to some minor deviations between the observed and calculated Bragg intensities, at least in the synchrotron case. However, the main reason for the degradation of the fit quality is the characteristic way in which the monoclinic splitting occurs. As can be for example seen in the left picture of Fig. 5.5, the two split peaks $(1, -3, 1)$ and $(1, 3, 1)$ have a strong asymmetric shape with a long tail in the direction of the neighbouring twin. The overlap of both tails leads to a hyperbolic cosine-like shape, which is very difficult to model and therefore lead to a noisier $((y_{obs}-y_{calc})/\sigma_{obs})$ -plot.

The monoclinic twinning was also the reason that prevented an accurate structure determination of the low temperature phase from single crystal neutron diffraction data. Conventional integration routines for multi-detector single crystal data (such as **RACER**) fail to separate the split peaks, since most of them strongly overlap.

In Tables 5.4, 5.5 and 5.6 the final structural parameter from the powder refinement of the $T = 10$ K data are summarized. As for the high temperature refinement no significant difference between the particular solutions can be noticed, verifying that the low temperature crystal structure is not (or only marginally) sample dependent. In contrast to the orthorhombic phase, the particular atoms in the monoclinic phase are no longer located at special Wyckoff position 4c $(x,y,1/4)$ and therefore the z -components of the atomic positions were also allowed to vary.

A main characteristic of the monoclinic phase is the angle between the b - and c -directions of the unit cell, which deviates from the right-angled orthorhombic one. This difference is $\Delta\alpha = \alpha_m - \alpha_o \approx 0.8^\circ$, which indicates that the monoclinic distortion is strong in CaV_2O_4 . In comparison, e.g. in the vanadium(III) based perovskite materials (RVO_3 , with R=lanthanide atom) which undergo a similar structural phase transition, the variation of the monoclinic angle is only $\Delta\alpha \approx 0.08^\circ$ [125], being one order of magnitude smaller than in the present case.

In addition, the refinement of the low temperature data reveals a slight reduction of the a - and c - lattice constants, leading to an $\approx 5\%$ -volume reduction compared to the structure at room temperature (see tables 5.3 and 5.6). An additional refinement of a synchrotron powder pattern taken at $T = 160$ K allowed some further information about the temperature dependence of the lattice constants to be deduced and will be discussed in the next subsection.

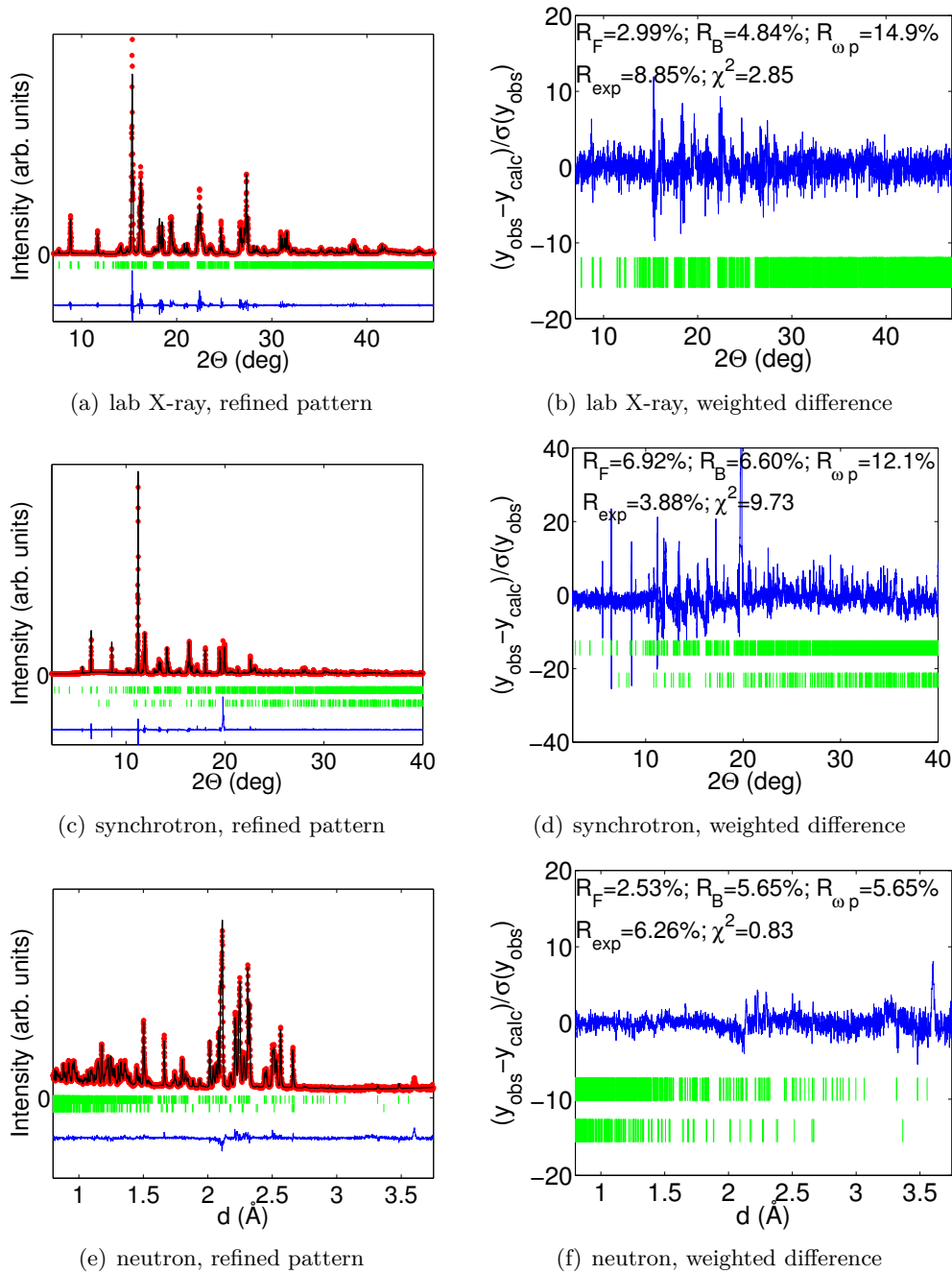


Figure 5.6.: (left) Powder diffraction pattern of CaV_2O_4 samples for different techniques taken at $T = 10$ K. The red dots indicate the measured data, the black line indicates the calculated data, the blue line represents the difference of both and the green bar indicate the (hkl) positions. For the neutron case an additional impurity phase was refined (CaVO_3). In this case the lower lying green bars stand for the (hkl) positions of the impurity. Note that in Figure (c) the lattice spacing d is displayed on the x -axis (conversion from time-of-flight to d via: $\text{tof} = 7535.57d - 3.74d^2 - 9.7366$). (right) Weighted difference plot for the fit of the corresponding figures on the left side. The inset contains the fit agreement factors.

Region of phase transition

For a better understanding of the nuclear phase transition, studies of selected Bragg reflections as a function of temperature were performed using single crystal neutron diffraction. In particular the measurements focused on two issues. Firstly, a temperature dependent investigation of strong Bragg peaks, which are known to split in the monoclinic phase, provided information about the character of the phase transition. On the other hand various forbidden Bragg reflections were investigated in order to confirm the assumed low temperature space group symmetry.

Depending on the crystal symmetry, interference effects can lead to a systematic cancellation of particular Bragg reflections. For the space groups of the high and low T structure of CaV_2O_4 ($Pnam$ and $P2_1/n11$), the following reflection conditions are valid:

$$Pnam : \quad h0l : \quad h = 2n; \quad 0kl : \quad k + l = 2n \quad (5.1)$$

$$P2_1/n11 : \quad h00 : \quad h = 2n; \quad 0kl : \quad k + l = 2n \quad (5.2)$$

where n is an integer. A list of Bragg reflections forbidden by these conditions in both phases, were measured in the temperature range $6 \leq T \leq 180$ K, where the list contained the following reflections: ((100), (300), (500), (010), (001), (021), (041)). None of those reflections showed any intensity throughout the whole T scan. Intensity found for the (1 0 0) reflection in a first scan, could be later identified as multi scattering processes and a second scan for which the scattering plane was rotated by a certain angle ϕ , resulted in zero Bragg intensity.

It should also be mentioned that no additional Bragg reflections appeared below the structural phase transition. For example, the reflection (101), which is not allowed in $Pnam$, but is allowed in $P2_1/n11$, did not have any intensity. Since the investigations brought no evidence for a further reduction of symmetry, the highest space group consistent with crystal symmetry was assumed for the low temperature phase. This space group is monoclinic $P2_1/n11$ ³.

Apart from the forbidden reflections, the intensity of several strong reflections has been measured as a function of temperature. Figure 5.7(a) displays the integrated intensity of the (031) Bragg position (orthorhombic notation). Below $T_S \approx 147$ K, the Bragg peak

³If for example the (100) Bragg reflection would have gotten some intensity in the low temperature phase, than the highest allowed space group would have been $Pn11$ (no. 7) instead of $P2_1/n11$ (no. 14).

Table 5.4.: Atomic coordinates of CaV_2O_4 in monoclinic space group $P2_1/n11$ as obtained from the nuclear structure refinement. The abbreviation (p) stands for powder.

$x(P2_1/n11)$	neutron (p)	lab X-ray	synchrotron	multi
Ca	0.7557(3)	0.7558(3)	0.7561(3)	0.7557(3)
V1	0.4324	0.4330(2)	0.4326(2)	0.4324(2)
V2	0.4198	0.4194(2)	0.4194(2)	0.4198(2)
O1	0.2087(2)	0.2105(8)	0.2115(5)	0.2093(5)
O2	0.1197(2)	0.1151(6)	0.1191(5)	0.1197(5)
O3	0.5217(2)	0.5180(9)	0.5193(7)	0.5206(6)
O4	0.4191(2)	0.4185(7)	0.4168(5)	0.4183(5)
$y(P2_1/n11)$	neutron (p)	lab X-ray	synchrotron	multi
Ca	0.6542(2)	0.6546(2)	0.6549(2)	0.6548(2)
V1	0.6116	0.6115(2)	0.6114(2)	0.6116(2)
V2	0.1047	0.1050(2)	0.1054(1)	0.1047(2)
O1	0.1611(2)	0.1625(7)	0.1625(5)	0.1642(5)
O2	0.4746(2)	0.4749(7)	0.4763(5)	0.4757(5)
O3	0.7802(2)	0.7811(7)	0.7804(5)	0.7813(5)
O4	0.4277(2)	0.4253(7)	0.4286(5)	0.4275(5)
$z(P2_1/n11)$	neutron (p)	lab X-ray	synchrotron	multi
Ca	0.250(1)	0.252(1)	0.250(1)	0.250(1)
V1	0.2557	0.2547(9)	0.2561(8)	0.2557(9)
V2	0.2532	0.2516(9)	0.2515(8)	0.2532(9)
O1	0.251(1)	0.240(3)	0.250(2)	0.250(2)
O2	0.260(1)	0.254(3)	0.252(2)	0.254(2)
O3	0.258(1)	0.262(3)	0.245(3)	0.252(3)
O4	0.246(1)	0.246(3)	0.240(3)	0.243(2)

Table 5.5.: Isotropic displacement factors, obtained from nuclear structure refinement at $T = 10$ K.

Pnam B(\AA^2)	neutron (p)	lab X-ray	synchrotron	multi
Ca	0.71(5)	0.67(6)	1.37(5)	0.83(4)
V1	0.59	0.35(3)	0.51(2)	0.59(2)
V2	0.59	0.35(3)	0.51(2)	0.59(2)
O1	0.62(2)	0.68(8)	1.05(6)	0.43(5)
O2	0.62(2)	0.68(8)	1.05(6)	0.43(5)
O3	0.62(2)	0.68(8)	1.05(6)	0.43(5)
O4	0.62(2)	0.68(8)	1.05(6)	0.43(5)

Table 5.6.: Lattice parameters of CaV_2O_4 in monoclinic space group $P2_1/n11$ as obtained from the nuclear structure refinement. The abbreviation (p) stands for powder. $\beta = \gamma = 90^\circ$

$P2_1/n11$	a(Å)	b(Å)	c(Å)	α	V(Å ³)
Neutron (p)	9.2035(1)	10.6873(1)	3.00246(4)	90.802(1)	295.294(7)
Lab X-ray	9.2018(3)	10.6849(3)	3.00216(8)	90.850(1)	295.14(1)
Synchrotron	9.19568(6)	10.68070(6)	2.99748(3)	90.755(1)	294.376(4)
Multi	9.19524(8)	10.68025(8)	2.99780(4)	90.767(1)	294.380(5)

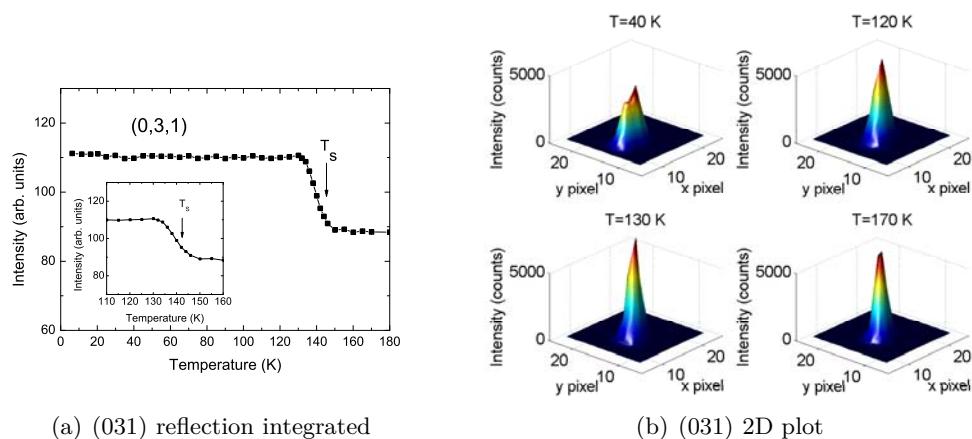


Figure 5.7.: (a) Integrated intensity of (031) Bragg reflection as a function of temperature. (b) Bragg intensity measured around the 2Θ position of the (031) reflection for different temperatures. Data were collected with the E5 2D multi detector.

intensity starts to increase, indicating the orthorhombic to monoclinic phase transition. Due to twinning the orthorhombic (031) reflection splits below the phase transition into the monoclinic (031) and $(0\bar{3}1)$ reflections. The total integrated intensity at this position increases at T_S , because of the increased mosaic spread, which results in a reduction of the extinction effect. This effect is illustrated in Figure 5.7(b), where the intensity distribution at the (031) position observed with the 2D detector for different temperatures is shown.

A closer look to the region of the phase transition reveals (see inset of Figure 5.7(a)), that the transition occurs smoothly within a $\Delta T \approx 10$ K interval. This in turn implies, that the structural transition in CaV_2O_4 is second-order.

An additional synchrotron powder pattern was collected at $T = 160$ K, slightly above the structural phase transition. The results from this refinement together with the ones from the data taken at $T = 300$ K and $T = 10$ K, allow some statements on the temperature dependence of the CaV_2O_4 lattice constants to be made. In Fig. 5.8 the three

lattice constants and the total unit cell volume for all three investigated temperatures are displayed, while a detailed list of the refined structural parameter at $T = 160$ K can be found Appendix B. Both the a - and c -lattice parameter decrease upon cooling, and the strength of the decrease becomes less below the transition temperature T_S . On the other hand, the b lattice parameter has a minimum around the structural phase transition and starts to increase again upon further cooling. Due to the small number of data sets, it is difficult to state, whether or not the lattice parameters change suddenly at the phase transition; however, detailed temperature dependent investigations by Yan *et al.* confirmed the continuous character of the phase transition, which was observed by single crystal neutron diffraction [120]. Finally, also the unit cell volume reduces upon cooling.

Beside the investigation of the lattice parameters, the powder pattern at $T = 160$ K was also checked for an appearance of phase coexistence. For this reason, a two phase refinement was performed including the orthorhombic and the monoclinic phase. This refinement, however, resulted in a vanishing scale factor for the monoclinic phase, indicating that only the orthorhombic lattice is formed by the crystal at $T = 160$ K and no phase coexistence occurs.

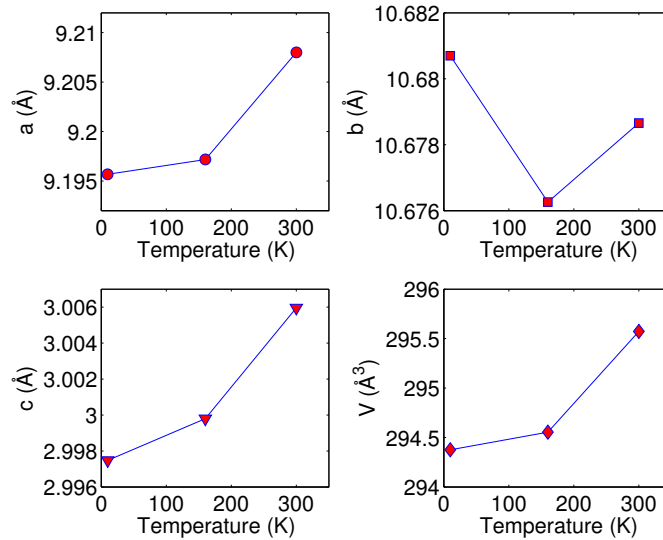


Figure 5.8.: Temperature dependence of lattice parameters of CaV_2O_4 , obtained from synchrotron powder refinement.

5.1.4. Discussion

By means of neutron and X-ray powder diffraction as well as single crystal neutron diffraction, detailed information about the nuclear structure of CaV_2O_4 could be obtained. It was found that the system undergoes a structural phase-transition at $T_S \approx 141$ K from the orthorhombic to the lower symmetry monoclinic phase. In this section the information obtained about the atomic configuration will be used to draw conclusions on the particular electronic and magnetic properties of the system. Therefore a closer look will be taken at the particular arrangement of the ions within the crystal lattice, and the specific inter-atomic distances, bond angles and bond valences will be investigated. Since the most accurate determination of the structural parameter in the high T orthorhombic phase were made from single crystal neutron diffraction, all further discussion of this phase will be based on results from this method. For the low T monoclinic case the structural parameters obtained from the multi pattern refinement of X-ray and neutron powder data will be used.

Figure 5.9 shows a schematic drawing of the CaV_2O_4 crystal structure. The crystallographic unit cell consists of two different vanadium sites (green and orange), both having octahedral symmetry coordinated by six oxygen ions. Neighbouring VO_6 octahedra of the same site share common edges and form double chains, which run along the crystallographic c -direction. Chains of different vanadium sites are connected via the octahedra's

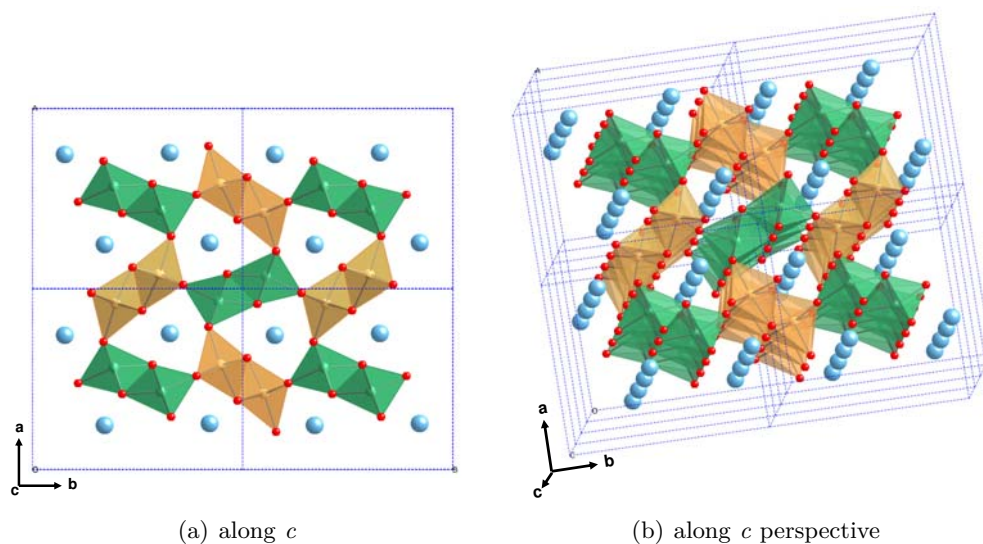


Figure 5.9.: The structure of CaV_2O_4 (a) projected on the a - b plane and (b) perspective view along the c direction. The two inequivalent VO_6 octahedra are highlighted in green (chain 1) and orange (chain 2), the oxygen atoms are red and the calcium atoms are blue.

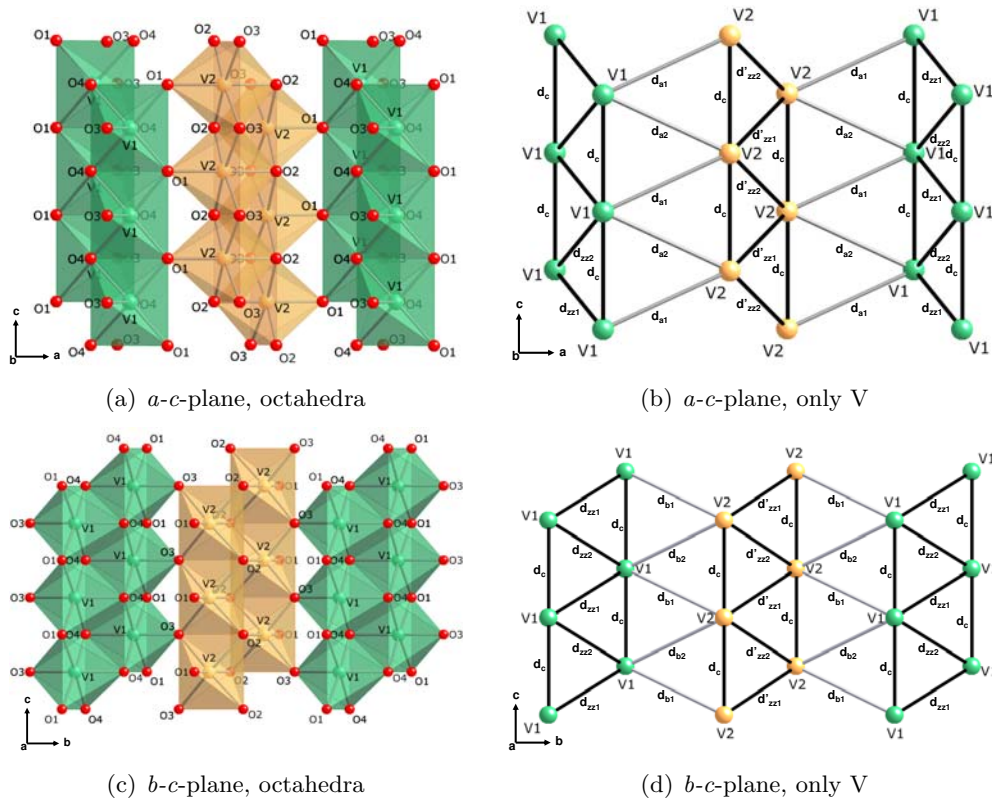


Figure 5.10.: The structure of CaV_2O_4 , focus on the zigzag structure. (a) and (c) display the two double chains of VO_6 -octahedra, while (b) and (d) only show the vanadium V geometry.

corners and four of such double chain units form closed tunnels which accommodate the large eight-coordinated Ca^{2+} -ions. The reason why CaV_2O_4 is an interesting sample to study quantum magnetism is that the magnetic V^{3+} -ions (spin $S = 1$) are arranged in a zigzag-like fashion with almost equal distances between nearest and next nearest neighbours. Since it is known that the leading exchange between the ions is antiferromagnetic in nature, such a structure potentially gives rise to geometrical frustration. Further, neighbouring chains are well separated by the non-magnetic Ca^{2+} -ions and the magnetic interactions are therefore quasi-one-dimensional.

The zigzag structure is visualized in Figs. 5.10(c) and 5.10(d) in which only the vanadium ions are shown for clarity. Apart from the frustrated arrangement within the chains, the interchain coupling paths also give rise to frustration due to the underlying triangular motif. The particular interatomic distances between neighbouring vanadium ions are summarized in Tab. 5.7. As a consequence of the two inequivalent vanadium sites (V1 and V2) the distances between neighbouring ions along the zigzags are different

Table 5.7.: Intra- and inter-ionic V-V distances in Å, zz stands for (along the) zigzags, c for (along the) chain and a and b for inter-ionic distances along a and b , respectively (see also Figure 5.10).

bond	$Pnam$	$P2_1/n11$
V1-V1(d_{zz1})	3.095(9)	3.079(3)
V1-V1(d_{zz2})	3.095(9)	3.076(3)
V1-V1(d_c)	3.005960(2)	2.998(4)
V2-V2(d_{zz1})	3.055(9)	3.064(3)
V2-V2(d_{zz2})	3.055(9)	3.075(3)
V2-V2(d_c)	3.005960(2)	2.998(4)
V1-V2(d_{a1})	3.570(8)	3.572(3)
V1-V2(d_{a2})	3.570(8)	3.566(3)
V1-V2(d_{b1})	3.652(9)	3.672(3)
V1-V2(d_{b2})	3.652(9)	3.617(3)

for chains of different sites. However, the distances between neighbouring ‘leg’-ions are equal for both chains due to translational symmetry. In the orthorhombic, as well as in the monoclinic phase, all intra-site vanadium distances are ≈ 3 Å, whereas the legs distances are slightly smaller for both chains than the zigzag distances ($\approx 3\%$ for chain(V1) and $\approx 1.5\%$ for chain(V2)). Rogers *et al.* [126] have reported that for systems with a V^{3+} - V^{3+} separation d that lies close to a critical cation-cation spacing $d_{\text{crit}} \approx 2.97$ Å, below which collective electron behavior sets in, strong antiferromagnetic direct cation-cation magnetic interactions occur. The structural results suggest that this is the case for CaV_2O_4 . Therefore, if interactions between the magnetic ions would only depend on inter-ionic distances, the antiferromagnetic coupling along the legs (d_c) would be slightly stronger than the one along the zigzags. In addition, in the room temperature phase the distances to the two nearest neighbours along the zigzags (d_{zz1} and d_{zz2}) are identical and the same is also true for nearest neighbours between different chains (d_{a1} , d_{a2} and d_{b1} , d_{b2}), underlining the frustrated character of the crystal lattice (see Fig. 5.10).

The situation changes completely with the onset of the monoclinic distortion. Due to a lowering of symmetry all ions are slightly shifted from their orthorhombic position. This in turn leads to a situation, where the separations of nearest neighbour ions on the zigzags are no longer equal ($d_{zz1} \neq d_{zz2}$, $d_{a1} \neq d_{a2}$, $d_{b1} \neq d_{b2}$). Even though the difference between the V-V distances is relatively small, it allows the development of preferred exchange pathways and thus the monoclinic distortion causes a lifting of the geometrical frustration. In addition the leg distances d_c become shorter, suggesting a further increase of interaction strengths along this direction.

Table 5.8.: Distances (in Å) and valences of the intra-octahedral V-O bond.

Bond	$Pnam$		$P2_1/n11$	
Bond	distance (Å)	bond valence	distance (Å)	bond valence
V1-O1	2.060(5)	0.425(5)	2.083(7)	0.399(7)
V1-O1	2.060(5)	0.425(5)	2.045(7)	0.442(8)
V1-O3	1.989(7)	0.51(1)	1.986(6)	0.519(8)
V1-O4	1.975(8)	0.53(1)	1.970(5)	0.542(8)
V1-O4	2.084(5)	0.397(5)	2.068(7)	0.416(7)
V1-O4	2.084(5)	0.397(5)	2.082(7)	0.400(7)
V2-O1	2.033(7)	0.457(8)	2.037(5)	0.451(6)
V2-O2	2.003(7)	0.494(9)	2.029(5)	0.462(6)
V2-O2	2.061(5)	0.423(6)	2.054(7)	0.432(8)
V2-O2	2.061(5)	0.423(6)	2.083(7)	0.399(7)
V2-O3	2.013(5)	0.481(6)	2.032(7)	0.458(9)
V2-O3	2.013(5)	0.481(6)	1.984(7)	0.522(10)

Up to now the magnetic interactions between vanadium ions were interpreted in terms of a simple picture based on interionic distances only. However, an important detail has been completely left out from the discussion so far, namely the O^{2-} -ions. For several reasons those play an important role for the electronic structure of the system. First of all, since the O^{2-} -ions are located at the corners of octahedra which enclose the V^{3+} -ions, they create a crystal field potential, that lifts the degeneracy of vanadium d -orbitals (see Sec. 2.1.1) and also leads to strong magnetic anisotropy. Moreover, they also provide a superexchange coupling path for magnetic interactions, especially also for those ions, where the large separation excludes direct exchange mechanisms. Each V^{3+} -ion carries two electrons in its d -shell. In a perfectly undistorted octahedral environment, the d -levels split into a lower lying triply-degenerate t_{2g} - and a higher energetic doubly-degenerate e_g -level. This would mean, that the two d -electrons of V^{3+} would randomly occupy the three t_{2g} -orbitals, with an average occupation of $\langle n_{xy} \rangle = \langle n_{xz} \rangle = \langle n_{yz} \rangle = 2/3$ electrons per orbital. The system therefore possesses an orbital degree of freedom.

However, in CaV_2O_4 the situation is much more complicated, since the VO_6 octahedra are highly distorted. The intra-octahedral V-O bond distances for both vanadium sites are summarized in Tab. 5.8 and visualized in Fig. 5.11. The data reveal, that the two different vanadium sites also differ strongly in their octahedral environments.

Already in the orthorhombic phase for both octahedra, four out of six V-O bonds have different lengths. The two equally distanced bond pairs build a trapezoidal equatorial plane, while the two remaining unequal bonds, are arranged perpendicular to this plane.

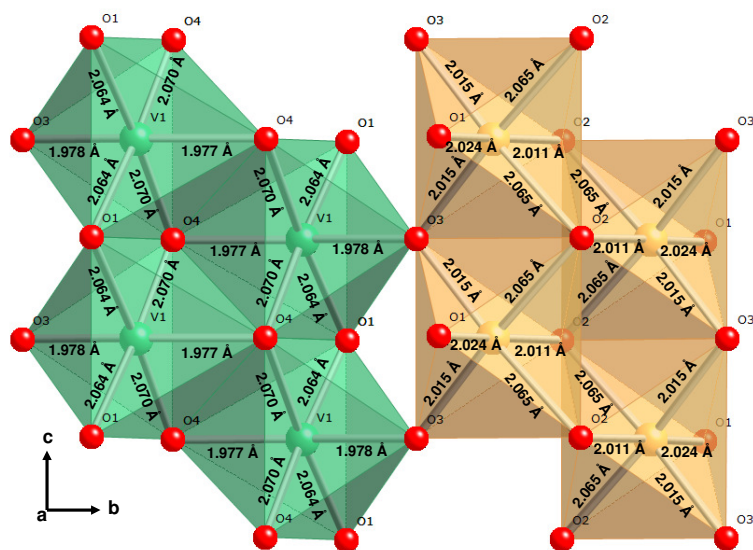
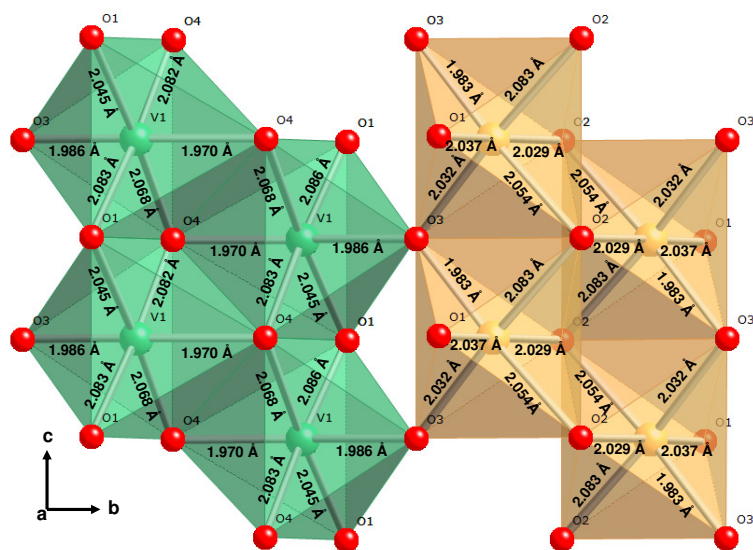
(a) $Pnam$ (b) $P2_1/n11$

Figure 5.11.: Distorted VO_6 -octahedra with V-O bond distances of CaV_2O_4 for the high- and low- T structure.

This arrangement not only shows that the octahedra are distorted, but also that the vanadium ions are shifted out of the center of the octahedra. If for the moment one neglects this last issue and only focuses on the average bond distances along each octahedra axis, the situation becomes clearest for the $V(1)O_6$ -octahedra. This octahedra contains two long bond pairs and one short one, resulting in a compression of the octahedra

along one of its main axis. The direction of this axis is $\approx 10^\circ$ away from the b -direction. A similar type of distortion can be found for the second octahedra ($\text{V}(2)\text{O}_6$), with a compression along the octahedra axis, which has an angle of $\approx 20^\circ$ to the a -axis and $\approx 70^\circ$ to the b -axis. However, this distortion is much less pronounced, with the difference between the long and short V-O axis being only $\approx 0.9\%$ (compared to $\approx 4.3\%$ for the $\text{V}(1)\text{O}_6$ -octahedra). A useful measure to express the degree of bond length distortion is Δ_d , which describes the mean square relative deviation from the average bond length:

$$\Delta_d = \sqrt{\frac{\sum_i [\langle V-O \rangle - (V-O)_i]^2}{\langle V-O \rangle^2}} \quad (5.3)$$

where $\langle V-O \rangle$ denotes the average bond length. The values Δ_{d1} and Δ_{d2} for both octahedra can be found in Tab. 5.9. The results underline the different degree of distortion between both octahedra. In comparison to other t_{2g} systems containing vanadium ions, the distortion for both V-sites is rather large. For instance, in the low temperature tetragonal phase of vanadium spinels, one finds distortion parameter of $\Delta \approx 0.015$ for CdV_2O_4 [127] and $\Delta \approx 0.011$ for ZnV_2O_4 [128]. Also, in NaV_2O_4 , a material which is isostructural to CaV_2O_4 the octahedral distortion is weaker, with $\Delta_1 \approx 0.015$ and $\Delta_2 \approx 0.021$ for the different sites, respectively [129].

In terms of orbitals, a compression of the octahedra along one of its main axis leads to a partial lifting of the t_{2g} -orbital degeneracy. Assuming that the compression takes place along the octahedral z -axis, the d_{xy} -orbital, lying perpendicular to this axis, becomes energetically favourable, while the d_{yz} - and d_{xz} -orbitals remain degenerate, but at a higher energy. Translated into the picture of CaV_2O_4 this means, that one of the two available V^{3+} d -electrons occupies the low lying d_{xy} -orbital, while the second electron occupies the remaining two t_{2g} -orbitals with equal probability ($\langle n_{xy} \rangle = 1; \langle n_{xz} \rangle = \langle n_{yz} \rangle = 1/2$). From Figure 5.11(a) one can conclude, that the compression for both VO_6 octahedra is such, that the orbital that has two of its lobes pointing along the chains legs is lowest in energy and therefore always occupied. Since neighbouring octahedra along the chains legs are edge-sharing, the neighbouring occupied orbitals point toward each other, giving rise to strong antiferromagnetic direct exchange interactions [9, 126]. The remaining doubly degenerated orbitals are located within the octahedra such, that their lobes point along the zigzags of the chains and again due to the edge-sharing arrangement neighbouring zigzag orbitals point toward each other, making direct exchange also favourable for this coupling path. However, since the two d -orbitals along the zigzags are only half occupied by one electron and since the distances between V^{3+} -ions along the zigzags

Table 5.9.: Distortion parameter, from single crystal- ($Pnam$) and multi pattern- ($P2_1/n11$) refinement. The first six rows show the average bond lengths along the three axis of the two VO_6 octahedra in Å. The next two rows show the total average V-O distance within the octahedra (also in Å). Δ_d is the octahedral distortion parameter and is defined in Eq. 5.3. In the last four rows the calculated Bond valence sum for each cation are given (with the theoretical value in brackets) and GII is the global instability index as defined in Eq. 5.5. GII gives the root mean of the valence deviations for the $j = 1 \dots N$ atoms in the asymmetric unit [130, 131].

	$Pnam$	$P2_1/n11$
$\langle V1 - O \rangle(1)$	1.982(8)	1.978(6)
$\langle V1 - O \rangle(2)$	2.072(5)	2.057(7)
$\langle V1 - O \rangle(3)$	2.072(5)	2.083(7)
$\langle V2 - O \rangle(1)$	2.018(5)	2.033(5)
$\langle V2 - O \rangle(2)$	2.037(4)	2.019(7)
$\langle V2 - O \rangle(3)$	2.037(4)	2.058(7)
$\langle V1 - O \rangle$	2.042(6)	2.039(7)
$\langle V2 - O \rangle$	2.031(6)	2.037(6)
Δ_d1	0.052	0.054
Δ_d2	0.028	0.036
V1 (BVS) [3.0]	2.69(2)	2.72(2)
V2 (BVS) [3.0]	2.76(2)	2.72(2)
Ca (BVS) [2.0]	2.280(1)	2.35(2)
GII	0.163	0.173

are slightly larger than along the leg direction, the nuclear structure suggests that the magnetic coupling strength is stronger along the legs than along the zigzags.

Up to this point, the discussion was focused on the high temperature structure only and the situation becomes more complicated when the system enters the low temperature monoclinic phase. The monoclinic distortion leads to a lowering of crystal symmetry, resulting in a further increase of VO_6 octahedral distortion, which is indicated by the increase of the Δ_d -parameter (Table 5.9). In the new phase, all six $\langle V-O \rangle$ bonds within the octahedra are different (Table 5.8), suggesting that the orbital degeneracy is completely lifted and that two of the three t_{2g} -orbitals are completely occupied by one d -electron, while the third orbital remains empty. However, due to the strong distortion and the off-centring of the V^{3+} -ions it is difficult to tell which are the occupied orbitals. Returning back to a simplified picture and averaging the bonds along the octahedral axes, one finds for both octahedral sites one (l)ong, one (s)hort and one (m)edium bond. The differences between the average bond-lengths $\langle V-O \rangle$ of $V1O_6$ are $\delta_m - \delta_s = 0.079\text{Å}$, $\delta_l - \delta_m = 0.026\text{Å}$ and between bonds of $V2O_6$ $\delta_m - \delta_s = 0.014\text{Å}$ $\delta_l - \delta_m = 0.025\text{Å}$. This indicates that the main distortion of the $V1O_6$ -octahedra is still the compression along

the octahedral axis, which points approximately along the b -direction. Therefore, one can assume that the orbital with the lobes pointing along the legs of the zigzag chains is also fully occupied by one electron in the monoclinic phase. On the other hand, due to the small difference in bond length, it is difficult to predict, which of the orbitals will be occupied by the second electron. Even more uncertain is the scenario for the V_2O_6 -octahedra, since there the differences between all three averaged bonds are small. At this point the discussion about orbital order will be interrupted and continued at a later part of this thesis, when the magnetic structure of CaV_2O_4 will be determined (Sec. 5.3). Once the arrangement of spins and the ratio of the exchange constants is known, it will be possible to draw further conclusions on the type of orbital order.

Apart from the issue of orbital ordering, it is also interesting to know, what causes the off-centring of the V^{3+} ions within the oxygen octahedra. To shed light on this issue a bond valence sum calculation was performed. Since the bond valence strongly correlates with the length of a bond, it can be accurately determined from the crystal structure using empirical formulas⁴ [130, 132]. Further, the ‘valence sum rule’ states, that the sum of all bonds around each atom equals the atomic valence V_i [130, 132].

$$V_i = \sum_j s_{ij}, \quad (5.4)$$

where s_{ij} denotes the j th bond of the i th atom. By comparing the experimental atomic valence and the expected theoretical valence, one can draw conclusions on the stability of the structure.

In CaV_2O_4 the two vanadium sites both are in the 3+ valence state. Since they are six-fold coordinated by oxygen atoms, the theoretical valence for each $\langle\text{V-O}\rangle$ -bond is 0.5. However, a look at Tab. 5.8 reveals, that most of the bonds within the octahedra are ‘underbonded’. In the orthorhombic phase there are 10 out of 12 $\langle\text{V-O}\rangle$ bonds, which have valences less than 0.5 and in the monoclinic phase still 9 do so. This leads to an experimental bond valence sum per vanadium ion, which is $\approx 10\%$ smaller than the expected value (see Tab. 5.9). In contrast, the bond valence sum of the eight coordinated calcium ions in the orthorhombic phase is $\approx 15\%$ ($\approx 18\%$ in the monoclinic phase) greater than the expected valence of 2+. This indicates, that the calcium ions are too large for their environment and the Ca-O bonds are in compression. On the other hand, the lattice strain induced by the calcium ions causes the vanadium ions to

⁴The two most commonly encountered formulas are: $(R = R_0 - A \log_{10} s)$ and $(s = (\frac{R}{R_0})^{-N})$, respectively, where R and s are the bond length and bond valence of interest, R_0 denotes the length of a bond of unit valence and $A(\sim -0.8)$ and $N(\sim 5)$ are numerical parameters [130, 132].

be ‘underbonded’. In return, in order to increase their valence, the vanadium ions move off-centre within their octahedra.

To which extend the bond valence sum rule is violated can be measured by the ‘global instability index (*GII*)’ defined by Salinas-Sanchez *et al.* [133]:

$$GII = \sqrt{\sum_i \left[\sum_j (s_{ij} - V_i)^2 \right] / N}. \quad (5.5)$$

This measure gives the root mean square of the bond valence sum deviations for all atoms N of the asymmetric unit cell. Values of *GII* greater than 0.05 suggest that the crystal structure is strongly strained [132]. This is exactly the case for CaV_2O_4 , as can be seen in Table 5.9. Furthermore, the orthorhombic-to-monoclinic phase transition leads to an increase of the *GII* and therefore to a further increase of lattice strain.

Role of superexchange interactions

The edge-sharing arrangement of VO_6 octahedra in CaV_2O_4 favours direct exchange interactions between neighbouring magnetic ions, since the t_{2g} orbitals are directed toward each other. It was already pointed out by Goodenough [9], that in edge- or face-sharing t_{2g} -systems where the number of t_{2g} -electrons per cation is equal or less than three, the leading exchange between nearest neighbours is antiferromagnetic direct exchange. Further, he stated that in such an arrangement cation-anion-cation interactions (with the anions located at the octahedra’s corner) are negligibly weak, a statement already made previously by Anderson. Anderson showed that superexchange coupling between two cations making an angle of 90° with interjacent O^{2-} -ions is weak [7]. In a more recent paper, Pen *et al.* investigated the orbital ordering effects in triangular LiVO_2 by means of a degenerate Hubbard model [134]. In their system under investigation, the V^{3+} -ions are in octahedral geometry (similar to CaV_2O_4), with nearest neighbour octahedra sharing common edges. They estimated, that superexchange interactions via 90° V-O-V pathways are about an order of magnitude smaller than the direct exchange interactions.

Even though, all V-O-V bond angles between cations within the double chain of CaV_2O_4 are slightly greater than 90° (see Tab. 5.10), superexchange interactions will be very weak. In addition, in contrast to LiVO_2 , the octahedral environment is strongly distorted, leading to a partial (total) lifting of t_{2g} -orbital degeneracy in the high (low) T phase. This fact might even lower the strength of the superexchange, since some of the orbitals remain unoccupied and cannot contribute to the coupling.

Table 5.10.: Vanadium-oxygen-vanadium bond angles (in deg) of CaV_2O_4 in the $Pnam$ and $P2_1n/11$ phase.

angle	$Pnam$	$P2_1/n11$
V1-O4-V1(zz1)	99.4(2)	99.3(1)
V1-O4-V1(zz2)	99.4(2)	98.8(1)
V1-O1-V1(c)	93.7(2)	93.1(1)
V1-O4-V1(c)	92.3(2)	92.5(1)
V2-O2-V2(zz1)	97.5(2)	97.3(2)
V2-O2-V2(zz2)	97.5(2)	96.8(2)
V2-O2-V2(c)	93.7(2)	92.9(2)
V2-O3-V2(c)	96.6(2)	96.6(2)
V1-O1-V2(a1)	121.4(2)	120.2(2)
V1-O1-V2(a2)	121.4(2)	121.7(2)
V1-O3-V2(b1)	131.7(2)	132.1(2)
V1-O3-V2(b2)	131.7(2)	131.3(2)

The situation is slightly different between vanadium ions on different sites. The connection between them occurs via the corners of the surrounding octahedra, with V-O-V bond angles greater than 120° , as can be seen from Tab. 5.10. For cation-anion-cation angles $\sim 135^\circ$, weak antiferromagnetic superexchange interactions are the predicted [9]. In the high T phase of CaV_2O_4 this leads to frustrated interchain coupling, since distances and bond angles between nearest and next nearest neighbour inter-site ions are equal. Below the structural phase transition, the frustration is lifted and preferred superexchange pathways can develop, leading finally to the onset of antiferromagnetic long range order. This will be discussed in detail in the next section.

5.1.5. Conclusions

In the current section a detailed study of the nuclear structure of CaV_2O_4 has been presented. The structure is characterized by a quasi-one-dimensional geometry that is built up of two inequivalent V^{3+} -zigzag chain units. The particular arrangement of the magnetic ions gives rise to strong frustrated antiferromagnetic direct exchange interactions within the zigzag chains and weak frustrated antiferromagnetic interactions between the chains. Additionally, the V^{3+} -ions possess an orbital degree of freedom and the high temperature orthorhombic phase suggests a partial lifting of t_{2g} -orbital degeneracy due to a predominantly tetragonally distorted octahedral environment. However, the investigations also revealed a structural phase-transition from orthorhombic to monoclinic upon cooling ($T_s \approx 147$ K), giving rise to a lifting of both, frustration as well as orbital

degeneracy. Since the structural phase-transition promotes the formation of preferred exchange paths, long range magnetic order can be expected below T_s . This issue will be addressed in the next section, where the static magnetic susceptibility of CaV_2O_4 will be analysed.

5.2. Magnetic susceptibility

The static magnetic susceptibility of a single crystal of CaV_2O_4 was measured using a Quantum Design Physical Property Measurement System (PPMS) with a Vibrating Sample Magnetometer (see Sec. 3.2.2). The single crystal was grown with the floating zone technique as reported in [119]. The aim of the measurement was to extract the sample specific thermodynamic and magnetic parameters. This was done by fitting the experimental data to a Curie-Weiss function as well as to a ($S = 1$) J_1 - J_2 -Heisenberg model. The latter was solved by means of exact diagonalization. The extracted fit parameter reveal important information about the strengths of the exchange couplings between neighbouring magnetic ions and the degree of frustration of the system.

5.2.1. Introduction

Some contradictory results regarding the dc-susceptibility of CaV_2O_4 can be found in literature. Kikuchi and coworkers measured the susceptibility of a CaV_2O_4 powder sample and observed a broad maximum at $T \approx 250$ K and a spin glass-like anomaly below $T \approx 20$ K [135]. Both features were interpreted as signatures of strong low-dimensional antiferromagnetic interactions and geometrical frustration. Furthermore, no long range magnetic order has been observed. In contrast, the low temperature susceptibility measurements by Zong *et al.* done on a single crystal of CaV_2O_4 clearly revealed a magnetic phase-transition from the paramagnetic to the antiferromagnetically ordered state at $T_N \approx 69$ K [136]. This manifests in the data as a bifurcation in the susceptibility along two different crystallographic directions. Also in this case, the single crystal data show a broad maximum at higher temperatures, indicating strong low-dimensional correlations. Motivated by results of the CaV_2O_4 nuclear structure investigations, which suggest strongly one-dimensional interactions (see previous Sec. 5.1), as well as by the findings mentioned above, the dc-susceptibility of a CaV_2O_4 single crystal has been remeasured. In order to obtain more detailed information the data were taken over a broad temperature range ($3 \leq T \leq 1000$ K), thus allowing the paramagnetic phase to be fitted by a Curie-Weiss law. Additionally, the low-dimensional character of the material was investigated by fitting the susceptibility to an one-dimensional spin-1 Heisenberg model with nearest and next nearest neighbour interactions.

5.2.2. Experimental details

To measure the static magnetic susceptibility of CaV_2O_4 , a small disc of sample was cut from a floating zone grown crystal by using a conventional wire saw. The disc was further

cleaved in order to get correctly sized pieces for all used crystal orientations. Data were collected for the crystal oriented along all three main crystallographic directions with respect to the direction of the applied magnetic field. For all measurements a constant magnetic field of $H = 1$ T was used, while the temperature was varied between 2 K - 1000 K.

For the high temperature measurements (300 K - 1000 K) a special oven set-up was utilized and the crystal was fixed on a special zirconia sample stick containing a wire system that heats the sample. The sample was glued on the stick with heat-resistant cement-glue and wrapped in low emissivity copper foil to minimize heat leak from the hot region to the surrounding coil-set. On the other hand, the low temperature measurements (2 K - 400 K) were performed with the sample glued on a conventional trough-shaped brass sample holder using GE varnish glue. In order to account for the diamagnetic background produced by the sample holders and the glue, the temperature dependence of the ‘empty sample stick’ was measured and subtracted from the data.

5.2.3. Experimental results

The final static magnetic susceptibility of CaV_2O_4 for the magnetic field along all main crystallographic directions is displayed in Fig. 5.12. Since in general no difference in signal could be detected between runs with increasing and decreasing temperature, those measurements were combined. Additionally, also the data in the overlap region, which were measured with both the high T and low T set-up have been averaged.

The most eye-catching feature in Fig. 5.12 is the kink at $T_N = 72$ K (Néel temperature), which indicates the magnetic transition from the paramagnetic phase to the antiferromagnetic phase. Below this transition the susceptibility of the crystal starts to depend strongly on its orientation with respect to the magnetic field. For $H||b$ the susceptibility drops significantly, indicating that this direction is the easy axis of the crystal. In contrast, the susceptibility for the field pointing along the other two directions increases below the transition, thus those directions define the medium and hard axis, respectively. A close range of the data in the magnetically ordered phase is displayed in Fig. 5.13(a). It is remarkable that the susceptibility remains finite for all field directions, even at lowest temperatures. This behaviour is different to that of a conventional fully ordered antiferromagnet, where the static susceptibility along the easy axis vanishes for $T \rightarrow 0$ K. There are two possible explanations for this unusual behaviour. One reason could be, that not all of the spins are fully ordered, e.g. as a result of quantum fluctuations in the ground state. Another possible scenario is that the underlying magnetic structure

shows spin canting. Both issues will be addressed later in this thesis (see Sec. 5.3.6 and 6.5).

A second kink in the dc-susceptibility was detected at $T_c = 142$ K (see Fig. 5.13(b)). This anomaly depicts the nuclear phase transition from orthorhombic to monoclinic. The phase transition introduces a distortion in the crystal lattice with a significant change of bond angles and bond distances. This in turn also causes a change of the exchange

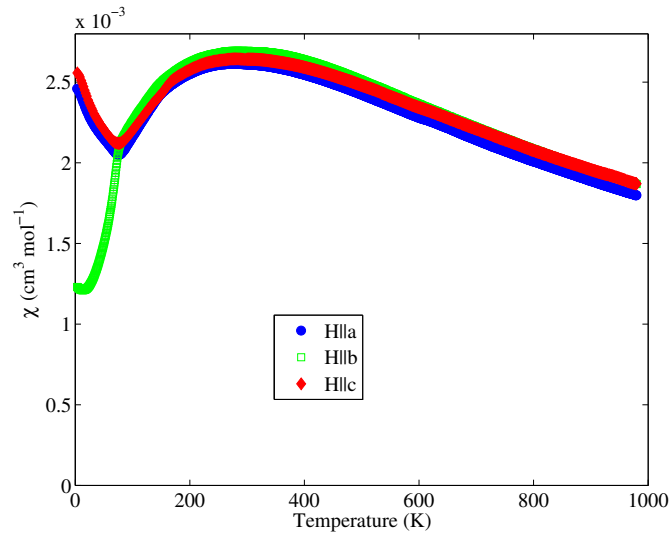


Figure 5.12.: Single crystal static magnetic susceptibility of CaV_2O_4 for all three crystallographic directions ($H = 1$ T). Reprinted from [137]. Copyright (2009) by the American Physical Society.

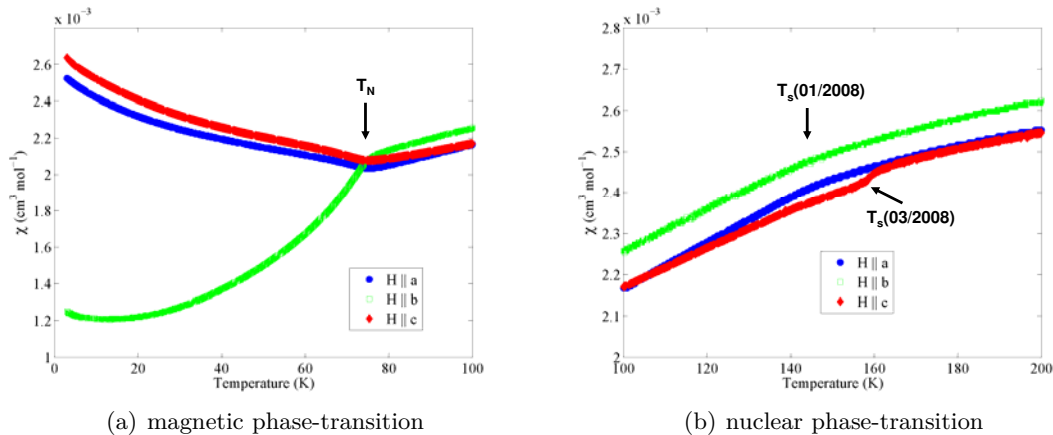


Figure 5.13.: Magnetic susceptibility of CaV_2O_4 for fields along all main crystallographic directions. (a) Region of the magnetic phase-transition, (b) Region of the structural phase-transition. In brackets the dates of the measurements are given.

interactions between the magnetic ions.

In fact, when comparing the data for the three field directions, one finds that the phase transition for $H||c$ occurs at a ~ 15 K higher temperature than for the other two directions. This is because the measurements for $H||c$ were performed at a later date, while the crystal was cooled and heated several times in the meantime. The repeated driving through the phase-transition caused slight modifications in the crystal structure, resulting in a higher transition temperature T_c . In contrast, the point of the magnetic phase-transition remains stable.

Another remarkable feature in the dc-susceptibility is the broad maximum around $T \approx 270$ K (see Fig. 5.12). Such a behaviour occurs when magnetic short range correlations are apparent and it is an indicator of low dimensional magnetism. Therefore, in order to gain further information about the low-dimensional spin-spin correlations, the data above the structural phase-transition have been analysed theoretically.

5.2.4. Data analysis and discussion

The experimental susceptibility χ_{exp} of CaV_2O_4 that is displayed in Fig. 5.12 can be written as the sum:

$$\chi(T) = \chi_s(T) + \chi_0, \quad (5.6)$$

where $\chi_s(T)$ is the spin susceptibility and χ_0 the temperature-independent orbital susceptibility. By comparing CaV_2O_4 to similar materials containing V^{3+} -ions (MgV_2O_4 [138], V_2O_3 [139]), the orbital contribution to the susceptibility for this material was estimated to be [119]:

$$\chi_0 \sim 4.0 \cdot 10^{-4} \text{cm}^3/\text{mol}. \quad (5.7)$$

However, for the following data analysis the estimated χ_0 will only serve as a benchmark and in order to get the most suitable value it will be included in the fitting process.

Curie Weiss Fit

In the high temperature region CaV_2O_4 is a paramagnet and the spin part of the static susceptibility (Eq. 5.6) can be fitted using the Curie-Weiss (CW) law⁵:

$$\chi_s(T) = \frac{C}{T - \Theta_{CW}} \quad (5.8)$$

with

$$C = \frac{\mu_B^2 p^2}{3k_B} \quad (5.9)$$

$$p = g\sqrt{S(S+1)} \quad (5.10)$$

In the above equations, C is the Curie constant, Θ_{CW} is the paramagnetic Curie temperature, μ_B is the Bohr magneton and p can be described as an effective moment of the magnetic ions carrying a spin S (assuming a quenched orbital angular momentum). g is the Landé-factor governing the splitting of the spin multiplet by a magnetic field. The value of g can be precisely determined by means of electron paramagnetic resonance measurements. For samples containing vanadium the value of g for the V-ion was found to lie within the range $1.92 \leq g \leq 2.00$ [140], where neither a dependence on the oxidation state of the vanadium ion, nor on the atomic environment within a particular material was found. The g -factor of CaV_2O_4 should therefore also be located in this region. Additionally, one can also expect slightly different values for g for different field directions, since CaV_2O_4 has a non negligible single ion anisotropy [136, 119].

Expressions 5.6, 5.8, 5.9 and 5.10 have been utilized to fit the high temperature region of the measured susceptibility, where a typical Curie-Weiss ($1/T$)-behaviour was observed above $T \approx 700$ K, such that all data in the region ($700 \leq T \leq 1000$ K) have been included in the fit. One can see, that there are three parameters which can be varied simultaneously throughout the fitting process (g, Θ, χ_0). However, these parameters are not completely independent from each other and some constraints had to be introduced in order to obtain trustable results. One physical constraint applies for the g -factor, which cannot be greater than 2, since this is the possible maximum for magnetic ions having two electrons in their d -shell. The second constraint was set for the temperature independent orbital susceptibility χ_0 which should have a value similar to Eq. 5.7. By allowing a 50% variation from this value, the most reasonable results were obtained for $\chi_0 = 4.8 \cdot 10^{-4} \text{cm}^3/\text{mol}$ and therefore χ_0 was set to this value.

⁵The Curie-Weiss law originates from the mean-field (MF) solution of the Heisenberg Hamiltonian: $\mathcal{H} = \sum_{ij} J_{ij} \mathbf{S}_i \cdot \mathbf{S}_j + g\mu_B \sum_j \mathbf{S}_j \cdot \mathbf{B}$, where \mathbf{B} denotes the magnetic field.

Table 5.11.: Results from Curie Weiss fit.

	g	$\chi_0/\frac{cm^3}{mol}$	$C/\frac{cm^3K}{mol}$	$\Theta/(K)$	$\mu_{\text{eff}}(\mu_B)$	J_{sum}/meV
$H a$	1.896(2)	0.00048	0.899(1)	-378(2)	2.7(1)	24.4(1)
$H b$	1.960(1)	0.00048	0.960(1)	-399(2)	2.8(1)	25.8(1)
$H c$	1.995(1)	0.00048	0.995(1)	-447(1)	2.82(9)	28.92(8)
Powder	1.949(4)	0.00048	0.949(4)	-407(5)	2.8(2)	26.3(3)

The crystal structure of CaV_2O_4 at high temperatures suggests strong antiferromagnetic interactions between nearest neighbour (NN) and next nearest neighbour (NNN) ions along the V^{3+} -zigzag chains. By assuming a simple model with antiferromagnetic exchange interactions J_1 and J_2 (see Fig. 5.15), it is possible to extract the sum $J_{\text{sum}} = J_1 + J_2$ from the Curie-Weiss fit. In a chain, where each spin has two NN and two NNN one gets:

$$k_B\Theta_{CW} = \frac{4}{3}S(S+1)(J_1 + J_2) \quad (5.11)$$

Here k_B is the Boltzmann constant.

The final results of the CW fitting for the susceptibility along all main crystallographic directions are listed in Tab. 5.11 and displayed in Fig. 5.14. Additionally, the three single crystal data sets have been combined in order to create an artificial powder average. The most remarkable result is the high negative Curie-temperature Θ , which indicates dominant antiferromagnetic interactions. Furthermore, the fact that Θ is much greater than the Néel temperature gives rise to geometrical frustration. An empirical measure of frustration is given by the quantity:

$$f = -\frac{\Theta}{T_N}. \quad (5.12)$$

In the case of CaV_2O_4 $f = 5.65$ for the powder averaged data⁶. Generally, each value of $f > 1$ corresponds to frustration, however, in other materials values of $f \gg 100$ have been observed (see [55]), thus indicating that CaV_2O_4 lies in the moderate frustration regime. In [55] materials with $f > 10$ are considered to be strongly geometrically frustrated magnets, since their magnetic behaviour cannot be described by simple meanfield theory. In this sense it can be concluded that CaV_2O_4 has some degree of frustration,

⁶It has to be mentioned that f is a classical measure, which becomes meaningless if the Néel temperature is reduced due to low-dimensionality. However, the parameter will be used in the following discussion for addressing the issue of geometrical frustration.

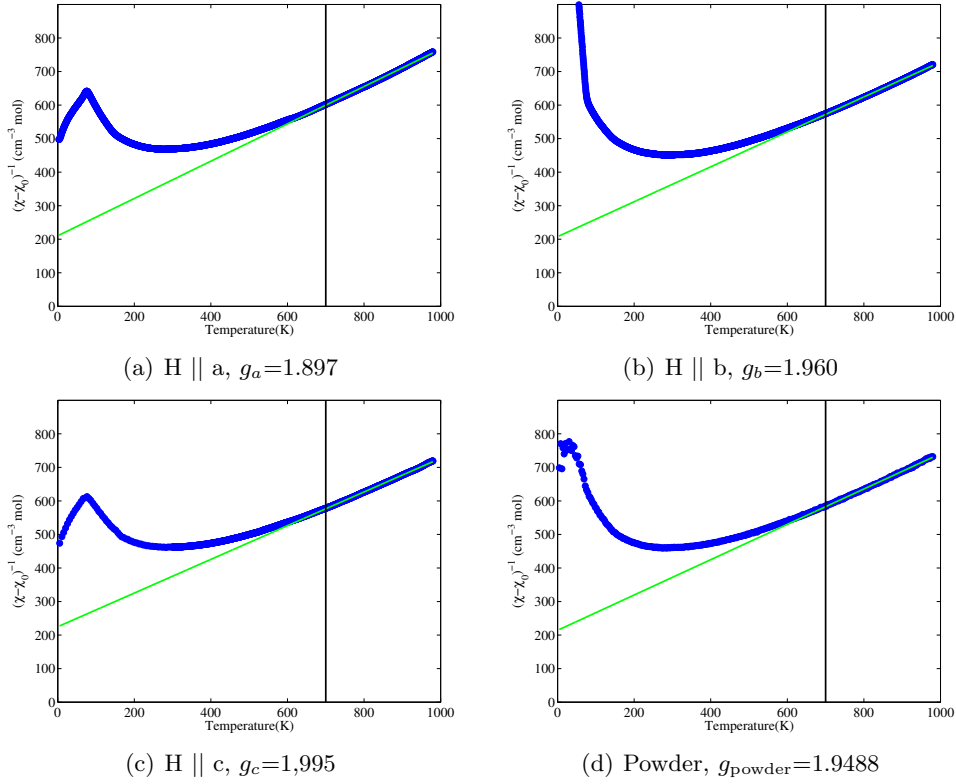


Figure 5.14.: Curie Weiss fit of susceptibility data in the region $700 \text{ K} \leq T \leq 1000 \text{ K}$. The figures display the inverse susceptibility $1/\chi$ vs. T . The straight black line indicates the minimum temperature used for the fitting. In all fittings a temperature independent background was considered ($\chi_0 = 0.00048 \frac{\text{cm}^3}{\text{mol}}$).

however, it is much lower than one would expect from the crystal structure. Later it will be shown, that this behaviour can be dedicated to orbital order, which partially lifts the frustration in CaV_2O_4 .

The difference between the g -factor for different field directions (see Tab. 5.11) indicates that the crystal is anisotropic even far above the Néel temperature. One finds $g_a < g_b < g_c$, however, since the absolute value of the susceptibility varied up to $\pm 5\%$ between different runs for the same crystal axis (most probably due to positioning effects), further conclusions cannot be drawn from this result.

The effective moment value, which was obtained from the Curie constant corresponds to the expected value for V^{3+} -ions in octahedral symmetry [140] and therefore underlines the validity of the Curie-Weiss fit in the selected region of χ .

Finally, the sum of magnetic exchange interactions apparent in CaV_2O_4 could be deduced. For the powder average one gets $J_{\text{sum}} \approx 26 \text{ meV}$. This value can be seen as

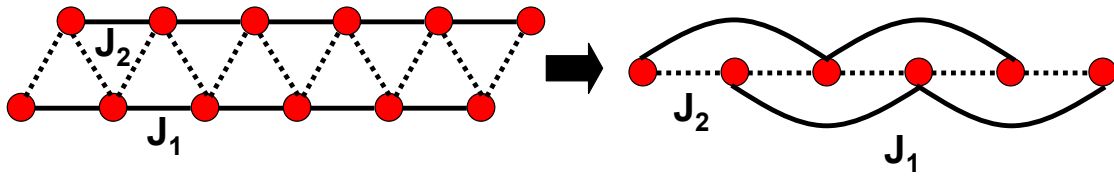


Figure 5.15.: Zigzag chain and its topological equivalent: a one dimensional chain with nearest and next nearest neighbour coupling J_1 and J_2 .

a first estimate for the energy scale in CaV_2O_4 . For instance, spin wave theory for a system of weakly coupled $S = 1$ chains predicts a maximum of the energy dispersion of $E_{\text{max}} = 2J$, being approximately 56 meV for CaV_2O_4 . However, this value can only be seen as a first ‘guess’, since effects of frustration and low dimensionality can lead to significant changes and to a renormalization of the spin wave energies. To get a more detailed picture about the ratio of the competing interactions in CaV_2O_4 , exact diagonalization calculations for a chain with frustrated interactions J_1 and J_2 were performed and calculated susceptibility was fitted to the experimental data.

Exact diagonalisation

The zigzag chain structure of magnetic ions in CaV_2O_4 can be mapped onto a simple chain model with nearest and next nearest neighbour interactions (see Fig. 5.15). For this model one can easily formulate the Heisenberg Hamiltonian to describe the interaction between the spins:

$$H = \sum_i^L S_i \cdot S_{i+1} + \alpha S_i \cdot S_{i+2} \quad (5.13)$$

$$\alpha = \frac{J_2}{J_1}. \quad (5.14)$$

In the above equation J_1 and J_2 are nearest and next nearest neighbour exchange coupling and L is the number of spin sites. For practical reasons the Hamiltonian is normalized to J_1 and α corresponds to the ratio of the two exchange constants. Assuming that a restriction to a finite chain size will still give an adequate description of the system under investigation, the model Hamiltonian (Eq. 5.14) can be solved using exact diagonalization (ED). This method provides direct access to the full eigenvalue and eigenvector spectra of the system and further allows to calculate the temperature depend thermodynamic properties, e.g. the static magnetic susceptibility. ED calculations

were performed using the code implemented in the ALPS software package [95]. A brief introduction to the ED method is given in Appendix A.

All the numerical results discussed here are based on ED calculations of a spin-1 chain with $L = 12$ sites. This number of sites provided a good compromise between system size and calculability. Further, periodic boundary conditions ($S_i = S_{L+i}$) have been assumed, such that the chain becomes a ring⁷. For the investigations the static magnetic susceptibility for a broad region of the coupling ratio α ($-1 \leq \alpha \leq 5$) was determined, where it was assumed that J_1 is positive (antiferromagnetic) and J_2 is either positive or negative (ferromagnetic). The numerically calculated susceptibility has the dimensionless form:

$$\frac{\chi_{ED} J_1}{L g^2 \mu_B^2} \quad \text{versus} \quad \frac{k_B T}{J_1}, \quad (5.15)$$

where L denotes the number of spins, g is the spectroscopic splitting factor, μ_B is the Bohr magneton and k_B is Boltzmann's constant. Since the calculated data are scaled with J_1 one can extract the values of J_1 , J_2 and g by providing a fine grid of susceptibility data points in the α - T phase-space and fitting the measured data using an interpolation function. For the current case the `Matlab` function `interp2` has been utilized [141]. The employed model contains four free parameters (g , α , J_1 and χ_0) and in order to obtain reliable results (and to account for correlations between these parameters) the values for g and χ_0 have been constraint to corresponding values derived from the CW fit.

An important issue is the selection of the correct temperature range, such that the employed model will provide trustable results. The validity of the J_1 - J_2 -model is given for the temperature region in which the system can be described with nearest and next nearest neighbour spin coupling only. The nuclear structure investigations revealed a structural phase transition from orthorhombic to monoclinic at $T_s \approx 145$ K, which also manifests in the susceptibility data (see Figure 5.13(b)). The structural distortion induced below T_s leads to different distances between neighbouring V^{3+} -ions along the chain's zigzags. This in return means, that the exchange along the zigzags can no longer be explained by a single J_2 parameter and thus the J_1 - J_2 -model is not a good approximation for the region below T_c . The situation becomes even worse below T_N , where the system develops antiferromagnetic long range order. In this region interchain coupling becomes important and the simple chain model is no longer valid.

Heat capacity as well as dc-susceptibility measurements using a SQUID magnetometer revealed another anomaly in CaV_2O_4 single crystal data at $T_s \approx 190$ K [119]. The ori-

⁷Periodic boundary conditions are useful in the current case, since one is only interested in the 'bulk' properties and not in edge effects.

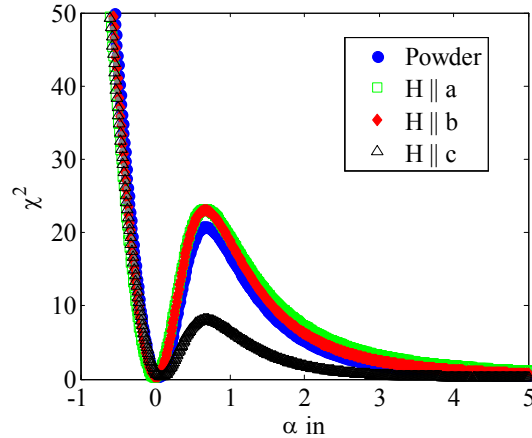


Figure 5.16.: Quality of ED fit with $L = 12$ sites vs. coupling ratio α for all field directions and the powder averaged data.

gin of this feature, which indicates another phase transition, is unclear at the moment, however, it was speculated that it might be the transition to a chiral ordered phase [119]. In this phase chiral order exists, without that the spins exhibit long range order [142]. However, since there is no clear explanation for this transition yet, the minimum temperature for the ED fits was chosen to lie *above* T_s .

Another issue which has to be taken into account when defining the fit region for ED data are effects which arise from the numerical technique itself. When using the ED technique one is restricted to a finite system size and one has to assume that the finite model system gives an accurate approximation of the real bulk material. Tests performed with the current chain model ($S = 1$) for various system sizes L revealed that finite size effects are particularly pronounced in the susceptibility at lower temperatures, below the characteristic broad maximum of χ .

Taking into account all the points mentioned above, one can conclude that the ED data of a spin-1 $J_1 - J_2$ model should provide reasonable fits of the CaV_2O_4 susceptibility in the temperature region $200 \leq T \leq 1000$ K.

In order to have the best control of the fitting parameters the following strategy was used to find the best solution for the given model. At first, only J_1 was kept as a free parameter, while α was constrained to a fixed value, which was manually varied over a broad region. For each value of α the fit-quality factor χ^2 was investigated⁸, therefore giving a first hint in which region of α the best solution will lie in. In a second step, also

⁸Note, that here χ^2 denotes the weighted difference between calculated and measured data and should not be confused with the square of the susceptibility.

α was allowed to vary, but choosing such starting parameters which lie in a region with high agreement (low χ^2).

Figure 5.16 displays the fit agreement factor as function of α for all measured field directions of χ and for the powder averaged data. The fits reveal two regions in which a high agreement is achieved. The first region is situated around $\alpha = 0$, where the NNN coupling J_2 approximates zero and the system becomes a simple antiferromagnetic $S = 1$ chain with NN coupling only (Haldane chain)⁹. The second region can be found at higher values of α ($\alpha > 4$). In this region J_2 becomes the dominant exchange and the system can be interpreted as two weakly coupled Haldane chains. For both regions one of the couplings is much stronger than the other, in contrast to what one would expect from the crystal structure, which suggests almost equal and frustrated couplings. In fact, the two solutions describe magnetically equivalent situations, since both suggest a single chain model with either J_1 or J_2 being the NN coupling.

After getting a clear picture about the relation between the two couplings, finally simultaneous fits of J_1 and α were performed, where the starting values have been chosen according to regions of high agreement in Fig. 5.16. The final results are summarized in Tab. 5.12 and in Figs. 5.17 and 5.18. The values underline the trend of Fig. 5.16. For all field directions, as well as for the powder averaged data, two solutions were obtained, depending on the particular starting values. For both solutions the obtained coupling parameter are very similar for all field directions, which is not surprising, since the susceptibility is almost field independent above the magnetic ordering temperature. The sum of the exchanges is $J_{\text{sum}} \approx 20$ meV and therefore somewhat smaller, than the values obtained from Curie-Weiss law. This is not unusual, since the mean field approximation leading to CW tends to overestimate the strength of the exchanges.

The two solutions are visualized in Fig. 5.19. Translated into the CaV_2O_4 zigzag chain picture, solution 5.19(a) corresponds to a situation where the coupling between ions along the zigzags is strong, whereas neighbouring ions along the legs are only very weakly coupled ($\alpha \approx 0$). For the susceptibility with the magnetic field along the a direction, even a small ferromagnetic leg coupling J_2 was observed. However, this value is very close to zero and should more likely be interpreted as ‘no leg coupling’, rather than ‘ferromagnetic leg coupling’.

Solution 5.19(b) corresponds to a scenario, where the leg coupling J_2 is the dominant interaction and where the coupling along the zigzags is only weakly pronounced. The value of the coupling ratio varies for different field directions from $\alpha \approx 4.5 - 7.6$. This

⁹The theoretical results for $\alpha = 0$ are in excellent agreement with those found from quantum Monte Carlo calculations [119]

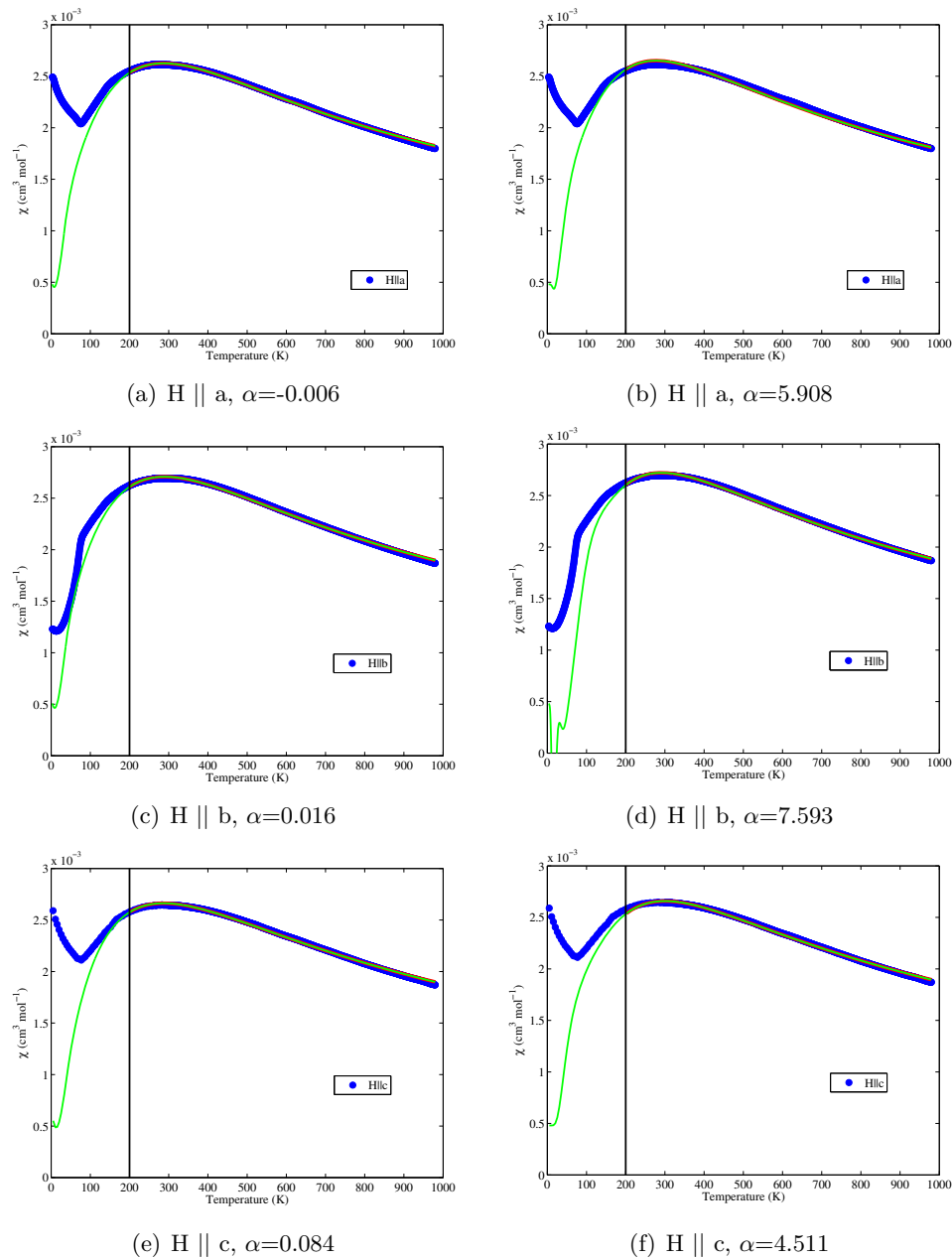


Figure 5.17.: ED data of $S = 1$ J_1 - J_2 model fit to dc-susceptibility of CaV_2O_4 in the region $200 \text{ K} \leq T \leq 1000 \text{ K}$. The left figures show the strong J_1 solution (single spin1 chain), while the right figures show the strong J_1 solution (two spin-1 chains). The straight line indicates the minimum temperature used for the fitting. In all fittings a constant susceptibility background is considered ($\chi_0 = 0.00048 \frac{\text{cm}^3}{\text{mol}}$).

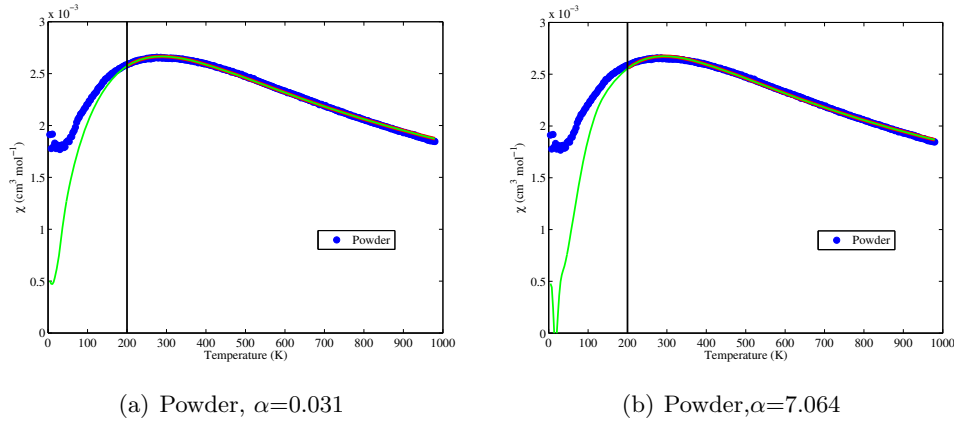


Figure 5.18.: ED data of $S = 1$ J_1 - J_2 model fit to dc-susceptibility powder averaged data of CaV_2O_4 in the region $200 \text{ K} \leq T \leq 1000 \text{ K}$. The left Figure show the strong J_1 solution (single spin1 chain), while the right Figure show the strong J_1 solution (two spin-1 chains). The straight line indicates the minimum temperature used for the fitting. In all fittings a constant background is considered ($\chi_0 = 0.00048 \frac{\text{cm}^3}{\text{mol}}$).

Table 5.12.: Isotropic exchange parameter for Eq. 5.14 deduced by fitting the susceptibility data of CaV_2O_4 . The fitted parameters strongly depend on the particular starting values.

	α_{start}	$J_{1,\text{start}}$	g	$\chi_0 / \frac{\text{cm}^3}{\text{mol}}$	α	J_1 (meV)	J_2 (meV)
$H a$	0	16	1.8961	0.00048	-0.006(1)	18.92(1)	-0.11(2)
	4	0	1.8961	0.00048	5.9(1)	2.96(7)	17.5(6)
$H b$	0	16	1.9600	0.00048	0.016(1)	19.48(1)	0.32(2)
	4	0	1.9600	0.00048	7.6(3)	2.4(1)	18(1)
$H c$	0	16	1.9954	0.00048	0.084(2)	20.6(1)	1.73(4)
	4	0	1.9954	0.00048	4.51(7)	4.21(6)	19.0(4)
Powder	0	16	1.9488	0.00048	0.031(3)	19.65(2)	0.62(6)
	4	0	1.9488	0.00048	7.0(4)	2.6(1)	18(1)

variation is in fact smaller than it seems and is a direct result of the small denominator in $\alpha = J_2/J_1$. Actually, the particular couplings J_1 and J_2 are very similar for different

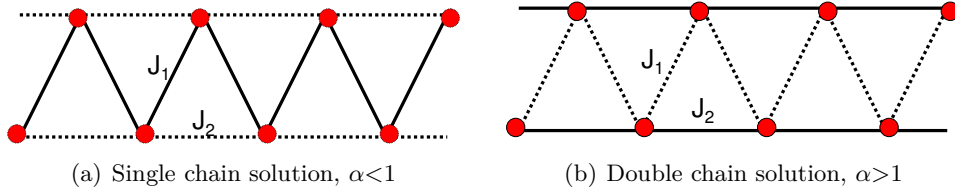


Figure 5.19.: Sketch of the two solutions found by fitting the dc-susceptibility of CaV_2O_4 using Eq. 5.14. Straight lines indicate strong coupling and dashed lines indicate weak coupling.

directions (see Tab. 5.12). However, it has to be mentioned that the accuracy of the fits gets inevitably poorer as α increases. This has two reasons. First of all, finite size effects become more pronounced in this region, since the strong leg coupling J_2 leads to a situation of two single chains, both having $N' = N/2$ sites. This means, that the spin-spin correlation lengths reaches the same order as the effective system size N' and the system can no longer be seen as ‘infinite’. The second reason is, that the ED calculations have been concentrated on the region $-1 \leq \alpha \leq 5$. Values of α above this region were interpolated and thus are less accurate, as can be seen from the error-bars.

The remaining open question is now, which of the two solutions really matches the physical properties of CaV_2O_4 ? Non of both solutions represent a situation which one would expect by simply inspecting the distances between the magnetic ions. As discussed in the previous section (see Sec. 5.1.3), the distances between NN and NNN V^{3+} -ions in the orthorhombic phase are $d_{\text{leg}}=3.01 \text{ \AA}$ and $d_{\text{zz}}=3.08 \text{ \AA}$. However, this small difference between the two distances can never account for the huge inequality between J_1 and J_2 . It can be shown that the strength of the exchange interaction mediated between directly overlapping d -orbitals is approximately $J \propto R^{-10}$, where R is the interionic distance [6]. The same law has been found experimentally by Bloch [143]. For CaV_2O_4 this relation leads to:

$$\alpha = \frac{J_2}{J_1} = \left(\frac{d_{\text{leg}}}{d_{\text{zz}}} \right)^{-10} \approx 1.25, \quad (5.16)$$

a value much different from what has been observed. These findings indicate that there must exist another mechanism which selects the exchange paths and ‘decides’ about the strengths of the interactions. The following two Chapters dealing with the magnetic structure and excitations of CaV_2O_4 will shed light on this issue. It will be shown that the exchange interactions are not only highly sensitive to orbital overlap, but (even more importantly) to the particular orbital occupation.

As the last point of this section it is worth to discuss possible extensions to the implemented J_1 - J_2 model (Eq. 5.14), which could help to improve the quality of the susceptibility fits. A closer look at Figs. 5.17 and 5.18 reveals that the calculated susceptibility falls off quite rapidly below the broad maximum at $\approx 270 \text{ K}$. This is different to the measured data, which are more flat in this region. The flattening effect could be caused by single-ion anisotropy, arising due to spin-orbit coupling and the particular octahedral environment of the magnetic V^{3+} -ions. The presence of single-ion anisotropy in CaV_2O_4 was verified by nuclear magnetic resonance and inelastic neutron scattering experiments, which both detected the opening of a spin gap in the magnetic excitations

below the magnetic ordering temperature (see [136] and Chapter 6).

In order to investigate the effects of anisotropy, some additional ED calculations have been performed using the following model:

$$H = \sum_i^L (S_i \cdot S_{i+1} + \alpha S_i \cdot S_{i+2}) + \frac{D}{J_1} \sum_i^L (S_i^z)^2. \quad (5.17)$$

$$(5.18)$$

Here D denotes the single ion anisotropy constant, where it was assumed that the anisotropy axis coincides with the direction of the magnetic moments. The calculations were performed for a spin-1 chain with $L = 8$ sites and NN coupling only ($\alpha = 0$). The temperature dependent susceptibility for various values of D/J_1 is displayed in Figure 5.20.

Indeed it can be seen, that with increasing D the susceptibility becomes flatter around

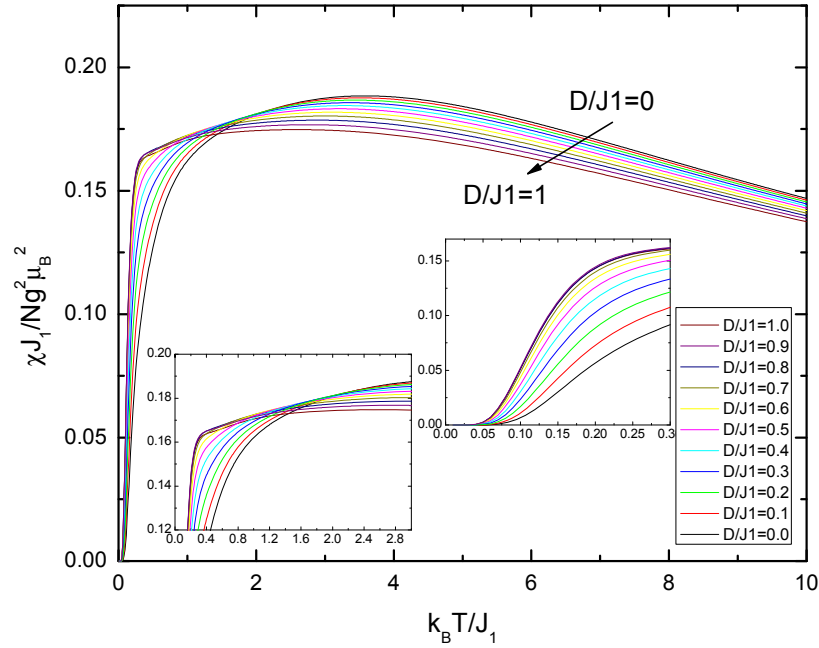


Figure 5.20.: Static magnetic susceptibility of a spin-1 chain with $L = 8$ sites as a function of temperature calculated from Eq. 5.18 using ED. The results for various values of the single ion anisotropy D are displayed.

the broad maximum. Further χ starts to drop down at a lower temperature as D increases, however, it also begins to drop down more rapidly. For values $D \approx J_1$ a kink develops, below which the susceptibility falls very fast down to zero. The calculated susceptibility curves are in excellent agreement with those found from TMRG (transfer

matrix renormalization group) calculations [144].

The calculations indicate that the extension of the Heisenberg model by an additional single-ion anisotropy term might be able to improve the fit quality. However, for several reasons a real fit including the anisotropy was not performed. Most importantly, the assumption that the spin direction corresponds with the direction of the anisotropy axis is not valid for real CaV_2O_4 . This is because the material consists of *two inequivalent* vanadium sites and thus of two inequivalent zigzag chain units. The fairly different octahedral environments for both sites give rise to very different single-ion anisotropy axes, such that the assumption made in Eq. 5.18 does not hold. In Sec. 5.3 it will be shown that the different anisotropies lead to a canting of magnetic moments of neighbouring chains.

Secondly, in order to describe the susceptibility data along all field directions, one would also need to calculate the transverse anisotropy, where the anisotropy axis lies perpendicular to the moment direction. The calculation of this quantity is more complex and not implemented in the ALPS software, so it was not accessible. Finally, even if one would find a possibility to perform accurate calculations of χ including single-ion anisotropy, it would still be hard to actually fit the data, since the high number of fit parameters (J_1 , α , D and eventually g) makes it very difficult to find a unique and physically correct solution.

Another important aspect is that the above mentioned two inequivalent magnetic vanadium sites not only give rise to different anisotropies, but also to different intrachain exchange interactions. Therefore the shape of the measured temperature-dependent susceptibility reflects the overall behaviour of all intrachain interactions and care has to be taken when interpreting the data calculated for a single chain model. In order to gain deeper insights into the various exchange interactions of CaV_2O_4 , careful investigations of the magnetic structure and of the magnetic excitation spectrum are necessary. While the former issue will be addressed in the following section, the latter is the topic of Chapter 6.

5.3. Magnetic structure

This section presents the magnetic structure of CaV_2O_4 in the antiferromagnetically ordered phase, as obtained from single crystal neutron diffraction. For the investigations, three single crystals prepared in different ways were used (triarc as grown, triarc annealed and floating zone grown annealed) and the neutron experiments took place on three different instruments, namely SXD at ISIS and E4 and E5 at HZB. The final analysis was focused on the data obtained on E5 with the floating zone grown crystal, since this crystal had the purest quality and was the only one consisting of a single grain.

5.3.1. Introduction

The magnetic properties of CaV_2O_4 have been already studied for more than 30 years. In 1967 Bertaut *et al.* [145] and Hastings *et al.* [146] published almost simultaneously their results on the magnetic structure of CaV_2O_4 . Both performed neutron powder diffraction experiments at liquid helium temperature ($T = 4.2$ K) and applied symmetry analysis in order to find a spin arrangement that is in agreement with the data. Further, both based their analysis on the assumption that the low temperature space group is orthorhombic $Pnam$ (setting $Pbnm$ is used in [145]), since it was not possible to resolve the weak monoclinic twinning (see Sec. 5.1) with former neutron powder diffractometers. Their data revealed a doubling of the unit cell perpendicular to the principle axis, which corresponds to a magnetic propagation vector $\mathbf{k} = (0, \frac{1}{2}, \frac{1}{2})$ (Hastings notation). In addition a strongly reduced magnetic moment of $\mu \approx 1.0 \mu_B$ was found (compared to the expected value of $2 \mu_B$ for $S = 1$ systems).

Using magnetic Shubnikov groups, Hastings *et al.* obtained three possible magnetic structures in agreement with the measured data. All solutions gave collinear arrangements of the magnetic moments, with the spins pointing along the crystallographic b direction [146]. The same results were derived by Bertaut *et al.* using representation analysis; however, they could exclude one of the proposed models, since it did not belong to an irreducible representation of the underlying space group [145].

More recently, the magnetic structure was reinvestigated by Zong and co-workers, who performed ^{51}V NMR measurements on single crystals of CaV_2O_4 . In contrast to the previous diffraction work, their measurements revealed the existence of two antiferromagnetic substructures, canted about the b axis by a total canting angle of $19(1)^\circ$. Further, the ordered spin moment was found to lie in the range 1.02 - $1.59 \mu_B$ [136].

The reduced moment value was also confirmed by muon-spin spectroscopy investigations ($\mu = 1.19(14) \mu_B$) [147].

Notwithstanding the considerable effort that has been devoted to solve and understand the magnetic structure of CaV_2O_4 , some of the most important questions remained unsolved up to now. For instance, there is still no final solution for the arrangement of the magnetic moments within the crystal. Possible models in agreement with neutron powder diffraction data have been proposed, however, only a single crystal diffraction experiment can distinguish between them [146]. Moreover, the lowering of crystal symmetry from orthorhombic to monoclinic has never been taken into account in the analysis of magnetic symmetry.

In addition, the results proposed from NMR measurements raise some further questions. For example, NMR failed to show which spins form the two predicted substructures or what is the relative ordering within them.

To clarify those issues, neutron diffraction experiments on high quality single crystals have been performed. With this technique it was not only possible to derive a unique solution for the magnetic structure of CaV_2O_4 , but it could also be shown, that the system consists of two substructures which are zigzag chains. The spins within each chain are collinear, while spins of different chains are canted with respect to each other.

5.3.2. The problem of twinning

The key point for a successful refinement of a nuclear or magnetic structure using single crystal diffraction, is the accurate determination of integrated Bragg intensities. Those intensities are proportional to the square of the structure factor ($I \sim F^2$) and can be compared to the calculated intensities of a proposed atomic model.

The measurement of Bragg intensities becomes significantly more difficult, when twinning is apparent in the crystal lattice. Twinning is a phenomenon which occurs, when individual crystals of the same species are joined together in some definite mutual orientation. The symmetry relation between the twins is described by the twin law and depending whether or not the twin law is a symmetry operator of the crystal lattice, one differentiates between merohedral and non-merohedral twins [148].

In the case of CaV_2O_4 non-merohedral twinning occurs, which means that the twin law does not belong to the crystal class of the structure nor to the metric symmetry of the cell. The monoclinic distortion in the $\mathbf{b}^*\text{-}\mathbf{c}^*$ -plane, with the monoclinic angle α close to 90° , results in two interpenetrating reciprocal lattices, where the related symmetry operation between both is a 180° rotation around the \mathbf{c}^* axis. The corresponding twin

law can be expressed with the following matrix equation:

$$\boldsymbol{\kappa}_{\text{twin1}} = \hat{\boldsymbol{T}} \boldsymbol{\kappa}_{\text{twin2}} = \begin{pmatrix} -1 & 0 & 0 \\ 0 & -1 & 0 \\ 0 & 0 & 1 \end{pmatrix} \boldsymbol{\kappa}_{\text{twin2}}. \quad (5.19)$$

In the above equation, $\boldsymbol{\kappa}$ is a reciprocal lattice vector where the subscript denotes the corresponding lattice and $\hat{\boldsymbol{T}}$ is the transformation matrix of the twin law. An equivalent notation of the twin law in terms of reciprocal lattice points (hkl) is given by:

$$(hkl)_{\text{twin1}} = (-hkl)_{\text{twin1}} = (-h - kl)_{\text{twin2}} = (h - kl)_{\text{twin2}}, \quad (5.20)$$

where the equals sign in the middle denotes the twin law, while the other two are due to the symmetry of the monoclinic space group.

An illustration of the twinning within the (0kl) plane is given in Fig. 5.21. Depending on the position in reciprocal space, the Bragg reflections of both twins either overlap (exactly or partially) or are completely separated. In terms of data processing, the most difficult part is to extract the intensities from overlapping reflections. This is because the degree of overlap is usually not exactly known and differs from reflection to reflection. For the determination of the magnetic structure of CaV_2O_4 with single crystal diffraction it was therefore extremely important to find an experimental set-up that allows the twinned peaks to be resolved with the highest possible accuracy.

5.3.3. Theoretical analysis - representation theory

In Sections 5.1 and 5.2 it was shown, that CaV_2O_4 undergoes two phase transitions upon cooling. At $T_S \approx 141$ K a structural phase transition from orthorhombic to monoclinic occurs, while at $T_N \approx 71$ K the material develops antiferromagnetic long range order. The crystallographic space group of the low temperature phase is monoclinic $P2_1/n11$ and there are two inequivalent vanadium sites in the unit cell which are responsible for the magnetism in the system. Due to the symmetry operations of the monoclinic space group, the total number of magnetic atoms per unit cell is eight (four of each site), which

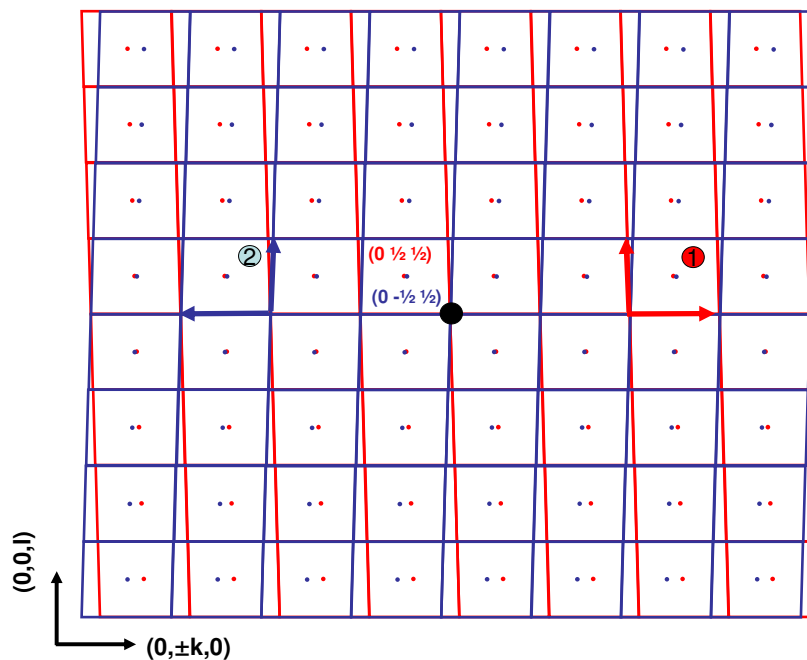


Figure 5.21.: Reciprocal space diagram of the $(0kl)$ lattice plane, showing the relationship between the monoclinic twins. Twin 1 is coloured red and twin 2 is coloured blue. Nuclear Bragg reflections are positioned at the vertices of the lattice, while magnetic Bragg reflections are indicated by dots (propagation vector $\mathbf{k} = (0, \frac{1}{2}, \frac{1}{2})$).

are generated by the following operations:

$$\begin{aligned}
 (1) : & \quad x, y, z & (5.21) \\
 (2) : & \quad x + \frac{1}{2}, -y + \frac{1}{2}, -z + \frac{1}{2} \\
 (3) : & \quad -x, -y, -z \\
 (4) : & \quad -x + \frac{1}{2}, y + \frac{1}{2}, z + \frac{1}{2}.
 \end{aligned}$$

Each vanadium ion is located at the general Wykoff position (4e), where the positions (x, y, z) are those given in Tab. 5.6. In addition, the spin of each magnetic moment, being an axial vector, has components along the three crystallographic directions, such that the total magnetic structure of CaV_2O_4 consists of $8 \times 3 = 24$ components. Those components form a representation for the magnetic structure and with the help of group theory, this representation can be decomposed into its irreducible representations [149].

The great advantage of the irreducible representations (IR) of magnetic structures arises as a consequence of Landau's theory of second order phase transitions (see e.g. [150] and references within). This theory states, that the order parameter of the phase transition is a linear combination of the basis vectors of only one single IR, while the basis vectors associated with the other IRs are necessarily zero. Therefore the number of symmetry allowed magnetic structures is strongly reduced, being simply the number of irreducible magnetic representations.

To obtain all magnetic IR for a given system, one needs to find the so called little group $g_{\mathbf{k}}$. This group contains all those point group operations g of the underlying crystallographic space group, which keep the magnetic propagation vector \mathbf{k} invariant. The point group associated with space group $P2_1/n11$ is $C_{2h} = \{E, 2_x, \bar{1}, m_{xy}\}$. It contains the unity element E , the point rotation 2_x around the crystallographic x -axis, an inversion center $\bar{1}$ and a mirror plane m_{xy} along the diagonal of x and y . The propagation vector of magnetic CaV_2O_4 is $\mathbf{k} = (0, \frac{1}{2}, \frac{1}{2})$ and stays invariant under each of the four symmetry operations of C_{2h} ¹⁰, and thus the little group $g_{\mathbf{k}}$ is equivalent to point group C_{2h} . Finally, the space group of wave vector \mathbf{k} , including both, point symmetry and translation symmetry elements, is $G_{\mathbf{k}} = \{E, 2_{1x}(\frac{1}{2}, 0, 0), \bar{1}(0, 0, 0), n(0, \frac{1}{2}, \frac{1}{2})\}$, where $2_{1x}(\frac{1}{2}, 0, 0)$ is a twofold screw axis positioned at $(x, \frac{1}{4}, \frac{1}{4})$, $\bar{1}(0, 0, 0)$ denotes an inversion symmetry centered at the origin and $n(0, \frac{1}{2}, \frac{1}{2})$ is a diagonal glide plane along $(\frac{1}{4}, y, z)$.

The full magnetic representation Γ_{mag} of $G_{\mathbf{k}}$ can be decomposed into four one dimensional irreducible representations $\Gamma_{\mathbf{k}\nu}$ ($\nu = 1, \dots, 4$), where each IR is included in Γ_{mag} three times:

$$\Gamma_{\text{mag}} = 3\Gamma_{\mathbf{k}1} + 3\Gamma_{\mathbf{k}4} + 3\Gamma_{\mathbf{k}3} + 3\Gamma_{\mathbf{k}4}. \quad (5.22)$$

In Tab. 5.13 the characters of the four IR of $G_{\mathbf{k}}$ are listed. Using the projection operator method implemented in the program `BasIreps` [151], one can finally derive all basis vectors Ψ_n which correspond to a certain IR. In the current case, there are three basis vectors for each $\Gamma_{\mathbf{k}\nu}$ and those are given in Tab. 5.14. Since any linear combination of basis vectors within one IR represents also a symmetry allowed basis vector, the magnetic moment of a particular atom is simply given by the sum of the basis vectors of a particular IR:

$$\mathbf{m}_j = \sum_n C_n \Psi_n. \quad (5.23)$$

¹⁰In fact, the inversion $\bar{1}$ and the point rotation 2_x lead to $\mathbf{k}' = (0, \frac{1}{2}, \frac{1}{2})$; however, this vector is equivalent to \mathbf{k} , since \mathbf{k} and \mathbf{k}' are connected via a reciprocal lattice vector $\mathbf{k} = \mathbf{k}' + \mathbf{G}$.

Table 5.13.: Irreducible representations of space group $G_{\mathbf{k}}$ for $\mathbf{k} = (0, \frac{1}{2}, \frac{1}{2})$

	E	2_x	$\bar{1}$	n
$\Gamma_{\mathbf{k}1}$	1	1	1	1
$\Gamma_{\mathbf{k}2}$	1	1	-1	-1
$\Gamma_{\mathbf{k}3}$	1	-1	1	-1
$\Gamma_{\mathbf{k}4}$	1	-1	-1	1

Table 5.14.: Basis vectors for axial vectors associated with irreducible representations $\Gamma_{\mathbf{k}1}-\Gamma_{\mathbf{k}4}$. In the last column a short hand notation is given, which is based on the symbols used for different types of magnetic order, F=(+,+,+,+), G(+,-,+,-), C=(+,-,-,+) and A=(+,+,-,-).

site	(1)	(2)	(3)	(4)	
$\Gamma_{\mathbf{k}1}$	(x, y, z)	$(x + \frac{1}{2}, -y + \frac{1}{2}, -z + \frac{1}{2})$	$(-x, -y, -z)$	$(-x + \frac{1}{2}, y + \frac{1}{2}, z + \frac{1}{2})$	short
Ψ_1	(1 0 0)	(1 0 0)	(1 0 0)	(1 0 0)	F_x
Ψ_2	(0 1 0)	(0 -1 0)	(0 1 0)	(0 -1 0)	G_y
Ψ_3	(0 0 1)	(0 0 -1)	(0 0 1)	(0 0 -1)	G_z
$\Gamma_{\mathbf{k}2}$	(x, y, z)	$(x + \frac{1}{2}, -y + \frac{1}{2}, -z + \frac{1}{2})$	$(-x, -y, -z)$	$(-x + \frac{1}{2}, y + \frac{1}{2}, z + \frac{1}{2})$	short
Ψ_1	(1 0 0)	(1 0 0)	(-1 0 0)	(-1 0 0)	A_x
Ψ_2	(0 1 0)	(0 -1 0)	(0 -1 0)	(0 1 0)	C_y
Ψ_3	(0 0 1)	(0 0 -1)	(0 0 -1)	(0 0 1)	C_z
$\Gamma_{\mathbf{k}3}$	(x, y, z)	$(x + \frac{1}{2}, -y + \frac{1}{2}, -z + \frac{1}{2})$	$(-x, -y, -z)$	$(-x + \frac{1}{2}, y + \frac{1}{2}, z + \frac{1}{2})$	short
Ψ_1	(1 0 0)	(-1 0 0)	(1 0 0)	(-1 0 0)	G_x
Ψ_2	(0 1 0)	(0 1 0)	(0 1 0)	(0 1 0)	F_y
Ψ_3	(0 0 1)	(0 0 1)	(0 0 1)	(0 0 1)	F_z
$\Gamma_{\mathbf{k}4}$	(x, y, z)	$(x + \frac{1}{2}, -y + \frac{1}{2}, -z + \frac{1}{2})$	$(-x, -y, -z)$	$(-x + \frac{1}{2}, y + \frac{1}{2}, z + \frac{1}{2})$	short
Ψ_1	(1 0 0)	(-1 0 0)	(-1 0 0)	(1 0 0)	C_x
Ψ_2	(0 1 0)	(0 1 0)	(0 -1 0)	(0 -1 0)	A_y
Ψ_3	(0 0 1)	(0 0 1)	(0 0 -1)	(0 0 -1)	A_z

In the above equation \mathbf{m}_j denotes the magnetic moment of the j th atom and C_n is the mixing coefficient of the basis vector Ψ_n . The C_n 's are those parameters, that can be refined throughout the analysis of the diffraction data and they give the orientation and the size of the magnetic moments.

What has not been taken into account so far is, that the unit cell of CaV_2O_4 contains two inequivalent magnetic ions (V_1 and V_2), which both transform according to the relations in 5.21. In the most general case, each site could have a different magnetic structure, being described by a different irreducible representation. However, the situation is simplified for CaV_2O_4 , because the magnetic long range order is a result of the coupling between the different magnetic sites. Accordingly, there is only a single critical temperature T_N (and therefore only one order parameter), meaning that the basis vec-

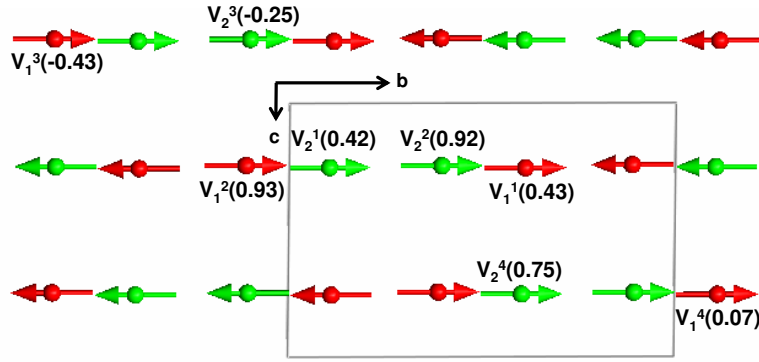


Figure 5.22.: Example of a possible magnetic structure of CaV_2O_4 , obtained with Γ_{k3} . The arrows indicate the direction of the magnetic moments and the different colors stand for the two inequivalent vanadium sites. The a component is given in brackets. Note, that the c axis has been slightly stretched for clarity reasons.

tors associated with both sites must belong to the same IR.

To exemplify the results obtained with representation analysis, a possible magnetic structure of CaV_2O_4 , which is described by the basis vectors of the IR Γ_{k3} , is displayed in Fig. 5.22. The two different vanadium sites can be distinguished by their different colours and subscripts, while the superscript labels the four symmetry related positions following the notation given in 5.21. For the sake of simplicity it is assumed, that all moments point along the b -direction and therefore only coefficient C_2 in Eq. 5.23 will be non-zero. What remains is the basis vector $\Psi_2(\Gamma_{k3})$. According to this vector, all symmetry related magnetic sites have the same moment direction (F-type). Finally, all additional magnetic sites (e.g. those to fill up the unit cell) can be simply generated by the usual lattice translations, however, one has to bear in mind, that antiferromagnetic order breaks the translation symmetry and an additional phase $e^{2i\pi\mathbf{k}\cdot\mathbf{t}}$ has to be introduced, where \mathbf{t} is the translation vector in units of the lattice vectors.

The task is now to use the data from single crystal neutron diffraction to identify the single IR involved in the magnetic phase transition and fit the mixing parameter C_n in order to get the magnetic structure of CaV_2O_4 .

5.3.4. Experimental details

Single crystal neutron diffraction experiments have been performed on three different instruments and three differently prepared samples. The samples differed in their quality (amount of impurity and graininess) and also in their nuclear and magnetic transition temperatures as can be seen from Tab. 5.15 (see also reference [119]).

Measurements on SXD

The neutron time-of-flight Laue diffractometer SXD at ISIS was used to check the magnetic propagation vector proposed by previous powder diffraction experiments [145, 146]. In detail, the structure was examined for possible incommensurability, which e.g. has been observed in isostructural β -CaCr₂O₄ [152]. SXD, which uses the white beam Laue technique, is an ideal instrument for such a task, since its eleven area detectors cover a broad region of reciprocal space ($\approx 2\pi$ steradians) and thus allow a detailed investigation of nuclear and magnetic ordering phenomena (see also Sec. 3.1.2). The crystal under investigation was grown with the triarc furnace and not annealed prior to the measurement. For the experiment it was mounted on an aluminium pin (see Fig. 5.23) and inserted into a closed cycle refrigerator allowing temperatures between 15 K and 300 K to be accessed. Measurements took place at room temperature and both, above T_N at 65 K and below T_N at 18 K, and for each temperature up to four different crystal orientations were used. The final data were corrected for detector efficiency by normalizing them to data from a vanadium/niobium standard collected under the same conditions. Further an ‘empty instrument’ measurement was performed and utilized to correct the data for the background.

Finally, the SXD2001 software was used to bin the observed data in three-dimensional volumes of reciprocal space on a $201 \times 201 \times 201$ grid. The volume data were further investigated by performing slices through selected regions of reciprocal space [65].

Measurements on E4

The same CaV₂O₄ crystal that was measured on SXD, was further investigated on the two-axis neutron diffractometer E4 at HZB; however, before the experiment it was annealed in order to remove internal stresses and thus to make the crystal structure more homogeneous. The annealing procedure resulted in a significant increase of the transition temperatures as can be seen in Tab. 5.15.

The E4 instrument is installed at the thermal neutron guide at HZB. During the experi-

Table 5.15.: Summary of single crystal neutron diffraction experiments on differently prepared crystals

Instrument	sample	synthesis	m (g)	V (mm ³)	T_N (K)	T_S (K)
SXD	an-2-50	triarc as grown	0.068	30	53	112
E4	an-2-50	triarc annealed	0.068	30	69	141
E5	an-3-077	OFZ annealed	0.3935	137	71	145

ment it was operated with a vertically focusing pyrolytic graphite (PG) monochromator selecting neutrons of incident wave length $\lambda = 2.44 \text{ \AA}$. The neutrons scattered by the sample were detected with a single ^3He tube detector which was confined to the horizontal scattering plane.

The sample was mounted on a sample stick and inserted inside a conventional orange cryostat. Measurements were performed at $T = 1.5 \text{ K}$ in the antiferromagnetically ordered phase and a substantial data set of magnetic and nuclear reflections was collected by performing ω (sample table) scans around the Bragg peak positions at constant 2Θ (fixed detector geometry). Reflections were measured from two scattering planes, being $(0kl)$ and $(hk\frac{h}{2})$, and thus allowing to access magnetic Bragg peaks according to propagation vector $\mathbf{k} = (0, \frac{1}{2}, \frac{1}{2})$.

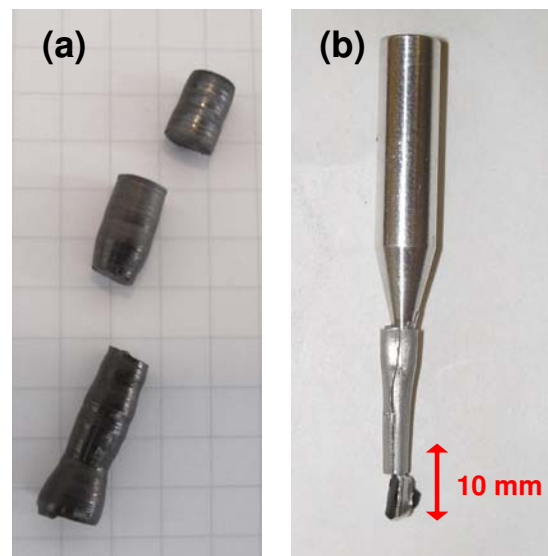


Figure 5.23.: Pictures of CaV_2O_4 single crystals: (a) growth from the image floating zone furnace, cut in three pieces (the smallest piece was used for the E5 experiment); (b) small piece of a triarc grown crystal mounted onto a sample stick for the SXD experiment.

Measurements on E5

For the experiment on the four-circle neutron diffractometer E5 at HZB, new single crystals of CaV_2O_4 were grown using an optical floating zone (OFZ) furnace (for details see [119]). These were single-grain samples of large mass and volume (see Fig. 5.23 (a)). The E5 instrument provides two features which make it perfect for the determination of magnetic structures. First, the four-circle geometry allowed to access a huge area in

reciprocal space, without being restricted to a certain scattering plane (see Sec. 3.1.2). Secondly, the instrument was equipped with a two-dimensional position sensitive ^3He detector, which allows to detect an extended region around a Bragg position and thus making it easier to detect and separate twinned peaks.

For this particular experiment E5 was operated with a pyrolytic graphite monochromator selecting an incident wave length of $\lambda = 2.36 \text{ \AA}$. A graphite filter was placed between the monochromator and the sample, to avoid higher order contributions e.g. $\lambda/2$. The crystal under investigation was glued on a sample stick and inserted into a close cycle helium refrigerator, enabling temperatures between 300 K and 6 K to be accessed.

In order to achieve the best resolution to separate the twinned structure the crystal was mounted such that the (monoclinic) b - c plane was perpendicular to the main goniometer axes, for which $\chi=180^\circ$ (see also Sec. 3.1.2). The advantage of this configuration was that it provided the best resolution for reflections within the monoclinic plane and therefore enabled the separation of most of the twinned reflections.

Data sets were collected at 160 K, well above the structural and magnetic phase transition and at 6 K in the antiferromagnetic long-range ordered phase. Different scan types were used for detecting nuclear and magnetic reflections. In the case of nuclear reflections, ω - 2θ bisecting scans were performed, such that the Bragg peak is always centred in the middle of the area detector by moving the detector on the 2θ circle simultaneously with ω . This scan type compensates for the mosaic spread of the monochromator, which leads to a small spread of incident neutron wavelength. On the other hand the magnetic reflections were collected by performing pure ω -scans (rocking curve). In this case the scanning path is described by a circle and provides the best angular resolution, especially in the low 2θ region, where the magnetic signal is strongest pronounced.

5.3.5. Experimental results

The triarc sample measured on SXD and E4 turned out to consist of multiple grains. For this reason, it was not possible to extract an accurate list of integrated Bragg intensities and thus no quantitative analysis of the data could be performed. However, both measurements gave some qualitative results, which helped to draw conclusions about the magnetic structure of CaV_2O_4 and also to make decisions for the experimental set-up of follow up experiments using crystals with higher quality.

Figure 5.24 displays the $(-2, k, l)$ reciprocal section of CaV_2O_4 for two different temperatures as obtained with the SXD instrument. While the data shown in Fig. 5.24(a) were measured well below the magnetic ordering temperature ($T_N \approx 54 \text{ K}$), the data in

Fig. 5.24(b) have been measured above T_N in the paramagnetic phase. By performing one-dimensional cuts along selected reciprocal directions, it can be clearly seen, that additional Bragg peaks at positions $(h, k, l) + (0, \frac{1}{2}, \frac{1}{2})$ appear below T_N , corresponding to a magnetic propagation vector of $(\mathbf{k} = 0, \frac{1}{2}, \frac{1}{2})$. Further, from the detailed inspection of the whole reciprocal space map any kind of incommensurate ordering could be excluded and therefore the data confirm the results given in [145, 146].

Two additional intensity maps showing reciprocal lattice reflections at $T = 18$ K from other selected lattice planes are displayed in Fig. 5.25. In the left side (Fig. 5.25(a)) the $(3, k, l)$ reflections are shown and again additional peaks can be seen at half integer positions of k and l in the low Q region (see red circles). Moreover, the plot reveals additional spots which are neither located at an integer, nor at a half integer position, indicating that those reflection originate from small crystal grains. The graininess of the investigated sample becomes most obvious when looking at the $(h, k, 0)$ lattice reflections in Fig. 5.25(b). Near each main Bragg reflection, several additional spots are apparent, which can not be associated with the lattice of the main crystal. It is important to mention, that this ‘fan-out’ of reflections in this plane is not due to the monoclinic twinning, since this only occurs for reflections with $l \neq 0$.

In conclusion, the graininess of the investigated sample made a further treatment of the

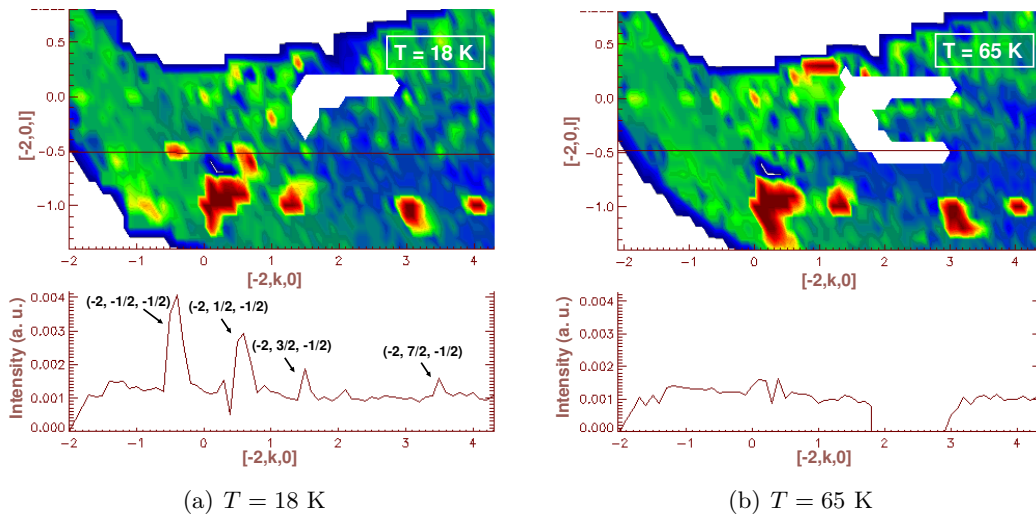


Figure 5.24.: Intensity map of selected reciprocal lattice planes from SXD data measured at (a) $T = 18$ K and (b) $T = 65$ K. Below the magnetic ordering temperature ($T_N(\text{triarc}) \approx 54$ K) additional peaks appear at $(h, k, l) + (0, \frac{1}{2}, \frac{1}{2})$ as can be clearly seen from the cuts along the $(-2, k, -0.5)$ direction, which are shown below. In the white regions of the intensity map no data were recorded.

data impossible, since no accurate intensity list could be extracted from them. In order to increase the quality of the triarc crystal for the follow up experiment on E4, it was annealed prior to the measurement (in flowing 5% H₂-He gas at 1200° for 96 hours). The annealing process caused an increase of T_N and T_s , indicating that the sample has become more homogenous. However, the multi grain character was also present in the data from E4 and from the two measured orientations, only the one with the $(0, k, l)$ plane as the scattering plane brought results which could be used for further analysis. In this orientation, 51 (12 unique) nuclear and 48 (21 unique) magnetic reflection were collected and as an example two of the measured magnetic reflections are illustrated in Fig. 5.26. In this Figure two ω (sample angle)-scans are shown, one at the nominal $(0, -\frac{1}{2}, \frac{1}{2})$ position and the second at the nominal $(0, \frac{1}{2}, \frac{1}{2})$ position. As expected, a distinct splitting of the reflections was observed, where the two split peaks can be assigned to different monoclinic twins, according to the twin law introduced in Eq. 5.20. Interestingly, the integrated intensities for the two twins at the same sample angle differ significantly. This difference cannot be explained in terms of unequal domain fractions, but is a result of their different magnetic structure factors. The observed magnetic and nuclear reflections within the $(0, k, l)$ -plane were fitted to Gaussian functions and corrected for a sloping background. If possible the twins were

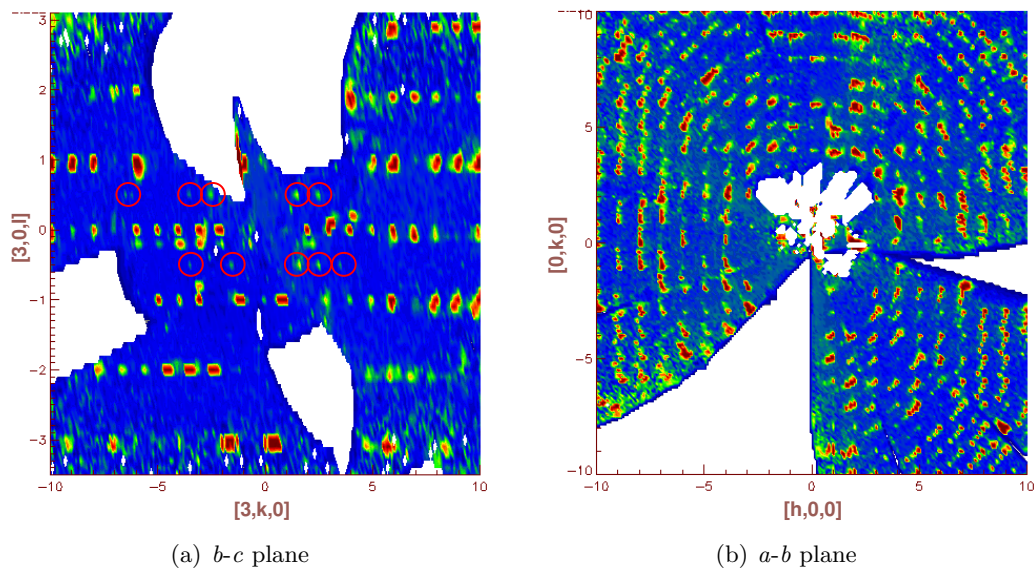


Figure 5.25.: Intensity map of selected reciprocal lattice planes from SXD data measured at $T = 18$ K. Below the magnetic ordering temperature additional peaks appear at $(h, k, l) + (0, \frac{1}{2}, \frac{1}{2})$. In (a) some of the magnetic Bragg peaks are highlighted by a red circle. In (b) the multi grain character of the crystal can be seen.

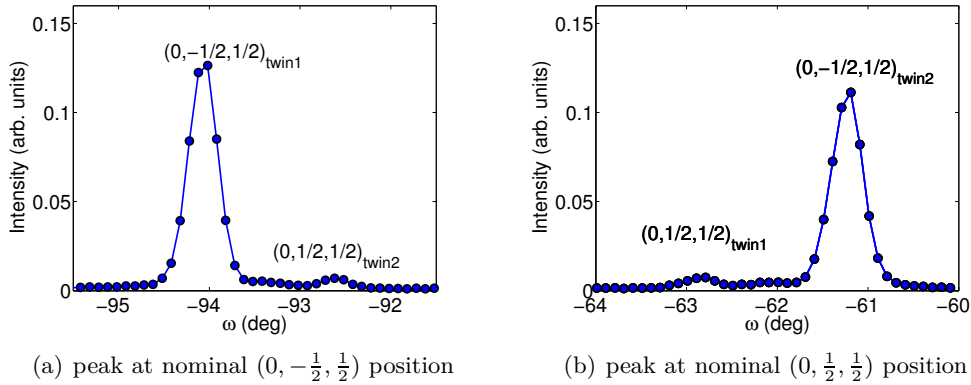


Figure 5.26.: Intensity vs. sample angle ω for two magnetic Bragg peaks observed at $T = 1.5$ K using the two circle diffractometer E4.

separated and a list containing the integrated intensities from each twin reflection was created. However, the small number of usable reflections was not sufficient to perform a meaningful refinement of the magnetic structure. However, some refinement tests performed with the program FULLPROF [122] using the least square method, indicated that they are canted, while the average spin direction is along the crystallographic \mathbf{b} -direction and that the ordered spin moment is reduced.

It was also proved that the peaks displayed in Fig. 5.26 are indeed magnetic reflections by following their temperature dependence. In Fig. 5.27(a) such a dependence is shown for the two twins at nominal $(0, \frac{1}{2}, \frac{1}{2})$ position and the disappearance of both peaks above the Néel temperature T_N is clearly visible. The integrated intensity for each twin as a function of temperature (Fig. 5.27(b)) shows a classical Brillouin function like behaviour with a continuous decrease of the order parameter, which becomes zero at the $T_N \approx 69$ K. In addition, this Figure shows, that both twin reflections are indeed described by the same order parameter, since they follow the same T -dependence and have the same transition temperature. This invalidates speculations, that one of the split reflections might only occur below a second magnetic phase transition, where a reorientation of the spins takes place¹¹.

In conclusion, while with the given E4 set-up it was in principle possible to resolve the peak splitting caused by the monoclinic distortion, in reality the multi grain structure of the triarc crystal only allowed a small number of integrated intensities to be extracted,

¹¹Zero field cooled and field cool susceptibility measurements of CaV_2O_4 crystals performed at Ames laboratory showed the onset of a small irreversibility below $T \sim 30$ K [119] and it was speculated that at this temperature another magnetic phase-transition might occur.

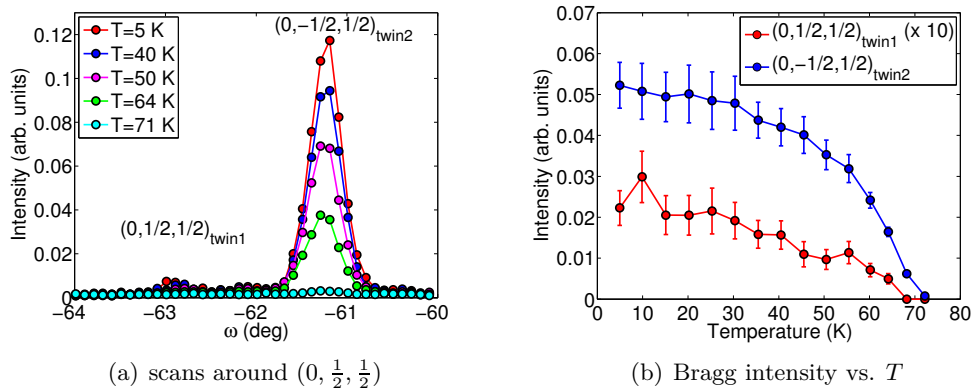


Figure 5.27.: Temperature dependence of twinned magnetic Bragg peaks at nominal $(0, \frac{1}{2}, \frac{1}{2})$ position.

such that a quantitative analysis of the data was not possible.

The final breakthrough in magnetic structure determination of CaV_2O_4 was achieved with the experiment at the four-circle diffractometer E5 at HZB using new high quality single crystals, which have been grown at Ames laboratory with the optical floating zone technique [119]. Those crystals were single grain and therefore allowed an accurate investigation of the twinned structure.

With the set-up described in Sec. 5.3.4 it was possible to collect a set of 170 (79 unique) nuclear and 132 (66 unique) magnetic reflections. To do so, ω (or $\omega - 2\theta$) scans were performed at each nominal Bragg position and for each scan step a two-dimensional intensity pattern was recorded. The number of total scan steps were chosen to be 52 for the magnetic and 36 for the nuclear reflections.

Despite the high quality of the crystal under investigation, the final extraction of integrated intensities from the scan data turned out to be rather challenging. This was, because the split structure of monoclinic twins did not allow conventional integration routines for multi-detector data (e.g. such as described in [153]) to be used. In fact, some of the peak integration programs do consider domain structures, but the split Bragg peaks have to be well separated in order to allow the precise determination of domain contributions. This was not the case for CaV_2O_4 , where most of the twin pairs partially overlap, especially those twin reflections in (hkl) with a large k component. For this reason, the correct intensities were extracted manually. A summation of all detector signal per scan step was performed and an one-dimensional data set containing the scattering intensity as a function of rotation angle ω was created. In those data sets the individual reflections had a Gaussian shape and thus their integrated intensity could

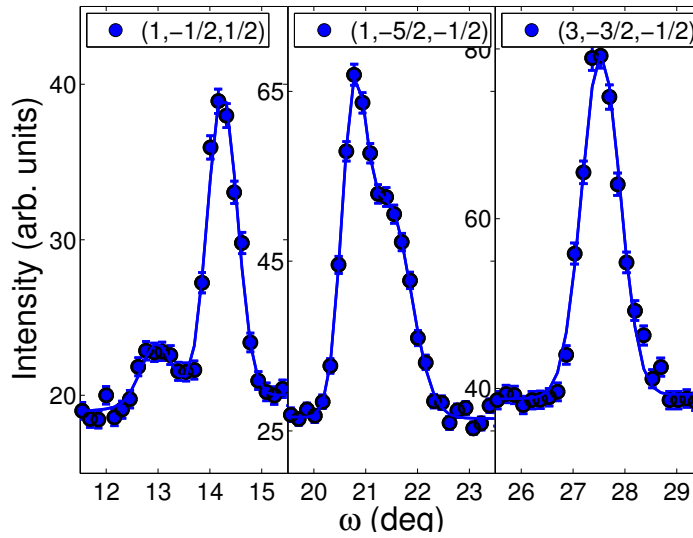


Figure 5.28.: Selected magnetic Bragg intensities as a function of sample angle ω . The different degree of twinning is displayed. If two peaks are resolved (left and middle figure), the twin at lower angles is at the nominal (hkl) position written in the legend, while the second twin is at position $(h-kl)$. In the very right Figure the twins overlap (almost) completely and only the sum of the integrated intensities could be extracted from the fit. The solid line is a fit the one or two Gaussian plus a slop background.

be easily extracted by fitting them to a Gaussian (area) function, where in addition a sloping background was subtracted. By applying this method to all nuclear and magnetic data, it was possible to separate the monoclinic domains with high accuracy and to create two separate lists of integrated intensities, one for each twin domain. Some selected (magnetic) Bragg reflections showing the different degrees of overlap are visualized in Fig. 5.28. While the reflections displayed in the left and middle part of the Figure could be easily separated, the right one is an example case of a pair of inseparable twin reflections. For such reflections a third intensity list was set-up, containing the summed integrated intensities of two completely overlapping reflections.

The final refinement of the magnetic structure was carried out using all three intensity lists, where the lists were further subdivided into those containing nuclear and those containing magnetic reflections. Prior to the actual magnetic structure refinement a nuclear refinement was performed in order to determine an overall scale factor and an extinction parameter. Those parameters were then fixed in the magnetic refinement, since they strongly correlate with the size of the magnetic moments and thus cannot be refined simultaneously with the magnetic structure. It has to be mentioned, that throughout

the nuclear refinement all other parameter (atomic positions and lattice parameter) have been fixed to the values determined from the combined neutron and synchrotron powder diffraction analysis (see Tables 5.4 and 5.6), since this method provided more accurate results concerning the nuclear structure.

Refinement procedure

The complete refinement of the magnetic structure was carried out using the `FULLPROF` software [122]. For integrated intensity data the software provides a refinement based on the least square method, where the sum of the square of the differences between the observed and calculated magnetic structure factors is minimized.

For the refinement of twinned structures `FULLPROF` provides two different methods, which in principle lead to the same solution, but give different information about the agreement between observed and calculated intensities. In the first method (single pattern method), a single input file is used, containing all integrated intensities together with a label according to their twin affiliation. In this case, `FULLPROF` tries to refine the selected parameter by minimizing the Bragg R -factor for the overall data, where the single scale factor is multiplied by the corresponding twin fraction.

In the second method (multi pattern method) several intensity lists can be used and weighted with a certain factor. `FULLPROF` then tries to find a solution by performing a simultaneous refinement and calculates an individual Bragg R -factor for each input file. This method in principle allows different scale factors and twin fractions for each given intensity list to be used. However, for the current case only one scale and one twin factor are used, since the given intensity files are all from the same neutron experiment. In both cases (single and multi pattern), the twin fraction appears as an additional free parameter and can also be refined.

Refinement strategies and results

The magnetic structure of CaV_2O_4 is completely described by the three spin components of each of the two symmetry inequivalent magnetic sites (more general: the mixing components of the basis functions) and by the underlying irreducible representation (see Sec. 5.3.3). Once the correct irreducible representation has been identified, a final simultaneous refinement of all six spin components can be performed. Another important requirement for a successful refinement is the assignment of good initial parameter values, which ideally should already lie in the vicinity of the final solution. If this is not the

Table 5.16.: Refinement results (single pattern method) assuming the collinear structures displayed in Fig. 5.29. The table lists the fit-quality factors, the magnetic moment values for both vanadium sites and the domain fractions for the two best IR.

Irreps.	R_F [%]	R_F^2 [%]	$R_F^2 \omega$ [%]	χ^2	μ_{V_1} (μ_B)	μ_{V_2} (μ_B)	Dom 1	Dom 2
$\Gamma_{\mathbf{k}2}$	16.2	20.7	23.6	27.1	0.91(2)	1.05(2)	0.46(1)	0.54(1)
$\Gamma_{\mathbf{k}3}$	13.0	15.6	18.3	16.3	1.04(1)	0.94(1)	0.459(9)	0.541(9)

case, it might occur, that the refinement either does not converge, or that it leads to a solution, which lies in a local minimum.

In the case of CaV_2O_4 , suitable starting parameter are given by the solutions derived from neutron powder diffraction data [145, 146]. Two possible magnetic models were suggested, which could not be distinguished from the powder data and it therefore stands to reason to investigate how these models agree with the new single crystal neutron diffraction data. Although the two models were derived on the basis of the orthorhombic space group $Pnam$, they coincide with the irreducible representations $\Gamma_{\mathbf{k}2}$ and $\Gamma_{\mathbf{k}3}$ derived within the actual monoclinic setting (see Sec. 5.3.3). Both models are depicted in Fig. 5.29. They represent collinear structures with the spins pointing along the crystallographic b -direction. To check those models, the refinement has been set up such, that the spins were constrained to point along the b -direction, while the size of the two individual magnetic moments and the twin fraction were allowed to vary. The results from the single pattern refinement are tabulated in Tab. 5.16. Both models provide a good fit of the data, where the one corresponding to IR $\Gamma_{\mathbf{k}3}$ leads to a slightly better result. As expected from the particular character of the twinning, both domains have almost the same fraction, indicating that the strong intensity difference between twins is not the result of a strong domain imbalance. Moreover, the moment size is strongly reduced for both magnetic sites and is in good agreement with the results from powder diffraction ($\mu = 1.06(6)\mu_B$ [146]). However, a close inspection reveals that both models systematically fail to assign a non-zero intensity to the small contributions, such as the $(0, \frac{1}{2}, \frac{1}{2})_{\text{twin}2}$ in Fig. 5.26(a). Therefore, in the next step of the refinement, the moment direction was no longer constrained and thus canted solutions were also allowed. With this approach, a much better agreement with the data was found. The canted solutions for IR $\Gamma_{\mathbf{k}2}$ and $\Gamma_{\mathbf{k}3}$ are listed in Tab. 5.17. While the size of the magnetic moment, as well as the twin fraction remained almost unchanged with respect to the collinear models, a significant canting out of the b -direction could be observed. Further it can be seen, that the solution corresponding to $\Gamma_{\mathbf{k}3}$ provides appreciably better agreement factors, than the $\Gamma_{\mathbf{k}2}$ solution.

Figure 5.30 compares the observed and calculated intensities for the best collinear and

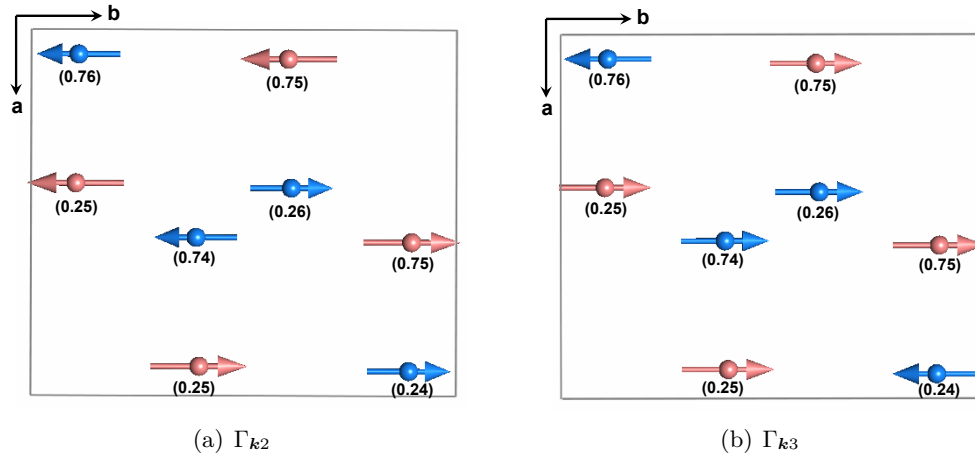


Figure 5.29.: Collinear magnetic structures of CaV_2O_4 in moderate agreement with the data. The projection on the a - b -plane is shown and the c -component is given in brackets.

Table 5.17.: Canted solutions for IR $\Gamma_{\mathbf{k}2}$ and $\Gamma_{\mathbf{k}3}$. The table lists the fit-quality factors, the total and individual magnetic moment values and the canting angles for both vanadium sites, as well as the domain fractions.

$\Gamma_{\mathbf{k}2}$	R_F	R_F^2	$R_F^2\omega$	χ^2	μ (μ_B)	ϕ	Θ	Dom 1	Dom 2
V1	7.39	12.4	14.7	11.1	0.95(1)	83(1)	77(2)	0.469(7)	0.531(7)
	μ_a	μ_b	μ_c						
	0.11(2)	0.92(1)	0.22(4)						
$\Gamma_{\mathbf{k}3}$	R_F	R_F^2	$R_F^2\omega$	χ^2	μ (μ_B)	ϕ	Θ	Dom 1	Dom 2
V2	7.39	12.4	14.7	11.1	1.06(2)	244(2)	76(2)	0.469(7)	0.531(7)
	μ_a	μ_b	μ_c						
	-0.45(3)	-0.93(2)	0.25(3)						
$\Gamma_{\mathbf{k}3}$	R_F	R_F^2	$R_F^2\omega$	χ^2	μ (μ_B)	ϕ	Θ	Dom 1	Dom 2
V1	5.33	9.28	11.0	6.31	0.96(1)	76(1)	105(2)	0.467(6)	0.533(6)
	μ_a	μ_b	μ_c						
	0.22(2)	0.90(2)	-0.25(4)						
$\Gamma_{\mathbf{k}3}$	R_F	R_F^2	$R_F^2\omega$	χ^2	μ (μ_B)	ϕ	Θ	Dom 1	Dom 2
V2	5.33	9.28	11.0	6.31	1.01(1)	105(1)	80(2)	0.467(6)	0.533(6)
	μ_a	μ_b	μ_c						
	-0.26(1)	0.97(1)	0.18(3)						

canted model and shows that only the canted model predicts intensity for all measured peaks. The canting could not be observed in the powder experiment, since the resolution function of neutron diffractometers does not allow to resolve the peak splitting. For this reason the reflections with a small intensity contribution were summed with their more intense twins, which led to a significant loss of information. This issue also becomes visible, if one investigates the fit agreement in terms of the particular domain affiliation.

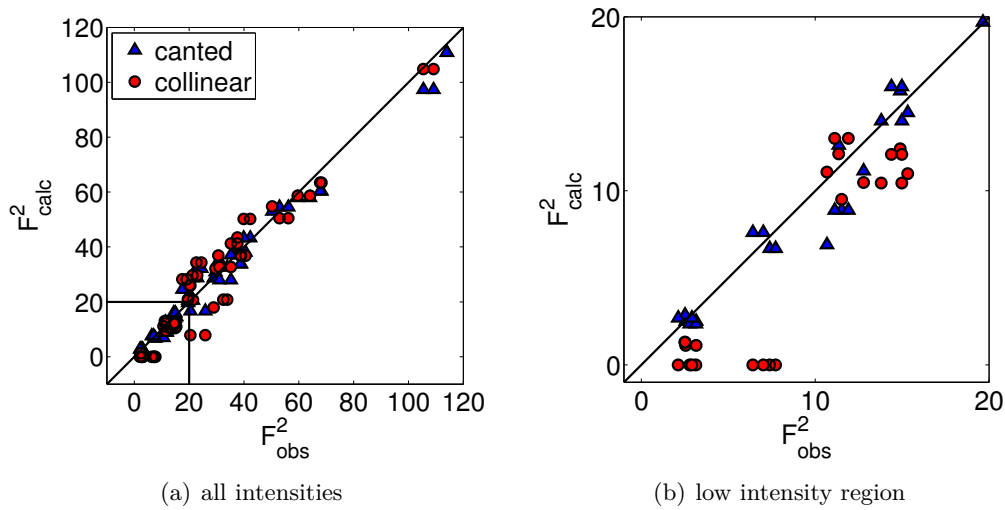


Figure 5.30.: Observed vs. calculated structure factor for the best collinear (red) and the best canted model (blue). The mismatch of the low intensity reflections for the collinear model are clearly visible.

Table 5.18.: Agreement factors for the best collinear and the best canted solution of IR Γ_{k3} .

Γ_{k3}	collinear		canted	
	R_F	$R_F^2\omega$	R_F	$R_F^2\omega$
I_{Dom1}	16.5	17.6	5.25	10.1
I_{Dom2}	16.6	18.7	4.90	8.11
I_{sum}	7.71	18.9	5.74	15.9

Therefore, the fit agreement factors of the multi pattern refinement are summarized in Tab. 5.18. In particular the refinement of the two lists containing the integrated intensities of the separated twin fractions leads to a significantly better quality when canting is introduced. In contrast, the list with the non-separable and therefore summed reflections provides already a fairly good agreement with the collinear model and only slightly lower R -factors are obtained with canting. In a sense, this list provides similar information, as a list obtained in a neutron powder measurement. It is therefore not surprising, that the data from the summed list can be fitted to the collinear model, as for the powder case the important information about the twin contribution is not given.

Before the final canted solution is discussed in detail, the existence of other solutions, which are in better agreement with the data and which were not possible to obtain with the given initial set-up parameter has to be ruled out. In particular, up to now, all investigations were based on preliminary results from powder diffraction experiments and

e.g. two of the four possible irreducible representations have not been considered so far. In order to do so, another more general method of magnetic structure determination was performed. This method is called simulated annealing (SA) and is an adaptation of the Metropolis algorithm, a Monte Carlo method to generate sample states of a thermodynamic system. It does not depend on initial parameters and is therefore ideal for solving complex and/or completely unknown structures. In detail, the SA method is based on the concept of minimizing a ‘cost’ function $E(\omega)$ with respect to a given configuration vector ω [154, 122]. This configuration contains all the parameters needed to describe the magnetic structure, such as polar angles of the spin and magnetic moment size or more general the set of mixing coefficients of the basis functions. The cost function itself can be simply chosen to be the crystallographic R -factor or some related function. Starting from a random configuration ω_{old} , a new configuration ω_{new} in the vicinity of the old one is chosen and this new configuration will be accepted with the probability $p = \min(1, \exp(-\frac{\Delta E}{T}))$, where $\Delta E = E(\omega_{\text{new}}) - E(\omega_{\text{old}})$ is the energy difference between the old and the new configuration. With each step of the process, the ‘temperature’ T decreases and thus also the probability that a worse configuration gets accepted becomes smaller. The iteration stops, if either convergence or the final number of defined steps have been reached.

In order to find possible solutions of the magnetic structure of CaV_2O_4 , a total number of 100 simulated annealing runs for each of the four irreducible representations were carried out and the best solution for each IR in terms of agreement factors (or ‘cost’-functions, respectively) is listed in Tab. 5.19. The results reveal, that the solutions obtained with IR’s Γ_{k2} and Γ_{k3} are in significantly better agreement with the data, than those obtained with IR’s Γ_{k1} and Γ_{k4} and therefore confirm the results from powder diffraction. Moreover, a detailed investigation of the obtained models for Γ_{k2} and Γ_{k3} revealed, that they are identical to the canted models derived with the collinear starting parameter. Hence, the single crystal neutron diffraction data clearly identified the canted model corresponding to IR Γ_{k3} as the one representing the magnetic structure of CaV_2O_4 .

The projections of the final canted model (Γ_{k3}) on the a - b and b - c plane are depicted in Fig. 5.31. The two inequivalent vanadium sites form two different magnetic substructures, with their spins canted by almost equal, but opposite amounts from the b -direction (see also Tab. 5.17). The total canting angle between the two substructures is $38(2)^\circ$, with the projections in the a - b and b - c planes of $29(1)^\circ$ and $25(2)^\circ$, respectively. However, the average spin direction remains along b , which is the reason why the dc-susceptibility measurements revealed b as the direction of the easy axis. The actual character of the spin substructures becomes clearer, when a connection between nearest and next nearest

Table 5.19.: Best simulated annealing results of the magnetic structure of CaV_2O_4 for each of the possible four irreducible representations ($\mathbf{k} = (0, \frac{1}{2}, \frac{1}{2})$)

Irrep	R_F	R_F^2	$R_{\omega F}^2$	χ^2
$\Gamma_{\mathbf{k}1}$	21.1	34.1	36.9	70.4
$\Gamma_{\mathbf{k}2}$	8.76	14.1	16.9	14.7
$\Gamma_{\mathbf{k}3}$	5.60	10.1	12.6	8.16
$\Gamma_{\mathbf{k}4}$	21.4	36.3	37.6	73.0

neighbour spins is drawn, as has been done in Fig. 5.32. This Figure clearly shows, that each of both substructures is a zigzag chain. Moreover, it can be seen that the spin canting only occurs between the chains of different sites, whereas within each chain the spins are arranged in a collinear fashion. In both chains, the neighbouring spins along the legs are aligned antiferromagnetically, while neighbouring spins along the zigzags are aligned in an alternating ferromagnetic-antiferromagnetic type fashion.

As mentioned earlier, the refined magnetic moment sizes per vanadium atom are strongly reduced from the expected value $\langle \mu \rangle = gS\mu_B = 2\mu_B$ (assuming that the orbital momentum is quenched), however, no significant difference was found between the moment values of different vanadium sites. The values are consistent, with neutron powder diffraction ($1.06(6)\mu_B$) as well as μSR ($1.19(14)\mu_B$) and NMR results ($1.02\text{-}1.59 \mu_B$) [146, 147, 136]. NMR was also able to observe the canting and reveals two antiferromagnetic substructures containing equal number of spins, canted about the b axis by a total canting angle of $19(1)^\circ$ and projections in the a - b and b - c plane of $18(1)^\circ$ and $6(1)^\circ$, respectively [136]. The canting angles in NMR are smaller than the ones obtain within this work. To test the model derived from NMR the single crystal neutron diffraction data were refitted using the NMR model by fixing the spin angles to the NMR values, while keeping the moment values free. The best result was obtained with a moment value $\langle \mu \rangle = 0.998(5)\mu_B$ and had a Bragg factor of $R = 8.3 \%$. Thus the NMR model gives an approximately 1.5 times worse agreement than the best model obtained by single crystal diffraction ($R = 5.33 \%$). Furthermore, when also fixing the ordered moment to the proposed NMR value of $\langle \mu \rangle = 1.3 \mu_B$, the Bragg factor is $R = 40 \%$, which gives a total mismatch. The reason for the discrepancy between the single crystal diffraction model and the NMR model remains unclear for the moment, however, it would be interesting to see, whether the results of this work would give a reasonable fit to the NMR data.

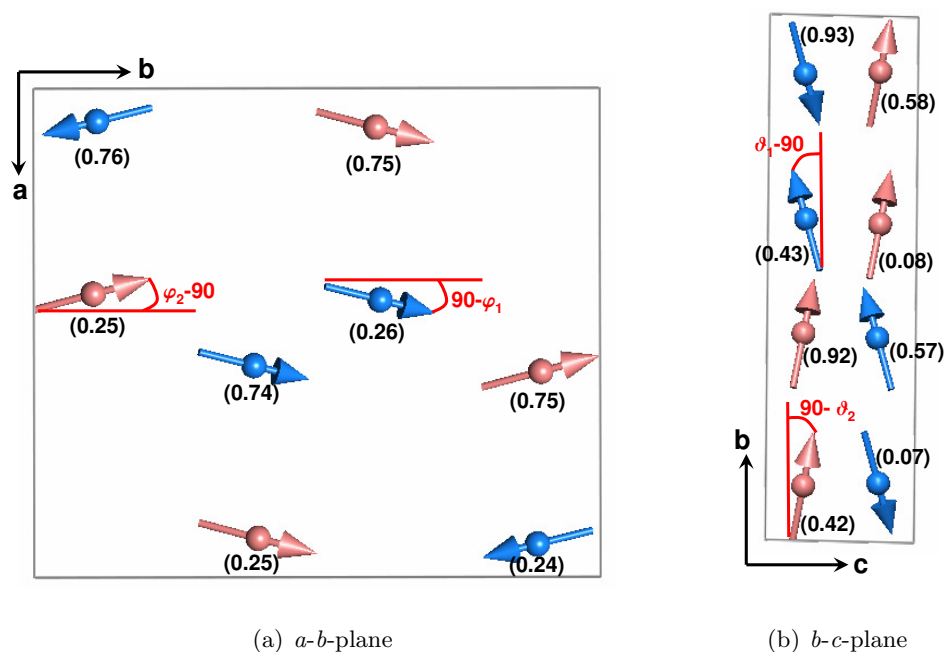


Figure 5.31.: Magnetic structure of CaV_2O_4 . The best canted solution (from Γ_{k3}) is displayed. The particular values for the angles ϕ and Θ can be found in Tab. 5.17.

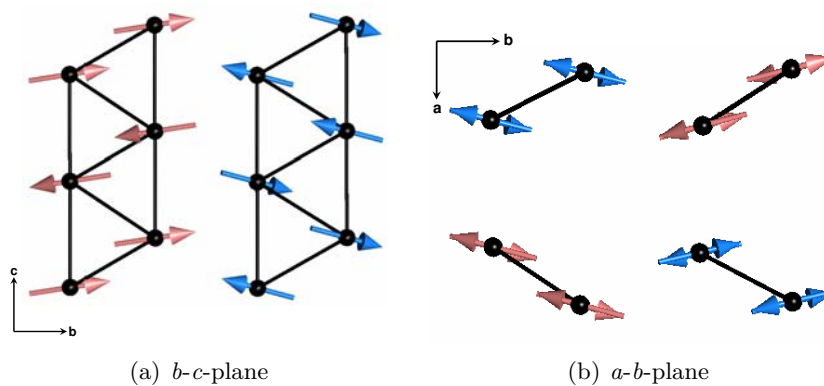


Figure 5.32.: Magnetic structure of CaV_2O_4 . The spin-projections onto the *b-c*- and the *a-b*-planes for the best canted solution (from Γ_{k3}) are displayed.

Other solutions

The Simulated Annealing runs have unambiguously identified the canted solution of IR Γ_{k3} (Tab. 5.17 and Figs. 5.31 and 5.32), as the one, that leads to the best agreement with the neutron single crystal diffraction data. While all solutions derived with irreducible representations other than Γ_{k3} gave significantly worse fits of the data, one other solution

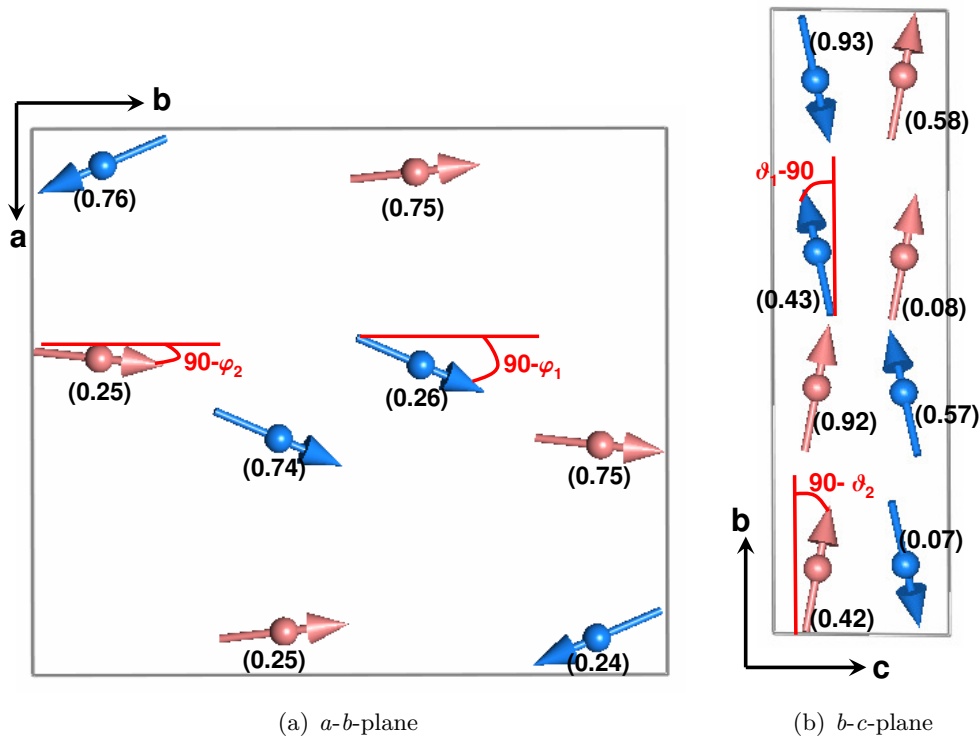


Figure 5.33.: Magnetic structure of CaV_2O_4 . The second best canted solution (from Γ_{k3}) is displayed. The particular values for the angles ϕ and Θ can be found in Tab. 5.20.

within Γ_{k3} was found, which had a R -value comparable to the one of the best model. This model is displayed in Fig. 5.33 and the particular canting angles and moment values are listed in Tab. 5.20. The only noticeable difference compared to the best solution is a flip of the spin component along the a -direction (μ_a) for the second vanadium site. Therefore, the canting out of the b -direction within the a - b plane appears in opposite direction to the one of the best solution. This causes a reduction of total canting angle between the two chains, being $28(2)^\circ$, with projections in the a - b plane being $17(1)^\circ$ and in the b - c plane being $22(2)^\circ$.

From the given diffraction data, it is difficult to distinguish between those both canted models and only a neutron diffraction experiment using spherical neutron polarimetry could shed light on this issue.

The best canted solution obtained with IR Γ_{k2} has an $\approx 30\%$ worse Bragg R -factor, than the best canted solution from IR Γ_{k3} . Although, this solution is not considered as a very possible magnetic structure of CaV_2O_4 , it is worse to mention, that the assignment of the different magnetic symmetry results in a systematic swap of the relative alignment

between spins along the zigzag direction. For example the zigzag pattern afm-fm-afm-fm within a chain of IR Γ_{k3} , has the arrangement fm-afm-fm-afm in the case of IR Γ_{k2} symmetry.

In other words, this states that the single crystal diffraction data clearly favour a certain relative spin order on the zigzags, a swap of the sign of both zigzag exchange couplings does not keep the fit quality invariant, but leads to a noticeable deterioration.

Table 5.20.: Refinement results for the second best canted model in IR Γ_{k3}

Γ_{k3}	R_F	R_F^2	$R_F^2\omega$	χ^2	μ (μ_B)	ϕ	Θ	Dom 1	Dom 2
V1	5.96	9.96	11.4	6.71	1.037(1)	67(1)	101(2)	0.468(6)	0.532(6)
	μ_a	μ_b	μ_c						
	0.40(2)	0.93(2)	-0.21(3)						
V2	5.96	9.96	11.4	6.71	0.96(1)	84(1)	79(2)	0.468(6)	0.532(6)
	μ_a	μ_b	μ_c						
	0.11(2)	0.94(1)	0.18(3)						

5.3.6. Discussion

The discussions subsequent to the previous two sections dealing with the nuclear structure and the magnetic susceptibility of CaV_2O_4 ground to a halt, because essential information concerning the spin structure were not available at that point. Now, with the knowledge of the precise magnetic structure of the antiferromagnetically ordered phase, the discussion can be continued. By comparing the various results from nuclear and magnetic structure determination, it is possible to draw conclusions about the particular arrangement of the vanadium d -orbitals and about the character and strength of the leading exchange interactions.

As mentioned earlier in the text, the two symmetrically inequivalent magnetic V^{3+} -ions ($S = 1$) of CaV_2O_4 are in octahedral symmetry, where neighbouring VO_6 octahedra of the same site are arranged in double chains and share their common edges. The octahedral crystal field splits the d -levels into a lower lying triply degenerate t_{2g} - and a higher energetic e_g -level, however, the degeneracy of these levels is partially lifted due to a distortion of the octahedra. In addition, CaV_2O_4 possesses an orbital degree of freedom, since its two V^{3+} d -electrons only partially occupy the three t_{2g} levels. Due to the particular edge sharing arrangement of the octahedra, lobes from t_{2g} orbitals of neighbouring nearest and next nearest neighbour ions point toward each other, such that the leading exchange interactions between spins are direct-exchange. In order to be able to state about the strengths and the character of the various magnetic interactions in CaV_2O_4 , it is essential to identify the filled and unfilled orbitals, since their contribution

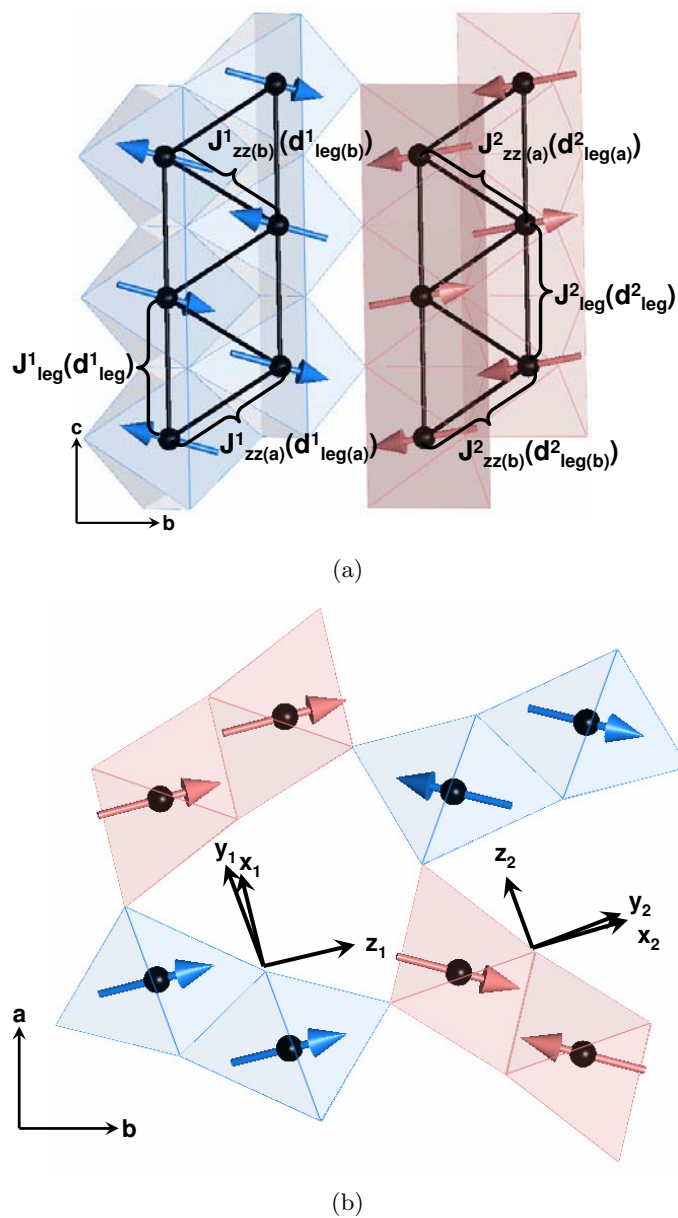


Figure 5.34.: Relative alignment of magnetic moments of CaV_2O_4 with respect to the VO_6 octahedra as obtained from the magnetic structure refinement. The spins and octahedra of the two different sites are coloured blue (chain 1) and pink (chain 2), respectively. (a) projection onto the b - c -plane, the intrachain exchange constants for the monoclinic phase are labelled. (b) projection onto the a - b plane, in addition the local octahedra axes are labelled, where z_n ($n = 1, 2$) corresponds to the direction of the tetragonal compression. Reprinted from [137]. Copyright (2009) by the American Physical Society.

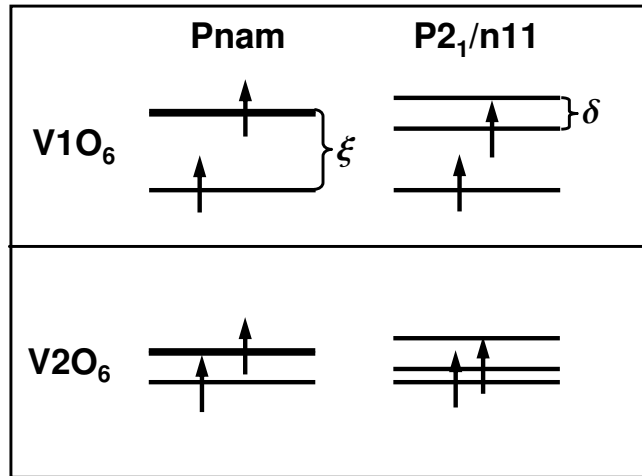


Figure 5.35.: Possible t_{2g} energy level for the two different vanadium sites of CaV_2O_4 . The size of the splitting is assumed to scale with the difference between the average V-O distances along the three octahedral axes.

to the coupling is significantly different (see Sec. 2.1.1).

For the beginning, inter-chain coupling will be neglected and thus there remain six possible exchange paths (three for each chain), whose strengths are dominated by the direct overlap and the particular occupancy of t_{2g} -orbitals. The corresponding exchange parameters are displayed in Fig. 5.34(a). Within each zigzag chain, one finds one coupling path between magnetic moments along the legs (J_{leg}^n) and two coupling paths along the chain's zigzag direction ($J_{\text{zz}(a)}^n$ and $J_{\text{zz}(b)}^n$), respectively. The superscript n denotes the two different chains. In the high temperature orthorhombic phase, the distances and environments for both zigzag paths are identical ($d_{\text{zz}(a)}^n = d_{\text{zz}(b)}^n$) and thus $J_{\text{zz}(a)}^n = J_{\text{zz}(b)}^n$. On the other hand, the monoclinic distortion of the low temperature phase lifts the frustrated zigzag arrangement, leading to slightly different distances $d_{\text{zz}(a)}^n$ and $d_{\text{zz}(b)}^n$. In this case, the two zigzag couplings can no longer be assumed to be equal. Further, for both chains and both phases the distances between neighbouring ions along the legs (d_{leg}^n) are slightly shorter, than the corresponding zigzag distances. However, the strength of the interactions cannot simply be deduced from distance arguments and the knowledge of the particular orbital arrangement is necessary.

Figure 5.35 shows a schematic energy level diagram of the t_{2g} -levels for the two vanadium sites. The diagram is based on the findings from nuclear structure determination and depicts the potential level splitting above and below the structural phase transition. It has to be mentioned, that the relative splitting of the energies is not true to scale and was just estimated from the difference of average $\langle V - O \rangle$ distances along the main

octahedral axes. If one neglects the off-centring of vanadium ions, then the two octahedra of the high- T phase ($Pnam$) are in pseudo-tetragonal¹² symmetry, with a tetragonal compression along the local z -axis of the octahedra (see also Figure 5.34(b)). This compression leads to a partial splitting of t_{2g} -levels into a lower lying d_{xy} -singlet and an higher energetic doublet (d_{yz} , d_{xz}) and is stronger pronounced for the first vanadium site V1 (cf. Tab. 5.9). Even though, the absolute size ξ of the tetragonal splitting is not known, it can be assumed that the two split levels are well separated and effects of state mixing play a minor role¹³. As a result of the distortion, one of the two V^{3+} -electrons occupies the energetically favourable d_{xy} -orbital, while the remaining one partially occupies both, the d_{yz} - and the d_{xz} -orbital. Considering the CaV_2O_4 topology, one finds that the fully occupied d_{xy} -orbitals point along the leg direction of the zigzag chain, giving rise to a strong antiferromagnetic coupling J_{leg}^n [126]. On the other hand, the remaining two orbitals being only half occupied, are responsible for the coupling along the zigzag directions. The corresponding interactions ($J_{\text{zz(a)}}^n$ and $J_{\text{zz(b)}}^n$) are identical in the orthorhombic phase ($J_{\text{zz(a)}}^n = J_{\text{zz(b)}}^n$), but due to the half filling, their strength is assumed to be significantly weaker than J_{leg}^n . For example, in the isovalent spinel compound CdV_2O_4 , which also shows a tetragonal distortion of VO_6 -octahedra, the estimated ratio between the coupling along the different t_{2g} -directions is $J(d_{xy})/J(d_{yz}) = J(d_{xy})/J(d_{xz}) \approx 1.7$ [127]. In the case of CaV_2O_4 this ratio is believed to be even larger, since the V-V distances along the chain's legs (d_{leg}^n) are slightly shorter than the ones along the zigzags (d_{zz}^n), resulting in a slightly stronger orbital overlap and therefore also in a slightly stronger exchange coupling (see Eq. 5.16). The predicted high temperature orbital states are illustrated in Fig. 5.36(a). The susceptibility analysis in Sec. 5.2 revealed, that one of the intrachain exchanges is much stronger than the other, but from the data it was not possible to distinguish which one. The particular orbital arrangement derived from the crystal structure clearly favours the scenario of a strong leg coupling, such that the system in the high- T phase can be seen as two weakly coupled Haldane chains. Since the zigzag coupling is supposed to be antiferromagnetic and equal along all rungs, the coupling is frustrated.

Before the focus will set onto the actual low temperature monoclinic structure, another important issue has to be discussed, which has been carelessly neglected so far. This is the relativistic spin-orbit coupling $\lambda(\mathbf{S} \cdot \mathbf{L})$, which describes the coupling of strength λ between the angular momenta of both, spin (\mathbf{S}) and orbital (\mathbf{L}). In many studies

¹²'Pseudo-tetragonal' only refers to the local symmetry of the octahedra and not to the full crystal structure. This assumption holds as long as off-centring effects are negligible.

¹³Optical and theoretical investigations on other t_{2g} -systems with a tetragonal distortion of octahedra revealed that the level splitting $\xi \sim 200$ meV [155, 156].

dealing with spin-orbit effects in transition metals, the spin-orbit coupling is neglected due to its relative weakness compared to other effects, such as magnetic interactions and crystal field effects. In addition, it is very often assumed, that due to crystal field effects, the orbital angular momentum is completely quenched ($\mathbf{L} = 0$). However, in materials with partially filled t_{2g} -orbitals, those assumptions are in general not valid any more. For example, the spin-orbit coupling in V^{3+} -ions has the strength of $\lambda \approx 20$ meV [157], which is the same order of magnitude as the magnetic exchange interactions in vanadates.

An octahedral crystal field provides a splitting between t_{2g} - and e_g -orbitals, which is of the order of ~ 2 eV. Due to this large energy gap, the mixing between both levels can be neglected and the orbital momentum \mathbf{L} can be written in terms of an effective or pseudo angular momentum \mathbf{L}' of length $L' = 1$, which operates in the t_{2g} -subspace [8]. The relation between the real and pseudo angular momentum is found to be $\mathbf{L} = -\alpha\mathbf{L}'$, where $\alpha \approx 1$ for well separated t_{2g} - e_g levels [157].

Turning back to the particular case of (orthorhombic) CaV_2O_4 , two scenarios concerning spin-orbit coupling are possible, depending on whether the coupling λ is weak or strong. In either cases, the tetragonal compression along the z -axis of the octahedra leads to the occupation of the d_{xy} -orbital by one of the two electrons. For the two remaining t_{2g} -orbitals, the spin-orbit interaction favours the formation of complex orbital states $d_{yz} \pm id_{xz}$. These mixed states are equally occupied by the second electron and their existence is accompanied by an easy axis anisotropy, which forces the spins to point along the local z -axis. The resulting orbital pattern remains similar to that presented in Fig. 5.36(a), with a strong antiferromagnetic exchange along the chain's legs and a weak, but frustrated antiferromagnetic exchange along the zigzags. While the former is again caused by the overlap of fully occupied d_{xy} -orbitals, the latter results from a partial occupation of the complex orbital states.

The difference of weak and strong spin orbit coupling manifests in the character of the particular ground states. While in the case of weak spin-orbit coupling \mathbf{L} and \mathbf{S} can be still assumed to be good quantum numbers, this is no longer true for the strong coupling limit, where an effective total angular momentum $\mathbf{J}' = \mathbf{L}' + \mathbf{S}$ of size $J' = 2$ comes into play. The resulting anisotropy is in both cases of single ion type being either proportional to S_z^2 or to $J_z'^2$. Therefore the spin chains consist either of staggered spin states of $S_z = \pm 1$ (small λ) or of such with staggered states of $J_z = \pm 2$ (large λ).

In particular, if strong spin-orbit coupling is apparent, the total angular momentum will be strongly reduced compared to the 'spin only' moment. This is because the orbital angular momentum prefers an antiparallel alignment with respect to that of the spin. The

reason for this is, that for a given site with spin value $S_z = \pm 1$, the orbital momentum becomes $L_z = -\alpha L'_z = \mp \alpha$. The total moment therefore takes the reduced value $(2 - \alpha)\mu_B$. This scenario has been predicted for the AV_2O_4 vanadium spinel compounds [157].

The analysis of the high temperature susceptibility data reveals small differences in the g -factor along different crystallographic directions. This indicates the presence of weak anisotropy, which indeed points to a situation where spin-orbit coupling is apparent. Therefore the formation of complex orbitals is very likely, even though it is difficult to state about the strength of the spin-orbit coupling.

The next step is to discuss the orbital pattern in the low temperature monoclinic phase. The induced monoclinic distortion lifts the geometrical frustration within and between the V^{3+} -chains and due to the formation of preferred coupling pathways, the system enters the antiferromagnetically ordered phase, with the ordering pattern as shown in Fig. 5.34.

The induced monoclinic distortion affects the octahedral environments of the two inequivalent vanadium sites in very different ways. Therefore, in contrast to the high- T phase, it can no longer be assumed that the corresponding orbital patterns are equal for both sites and a separate investigation of both zigzag chains is necessary. In the following it will be therefore referred to the chains as chain 1 and 2, where the notation is explained in Fig. 5.34. Among both VO_6 -subunits, the low temperature phase is characterized by the onset of an additional pseudo-orthorhombic distortion¹⁴. As a result, the average $\langle \text{V-O} \rangle$ bond distances along the three octahedral axes become all different and can be subdivided into bonds of short, medium and long type. As for the high- T case, the vanadium ions are somewhat off-centre, however, the corresponding effects on the crystal field are assumed to be weak and will therefore be neglected throughout the further discussion. Additionally, the distortion leads to a splitting of the previously degenerate d_{yz} - and d_{xz} -orbitals, resulting in a complete lifting of the t_{2g} -orbital degeneracy in the low- T phase. The situation is visualized for both octahedral sites in the right part of Fig. 5.35, where the strength of the orthorhombic distortion is denoted with δ . Since all t_{2g} -orbitals have different energies, the two electrons per V^{3+} -ion will occupy the two lowest energetic ones. The different size of the level splitting for the two VO_6 -subunits refers to their different degrees of octahedral distortion (cf. Tab. 5.9) and further also gives a first indication about their different character. The issue is now to identify the occupied orbitals and to derive the corresponding orbital pattern.

For the beginning the focus will be set on chains of type 1. By inspecting the average

¹⁴Again, ‘pseudo-orthorhombic’ refers to the local symmetry of the octahedra.

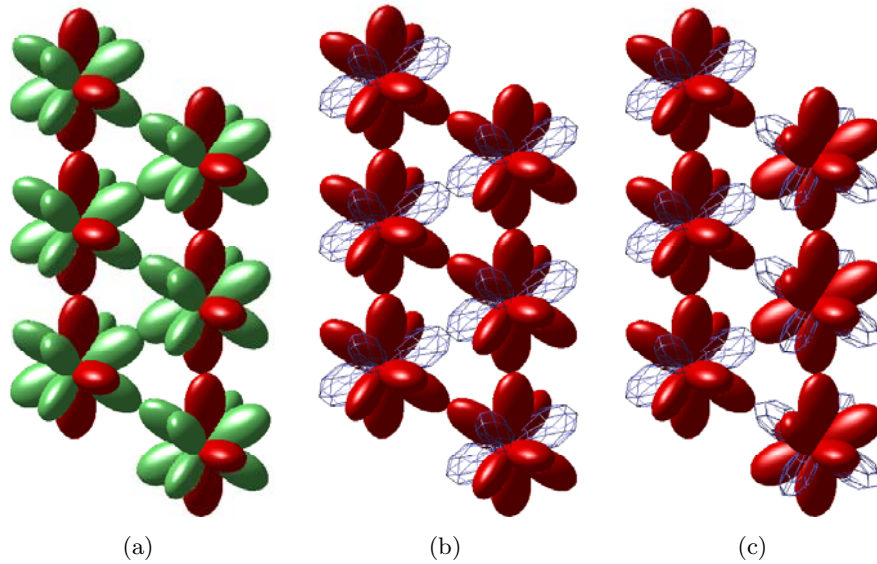


Figure 5.36.: The orientation and occupancy of the vanadium t_{2g} -orbitals in CaV_2O_4 . (a) displays the high temperature phase ($Pnam$), while (a), (b) and (c) also represent different possible scenarios for the low temperature monoclinic phase ($P2_1/11$). Colour code: red - fully occupied by one electron, green - partially occupied by one electron, blue (skeleton) - empty. Reprinted from [137]. Copyright (2009) by the American Physical Society.

$\langle\text{V-O}\rangle$ -bonds along the three different axis of the V1O_6 octahedra, one finds, that the main distortion still remains the tetragonal compression along the local z_1 -axis. This axis almost coincides with the crystallographic b axis, with the included angle being $\angle(b, z_1) \approx 10^\circ$. More interestingly, the spin canting out of the b -direction in the anti-ferromagnetically ordered phase seems to follow exactly the octahedral z_1 -axis (see Fig. 5.34(b)). This signifies that single ion anisotropy, caused by spin-orbit coupling, plays an important role for stabilizing the magnetic structure of CaV_2O_4 ¹⁵. For what concerns the particular arrangement of the t_{2g} -orbitals, different scenarios are possible, depending whether the additional orthorhombic distortion is strong or weak and on the size of the spin-orbit coupling. In any case, the strong tetragonal distortion guarantees, that the d_{xy} -orbital is lowest in energy and therefore always fully occupied by one electron. If the orthorhombic distortion is sufficiently strong, the remaining d_{yz} - and d_{xz} -orbitals are well separated in energy and the second electron always occupies that orbital which is lower in energy. In this case, there exist two exchange paths, which provide strong antiferromagnetic coupling due to the overlap of fully occupied orbitals (ferro orbital

¹⁵Note, that the second best canted solution (Fig. 5.33) shows the same canting of chain-1 spins as the best solution, which is discussed here. This means, that from the point of view of magnetic structure determination, there is no doubt about the relative spin canting for chain 1.

order). One of these paths runs along the chain's legs, while the second one is along one of the zigzag rungs. On the other hand, the coupling along the second zigzag rung is very weak, since the orbitals, which point along that direction are all empty. Such an arrangement where every second interaction along the zigzags is strong, combined with a strong leg exchange, is a spin-1 ladder. The corresponding orbital pattern is depicted in Figure 5.36(b). The obtained magnetic structure is in agreement with this proposed scenario. As can be seen from Fig. 5.34(a), neighbouring spins along the legs, as well as along half of the zigzags are aligned antiparallel, indicating that the corresponding exchange interactions J_{leg}^1 and $J_{zz(a)}^1$ are antiferromagnetic. If the remaining interaction $J_{zz(b)}^1$ is weak, the spins along the second zigzag direction are forced to point parallel to each other, since their relative orientation is dominated by the strong antiferromagnetic exchange with the other neighbours. This is indeed the case.

From the simple inspection of intra-octahedral bond distances it is difficult to state, whether the second occupied orbital is the d_{yz} - or d_{xz} -one. If only the $\langle\text{V-O}\rangle$ average distances along the octahedral axis would matter, one could assume that the second occupied orbital corresponds to the bonds of medium length (cf. Tab. 5.9). In the local reference frame of the octhedra this would be the one along the x_1 -axis and therefore the second occupied orbital would be the d_{yz} -orbital. However, this does not agree with the results from the magnetic structure refinement, which state a parallel spin alignment for the corresponding spin path and thus a weak exchange interaction. In any case, due to the strong octahedral distortion and the additional off-centring of the vanadium ions, more sophisticated methods, such as band structure calculations using density functional theory are needed to clarify this issue.

Another scenario was proposed by Chern *et al.* [158] for the case of a weak orthorhombic octahedral distortion ($\delta \ll \xi$). If so, the system could gain more energy (compared to the spin ladder formation) from a staggered arrangement of d_{yz} - and d_{xz} -orbitals, since in this case all zigzag bonds could take advantage of an antiferro orbital order. This is depicted in Fig. 5.36(c). The antiferro orbital arrangement leads to a weak ferromagnetic exchange along both of the zigzags ($J_{zz(a)}^1 \approx J_{zz(b)}^1 < 0$) and due to the additional strong antiferromagnetic leg exchange (J_{leg}^1), the system remains frustrated. This orbital configuration is also in agreement with the obtained magnetic structure of CaV_2O_4 . In contrast to the spin ladder solution, the system in this case can be viewed as two weakly (ferromagnetically) coupled Haldane chains.

The spin arrangement of type 1 chains suggests the existence of single ion anisotropy, which results from spin-orbit coupling. If this coupling (λ) is sufficiently strong, there is another possible orbital configuration. This configuration would be similar to the one

suggested for the high- T phase, which is displayed in Fig. 5.36(a). In this case, the weak orthorhombic octahedral distortion is not sufficient to split the d_{yz} and d_{xz} orbitals and therefore the formation of complex orbitals ($d_{yz} \pm id_{xz}$) is preferred. The result would be again a formation of weakly coupled Haldane chains, but with the coupling between them being antiferromagnetic and frustrated. Further, as discussed earlier, strong SO coupling leads to a significant reduction of the magnetic moment per V^{3+} -site. This has been indeed observed for CaV_2O_4 , being $\approx 1.0 \mu_B$ (compared to $2.0 \mu_B$ for free V^{3+} -ions).

What is missing, is the discussion about chains of type 2, which consist of V_2O_6 -octahedra. As can be seen from Tab. 5.9, the octahedral distortion is generally less pronounced for this chain type. In addition the nuclear structure data reveal, that the main octahedral distortion in the monoclinic phase is an elongation of the octahedra along its local y_2 -axis. This issue is also sketched in Fig. 5.35, where the corresponding energy level diagram is displayed. Due to the relative elongation, the d_{xz} -orbital is lifted up in energy, while the remaining two orbitals (d_{xy} and d_{yz}) are lower in energy and therefore they are both always occupied by one electron.

Further, the magnetic structure below T_N reveals, that the direction of spins within the second chain is almost orthogonal to the tetragonal z_2 -axis of V_2O_6 octahedra ($\angle(b, z_2) \approx 75^\circ$), as can be seen from Fig. 5.34. This means, that the corresponding single ion anisotropy is small and an additional easy plane anisotropy might be apparent.

Since the general strength of the octahedral distortion is not known, chain 2 could in principle provide the same three orbital pattern as proposed for chain 1. However, the particular type of octahedral distortion, together with the possible easy-plane anisotropy suggests that chains of type 2 can be seen as spin-1 ladders [158].

5.3.7. Conclusions

The magnetic structure of the antiferromagnetically ordered phase of CaV_2O_4 has been determined by means of single crystal neutron diffraction. The key results are a relative spin canting between spins of neighbouring V^{3+} zigzag chains (while the spin arrangement within each chain is collinear) and a strongly reduced magnetic moment. Along the zigzag rungs of the chain the spins are arranged in an ‘up-up-down-down’-fashion. By taking also into account the results from nuclear structure refinement and dc-susceptibility measurements, it was possible to interpret the magnetic structure in terms of particular t_{2g} -orbital arrangements. It was concluded that the low temperature monoclinic phase can be explained by three different orbital models, which are all in

agreement with the observed magnetic structure (see Fig. 5.36). Which of those models actually represents the true physics of CaV_2O_4 depends on the relative strengths of octahedral distortion (and thus the size of the t_{2g} -level splitting), as well as on the strength of spin-orbit coupling. Since no quantitative statements can be given about the strength of the t_{2g} -level splitting, it is hard to clearly identify the correct model. However, the magnetic excitation spectra for all three proposed models are very different [159] and thus an inelastic neutron scattering experiment can help to differ between them. This is the topic of the next chapter.

6. Magnetic excitations in CaV_2O_4

In this chapter the magnetic excitation spectrum of CaV_2O_4 in the antiferromagnetically long range ordered phase will be discussed. Various inelastic neutron scattering experiments have been performed in order to investigate the spin wave dispersions and spin-spin correlation functions within and between the CaV_2O_4 zigzag chains. The experiments reveal that the material is indeed a low dimensional magnet, as has been suggested by the neutron diffraction and magnetization measurements presented in the previous chapter. By comparing the experimental results to a Heisenberg model for localized spins and applying linear spin wave theory to it, the leading exchange interactions could be determined. Further the systems anisotropy could be probed, since it manifests in the experimental data as an energy gap that separates the magnetic ground state from the spin wave excitation spectra.

The experimental findings enable a detailed discussion about the various ordering scenarios of the V^{3+} t_{2g} -orbitals that have been proposed on the basis of the nuclear and magnetic structure refinement and by theoretical studies [158]. Additionally, possible signatures of low-dimensionality that persist in the long range ordered phase will be investigated.

6.1. Introduction

Considering the fact that the magnetic structure of CaV_2O_4 has been the subject of intensive studies for more than 40 years [145, 149, 136, 147, 89], surprisingly less is known about the spin dynamics in this material. For what concerns this issue, the articles published so far have mostly concentrated on the question whether the magnetic excitations are gapped or gapless. In an earlier work by Kikuchi *et al.*, powder samples of CaV_2O_4 have been investigated by means of dc-susceptibility and ^{51}V -NMR measurements [135, 160]. No long range order was found down to lowest temperatures and the authors proposed the existence of a novel gapless chiral phase. However, the fact that the existence of magnetic long range order in CaV_2O_4 was confirmed by several authors [146, 136, 119, 89, 147, 161], raised some doubts about the quality of the samples

measured by Kikuchi and coworkers. In fact, Sakurai *et al.* have studied the electronic properties of $\text{Ca}_{1-x}\text{Na}_x\text{V}_2\text{O}_4$ for $0 \leq x \leq 1$ and found that the antiferromagnetically ordered phase is only stable in the vicinity of $x = 0$. It is therefore quite likely that the presence of impurities has led to the absence of long range order in [135, 160].

More recently NMR measurements on CaV_2O_4 single crystals revealed a peculiar temperature behaviour of the vanadium ordered moments. This was interpreted in terms of single ion anisotropy causing an energy gap in the excitation spectrum [136]. By using a simple single chain spin wave model, a gap size of $\Delta \approx 5.5 - 8.4$ meV was estimated. The complex interplay of lattice, spin and orbital degrees of freedom in CaV_2O_4 has been investigated theoretically by Chern *et al.* using an effective super-exchange model [158]. It was shown that depending on the strength of spin-orbit coupling and the degree of octahedral distortion various orbital ordering patterns can appear along the zigzag chains of CaV_2O_4 . All theoretically proposed scenarios are in agreement with the nuclear and magnetic structure discussed in Chapter 5, however, based on the structural data it is not possible to identify an *unique* orbital pattern. Since magnetic interactions are strongly affected by the particular overlap and occupation of neighbouring t_{2g} -orbitals, an in-depth study of magnetic exchange interactions by means of inelastic neutron scattering will shed light on the issue of orbital ordering.

6.2. Experimental details

Inelastic neutron scattering experiments have been performed on the time-of-flight spectrometer MAPS at ISIS, UK and on the triple axes spectrometers V2 at Helmholtz-Zentrum Berlin and IN20 at ILL, France. In the following subsections, the particular experimental details will be discussed.

6.2.1. MAPS experiment

For the measurements at the time-of-flight spectrometer MAPS at the ISIS spallation source, an array of five co-aligned single crystals of CaV_2O_4 ($m_{\text{total}} = 4.66$ g) has been prepared, with a mosaicity of $< 1.1^\circ$ (see Fig. 6.1(a)). The crystals were arranged such, that they covered the greatest possible area of the beam window, which helped to achieve the maximum neutron flux at the sample position and the maximum signal-to-background ratio. All crystals were grown at Ames laboratory, US, with the optical floating zone technique [119] and crystals from two different growths were used for the experiment. The samples were placed inside a helium filled aluminium container and positioned inside a closed cycle refrigerator. In order to map out the spin correlations

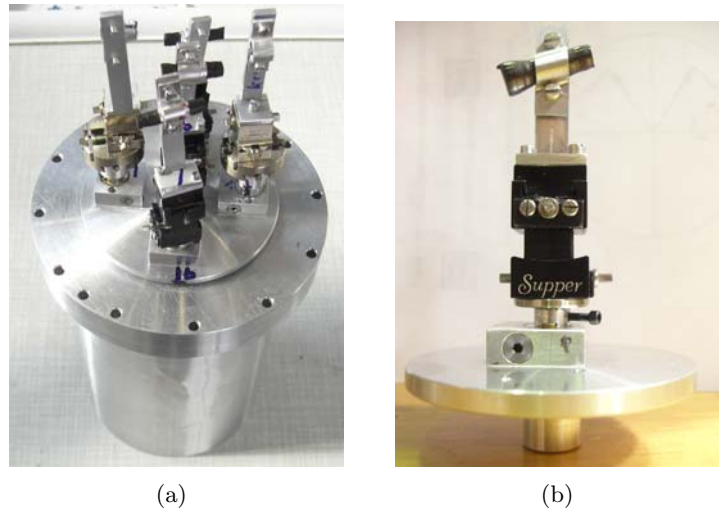


Figure 6.1.: (a) Five co-aligned crystals of CaV_2O_4 prepared for the experiment on MAPS. (b) Crystal of CaV_2O_4 mounted on a goniometer for the IN20 and V2 experiments.

along the chain direction (crystallographic c -direction), the b - c -plane was chosen as the horizontal scattering plane, where the b axis was set parallel and the a axis perpendicular to the direction of the incident beam (\mathbf{k}_i). This set-up allows a large range of \mathbf{Q} in the a - c -plane to be recorded, while contributions from b are projected into the a - c -plane. Data were collected at incident neutron energies $E_i = 70, 100, 140$ and 220 meV with the corresponding frequency of the Fermi chopper being 250, 300, 350 and 450 Hz, respectively (energy resolution at the elastic line: 2.9, 4.2, 5.9 and 9.1 meV). The measurements took place in the antiferromagnetically ordered phase at $T \approx 5$ K and in addition the temperature dependence of the excitation spectra was investigated by performing measurements up to $T = 160$ K.

The collected raw data were transformed from time-of-flight into energy-transfer using the `Homer` software and the conversion from detector angle to wavevector-transfer was done with the `mslice`-program. `Homer` also corrects for the efficiency of the detectors, which has been determined by a white beam vanadium measurement. Finally, the scattering intensity was also corrected for the $(\frac{k_f}{k_i})$ -factor of the scattering cross section (Eq. 3.17).

6.2.2. IN20 set-up

The thermal neutron triple axis spectrometer IN20 at ILL was used to study the spin wave excitations in CaV_2O_4 at distinct regions in reciprocal space. In particular the focus was set on the investigation of interchain interactions, since they could not be

studied in detail with the MAPS spectrometer.

IN20 was operated in two different configurations, which differed by the scattering sense of the analyser crystals. In the first configuration, the scattering sense was (SM=-, SS=+, SA=-), while in the second one it was (SM=-, SS=+, SA=+)¹. For both set-ups, the final momentum transfer was fixed to $k_f = 2.66278 \text{ \AA}^{-1}$. The incoming neutron beam was monochromated using a double focusing Si-monochromator. Between the sample and the analyser a pyrolytic graphite (PG) filter was positioned in order to remove higher order contributions of the neutron wave length. Finally, a PG analyser was used to select scattered neutrons with the energy and momentum of interest (for a detailed description of the IN20 spectrometer see Sec. 3.1.3).

In order to be able to investigate the spin dynamics along all three crystallographic axes, two single crystals of CaV_2O_4 with different orientations have been used (mass: 1.5 g and 1.0 g, respectively). Those crystals came from the same set of samples which have been utilized in the MAPS experiment. The first crystal was chosen to have the $(0, k, l)$ plane as the scattering plane, while the second crystal was oriented with (h, k, k) as the scattering plane. The crystals were mounted on small goniometers (see Fig. 6.1(b)), which were attached to a sample stick and inserted into a conventional orange cryostat. All measurements took place well below T_N in the antiferromagnetically ordered phase at $T = 1.5 \text{ K}$.

6.2.3. V2 experiment

The inelastic neutron scattering investigations of CaV_2O_4 were continued with an experiment at the cold neutron triple-axes spectrometer V2, FLEX at the Helmholtz-Zentrum Berlin. The aim of this experiment was to study the magnetic field and temperature dependence of the low energy spin excitations in CaV_2O_4 .

FLEX was operated in the (SM=-, SS=-, SA=+)-configuration with collimation setting 'guide-60'-open-open', meaning that the beam was only collimated after the monochromator ($\alpha = 60'$ denotes the angular beam divergence). Both, the monochromator and the analyser were made of pyrolytic graphite and had a variable curvature, which was vertical for the monochromator and horizontal for the analyser.

All measurements were performed at a fixed final wave vector $k_f = 1.55 \text{ \AA}^{-1}$ (and $k_f = 1.3 \text{ \AA}^{-1}$, respectively). For the measurements the same two samples with the same orientations as for the IN20 experiment were used (scattering planes $(0, k, l)$ and

¹The reason for the different configurations was technical in nature and had nothing to do with the actual experiment. However, the different set-ups provide quite different instrumental resolutions, which has to be considered for the data analysis.

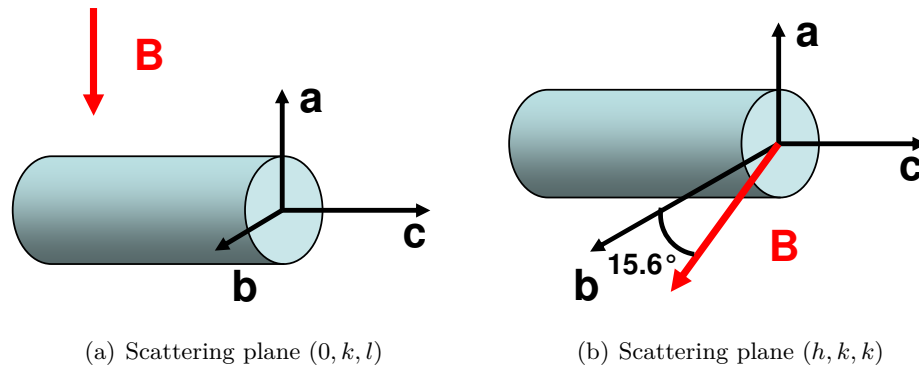


Figure 6.2.: Direction of the magnetic field with respect to the sample for the V2 experiment.

(h, k, k), respectively). The crystals were inserted into a cryomagnet providing vertical fields up to $B = 6.5$ T and temperatures down to $T = 1.5$ K. The two different crystal orientations made it possible to study the magnetic excitations in a field applied along two different directions. This is shown in Figure (6.2). While for the first orientation the field points along the crystallographic a direction, it points almost along b in the second case². Since the average spin direction in CaV_2O_4 is the crystallographic b direction (see previous chapter), the two orientations allow the spin excitations in a field to be probed both parallel and perpendicular to the spin direction.

6.3. Theoretical model, spin wave calculations

The magnetism in CaV_2O_4 arises from exchange interactions between the localized magnetic moments of V^{3+} . The particular nuclear structure of the material gives rise to strong direct exchange interactions within the vanadium zigzag chains, promoted by the direct overlap of vanadium t_{2g} -orbitals. On the other hand, the coupling between those chains is mediated via super-exchange paths involving O^{2-} ions and is weak. However, below the antiferromagnetic ordering temperature T_N , these interactions are sufficiently strong, such that the correlation length between the local moments becomes infinite and long range antiferromagnetic order establishes throughout the system. Such a system of localized exchanged coupled magnetic ions can be described by the (isotropic)

²Assuming orthorhombic setting for simplicity, the angle between the field and the b direction is given by: $\alpha = \arctan(\frac{b^*}{c^*}) = \arctan(\frac{c}{b}) = \arctan(\frac{3.0\text{\AA}}{10.68\text{\AA}}) \approx 15.6^\circ$. Therefore, the huge difference between the unit cell parameters is the reason, why the field points almost along the b direction for the second crystal orientation.

Heisenberg Hamiltonian:

$$\mathcal{H} = \sum_{ij} J_{ij} \mathbf{S}_i \mathbf{S}_j, \quad (6.1)$$

where J_{ij} is the exchange coupling between the spins \mathbf{S} at sites i and j .

For the particular case of CaV_2O_4 it was shown (Chapter 5), that the magnetic propagation vector is $\mathbf{k} = (0, \frac{1}{2}, \frac{1}{2})$, meaning that the magnetic unit cell is doubled along the crystallographic b and c directions. Since in each nuclear unit cell there are 2×4 vanadium ions (two different vanadium sites), the total magnetic unit cell consists of 32 magnetic ions. This is indicated in Fig. 6.3 by the solid lines. Another (primitive) unit cell, containing only 16 magnetic atoms can be found, if one chooses a different set of cell axes, as indicated by the dotted lines in the same figure. Since the number of magnetic sites in the (primitive) magnetic unit cell equals the number of spin wave modes for a given system, one can expect that there will be 16 spin wave branches in the case of CaV_2O_4 . For the actual spin wave calculations, however, it was chosen to use the conventional 32 sublattice unit cell, which retains all the symmetry elements of the nuclear unit cell. Later it will be shown, that the 32-sublattice spin wave model leads to 32 spin wave modes, but with only 16 of them having nonzero intensity and forming 8 doubly degenerate modes.

In order to enable an easier discussion in terms of exchange couplings with respect to the particular zigzag chains in CaV_2O_4 , the unit cell which served as a basis for all spin wave calculations, has been shifted by $\mathbf{r} = (0.1, 0.3, -1)$ with respect to the one shown in Fig. 6.3 and is depicted in Fig. 6.4(a). The actual magnetic structure is characterized by a small canting between the spins of different vanadium sites (see Sec. 5.3), this will be neglected in the following in order to simplify the calculations and instead a collinear spin arrangement will be assumed, with all the spins pointing along the crystallographic b direction. Taking into account nearest and next-nearest neighbour exchange interactions within and between different vanadium chains (see Figs. 6.4(b) and 6.4(c)), the magnetism in CaV_2O_4 can be modelled by the following Heisenberg Hamiltonian:

$$\mathcal{H} = \mathcal{H}_{\text{chain}_1} + \mathcal{H}_{\text{chain}_2} + \mathcal{H}_{\text{inter}} + \mathcal{H}_{\text{ani}}, \quad (6.2)$$

where the first two components ($\mathcal{H}_{\text{chain}_1}$ and $\mathcal{H}_{\text{chain}_2}$) contain all spin-spin interactions within the two zigzag-chains and $\mathcal{H}_{\text{inter}}$ describes all relevant inter-chain interactions. Lastly, \mathcal{H}_{ani} accounts for the fact, that the system possesses spin-orbit coupling, which leads to a non-negligible single ion anisotropy. According to Fig. 6.4, the first two

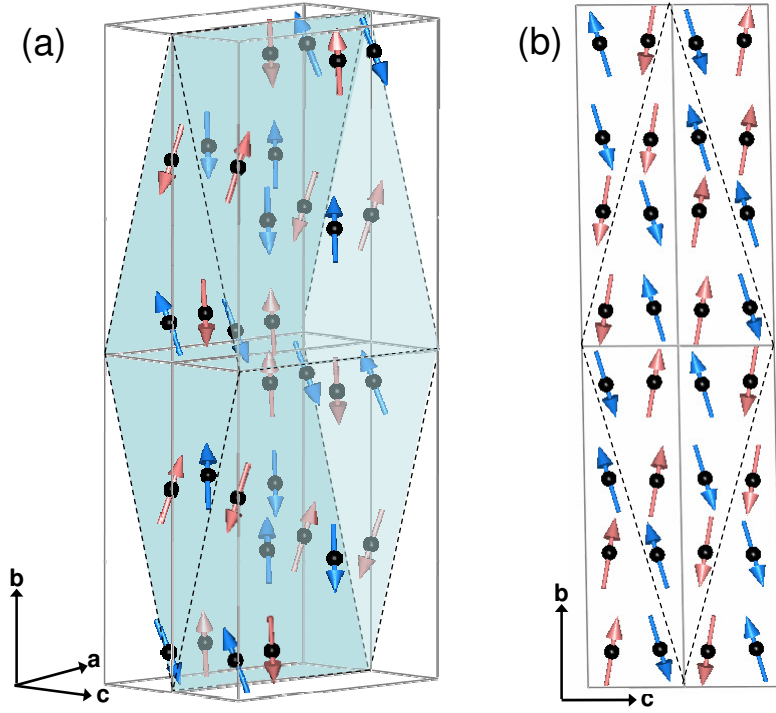


Figure 6.3.: Magnetic unit cell of CaV₂O₄ counting 32 magnetic ions. The primitive unit cell (16 ions) is shaded in turquoise.

components of Hamiltonian 6.2 can be decomposed into four parts each; with $i = 1, 2$ denoting the particular vanadium site of the corresponding zigzag chain:

$$\mathcal{H}_{\text{chain}_i} = \mathcal{H}_{\text{chain}_i}^{\alpha} + \mathcal{H}_{\text{chain}_i}^{\beta} + \mathcal{H}_{\text{chain}_i}^{\gamma} + \mathcal{H}_{\text{chain}_i}^{\delta}, \quad (6.3)$$

where $\alpha, \beta, \gamma, \delta$ represent the four chain components being present in the unit cell. For example, the first term of Eq. 6.3 for chain one (blue arrows) is given by:

$$\begin{aligned} \mathcal{H}_{\text{chain}_1}^{\alpha} = & J_{zz(a)}^1 \sum_{klm} \left(\mathbf{S}_{A_{klm}}^{\alpha} \mathbf{S}_{B_{klm}}^{\alpha} + \mathbf{S}_{C_{klm}}^{\alpha} \mathbf{S}_{D_{klm}}^{\alpha} \right) \\ & + J_{zz(b)}^1 \sum_{klm} \left(\mathbf{S}_{B_{klm}}^{\alpha} \mathbf{S}_{C_{klm}}^{\alpha} + \mathbf{S}_{D_{klm}}^{\alpha} \mathbf{S}_{A_{klm+1}}^{\alpha} \right) \\ & + J_{\text{leg}}^1 \sum_{klm} \left(\mathbf{S}_{A_{klm}}^{\alpha} \mathbf{S}_{C_{klm}}^{\alpha} + \mathbf{S}_{C_{klm}}^{\alpha} \mathbf{S}_{A_{klm+1}}^{\alpha} + \mathbf{S}_{B_{klm}}^{\alpha} \mathbf{S}_{D_{klm}}^{\alpha} \right. \\ & \left. + \mathbf{S}_{D_{klm}}^{\alpha} \mathbf{S}_{B_{klm+1}}^{\alpha} \right). \end{aligned} \quad (6.4)$$

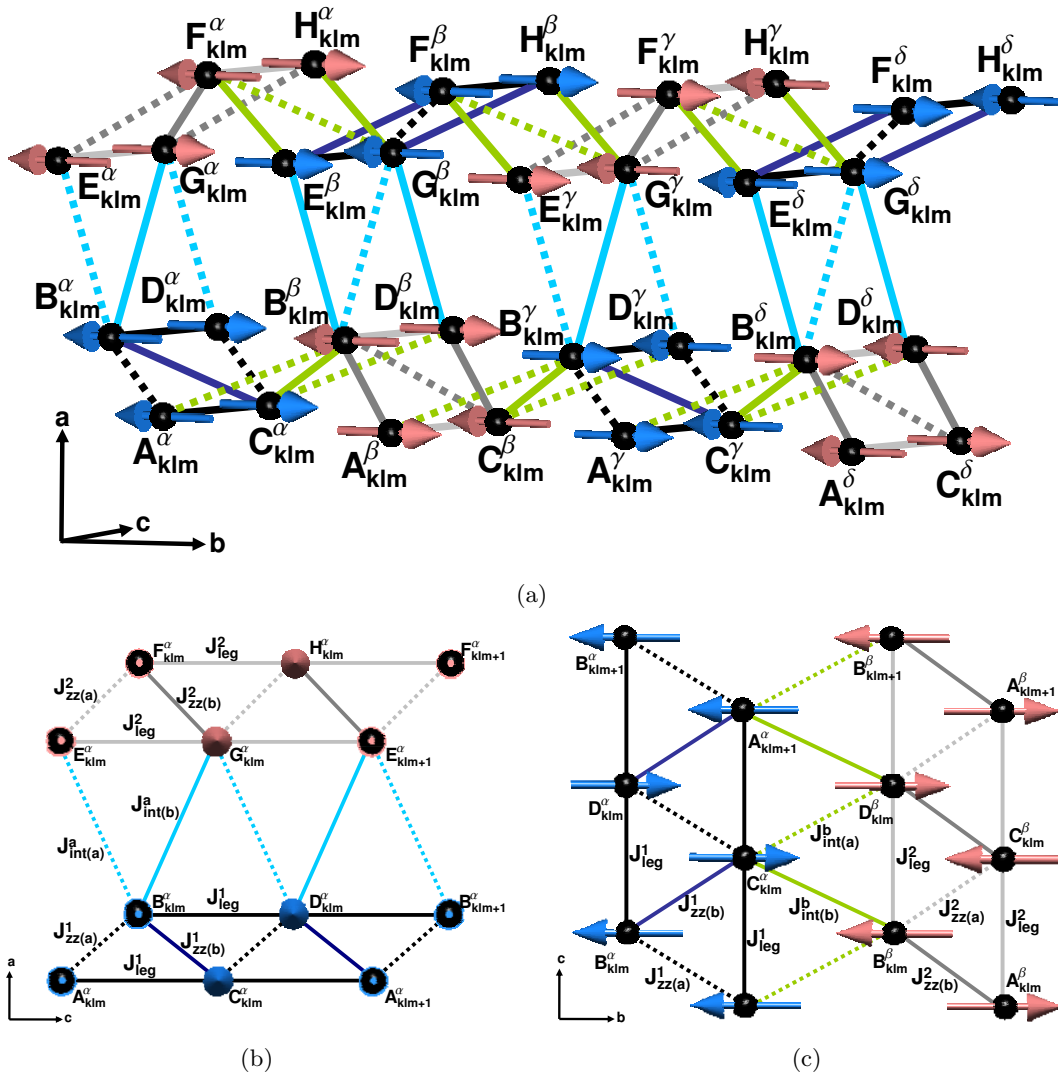


Figure 6.4.: (a) The full magnetic unit cell of CaV_2O_4 . The arrows indicate the direction of the magnetic moments for both vanadium sites. Spins belonging to site V1 are blue, while those belonging to V2 are pink. (b) Exchange coupling paths in the a - c -plane and (c) in the b - c -plane. Dotted lines indicate ferromagnetic coupling and solid lines indicate antiferromagnetic coupling. A, B, C, D, E, F, G and H are site indices.

In the above expression, $J_{zz(a)}^1, J_{zz(b)}^1$ and J_{leg}^1 denote the exchange interactions along the two zigzag rungs and along the legs of chain one, respectively. Further, the indices k, l, m label the particular magnetic unit cell and $(A_{klm}^\alpha, B_{klm}^\alpha, \dots)$ are the site indices. Similar expressions can be found for all the remaining spin interaction terms in Eq. 6.2 and a full list of them is given in Appendix C.2. Finally, the anisotropy term is given by:

$$\mathcal{H}_{\text{ani}} = - \sum_{i=1,2} D_i \sum_{klm} \sum_{j=1}^{16} (S_{jklm}^y)^2, \quad (6.5)$$

where D_i is the single ion anisotropy constant for spins of site i . The last sum in Eq. 6.5 runs over all 16 magnetic ions belonging to the same site within the unit cell and S_{jklm}^y is the y-component of the j th spin operator in the unit cell (klm) . Starting from Hamiltonian 6.2, linear spin wave theory was employed to evaluate the spin wave excitation spectrum of CaV_2O_4 . To do so, it is useful to introduce a set of (4×8) magnon creation and annihilation operators $\hat{\alpha}_{klm}, \hat{\beta}_{klm}, \hat{\gamma}_{klm}, \hat{\delta}_{klm}$, with the row vectors:

$$\hat{\alpha}_{klm}^\dagger = (a_\alpha^\dagger, b_\alpha^\dagger, c_\alpha, d_\alpha, e_\alpha^\dagger, f_\alpha^\dagger, g_\alpha, h_\alpha)_{klm} \quad (6.6)$$

$$\hat{\beta}_{klm}^\dagger = (a_\beta, b_\beta^\dagger, c_\beta^\dagger, d_\beta, e_\beta, f_\beta^\dagger, g_\beta^\dagger, h_\beta)_{klm} \quad (6.7)$$

$$\hat{\gamma}_{klm} = (a_\gamma, b_\gamma, c_\gamma^\dagger, d_\gamma^\dagger, e_\gamma, f_\gamma, g_\gamma^\dagger, h_\gamma^\dagger)_{klm} \quad (6.8)$$

$$\hat{\delta}_{klm}^\dagger = (a_\delta^\dagger, b_\delta, c_\delta, d_\delta^\dagger, e_\delta^\dagger, f_\delta, g_\delta, h_\delta^\dagger)_{klm} \quad (6.9)$$

By using Holstein-Primakoff transformation one can rewrite Eq. 6.2 in terms of the magnon operators, where e.g. for up-spins $S_{A_{klm}^\alpha}$ and down-spins $S_{B_{klm}^\gamma}$ one writes:

$$(S_{A_{klm}^\alpha}^+)^+ = \sqrt{2S} a_\alpha(klm); \quad (S_{B_{klm}^\gamma}^+)^+ = \sqrt{2S} b_\gamma^\dagger(klm) \quad (6.10)$$

$$(S_{A_{klm}^\alpha}^-)^- = \sqrt{2S} a_\alpha^\dagger(klm); \quad (S_{B_{klm}^\gamma}^-)^- = \sqrt{2S} b_\gamma(klm) \quad (6.11)$$

$$(S_{A_{klm}^\alpha}^y)^y = S - a_\alpha^\dagger(klm) a_\alpha(klm); \quad (S_{B_{klm}^\gamma}^y)^y = -(S - b_\gamma^\dagger(klm) b_\gamma(klm)). \quad (6.12)$$

In the next step, a Fourier transform to momentum space was performed, where for the sake of convenience, slightly different expressions have been introduced for magnon

operators resulting from up-spins and those resulting from down-spins, e.g.:

$$a_{\alpha(klm)} = \frac{1}{\sqrt{N}} \sum_{\mathbf{Q}} e^{i\mathbf{Q}\mathbf{R}_{klm}^{a\alpha}} a_{\mathbf{Q}}^{\alpha} \quad (6.13)$$

$$b_{\gamma(klm)} = \frac{1}{\sqrt{N}} \sum_{\mathbf{Q}} e^{-i\mathbf{Q}\mathbf{R}_{klm}^{b\gamma}} b_{\mathbf{Q}}^{\gamma}. \quad (6.14)$$

In the expression above, N is the number of lattice sites belonging to one sublattice and $\mathbf{R}_{klm}^{a\alpha}$ is the position vector of the magnetic moment $\mathbf{S}_{A_{klm}^{a\alpha}}$ of the (klm) 's unit cell.

By using the formalism described above, the Hamiltonian 6.2 can be rewritten in the following form:

$$\mathcal{H} = \sum_{\mathbf{Q}} (\hat{\alpha}^{\dagger}(\mathbf{Q}), \hat{\beta}^{\dagger}(\mathbf{Q}), \hat{\gamma}(\mathbf{Q}), \hat{\delta}(\mathbf{Q})) \times \begin{pmatrix} \mathbf{A}^1(\mathbf{Q}) & \mathbf{B}(\mathbf{Q}) & \mathbf{0} & \mathbf{D}^*(\mathbf{Q}) \\ \mathbf{B}^*(\mathbf{Q}) & \mathbf{A}^2(\mathbf{Q}) & \mathbf{D}(\mathbf{Q}) & \mathbf{0} \\ \mathbf{0} & \mathbf{D}^*(\mathbf{Q}) & \mathbf{A}^1(\mathbf{Q}) & \mathbf{B}(\mathbf{Q}) \\ \mathbf{D}(\mathbf{Q}) & \mathbf{0} & \mathbf{B}^*(\mathbf{Q}) & \mathbf{A}^2(\mathbf{Q}) \end{pmatrix} \begin{pmatrix} \hat{\alpha}(\mathbf{Q}) \\ \hat{\beta}(\mathbf{Q}) \\ \hat{\gamma}^{\dagger}(\mathbf{Q}) \\ \hat{\delta}^{\dagger}(\mathbf{Q}) \end{pmatrix}, \quad (6.15)$$

where $\mathbf{A}^1(\mathbf{Q})$, $\mathbf{A}^2(\mathbf{Q})$, $\mathbf{B}(\mathbf{Q})$ and $\mathbf{D}(\mathbf{Q})$ are 8×8 matrices, which depend on the particular geometry of the crystal lattice and on the particular spin arrangement. The individual elements of these matrices are given in Appendix (C.2). Further, $\mathbf{B}^*(\mathbf{Q})$ and $\mathbf{D}^*(\mathbf{Q})$ are the complex conjugate of $\mathbf{B}(\mathbf{Q})$ and $\mathbf{D}(\mathbf{Q})$.

Finally, the magnon-Hamiltonian matrix in Eq. 6.15 could be diagonalized following the theory presented in [162] and from this, the spin wave modes $\omega_N(\mathbf{Q})$ ($N = 16$ is the number of modes) and spin-spin correlation functions $S_{xx}(E, \mathbf{Q})$, $S_{zz}(E, \mathbf{Q})$ were calculated numerically (see also Sec. 2.3 and Appendix C). By comparing the calculations with the experimental data, it was possible to extract the relevant exchange interactions as well as the anisotropy parameters.

However, the data obtained with INS were not sufficient to fit all 12 free exchange coupling- and anisotropy-parameters of the 32 sublattice model simultaneously and instead the following strategy was employed in order to extract the most reasonable values. At first, a simplified model was used to investigate the dominant intra-chain interactions. In the framework of this model, the magnetic unit cell was assumed to consist of one type of zigzag chains only, with interchain coupling only along one direction (see Fig. C.1). This approach allowed the number of magnetic sites per unit cell to be reduced

down to four and the resulting four-sublattice Hamiltonian could be solved analytically giving rise to two doubly degenerate spin wave modes. The explicit derivation of those spin wave modes as well as the corresponding spin wave intensities is given in Appendix C.1. Although, the four-sublattice model oversimplifies the physics of the real system, it is very useful for estimating the size of the three intra-chain exchange constants J_{leg} , $J_{\text{zz(a)}}$ and $J_{\text{zz(b)}}$. These parameters (together with an anisotropy constant D) could be determined by fitting the experimentally observed spin wave dispersions along the chain direction using the analytical expression given in Eq. C.39.

Based on the findings from the simplified model, the full 32 sublattice model was used to find the most suitable sets of parameters, representing the full spin physics of CaV_2O_4 . Further, by comparing the single chain model to the full model, it was possible to check, which features in the CaV_2O_4 excitation spectrum can be exclusively attributed to the double chain nature of the system. In contrast to the simplified model, the full model also allowed a detailed investigation of the coupling perpendicular to the chain direction.

6.4. Experimental results and data analysis

The crystal structure of CaV_2O_4 suggests that strong magnetic interactions occur only along the direction of the zigzag-chains $(0, 0, l)$. For this reason, the orientation of the crystal for the MAPS experiment was chosen such, that the data obtained with the spectrometer were projected onto the $(h, 0, l)$ plane and the k dependence of the spin wave excitations was ignored. Further, due to the quasi-1D nature of the magnetic excitations, the measured data were also summed along the h direction, providing better counting statistics without leading to significant information loss. The spin wave dispersion projected onto the chain direction can be visualized in a 2D energy-wave vector colourmap, where the colour represents the differential neutron scattering cross section $\frac{k_i}{k_f} \left(\frac{d^2\sigma}{d\Omega dE_F} \right) (\mathbf{Q}, \omega)$. As an example, Fig. 6.5(a) shows a data set without background subtraction, which was obtained at $T = 5$ K with an incident neutron energy of $E_i = 100$ meV. The most obvious features are the two steep spin wave dispersion branches, which show a minimum at the magnetic zone centre ($L = \frac{1}{2}n$ r.l.u., $n = 0, \pm 1, \pm 2, \dots$) and which are separated from each other by an energy gap of ≈ 23 meV (taking the difference between the two dispersion minima). Most of the spectral weight is centred around the antiferromagnetic zone centre at ($L = \frac{1}{2}n$ r.l.u., $n = \pm 1, \pm 3, \dots$), while the scattering intensity decreases gradually towards the zone boundaries. The magnetic character of both features is underlined by the weakening of intensity at higher Q , which is due to the form factor of the magnetic V^{3+} -ions.

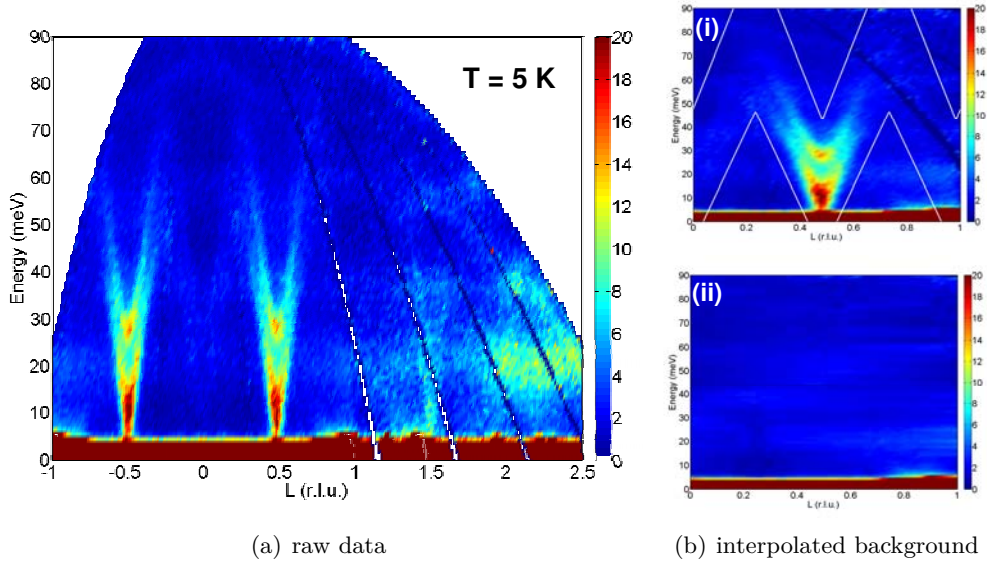


Figure 6.5.: Inelastic neutron scattering data of CaV_2O_4 measured with the MAPS spectrometer at $T = 5$ K with $E_i = 100$ meV. The energy-wavevector colourmap is displayed, where the colour represents the differential neutron scattering cross section. (a) The full untreated spectra is shown. In (b)(i) the symmetrized data in the low Q_L region are depicted, where the white lines indicate the regions which have been used for the background correction. (b)(ii) The pure background is displayed, obtained by interpolating the selected non magnetic regions over the whole (E, Q) -space.

Further, the strong signal around $E = 0$ meV arises from incoherent elastic scattering. Additionally, the spectra shows three almost dispersionless modes at $E \approx 20, 38$ and 60 meV. These modes can be attributed to phonons and (as it is typical for lattice vibrational modes) their intensity increases with increasing Q . Since the phonon modes do not disperse out of the nuclear Bragg peaks, they are probably optical in nature.

The fact, that the high Q part of the spectra is dominated by phonons, restricts the reliable range that can be considered for a quantitative analysis of the magnetic excitations to the region in Q_L close to the origin ($-1 \leq L \leq 1$ r.l.u.). By symmetry the spectrum is identical for $+Q_L$ and $-Q_L$ and it is therefore convenient to project the negative Q_L part onto the positive one and thus improve the counting statistics³. The resulting part of the spectra that was used for further analysis is displayed in Figure (6.5(b)(i)).

However, even for the remaining data, an accurate background correction was needed to enable a quantitative analysis of the spin wave dispersion. The background correction was done by ‘cutting out’ those regions from the data, which do not contain any mag-

³The symmetrization is also justified for the monoclinic phase. This is because the particular twin law for CaV_2O_4 gives an identical spectra for $+Q_L$ and $-Q_L$.

netic signal and then creating an overall background file by interpolating between these regions. In particular, there is no magnetic signal in a distinct triangular shaped region below the dispersion maximum of the lower spin wave mode (see lower white line in Fig. 6.5(b)(i)). Further, it was assumed, that also the triangular shaped region above the dispersion minimum of the upper spin wave branch contains no magnetic signal (upper white line in Fig. 6.5(b)(i)). Although, some magnetic spectral weight can appear at higher energies as a result of multi-magnon scattering, such processes are expected to be weak and will therefore be neglected for the moment. The interpolated background file for the $E_i = 100$ meV data is depicted in Fig. 6.5(b)(ii). Finally, this background was subtracted from the raw data, providing a data set which can be used for further investigations.

The final corrected data for measurements at $T = 5$ K with incident energies $E_i = 70$ and 100 meV are depicted in Figs. 6.6(a) and 6.6(b). In particular the high resolution data obtained with $E_i = 70$ meV provide a clear picture of the double spin wave structure of the material. Both spectra were used to extract the intra chain dispersion of CaV_2O_4 . While the high resolution $E_i = 70$ meV data allowed the fine structure of the two spin wave branches to be investigated in the low energy region, the data obtained with $E_i = 100$ meV enabled the investigation of the entire magnetic spectrum. It is further important to mention that additional measurements performed with higher incident neutron energies ($E_i = 140$ and 220 meV) revealed the absence of any magnetic signal above $E = 90$ meV.

The spin wave dispersion was extracted from the data by performing a large number of constant Q_L - as well as constant energy-cuts and determining the position of the observed peaks by fitting them to Gaussian line shapes. The former type of cuts gave more accurate information about the (almost flat) dispersion in the vicinity of the magnetic zone boundaries, while the latter cut type provided more precise results for the region around the zone centre, where the dispersion is very steep. Some typical cuts are presented in Figs. 6.6(c) and 6.6(d). For all spectra, a small offset in Q_L was detected, e.g. magnetic Bragg peaks were found to be positioned at $(\langle Q_h \rangle, \langle Q_k \rangle, 0.5 - Q_{\text{offset}})$, with $Q_{\text{offset}} = 0.017 \text{ \AA}^{-1}$. This slight shift in Q_L was considered in the data analysis. It is most probably due to a small misalignment of the crystal with respect to the main spectrometer axes.

The spectra reveals that the magnetic excitations are gapped, where the dispersion minimum for both branches is located at the centre of the magnetic Brillouin zone. A cut in energy with Q_L being fixed at the zone centre position shows two broad peaks centred at $E = 11.0(2)$ and $27.7(2)$ meV. The width of those two peaks is much broader than

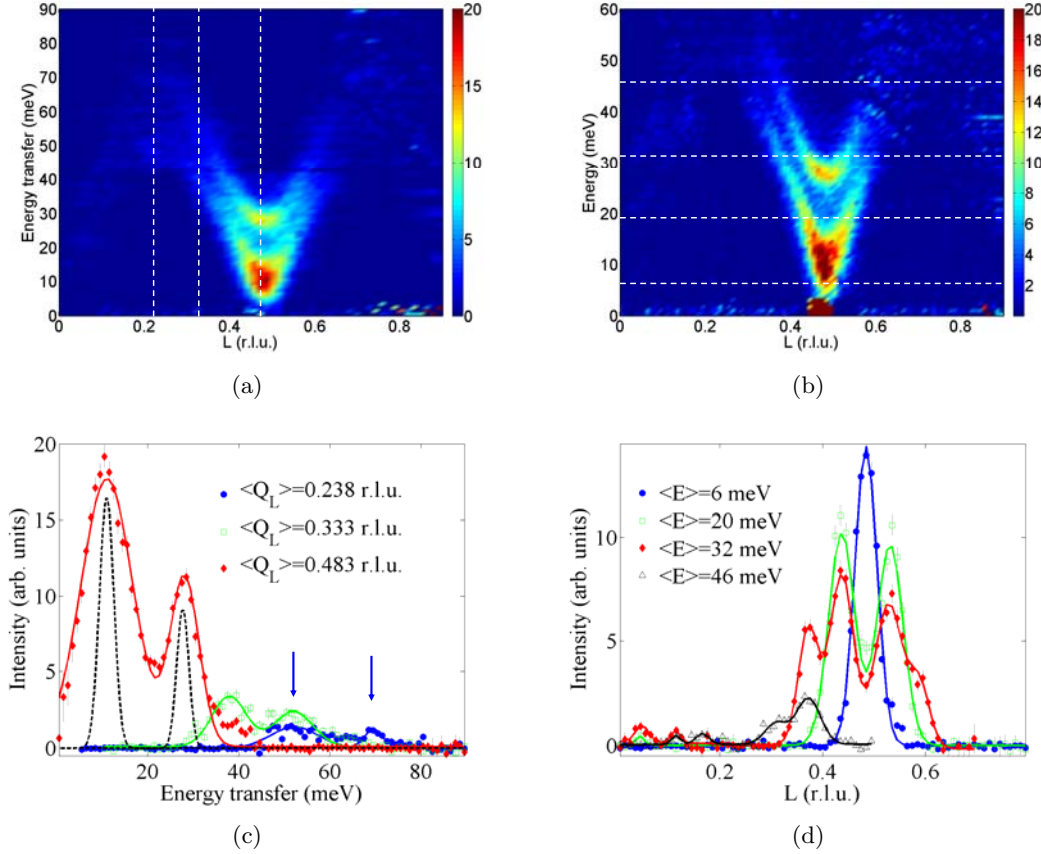


Figure 6.6.: Spin wave spectra along the chain direction of CaV_2O_4 , measured with the MAPS spectrometer. (a) and (b) Energy wavevector colourmap obtained with incident neutron energies (a) $E_i = 100$ meV and (b) $E_i = 70$ meV, with the colour representing the differential neutron scattering cross section. The white dashed lines indicate the direction of the cuts, which are taken at a finite width, being (c) $\langle Q_L \rangle = Q_L \pm 0.01$ and (d) $\langle E \rangle = E \pm 1$. The solid lines in (c) and (d) show Gaussian line-shapes which have been fitted to the data. The dashed lines in (c) show the instrumental resolution at the observed peak positions and two arrows indicate the maxima of two dispersion branches.

the instrumental resolution⁴, as can be seen from Fig. 6.6(c). The peak at lower energy has FWHM=11.8 meV (compared to an instrumental resolution $dE = 3.7$ meV for this energy), while the one higher in energy has FWHM=7.4 meV (compared to $dE = 3.1$ meV). The reason for this broadening is the weak (but finite) interchain coupling. This coupling causes a dispersive behaviour of the magnetic excitations in Q_h and Q_k direction. Since the spectra was obtained by summing over both interchain directions, the observed peak-widths correspond to the overall bandwidths of the interchain dispersions.

⁴The energy resolution of the MAPS spectrometer was calculated using the program `mchop`.

From this it follows that the high energy mode is less dispersive perpendicular to the chain direction than the one at lower energies. Another issue that contributes to the mode broadening is the great number of magnetic ions (8) in the unit cell. In fact, even though the MAPS data only show two distinct dispersion branches, the whole spin wave spectra consists of eight doubly degenerate modes. For this reason, the observed peak broadening is not only the result of interchain dispersion, but more general due to different spin wave modes having similar energies.

The gap size of both modes was determined by investigating the lower boundary regions with cuts at constant energy. As can be seen from Fig. 6.6(d), there is already a strong magnetic signal at the zone centre for $\langle E \rangle = 6 \pm 1$ meV. From various cuts, the gap size was estimated to be $\Delta_1 = 4(2)$ meV for the lower mode and $\Delta_2 = 26(2)$ meV for the upper one. The maximum of both spin wave modes was found at the magnetic zone boundaries, being $E_{\max,1} = 52(6)$ meV for the lower mode and $E_{\max,2} = 70(3)$ meV for the upper mode (see blue arrows in Fig. 6.6(c)), where the values in parentheses correspond to the FWHM, defining the bandwidth of the interchain dispersion at this position.

The full experimentally observed spin wave dispersion along the chain direction is depicted in the left site of Fig. 6.7. In order to get an idea about the size of the leading exchange interactions, the extracted data were manually fitted using a simplified four-sublattice spin wave model of weakly coupled zigzag chains. The dispersion relation $\omega(\mathbf{Q})$ for this model is given in Eq. C.42. It contains the leg coupling J_{leg} , the two intrachain zigzag couplings $J_{\text{zz(a)}}$ and $J_{\text{zz(b)}}$, as well as two interchain coupling parameter $J_{\text{int(a)}}$, $J_{\text{int(b)}}$ and an overall single ion anisotropy constant D . All extracted data points shown in Fig. 6.7 were considered in the fit. The size of the energy gap between the ground state and the lowest spinwave branch is strongly dominated by the size of the anisotropy constant D and in order to give the experimentally obtained gap of $\Delta_1 \approx 4$ meV, its value has been estimated to be $D = 0.05$ meV.

Since the extracted MAPS data are not sufficient to get accurate information about the particular size and behaviour of the interchain dispersion, the two parameters $J_{\text{int(a)}}$, $J_{\text{int(b)}}$ were fixed to reasonable values in agreement with the estimated interchain dispersion bandwidth. As the crystal and electronic structure of CaV_2O_4 suggests a frustrated antiferromagnetic coupling between the chains, the following values have been used for the further discussion: $J_{\text{int(b)}} = 3J_{\text{int(a)}} = 0.6$ meV. These values are consistent with the experimental data as can be seen from the right side of Fig. 6.7, where the dispersion perpendicular to the chain direction is displayed.

Even though the simplified model is not able to describe all details of the observed

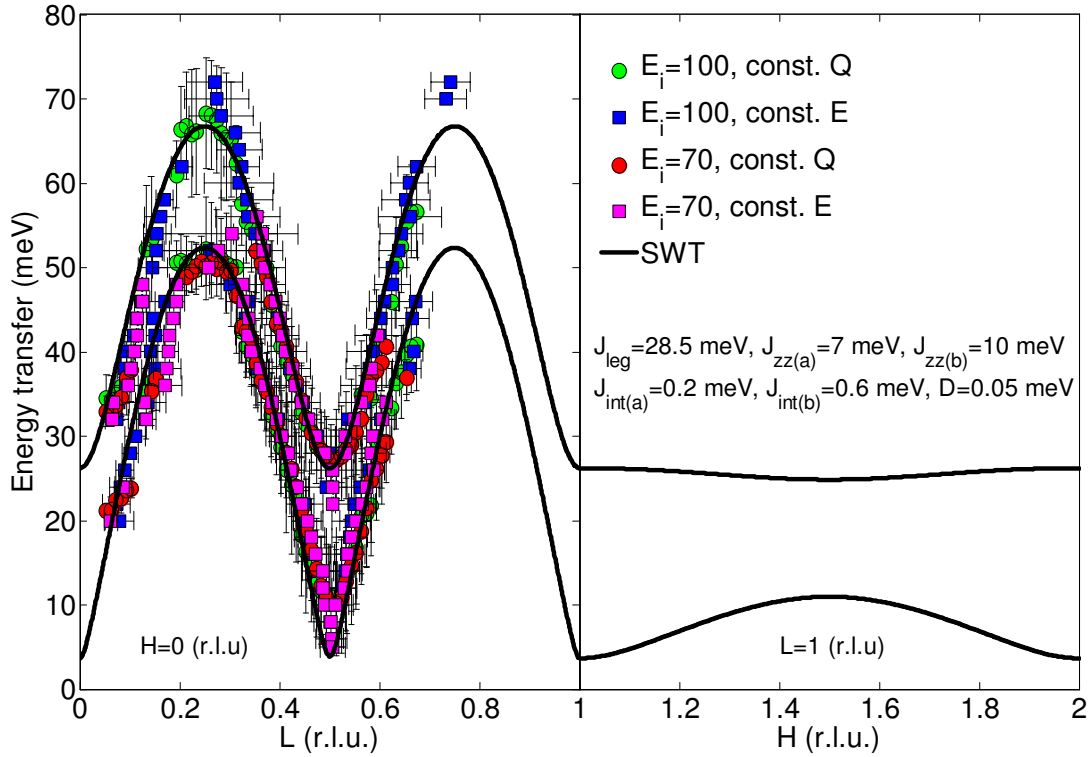


Figure 6.7.: Intra-chain spin wave dispersion of CaV_2O_4 . The data points were extracted from the MAPS data by fitting the peaks apparent in constant Q and constant E cuts to Gaussian line shapes. The MAPS data were collected at an incident neutron energy of $E_i = 70$ and 100 meV. The black line represents a fit to the data using spin wave theory (SWT) based on a four-sublattice model.

spectra, it can reproduce the characteristic double spin wave structure along the chain direction. It is interesting to mention, that the two modes separate for any finite interaction between the legs of the chain, however, the particular shape of the two dispersion branches can only be achieved, if interactions along the zigzags of the chain are frustrated, e.g. if the zigzag couplings are both ferro- or antiferromagnetic. The theoretical investigations reveal two sets of intra-chain parameters, which are in agreement with the experimental data. The first set is given by $J_{leg} = 28.5$ meV, $J_{zz(a)} = 7.0$ meV and $J_{zz(b)} = 10.0$ meV, with all couplings being antiferromagnetic and the corresponding dispersion is displayed in Fig. 6.7. The bandwidths of the two spin wave branches are mainly determined by the size of J_{leg} and by the ratio $\alpha = J_{zz(a)}/J_{zz(b)}$. It was found that α controls the size of the bandwidths of both branches relative to each other, e.g. for α close to one, both branches have approximately the same bandwidth. Further, the absolute value of $J_{zz(b)}$ (and therefore of $J_{zz(a)} = \alpha J_{zz(b)}$) is responsible for the particular

up-shift between the two dispersions.

Another solution in good agreement with the data was achieved with the following parameters: $J_{\text{leg}} = 28.5$ meV, $J_{\text{zz(a)}} = -8.7$ meV and $J_{\text{zz(b)}} = -7.0$ meV, where anisotropy and interchain couplings were fixed to the previous values. In this case, the two zigzag interactions are both ferromagnetic, while the antiferromagnetic leg coupling remains the strongest interaction.

Despite the different signs of the zigzag exchange interactions, both solutions reveal a similar situation in which the two zigzag interactions are approximately equal in size, thus representing a frustrated intra-chain scenario. However, the degree of frustration is relatively weak and the energy scale of the spin wave dispersion is dominated by the leg coupling, taking a value of about three times the size of the zigzag interactions.

Although, this (simplified) spin wave model should not be used for a detailed physical interpretation of the observed excitation spectra, since e.g. it does not account for the particular double chain structure that is apparent in 'real' CaV_2O_4 , it already provides some clear information about the relative strengths of the exchange interactions. Interestingly, with the given model it is not possible to reproduce the measured spin wave excitations, if one neglects one of the zigzag interactions. For instance, if one assumes a pure antiferromagnetic spin ladder ($\alpha = 0$, $J_{\text{leg}}, J_{\text{zz(b)}} \neq 0$), the calculated spin wave spectra results in two equal branches, which are shifted by a phase of π/c with respect to each other. Neither the periodicity of $\delta Q_L = 2\pi/c$ (being twice the observed one), nor the size of the energy gap at the zone boundaries, which is significantly enhanced in the ladder case, are in agreement with the measured intrachain dispersion.

A deeper understanding of the system can be achieved if one compares the experimentally observed data to the more realistic spin wave model introduced in Sec. 6.3. To be able to do so, more detailed experimental data are required. For this reason, additional experiments were performed with the thermal triple axes spectrometer (TAS) IN20 at ILL, France. The main advantage of a TAS is that its particular construction allows almost any desired coordinate in energy-momentum space to be probed in a controlled manner. As such, it provides the possibility to follow spin wave dispersions along all three dimensions in reciprocal space.

The focus in the IN20 experiment was the investigation of the CaV_2O_4 spin wave dispersion perpendicular to the chain direction. This was done by performing a series of constant wavevector-scans and the spin wave spectra along the interchain directions Q_H and Q_K and are presented in Figs. 6.8(a) and 6.8(b).

The data reveal a complex dispersion behaviour with multiple spin wave modes along both interchain directions. The characteristic separation into a lower and an upper spin

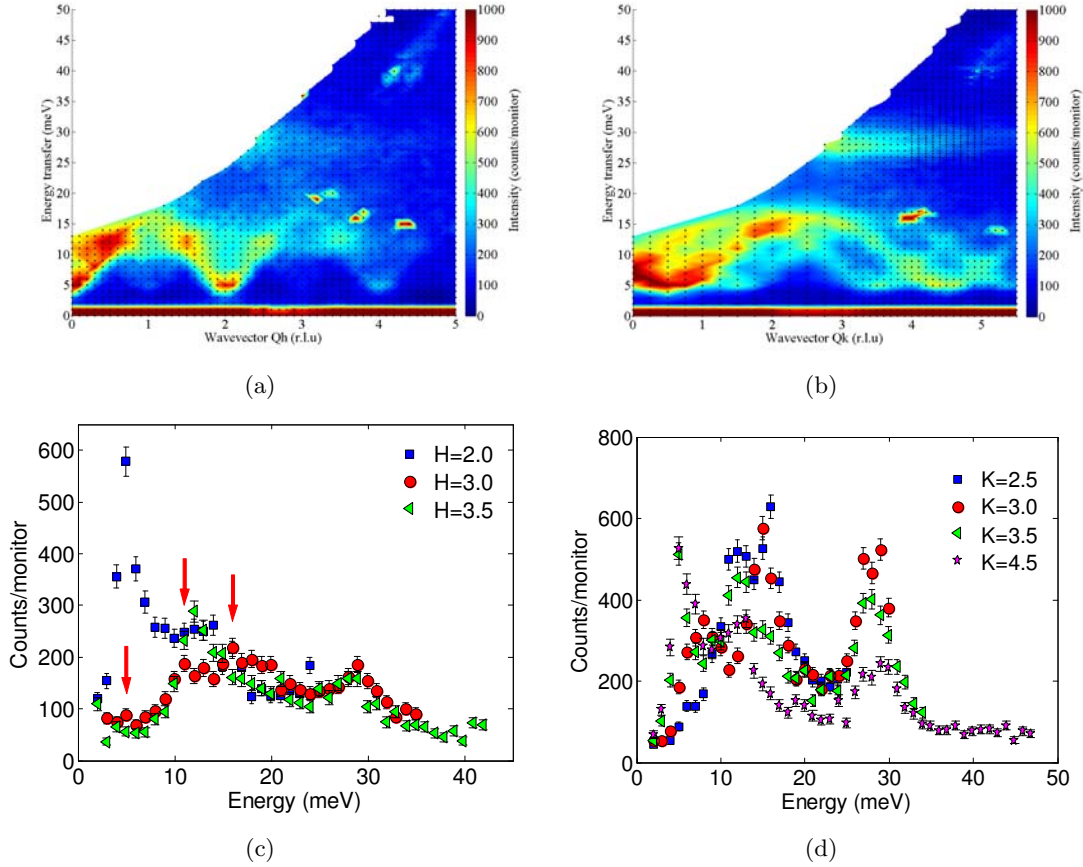


Figure 6.8.: Spin wave spectra of CaV_2O_4 perpendicular to the chain direction. (a) and (b): Energy wave vector colourmaps along the Q_H and Q_K direction, respectively. The maps were generated from a large set of single constant wavevector scans (indicated by dotted black lines), which were interpolated and smoothed in order to visualize the full spectra. (c) and (d). selected constant Q -scans along the magnetic zone centre and zone boundary in Q_H and Q_K .

wave part, which was observed on MAPS, is also clearly visible in the IN20 data. The upper excitations are centred at $E \approx 27$ meV and are almost dispersionless, however, the broadening of this branch is larger than the instrumental resolution, such that one can assume that several close lying modes contribute to its shape. On the other hand, the lower modes reveal a pronounced modulation with a bandwidth of ≈ 12 meV in energy. The bandwidths of the lower excitations are almost equal along Q_H and Q_K , indicating that the exchange interactions along the two interchain directions have approximately the same size.

The most obvious feature along the Q_H direction is the very intense mode with minima at $Q_H = h\frac{2\pi}{a}$, with $h = 2n$ and n integer. The Q dependence of the spin wave intensity

of this mode (and also of all other ones) is strongly dominated by the magnetic form factor of the V^{3+} -ions, which decreases with increasing momentum transfer. In addition to the very intense mode, a further much weaker one was also observed. This mode has the same periodicity as the first one, but shows a phase-shift $\frac{2\pi}{a}$ with respect to it, with minima located at $Q_H = h\frac{2\pi}{a}$, with $h = (2n - 1)$ and n integer. A closer look at particular selected Q scans (see Fig. 6.8(c)), reveal an even greater number of spin wave branches. For instance, the cut at $Q_H = 3\frac{2\pi}{a}$ reveals three peaks at low energy (see red arrows in the Figure), where the lower one at ≈ 5 and one of the two higher ones at ≈ 11 meV and at ≈ 17 meV belong to the previously mentioned modes, while the remaining third peak indicates that at least one more mode is apparent. The available resolution of the IN20 spectrometer did not allow the fine structure of the low energy excitations to be resolved in more detail; however, the spin wave analysis presented later in this chapter will shed light on this issue.

A similar scenario is given for the spin wave excitation spectrum along the Q_K direction. From the energy wavevector colourmap it seems that apart from the flat mode at $E \approx 27$ meV, there are at least three further modes at lower energy, all having the same periodicity of $4\frac{2\pi}{b}$, but all being phase shifted by $\frac{2\pi}{b}$ with respect to each other.

6.4.1. Low energy excitations

Before the IN20 data will be analysed by means of linear spin wave theory, it is helpful to provide some further justification for the proposed model Hamiltonian (Eq. 6.2). For this reason, additional investigations of the low energy part of the spin wave spectra have been performed using the cold neutron triple axis spectrometer V2, FLEX. Due to the better resolution of FLEX (compared to IN20) it is well suited to study the fine structure of magnetic spectra and in particular their behaviour as a function of magnetic field and temperature. The magnetic field dependence reveals details about the character of the magnetic excitations, while the temperature dependence provides information about the origin of the energy gap.

Figure 6.9(a) displays two energy scans measured at the magnetic zone centre at $Q = (0, \frac{1}{2}, \frac{1}{2})$ in zero field (green squares) and in a magnetic field of $B = 6.5$ T (red squares). The crystal was oriented such that the field pointed approximately along the crystallographic b -direction, which coincides with the average direction of the magnetic moments. In the absence of a field, the data reveal a well pronounced single peak at ≈ 4.6 meV. The peak position corresponds to the size of the energy gap and the findings are in agreement with those from IN20 (cf. Fig. 6.8). However, the situation changes when a

field acts on the magnetic moments. In this case the spin Hamiltonian (Eq. 6.2) has to be extended by a Zeeman term:

$$\mathcal{H}_Z = -g\mu_B \left(\sum_i^{\in A} \mathbf{S}_i \cdot \mathbf{B} - \sum_j^{\in B} \mathbf{S}_j \cdot \mathbf{B} \right) \overset{B \parallel b}{\approx} -g\mu_B B_y \left(\sum_i^{\in A} S_i^y - \sum_j^{\in B} S_j^y \right), \quad (6.16)$$

where g is the Landé factor, μ_B is the Bohr magneton and \mathbf{B} is the magnetic field vector. The two sums in Eq. 6.16 run over all spin-up (A) and spin-down (B) sublattices, respectively, and the expression on the right side indicates that the spin direction is approximately along b (or y , respectively). The Zeeman term results in a splitting of the twofold degenerate spin wave modes by equal amounts above and below the zero field energy. This was indeed observed as can be seen in Fig. 6.9(a). The split peaks of the field-scan were fitted to Lorentzian lineshapes and the extracted size of the splitting ($\Delta E = 1.2(2)$ meV) is in qualitative agreement with the theoretically expected value ($\Delta E = 2g\mu_B B_y \approx 1.506$ meV), where $g = 2$ was assumed. One probable reason for the small difference between the experimental and theoretical value is the spin canting, which has not been taken into consideration. The observed splitting into two peaks is an important finding, since it underlines the spin wave character of the magnetic excitations and thus justifies the applicability of spin wave theory. For instance, if the magnetic excitations would be purely 1D, they would be rotationally invariant and the corresponding excitations would be threefold degenerate, which would give rise to three peaks in the field data.

In contrast, no mode splitting was detected for the field pointing along the crystallographic a -direction (perpendicular to the spins). Figure 6.9(b) displays the resulting energy-scan at fixed $Q = (0, \frac{1}{2}, \frac{1}{2})$, where no difference between the zero-field and high-field measurements can be seen. This orientation-dependent lifting of mode degeneracy can be explained in the following qualitative way. Due to the antiferromagnetic spin structure, a magnetic field that points along the ordering direction has a different effect for spins that are parallel and those that are antiparallel aligned with respect to it. Therefore while the spin-flips on one of the sublattices decrease the energy with respect to the field, they increase the energy on the other sublattice. The resulting energy difference is manifested as a splitting of the formerly degenerate mode pair. On the other hand, when the field points perpendicular to the spin direction it mixes the spin-wave modes into fluctuations parallel and perpendicular to B . At the antiferromagnetic zone centre the fluctuations parallel to the field are unchanged, while those perpendicular to the field are raised in energy [163]. Due to the geometry of the measurement only

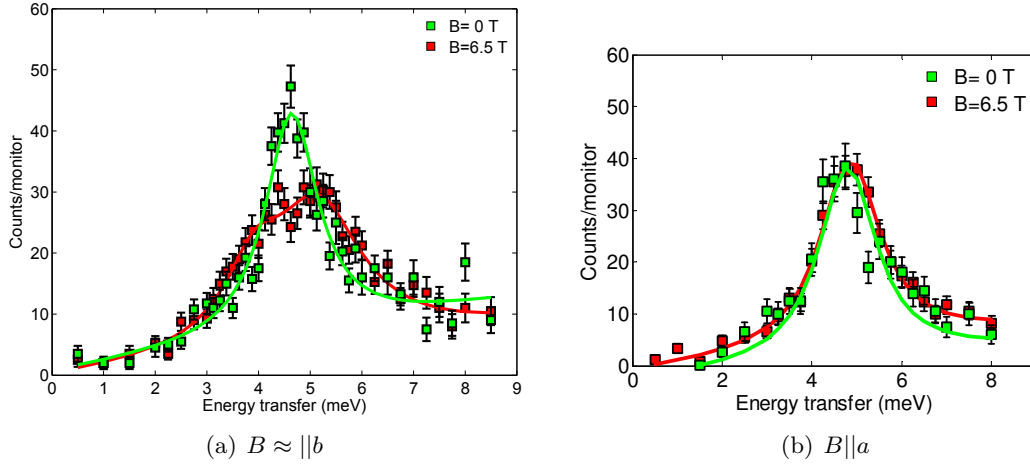


Figure 6.9.: Constant Q scan at $(0, \frac{1}{2}, \frac{1}{2})$ for a magnetic field applied (a) along the b direction and (b) along the a direction of CaV_2O_4 . The measurement took place in the antiferromagnetically ordered phase at $T = 1.5$ K.

fluctuations parallel to the field were observed. These indeed showed no shift from the zero field position, thus confirming this picture⁵.

The second task of the FLEX experiment was the investigation of the temperature dependence of the low energy excitations. For this reason, the energy scan shown in Fig. 6.9 was repeated for several temperatures between $T = 1.5$ K and $T = 80 > T_N = 71$ K. The resulting data are depicted in Fig. 6.10(a). It can be seen, that upon heating a considerably amount of spectral weight shifts towards lower energies, thus reducing the size of the energy gap. The peak width of the spin wave mode becomes significantly broader at higher temperatures, indicating that spin wave damping effects become apparent. For temperatures $T > \Delta/k_B \sim 53$ K, where $\Delta \approx 4.5$ meV denotes the energy gap, thermal fluctuations start to smear out the gap. The overall temperature dependence of the energy gap is clearly visible from Fig. 6.10(b). This figure shows an energy-temperature colourmap, created with the scans of Fig. 6.10(a). The observed behaviour is characteristic for an energy gap caused by single ion anisotropy. The anisotropy gap scales with the order parameter of the antiferromagnetic system [164]. Indeed, the temperature dependence of the integrated Bragg intensity, which is proportional to the sublattice magnetization of CaV_2O_4 (see Fig. 5.27) follows a very similar behaviour to the gap, thus

⁵Of course, these results can also be derived theoretically using spin wave theory and including Eq. 6.16 in the overall spin Hamiltonian. Note that for the field along a , Eq. 6.16 changes into: $\mathcal{H}_z \approx -g\mu_B B_x \left(\sum_i^{\in A} S_i^x - \sum_j^{\in B} S_j^x \right)$. Eventually, the different behaviour of S_x and S_y components under Holstein-Primakoff-transformation finally results in the different dispersion relations for $B||a$ and $B||b$, respectively.

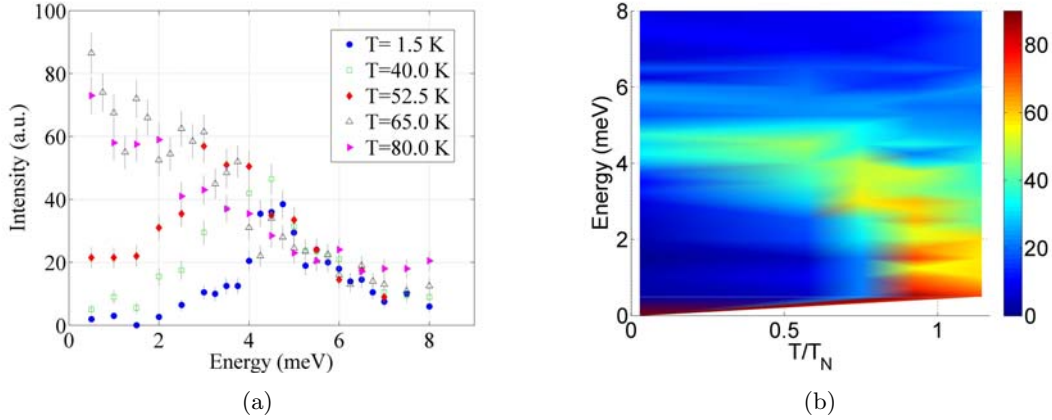


Figure 6.10.: (a) Constant wavevector scan at $(0, -\frac{1}{2}, \frac{1}{2})$ for different temperatures. (b) Energy-temperature colourmap made from the scans presented in (a). The temperature is normalized to $T_N = 71$ K.

underlining the anisotropy nature of the gap. In contrast, a pure spin gap such as the $S = 1$ Haldane gap only starts to emerge *above* the antiferromagnetic Néel-temperature.

6.4.2. Spin wave analysis

In order to be able to compare the measured data to the theoretical model introduced in Sec. 6.3, the spin wave dispersions have been extracted from the data by fitting the peaks observed in the IN20 scans to Lorentzian lines shapes. This Lorentzian function was found to account for the peak profile that is characteristic for a TAS. However, it is important to stress that the resolution of a triple axis spectrometer is in general a complex quantity, which depends on the phase space volume that is transmitted by the monochromator and analyser crystals (resolution ellipsoid) and also on the particular slope of the measured excitations [61]. This dependence can lead to small differences between the fitted mode positions and their real values. To account for this, the following discussion will be split in two parts. First, the data will be fitted to Lorentzians to provide a qualitative analysis, where the main focus is to investigate the various coupling scenarios belonging to different orbital ordering patterns that have been suggested from magnetic structure investigations (see Chapter 5.3.6) and from theory [158]. Subsequently, a more quantitative analysis of the most suitable model will be presented. This will be done by simulating selected scans of the IN20 measurement under consideration of the correct instrumental resolution as well as the particular slope of the calculated spin

wave modes. By doing so, it is possible to ‘fine-tune’ the free parameters of the model and therefore present a final solution that is in best agreement with the experimental data. Further, it enables the investigation of the data for anomalous line broadening, which in turn allows conclusions to be drawn about finite lifetime effects.

The 32 sublattice spin wave model which has been introduced in Sec. 6.3 was employed for further data analysis. It contains the full crystal structure of CaV_2O_4 and therefore enables a detailed study of both, the spin wave dispersions as well as the corresponding spin-spin correlation functions. The latter are directly proportional to the differential neutron scattering cross section, the quantity which is directly accessible in a neutron scattering experiment. The overall number of free parameters is twelve and includes ten exchange coupling parameter describing the magnetic coupling within and between the two inequivalent V^{3+} zigzag chains (see Fig. 6.4) and two single ion anisotropy parameters that account for the different octahedral crystal fields acting on both magnetic sites. Despite the fact that the IN20 and MAPS data provide an accurate picture of the spin wave spectra of CaV_2O_4 , the data are not sufficient to fix all free parameter and consequently some constraints are required. The investigations of the low temperature nuclear and magnetic structure revealed that the strongest interactions within the two vanadium chains are the (antiferromagnetic) leg couplings J_{leg}^1 and J_{leg}^2 , and (unless stated otherwise), those couplings will be assumed to be equal in the following. Moreover, also the interchain interactions $J_{\text{int(b)}}^a = \beta J_{\text{int(a)}}^a$ and $J_{\text{int(b)}}^b = \beta J_{\text{int(a)}}^b$ were set to be equal (β is a coupling ratio). This is justified, since the bandwidths of the dispersion along Q_H and Q_K have approximately the same size. Furthermore, the coupling between the chains arises from weak super exchange interactions involving oxygen and the particular V-O-V bond angles ($\sim 120^\circ - 130^\circ$) give rise to the assumption that those interactions are all antiferromagnetic in nature [9]. Finally, for the beginning the single ion anisotropy parameter D_1 and D_2 have been set to equal values. Once the best suited set of coupling parameters is found, the effect of different D parameters will be discussed in detail.

As has been pointed out in the previous chapter, the low temperature nuclear and magnetic structure of CaV_2O_4 gives rise to various ordering scenarios of the three vanadium t_{2g} orbitals. Which of those scenarios corresponds to the particular case of the two CaV_2O_4 chains depends on two quantities: the degree of distortion of the VO_6 octahedra and the size of spin orbit coupling.

Concerning the t_{2g} orbital occupation, it seems to be fairly certain that due to the dominant pseudo-tetragonal distortion of both VO_6 octahedra, the local d_{xy} -orbitals at both vanadium sites are always occupied. The lobes of these orbitals are arranged along

the legs of the zigzag chains and as such they are responsible for the strong (antiferromagnetic) interactions J_{leg}^a and J_{leg}^b (see Figure (5.36)). The situation is less clear for the four intra chain zigzag interactions $J_{\text{zz}(a)}^1, J_{\text{zz}(b)}^1, J_{\text{zz}(a)}^2$ and $J_{\text{zz}(b)}^2$. Depending on the strength of spin orbit coupling and the degree of orthorhombic octahedral distortion, different coupling scenarios, ranging from frustrated antiferromagnetic coupling (ferro-orbital order) to frustrated ferromagnetic coupling (antiferro-orbital order) can occur. Also a situation, where strong exchange is only mediated via every second zigzag rung (spin ladder) is possible [158, 89]. The inelastic neutron data allow the strength and character of all magnetic interactions to be determined and therefore enable the correct orbital configuration of CaV_2O_4 to be identified.

A reasonable starting point for the current analysis are the exchange coupling parameters that have been obtained with the simplified ‘single zigzag chain model’ earlier in the text. Those preliminary investigations revealed, that the particular double spin wave structure of CaV_2O_4 can be reproduced only, if (beside the strong leg coupling) frustrated ferro- or antiferromagnetic coupling along the zigzags is introduced. Further, it was found that the ratio between leg and zigzag interactions has to be $|J_{\text{zz}(a,b)}| \approx \frac{1}{3}J_{\text{leg}}$ in order to match the experimental data. However, in contrast to the simplified model, the 32 sublattice spin wave model considers the full 3D crystal structure of CaV_2O_4 . In particular, it accounts for the two inequivalent zigzag chains that are present in the real system and also for the coupling between them. Therefore the spin wave dispersion along the direction of the chains will not only be affected by the different intra chain interactions that couple the spins within the two different chains, but also by the exchange coupling *between* the chains.

By knowing the approximate strength of the intra chain coupling from the simplified model, it is reasonable to assume that similar results concerning the dispersion of CaV_2O_4 should be achievable, if the intra chain coupling parameters of the full model take values similar to those obtained with the simplified model (e.g., with each of both chains showing either frustrated ferro- or antiferromagnetic zigzag interactions). Starting with the assumption that both vanadium chains possess frustrated *antiferromagnetic* zigzag coupling and introducing reasonable interchain coupling values, it is indeed possible to reproduce the measured spin wave spectra. The calculated spin wave modes and spin wave intensities for Q along all three main directions of the reciprocal lattice are depicted in Figure (6.11) together with data from IN20 and MAPS⁶. More precisely, the

⁶Note that the data from MAPS do not exactly correspond to the calculated dispersion, since on MAPS the spectra was summed along the two interchain directions Q_H and Q_K . Those data are only shown to give an overview of the intra chain bandwidth.

sub-figures on the right side (Figs. 6.11(d), 6.11(f) and 6.11(b)) show the calculated differential neutron scattering cross sections, which correspond to the particular spin wave modes displayed on the left side (Figs. 6.11(c), 6.11(e) and 6.11(a)). Both, the magnetic form factor of V^{3+} as well as the polarisation factor (see Eq. 3.17) have been taken into consideration. Further, in order to obtain accurate results, it is important to account for the effects of monoclinic twinning (see Chapter 5.3.2). The twinning causes overlap of magnetic signal arising from the Bragg reflections $(h, k, l)_{\text{twin } 1}$ and $(h, -k, l)_{\text{twin } 2}$. Since in contrast to the spin wave dispersions, the spin wave intensities are not symmetric in Q , the twin overlap changes the spin wave spectra significantly⁷. To account for this, the cross section at each position in (\mathbf{Q}, E) -space was averaged over positive and negative Q_K , where equal twin fractions were assumed:

$$\left(\frac{d\sigma}{dE_f d\Omega} \right)_{\langle \text{twins} \rangle} (\omega_N, \mathbf{Q}) = \frac{1}{2} \left(\frac{d\sigma}{dE_f d\Omega} (\omega_N, Q_x, Q_y, Q_z) + \frac{d\sigma}{dE_f d\Omega} (\omega_N, Q_x, -Q_y, Q_z) \right), \quad (6.17)$$

where ω_N is the energy of the N th spin wave mode.

The model leads to 16 double degenerate spin wave modes, with half of them having no intensity. Therefore, the remaining eight double degenerate modes represent the spin wave spectra of CaV_2O_4 .

Model 1: The use of the intra chain coupling parameters $J_{\text{leg}}^1 = J_{\text{leg}}^2 = 29.5$ meV, $J_{\text{zz(a)}}^1 = J_{\text{zz(a)}}^2 = 7.81$ meV, $J_{\text{zz(b)}}^1 = J_{\text{zz(b)}}^2 = 11.0$ meV and single ion anisotropy parameter $D_1 = D_2 = 0.08$ meV enabled the correct modeling of the two steep spin wave branches along the Q_L (chain) direction (see Fig. 6.11(a)). Both, the upper and lower part of the spectra consist each of four spin wave modes. A closer look reveals that these four modes merge at the zone boundaries in Q_L , while they split apart near the zone centre. This particular behaviour is controlled by the interchain coupling parameter. The values $J_{\text{int(b)}}^{a,b} = \beta J_{\text{int(a)}}^{a,b} = 0.62$ meV (with $\beta = 0.27$) have been found to be in good agreement with the experimental data, as can be seen from Figs. 6.11(c) and 6.11(e).

The calculated modes along the interchain directions Q_H and Q_K possess a periodicity of 2 r.l.u., where the mode minima are positioned at $Q_H = n \frac{2\pi}{a}$ and $Q_K = \frac{2n+1}{2} \frac{2\pi}{b}$ (n is an integer number). The four upper and lower spin wave modes are further separated into pairs, where the modes belonging to each pair have exactly the same amplitude

⁷The resolution of IN20 did not allow the twinning to be resolved.

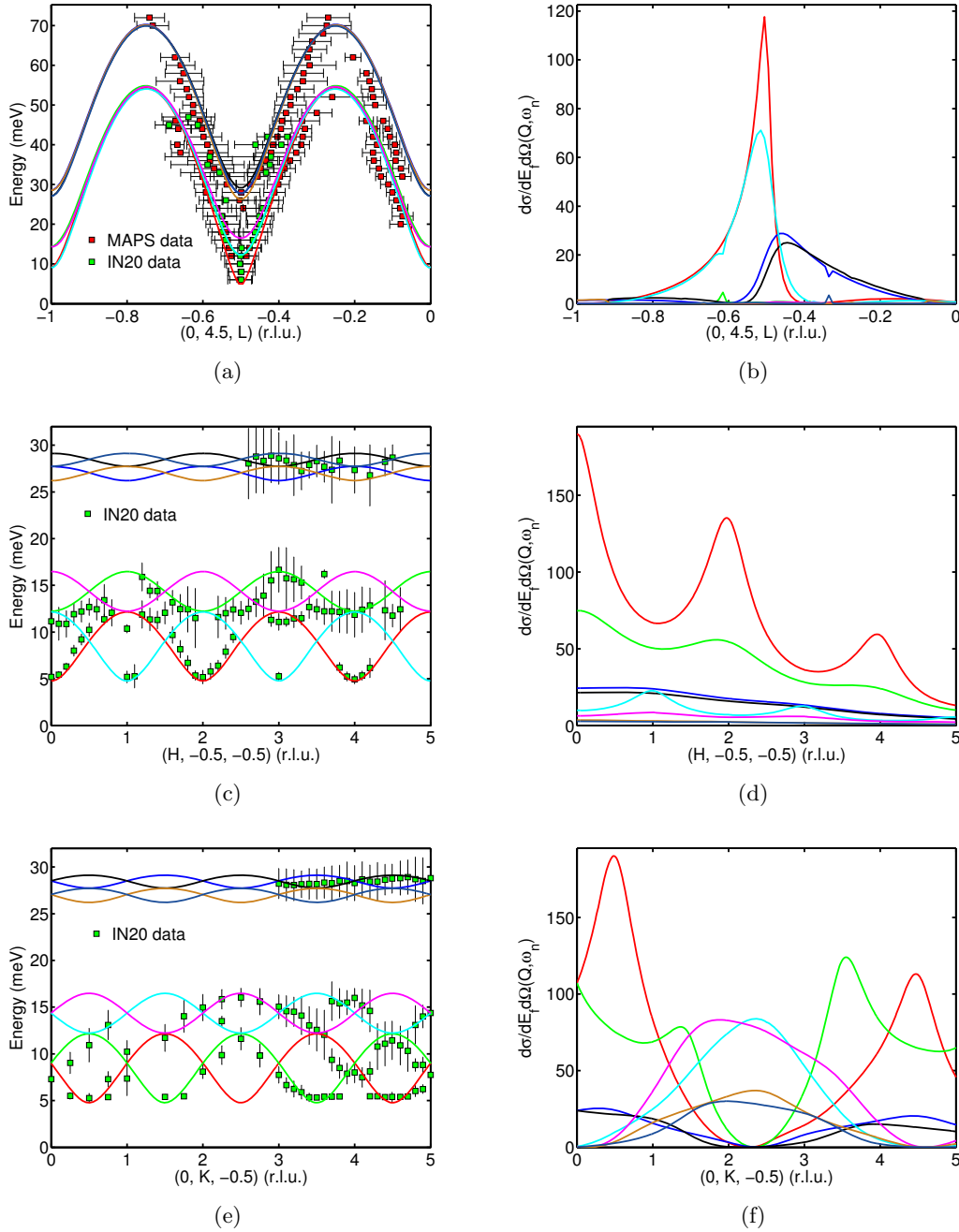


Figure 6.11.: *Model 1:* Calculated spin wave dispersion and intensities of CaV_2O_4 , assuming that both zigzag chains possess antiferromagnetic rung coupling. The following parameters have been used: $J_{\text{leg}}^1 = J_{\text{leg}}^2 = 29.5$ meV, $J_{\text{zz}(a)}^1 = J_{\text{zz}(a)}^2 = 7.81$ meV, $J_{\text{zz}(b)}^1 = J_{\text{zz}(b)}^2 = 11.0$ meV, $J_{\text{int}(a)}^a = J_{\text{int}(a)}^b = 0.17$ meV, $J_{\text{int}(b)}^a = J_{\text{int}(b)}^b = 0.62$ meV, $D_1 = D_2 = 0.08$ meV. In addition the data obtained from IN20 and MAPS are shown. The small kinks in the graphs of Fig. 6.11(b) are numerical artifacts.

and periodicity, but are phase shifted by 1 r.l.u. with respect to each other. The two spin wave pairs at lower energies have different bandwidths, being (for the chosen set of parameter) ≈ 7.3 meV for the lower and ≈ 4.2 meV for the upper pair. The pairs touch each other at the magnetic zone centres and therefore give rise to an overall bandwidth that corresponds with the experimentally observed one (≈ 11.5 meV). Similar behaviour can be seen for the upper mode pairs, however, the bandwidths of those are almost equal, being ≈ 1.4 meV each.

It has to be mentioned that the particular coupling parameters chosen in Fig. 6.11 are not the only ones that allow the dispersion perpendicular to the direction of the chains to be reproduced. This is, because the particular bandwidths of the intra chain modes are influenced by two quantities, the absolute values of the interchain coupling ($J_{\text{int}(a)}^a, J_{\text{int}(a)}^b, J_{\text{int}(b)}^a, J_{\text{int}(b)}^b$), as well as the relative ratio between them. As can be seen from Figs. 6.4(b) and 6.4(c), neighbouring spins of different chains are also coupled in a zigzag like fashion and since both interchain zigzag interactions are antiferromagnetic, this gives rise to frustration. The degree of frustration is controlled by the coupling ratio β . In general the higher the degree of interchain frustration, the higher the absolute strength of the interactions has to be, in order to achieve good agreement between the model and the experiment. In other words, strong frustration between the chains leads to a renormalization of the spin waves. For instance, the following very different set of interchain interactions lead to similar dispersion bandwidths: $J_{\text{int}(a)}^{a,b} = \beta J_{\text{int}(b)}^{a,b} = 0.45$ meV, $\beta = 0$ and $J_{\text{int}(a)}^{a,b} = \beta J_{\text{int}(b)}^{a,b} = 5.0$ meV, $\beta = 0.9$.

It is difficult to determine the degree of interchain frustration. Due to the monoclinic distortion at low temperatures the bond lengths and bond angles along the interchain triangular bonds are not equal; however, it is not clear how strongly this effects the actual strength of the super exchange coupling. A way to set limits on the interchain interactions, is to investigate their influence on the intrachain dispersion. It was found that a strong interchain frustration splits the modes at the magnetic zone boundary in Q_L , while in the case of weak frustration, they merge together (cf. Figs. 6.11(a) and 6.12(a)). As the MAPS data have revealed a broadening which is much greater than the instrumental resolution, this tends more to a scenario of strong interchain frustration, with β being close to one.

A remarkable aspect is, that the model is not only able to reproduce the spin wave modes correctly, but also provides very good results for the corresponding spin wave intensities. In particular the calculated spectra along the interchain direction accounts for all main experimentally observed features of the spectra. This can be seen by comparing Fig. 6.11 with Figs. 6.8(a) and 6.8(b). For example, the observed strong intensity difference

of the two phase-shifted low energy modes along Q_H also manifests in the corresponding calculated intensities. Interestingly, the apparent periodicity of $4\frac{2\pi}{b}$ of the spin waves along the Q_K direction (see Fig. 6.8(b)) turns out to be only half of that value. This is because the particular intensity distribution of the two mode pairs at low and high energy appears to have alternating periods of strong and weak signal, such that the overall spectra gives the impression that the modes have a larger period than actually predicted from the model.

Despite the generally good agreement between theory and experimental, there is one major aspect that speaks against the scenario of *two* weakly coupled antiferromagnetic zigzag chains. The calculations of the intrachain spin wave spectrum reveal a very asymmetric intensity distribution for the spin wave modes around the magnetic zone centre (see Fig. 6.11(b)). While the four lower modes only get significant signal for $Q_L < 0.5$ r.l.u., the four upper modes solely show strong signal for $Q_L > 0.5$ r.l.u. Such a behaviour was not observed experimentally, e.g. additional constant energy scans on IN20 revealed a very homogeneous intensity distribution of all modes in the vicinity of the magnetic zone centre (see Fig. 6.16).

Model 2: A second set of intra chain parameters, which leads to reasonable agreement with the experimental data is one, where the zigzag interactions along both chains are ferromagnetic. Using the intrachain coupling values $J_{\text{leg}}^1 = J_{\text{leg}}^2 = 29.5$ meV, $J_{\text{zz(a)}}^1 = J_{\text{zz(a)}}^2 = -8.5$ meV, $J_{\text{zz(b)}}^1 = J_{\text{zz(b)}}^2 = -6.3$ meV and $D_1 = D_2 = 0.08$ meV, one obtains the spin wave spectra depicted in Figure 6.12. The calculations reveal many similarities with respect to the antiferro zigzag scenario. In particular the spin wave dispersion and the corresponding intensities along the interchain directions are almost identical.

In order to demonstrate the effect of strong interchain frustration the values: $J_{\text{int(a)}}^{a,b} = \beta J_{\text{int(b)}}^{a,b} = 2.0$ meV, $\beta = 0.73$ have been used. As mentioned above, stronger interchain frustration tends to spread out the spin wave modes around the magnetic zone centre along Q_L (cf. Figs 6.12(a) and 6.11(a)) and therefore seems to agree better with the experimental observations.

However, as for the previous case, the spin wave spectra along the chain direction shows a very asymmetric intensity distribution, although, strong and weak intensity parts of the upper and lower modes are inverted with respect to the magnetic zone centre (compared to the antiferromagnetic zigzag scenario). Therefore, the same arguments as for the previous solution also hold for this one. The inhomogeneous spin wave spectra was not observed experimentally and therefore it rules out the case of two chains with ferromagnetic zigzag coupling.

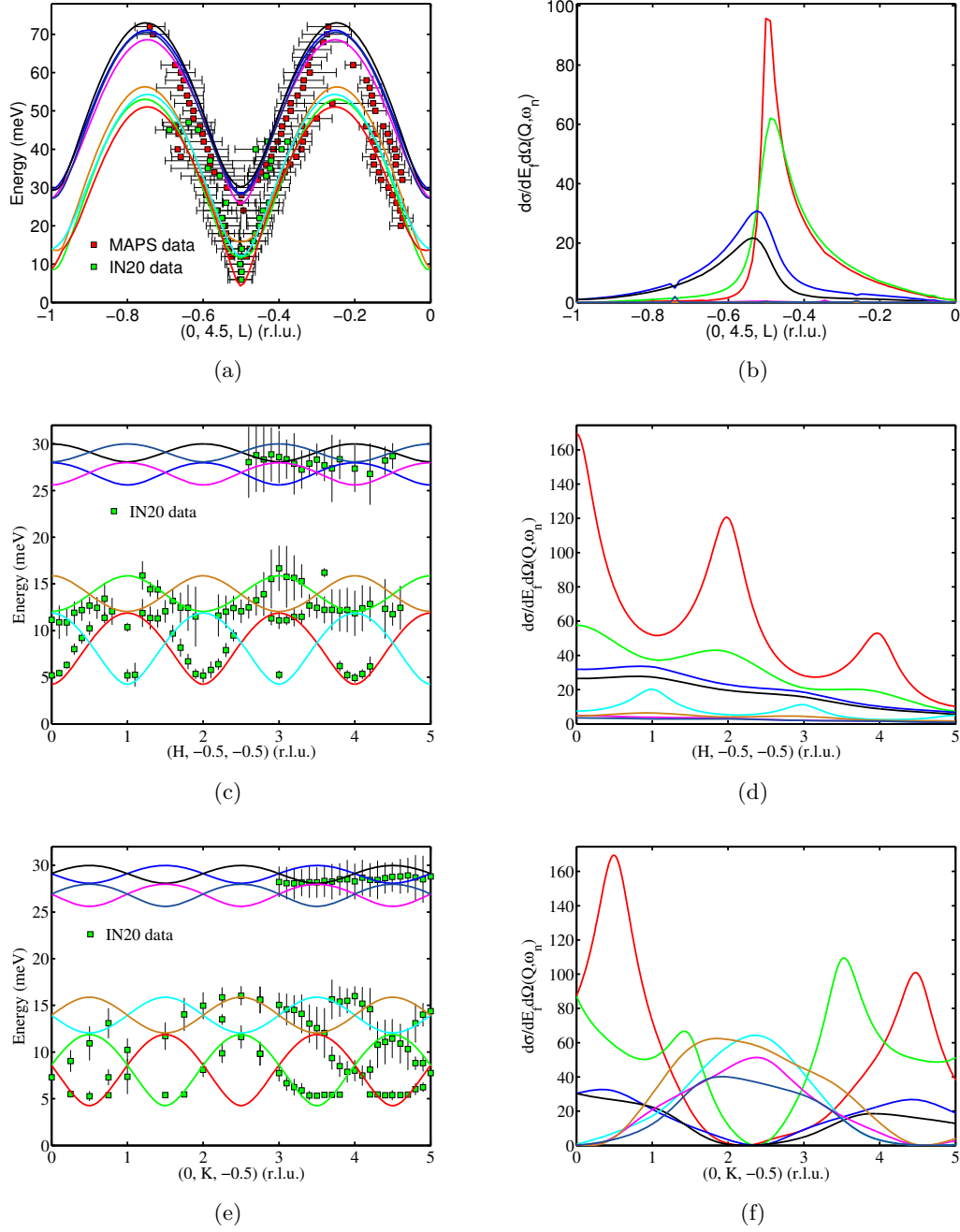


Figure 6.12.: *Model 2:* Calculated spin wave dispersion and intensities of CaV_2O_4 , assuming that both zigzag chains possess ferromagnetic rung coupling. The following parameters have been used: $J_{\text{leg}}^1 = J_{\text{leg}}^2 = 29.5$ meV, $J_{\text{zz}(a)}^1 = J_{\text{zz}(a)}^2 = -8.5$ meV, $J_{\text{zz}(b)}^1 = J_{\text{zz}(b)}^2 = -6.3$ meV, $J_{\text{int}(a)}^a = J_{\text{int}(a)}^b = 1.46$ meV, $J_{\text{int}(b)}^a = J_{\text{int}(b)}^b = 2.0$ meV, $D_1 = D_2 = 0.08$ meV. In addition the data obtained from IN20 and MAPS are shown.

Model 3: Due to the discrepancies observed in the case of identical exchange interactions within the two different CaV_2O_4 chains, the next step is to introduce different interactions for the two chains. By doing so, it turned out that very good agreement between theory and experiment could be achieved, if one of the two chains possesses ferromagnetic and the other one antiferromagnetic zigzag interactions. The relative strengths of the interactions remain similar to the previous cases: $J_{\text{leg}}^1 = J_{\text{leg}}^2 = 29.5$ meV, $J_{\text{zz(a)}}^1 = 7.92$ meV, $J_{\text{zz(b)}}^1 = 11.0$ meV, $J_{\text{zz(a)}}^2 = -9.0$ meV, $J_{\text{zz(b)}}^2 = -6.48$ meV. At this point it is important to mention that a simple swapping of all intrachain interactions between the two chains does not effect the spin wave dispersion, while it does slightly change the corresponding spin wave intensities. Those differences are small, however, a careful check of the experimental data revealed a better agreement with the theoretical calculations, if interactions along the zigzags of the first chain (blue arrows in Fig. 6.4) are antiferromagnetic. This is an important result, since it means that the current spin wave model is able to uniquely identify the leading interactions within each chain and thus enables detailed conclusions to be drawn about the corresponding orbital physics.

The results obtained with the parameters given above are depicted in Fig. 6.13. The inequivalent zigzag couplings within the two chain units introduce a gap of ≈ 1.7 meV between the two lower mode pairs and a gap of ≈ 0.8 meV between the two upper ones. The existence of such a splitting can be proven by simulating IN20 scans by convolving the calculated neutron scattering cross section with the resolution function of the spectrometer. This issue will be discussed in the next subsection (see Sec. 6.4.3). However, different zigzag interactions within the two chains are not the only causers of the splitting of mode pairs. This could also arise from different coupling strengths along the two interchain directions and/or by non equal anisotropy parameters $D_1 \neq D_2$. Generally, due to the low symmetry of the crystal structure and the two different magnetic sites, it is most likely that all three factors occur.

Concerning the intensities of the eight spin wave modes, their behaviour along the interchain directions Q_H and Q_K is somewhat less smooth than that of the two previous models; however, the agreement with the experimental observations is still very good. More importantly, the calculations of the intensities along the Q_L direction reveal a homogeneous intensity distribution in the vicinity of the magnetic zone centre, which is in excellent agreement with the experimental data.

Before discussing the solution above in more detail, it is important to examine, whether the employed spin wave model provides further sets of parameters that enable a good fit of the experimentally observed dispersion. In particular the formation of spin ladders ($J_{\text{leg}} \approx J_{\text{zz(b)}}, J_{\text{zz(a)}} \approx 0$) has to be checked carefully, since such a scenario has been

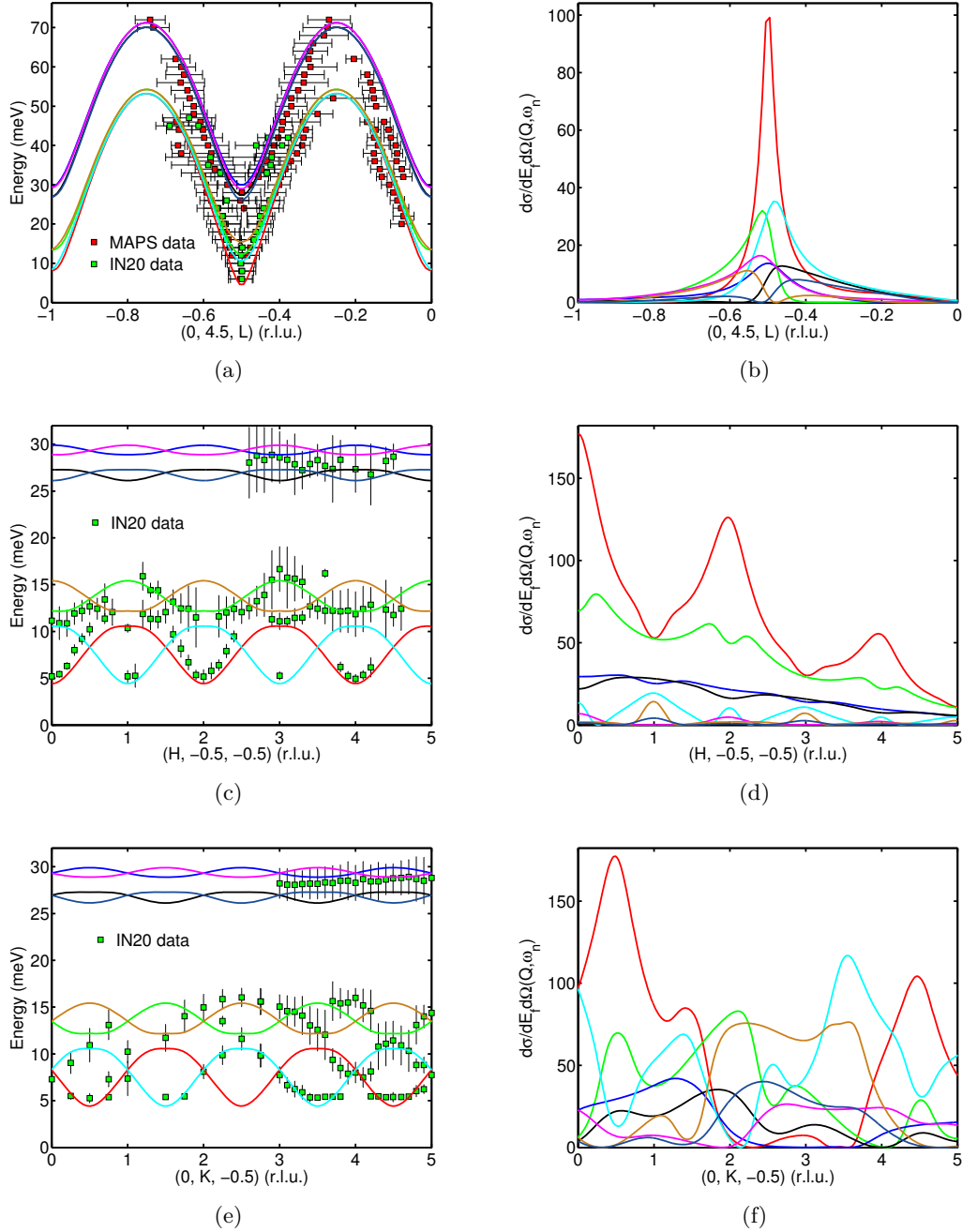


Figure 6.13.: *Model 3:* Calculated spin wave dispersion in intensities of CaV_2O_4 , assuming that one of the zigzag chains possesses ferromagnetic rung coupling, while the second possesses antiferromagnetic rung coupling. The following parameters have been used: $J_{\text{leg}}^1 = J_{\text{leg}}^2 = 29.5$ meV, $J_{\text{zz}(a)}^1 = 7.92$ meV, $J_{\text{zz}(b)}^1 = 11.0$ meV, $J_{\text{zz}(a)}^2 = -9.0$ meV, $J_{\text{zz}(b)}^2 = -6.48$ meV, $J_{\text{int}(a)}^a = J_{\text{int}(a)}^b = 0.17$ meV, $J_{\text{int}(b)}^a = J_{\text{int}(b)}^b = 0.62$ meV, $D_1 = D_2 = 0.08$ meV. In addition the data obtained from IN20 and MAPS are shown.

proposed by both experiment and theory (see Chapter 5 and [158, 89]).

Model 4: The investigations reveal no reasonable results for the case of both chain units being spin ladders and thus such a scenario can be excluded immediately. The situation improves, if only one of the two chains is assumed to be a spin ladder, while the other one remains a frustrated chain with antiferromagnetic zigzag coupling. In this case one obtains the spin wave spectra depicted in Fig. 6.14, where the following coupling parameters were chosen: chain 1: $J_{\text{leg}}^1 = 29.5$ meV, $J_{\text{zz(a)}}^1 = 8.28$ meV, $J_{\text{zz(b)}}^1 = 11.5$ meV; chain 2: $J_{\text{leg}}^2 = J_{\text{zz(b)}}^2 = 23.5$ meV, $J_{\text{zz(a)}}^2 = -6.0$ meV. Note, that in the current case the two leg couplings J_{leg}^1 and J_{leg}^2 are not equal anymore. Further it has to be pointed out that chain 2 is not a pure ladder, since it was necessary to introduce a small ferromagnetic contribution $J_{\text{zz(a)}}^2$ along the second zigzag path.

Compared to the previous models, the current one has some differences in the calculated spin wave spectra. For instance, the calculations reveal the appearance of an additional almost flat mode at around $E \approx 80$ meV, in addition to the characteristic double spin wave structure. The exact position of this mode is mainly controlled by the size of the ferromagnetic coupling $J_{\text{zz(a)}}^2$ and is shifted upwards if the strength of this coupling increases. Such a mode was not observed experimentally, however, its corresponding calculated intensity is very weak, such that an experimental detection might not be possible.

Another interesting feature is the completely flat mode at $E \approx 28$ meV. In contrast to the previously presented solutions this mode shows absolutely no dispersion and therefore should show up in the TAS scans as a narrow and resolution limited peak. However, the IN20 data revealed a quite broad feature at this energies, indicating a finite bandwidth of this mode. In addition, the intensity distribution of the spin waves in the vicinity of the magnetic zone centre along Q_L is strongly asymmetric, a behaviour which has not been observed experimentally. Altogether it seems unlikely that the ladder model can explain the spin wave spectra of CaV_2O_4 .

Apart from the models discussed in this section, no other sets of considerably different parameters were found that match the observed spin wave dispersion. If one additionally considers the corresponding spin wave intensities, the calculations reveal only *one* model in agreement with the data. This model (model 3) is characterized by two different chain units, both possessing strong antiferromagnetic leg exchanges and frustrated antiferromagnetic and ferromagnetic zigzag interactions, respectively.

Before studying the best model in more detail, it is useful to include a short discussion about the role of anisotropy on the spin wave spectra. The single ion anisotropy in CaV_2O_4 is important to stabilize the Néel order at low temperatures, with the spins

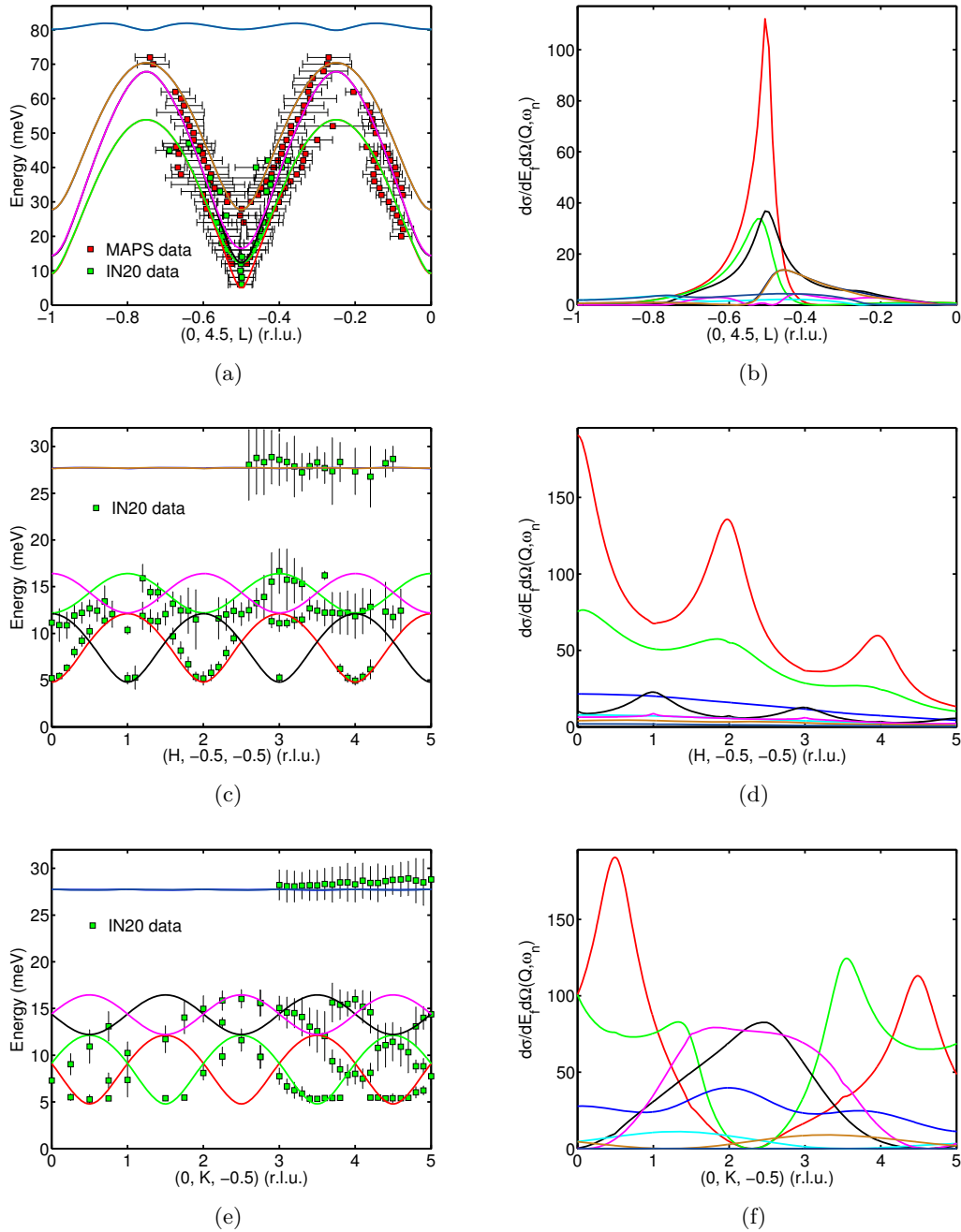


Figure 6.14.: *Model 4:* Calculated spin wave dispersion in intensities of CaV_2O_4 , assuming that one of the zigzag chains possesses antiferromagnetic rung coupling, while the second one is a spin ladder with antiferromagnetic coupling along one of the zigzags and weak ferromagnetic coupling along the other zigzag rung. The following parameters have been used: $J_{\text{leg}}^1 = 29.5$ meV, $J_{\text{leg}}^2 = 23.5$ meV, $J_{\text{zz}(a)}^1 = 8.28$ meV, $J_{\text{zz}(b)}^1 = 11.5$ meV, $J_{\text{zz}(a)}^2 = -6.0$ meV, $J_{\text{zz}(b)}^2 = 23.5$ meV, $J_{\text{int}(a)}^a = J_{\text{int}(a)}^b = 0.16$ meV, $J_{\text{int}(b)}^a = J_{\text{int}(b)}^b = 0.60$ meV, $D_1 = D_2 = 0.08$ meV. In addition the data obtained from IN20 and MAPS are shown.

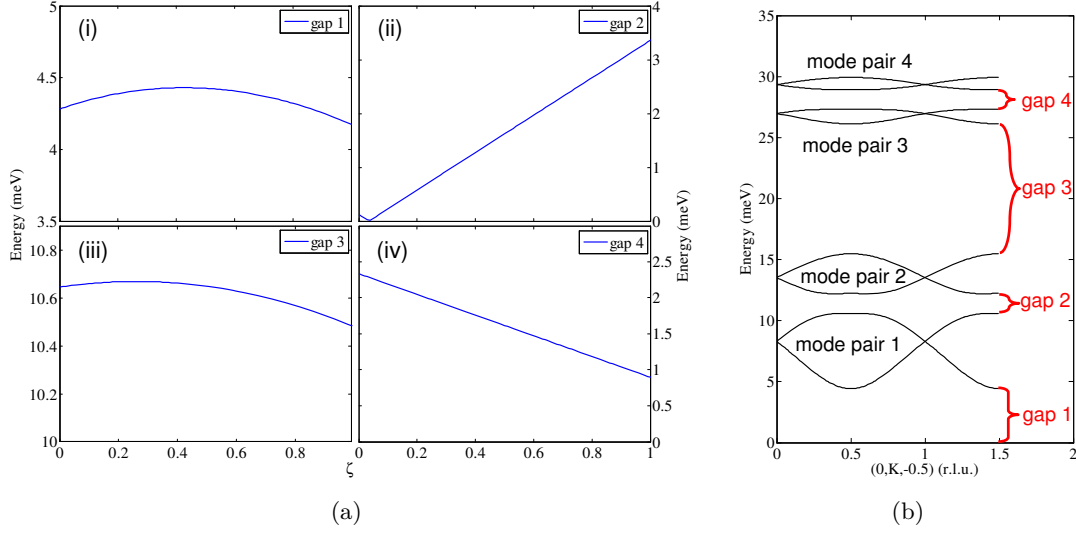


Figure 6.15.: Dependence of the CaV_2O_4 spin wave spectra on the ratio ζ of the single ion anisotropy parameters D_1 and D_2 . (a) The size of the various energy gaps being present in the spin wave spectra of CaV_2O_4 as a function of ζ . The calculations were performed at the magnetic zone centre at $Q = (0, 0.5, -0.5)$ and the utilized magnetic exchange coupling parameter correspond to those of model 3 (see Fig.6.13). (b) Part of the calculated spin wave spectra along $(0, K, -0.5)$ to show the four energy gaps. For the figure $\zeta = 0.5$ was assumed.

being collinear within each chain unit, but canted between those chains. The average spin direction is along the crystallographic b -direction, such that the anisotropy can be modeled approximately with the expression given in Eq. C.79. Due to the crystal anisotropy the magnetic moments below T_N are no longer able to rotate freely, causing an energy gap in the magnetic spin wave spectrum.

So far, all calculations have been performed assuming equal anisotropy values $D_1 = D_2$. Those parameters have been set to be positive, implying that the anisotropy is of single ion type⁸. However, investigations of the crystal structure reveal that the two inequivalent magnetic sites in CaV_2O_4 have very different octahedral environments, which would give rise to different anisotropy values. In particular, it was found that the spins point along the easy axis of chain 1, indicating the single ion character of the anisotropy, while the spins of chain 2 point away from their easy axis direction and tend to follow the spins of chain 1 (cf. Fig. 5.34). This implies that the single ion anisotropy of chain 2 spins might be very weak or of easy-plane type [158].

Due to the 3D exchange coupling of the spin moments, the size of the energy gap is influenced equally by the parameters D_1 and D_2 . For realistic exchange parameters

⁸Note the convention that is used in the spin Hamiltonian (Eq. C.79).

(e.g. those obtained for model 3) it was found that the gap size only varies marginally with the ratio D_1/D_2 and is mostly determined by the sum $D = D_1 + D_2 \approx 0.16$ meV. Therefore, if one wants to study the implications of inequivalent anisotropy parameters on the spectra, it is appropriate to introduce the parameter ζ with $D_1 = \zeta D$ and $D_2 = (1 - \zeta)D$, such that the gap size is kept at its experimentally observed value of ≈ 4.4 meV. Calculations of the spin wave dispersion at the magnetic zone centre as a function of ζ reveal that the introduction of different anisotropy parameters strongly influences the splitting of the spin wave mode pairs as well as the bandwidth of those pairs. To exemplify this issue, Fig. 6.15(a) displays the size of the mode pair splitting at the magnetic zone centre as a function of ζ , where the exchange parameters of model 3 have been used. While the energy gap between the ground state and the lowest spin wave mode as well as the one between the two lower and upper mode pairs are only marginally effected by unequal anisotropy parameters, a strong dependence can be observed for the gap between the two lower pairs and that between the two upper ones. For the particular set of exchange parameters presented here, the gap between the two lower mode pairs increases significantly if D_1 increases compared to D_2 , while in the case of the upper mode pairs the trend is vice versa.

Even though, the exact effect of D_1 and D_2 on the spectra also depends on the particular set of exchange interactions, a detailed modelling of the experimental data including the resolution of the instrument will provide more information about the relative strengths of D_1 and D_2 .

6.4.3. Resolution effects

Using the exchange and anisotropy parameters of the best model (model 3) as a starting point, selected scans from the IN20 experiment have been simulated. To do so, the program `rescal` has been employed [76, 75]. This program allows scans of a triple axes spectrometer to be simulated by calculating the particular instrumental resolution function using a 4D Monte Carlo convolution, while taking into account the particular dispersion that is given by the underlying model. By comparing the calculated and measured scans and adjusting the model parameters and the linewidth of the spin wave excitations, it was possible to gain detailed information about the model and to study anomalous line broadening effects. The correctness of the calculated instrumental resolution has been verified by comparing it to scans through the incoherent elastic line. For instance, for a scan at $Q = (0, 4.0, -0.5)$ (where no magnetic Bragg peak is present), a width of $\approx 1.0(2)$ meV has been obtained, which is in good agreement with the calculated resolution at this position of $dE = 0.91$ meV.

The spin wave scattering was assumed to have a Gaussian line shape. For CaV₂O₄ the model reveals eight spin wave modes, such that the magnetic scattering function is given by:

$$S(\mathbf{Q}, \omega) = \sum_{n=1}^8 \frac{C}{1 - e^{-\frac{\omega_n}{k_B T}}} \frac{s_n(\mathbf{Q})}{\gamma_n} e^{-4 \ln 2 \left(\frac{\omega - \omega_n}{\gamma_n}\right)^2}, \quad (6.18)$$

where the sum runs over all spin wave modes with energy ω_n , scattering intensity s_n and (FWHM) linewidth γ_n . Further, C is a constant and the exponential prefactor accounts for Bose statistics.

In the case of an ideal collinear Heisenberg 3D antiferromagnet, the linewidth of the detected magnetic excitations is only limited by the resolution of the spectrometer, since the excited magnons do have an infinite lifetime, which in return leads to $\gamma \rightarrow 0$, such that the scattering function $S(\mathbf{Q}, \omega)$ shows a delta-function-like resonance at the spin wave excitation energy. However, in real systems various effects, e.g. quasi-particle interactions or a fine-splitting of the spin wave modes due to additional terms in the spin Hamiltonian can alter the linewidth of the observed excitations.

In order to find out whether the spin wave modes show a significant broadening, the following strategy was used for modeling the scans obtain on IN20. Firstly, the spin wave linewidth was assumed to be much smaller than the instrumental resolution (e.g. $\gamma \sim 0.25$ meV) and the free model parameters were adjusted manually in order to find the most suitable match between the simulation and the experimental data⁹. In particular the focus was set on ‘fine-tuning’ the intrachain exchange parameters as well as the single ion anisotropy values, while the interchain interactions were estimated as discussed earlier in this section. In a second step, the linewidths of the eight spin wave modes were also adjusted until the best match was found.

Figure 6.16(a) displays two selected constant wavevector scans measured with the IN20 spectrometer; one performed at the magnetic zone centre at $Q = (0, 4.5, -0.5)$ and the second at the magnetic zone boundary at $Q = (0, 4.0, -0.5)$. The solid red line in this figure represents the best fit to the experimental data and the corresponding fit parameters are listed in Table 6.1. For comparison, the dotted black line in Fig. 6.16(a) represents a simulated scan using the exchange parameters of model 4 (ladder model). In particular the broad peak at ≈ 28 meV could not be reproduced correctly, underlining the failure of the ladder model to describe the experimental data.

⁹Since both, the spin wave excitations and the instrumental resolution are assumed to give Gaussian linewidths, the convolution of both function leads to another Gaussian function with $\Gamma = \sqrt{\gamma_{\text{sw}}^2 + \gamma_{\text{instr.}}^2}$, which in case $\gamma_{\text{sw}} \ll \gamma_{\text{instr.}}$ is strongly dominated by $\gamma_{\text{instr.}}$.

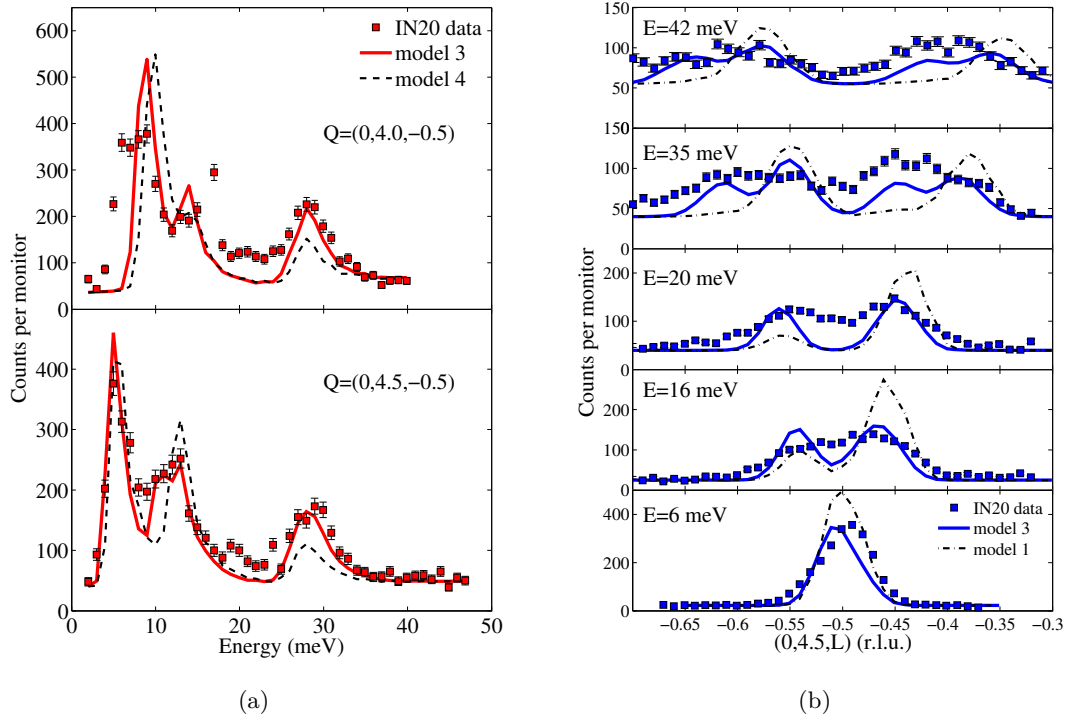


Figure 6.16.: Comparison of IN20 scans with theoretical calculations. (a) Constant Q scans at the magnetic zone boundary (top) and magnetic zone centre (bottom) along Q_K . The red and black solid lines represent the calculated spin wave cross-section of models 3 and 4, convolved with the resolution function of the spectrometer. Note that the feature at ≈ 17 meV in the top figure is not magnetic in nature, but spurious. (b) Various constant energy scans at $Q = (0, 4.5, Q_L)$. The blue and black solid lines correspond to spin wave calculations using models 3 (for parameters see Table 6.1) and 1 (see Fig. 6.11).

The numerical investigations reveal two important results. First of all, it was found that the introduction of inequivalent anisotropy parameters $D_1 \gg D_2$ leads to a significant improve of the fit. Setting $D_1 = 2.75 \cdot D_2 = 0.11$ meV introduces a gap between the two lower mode pairs of the spectra ($\Delta_2 = 2.44$ meV), which was necessary to model the low energy section of the constant Q -scans correctly. Further, the energy gap between the ground state and the lowest excitation branch was determined to be $\Delta_1 = 4.47$ meV.

At this point it should be mentioned, that the accuracy of the extracted anisotropy and magnetic exchange parameters is limited by the fact that those parameters do not influence the spectra independently but are correlated so that slightly different values also lead to reasonable results. Based on the findings of the numerical investigations, the uncertainties of the fit parameters were estimated to be approximately ten percent of their given value.

Table 6.1.: Best parameter from the spin wave model (in meV).

chain 1	J_{leg}^1	$J_{\text{zz(a)}}^1$	$J_{\text{zz(b)}}^1$	D_1
	30(3)	11(1)	7.9(8)	0.11(1)
chain 2	J_{leg}^2	$J_{\text{zz(a)}}^2$	$J_{\text{zz(b)}}^2$	D_2
	30(3)	-7.8(8)	-5.7(6)	0.04(1)
interchain	$J_{\text{int(a)}}^a$	$J_{\text{int(a)}}^b$	$J_{\text{int(b)}}^a$	$J_{\text{int(b)}}^b$
	1.5(2)	2.0(2)	1.5(2)	2.0(2)

The second considerable result of the resolution studies is, that the observed spin wave excitations are *not* limited by the instrumental resolution. In order to achieve reasonable agreement between the simulation and the IN20 constant Q -scans, the introduction of a noticeable linewidth broadening of the spin wave excitations was necessary. The particular scans depict in Fig. 6.16 have been modelled using spin wave linewidths of $\gamma_{1-4} = 1.5$ meV for the four lower modes and $\gamma_{5-8} = 2.5$ meV for the four upper ones and similar results have been obtained from simulating other constant Q -scans. It is important to notice that the difference in broadening between the upper and lower modes is not an artefact of certain single scans but turned out to be the case for all investigated scans. The reason for this anomalous spin wave broadening is not entirely clear at the moment and remains a matter of speculations. This issue will be addressed in the discussion section.

Despite the generally excellent agreement between model 3 and the experimental data, the simulated spectra at $Q = (0, 4.0, -0.5)$ reveals some minor discrepancies at low energies. In detail, the calculated energy gap at the magnetic zone boundary is $\Delta_1 \approx 8.61$ meV, while the experimentally observed gap has almost the same value than the one at the magnetic zone centre (≈ 4.5 meV). Indeed, a careful investigation of all measured constant Q_K -scans revealed almost no change of the lowest energy gap as a function of Q_K . This behaviour cannot be explained within linear spin wave theory and might indicate that an additional flat mode located at ≈ 5 meV appears in the spectra along Q_K (cf. Fig. 6.8(b)). However, the origin of such a mode remains unclear at the moment. In contrast, the calculated dispersion along the Q_H -direction is in complete agreement with the experimental data (not shown).

Up to now the focus has been on the energy resolution, however, simulations have also been performed for a series of constant energy scans in the vicinity of the magnetic zone centre at $Q = (0, 4.5, -0.5)$, enabling the investigation of the resolution in Q_L . Those

scans are presented in Fig. 6.16(b), where the solid blue lines correspond to calculations using the parameters listed in Table (6.1)¹⁰. Even though, the simulated scans are able to reproduce the characteristic peak structure of the experimental data, the calculated Q -resolution turned out to be smaller than the experimentally detected widths. Those differences can be attributed to mosaic spread caused by monoclinic twinning and by a small amount of disorder that is present in the crystal. The monoclinic twinning was included in the simulations by averaging the differential neutron cross section at each position in energy-momentum space over the two twins, however, the fact that the twin pairs appear at slightly different positions in Q was neglected, giving rise to an additional broadening along this direction. The Q_L scan at $E = 20$ meV displays a particularly strong amount of peak broadening. The MAPS data revealed the appearances of an optical phonon mode at this energy (cf. Fig. 6.5), which certainly adds to the broadening at this position.

In order to demonstrate the complete mismatch of the other models discussed earlier in the text, the dash-dotted lines in Fig. 6.16(b) correspond to simulations performed for model 1 (two chains with antiferromagnetic zigzag coupling). One clearly sees the discrepancies produced by this model due to the asymmetric intensity distribution around the magnetic zone centre. Similar behaviour was observed for models 2 and 4, proving their inability to explain the observed spectra.

6.5. Discussion

The spin wave analysis brought a clear picture of the variety of magnetic interactions in CaV_2O_4 , resulting in a complex spectra of spin wave excitations below the Néel temperature. It was unambiguously revealed that the two chain units, composed of two inequivalent magnetic sites, possess very different interactions along the zigzag rungs (afm or fm), while the dominant interactions for both cases are along the chains legs. In addition inequivalent single ion anisotropy values were found, taking account of the different crystal field potentials acting on the two magnetic sites. The obtained parameters enable a qualitative discussion about the interplay of spin and orbital degree of freedoms in CaV_2O_4 . This will be done in the following, where for the sake of convenience the two different chains will be discussed separately. It is also important to mention that for the following discussion the results of the nuclear and magnetic structure analysis presented in Chapter 5 are presumed to be known.

Chain 1: The two zigzag interactions $J_{zz(a)}^1$ and $J_{zz(b)}^1$ between neighboring magnetic

¹⁰The same spin wave linewidths in energy as for the constant Q -scans have been assumed.

sites of chain 1 are both antiferromagnetic and about 1/3 of the size of J_{leg}^1 (see Table 6.1), giving rise to moderate intrachain frustration. The small difference between the two zigzag couplings is a consequence of the monoclinic crystal distortion, which causes slightly different distances between the magnetic ions along the two zigzag paths. In terms of t_{2g} -orbital occupation, the ratios between the intrachain interactions points to a scenario, where the main local octahedral distortion is pseudo-tetragonal in nature, while the additional pseudo-orthorhombic distortion, induced by the monoclinic phase-transition at low temperatures, is only very weak, such that the orbital angular momentum is not entirely quenched (only the x and y component). In this case the t_{2g} orbital that is lowest in energy is the d_{xy} one, while the remaining two orbitals (d_{xz} and d_{yz}) stay almost degenerate. Thus, in the presence of finite spin-orbit coupling λ , the system can gain energy by forming complex orbital states $(d_{xz} \pm id_{yz})/\sqrt{2}$ [165]. As has been pointed out in Chapter 5, the local d_{xy} orbitals are arranged such that with respect to the zigzag chains, their lobes point towards each other along the legs of the chain (cf. Fig. 5.36). Since due to the flattening of the VO_6 octahedra along the local z -axis this orbital is lowest in energy, it is always occupied by one of the two V^{3+} d -electrons, thus giving rise to strong antiferromagnetic leg-coupling. On the other hand, the remaining two t_{2g} orbitals favour complex states and therefore neighbouring orbitals along the zigzags share the remaining second d -electron (see Fig. 5.36(a)). This interaction is also antiferromagnetic; however, it is weaker than the leg-coupling. Using an effective Hamiltonian with spin-orbit super exchange interactions, Di Matteo *et al.* investigated the various coupling scenarios between magnetic V^{3+} -sites, whose t_{2g} -orbitals point towards each other (so called $dd\sigma$ -bonding) [165]. Applying their findings to the case of CaV_2O_4 type 1 chains, the ratio between leg and zigzag interactions (assuming perfect site symmetry) is given by $\frac{J_{zz}^1}{J_{\text{leg}}^1} = \frac{1-2\eta}{2(1-\eta)}$, where $\eta = \frac{J_H}{U}$ is a small parameter which depends on the size of the Hund-coupling J_H and the on-site Coulomb-repulsion U [158, 165, 166]. Based on photoemission spectroscopy data of other V^{3+} -compounds, it can be estimated that $\eta \approx 0.11$ [167, 168], which finally leads to $J_{zz}^1 \approx 0.44J_{\text{leg}}^1$. Even though, this ratio is slightly higher than that found from spinwave analysis, it is still highly consistent, especially if one considers the different interionic distances that appear in real CaV_2O_4 between spins along legs and between those along the zigzags.

The formation of complex orbitals $(d_{xz} \pm id_{yz})/\sqrt{2}$ due to spin-orbit coupling is also in agreement with the extracted single ion anisotropy of $D_1 = 0.11(1)$ meV acting on spins of chain 1. Spin-orbit coupling forces the spins to point along the local octahedral z -direction (\approx along the crystallographic b -direction), while the orbital angular momentum points antiparallel to it.

Chain 2: The situation for the second type of chains in CaV_2O_4 appears to be rather different. Here, the leg coupling is also antiferromagnetic and equally strong (with respect to that of chain 1), while the zigzag interactions are now ferromagnetic, with $J_{zz}^2 \approx -\frac{1}{4}J_{\text{leg}}^2$ (see Table 6.1). These findings suggest that the tetragonal distortion with a flattening of octahedra is also dominant in this case, such that the d_{xy} -orbital (being responsible for the leg coupling) is lowest in energy and occupied everywhere. However, the observed ferromagnetic zigzag interactions reveal that an additional pseudo-orthorhombic distortion becomes important, causing a complete lifting of t_{2g} orbital degeneracy. Chern *et al.* have shown that for a moderate orthorhombic distortion the system prefers an arrangement of staggered d_{xz} and d_{yz} orbitals along the zigzags, leading to antiferro-orbital order and thus to ferromagnetic zigzag exchange interactions [158] (see Fig. 5.36(c)). The ratio between the intrachain interactions of chain 2 can be estimated using an effective super-exchange model. Based on the results of Reference [165] one gets $\frac{J_{zz}^2}{J_{\text{leg}}^2} = -\frac{\eta}{1-\eta}$. Using $\eta = 0.11$ this leads to $J_{zz}^2 \approx -\frac{1}{10}J_{\text{leg}}^2$, a ratio considerably smaller than what has been found from spinwave analysis. Although the structural distortions being present in real CaV_2O_4 can cause slight changes in the electronic structure (e.g. they give rise to small differences between the two zigzag couplings), they cannot explain the relatively strong ferromagnetic rung exchange obtained from spin wave analysis. Another coupling mechanism that might contribute to the leg-exchange is super-exchange coupling via V-O-V bonds. As has been shown in Chapter (5), the V-O-V bond-angles between magnetic ions of chain 2 are slightly larger than 90° (see Table 5.10) and according to the well known Goodenough-Kanamori rules [10] such an arrangement gives rise to weak ferromagnetic exchange interactions. However, the strength of 90° superexchange interactions between V^{3+} -ions is expected to be rather small [134] and it remains uncertain if this effect can account for the interaction values determined by linear spin wave theory. It is also quite possible that the approximations included in linear spin wave theory simply lead to an overestimation of the size of exchange interactions.

The observed very weak single ion anisotropy acting on chain 2 spins can be interpreted as a direct consequence of the totally quenched orbital angular momentum due to pseudo-orthorhombic octahedral distortion, which strongly reduces the effects of spin-orbit coupling and consequently single ion anisotropy plays a negligible role in this case.

Interchain coupling: Interchain interactions in CaV_2O_4 are mediated via V-O-V superexchange between different Vanadium sites ($\angle \approx 120^\circ$) and are responsible for the development of long range magnetic order at low temperatures. Analysis of the spinwave spectra revealed that the size of this coupling is about 6% of the strongest intrachain coupling

(J_{leg}), a value slightly larger than that estimated numerically using the results from susceptibility measurements and assuming a system of coupled $S=1$ Haldane chains [119]. However, those calculations have been performed for an unfrustrated system, whereas interchain interactions in CaV_2O_4 are frustrated, giving rise to renormalization effects and thus to larger coupling strengths along the individual exchange paths.

Comparison with former results: In Section (5.2), the high temperature susceptibility data for CaV_2O_4 have been modelled by means of exact diagonalization calculations of a J_1 - J_2 -model, with $J_1 = J_{zz}$ and $J_2 = J_{\text{leg}}$. The best fit results were obtained with $J_{\text{leg}} \approx 20$ meV and $J_{zz} \approx 1$ meV, suggesting that the system consists of very weakly coupled $S = 1$ chains, in contrast to what has been found from spin wave analysis. Further, the size of the strong leg coupling obtained from susceptibility differs by about 30 % from the value obtained with the spin wave model. These discrepancies can be attributed to the fact that the susceptibility data have been analyzed with a simplified model, which did not account for the two different zigzag chains. Even though, the analysis has concentrated on the high temperature orthorhombic region, where the VO_6 octahedra are less distorted, differences in the resulting intrachain exchange parameter of both chain sites can still be expected. Therefore, these different interactions might effectively provide an overall magnetic response, which is very similar to that of a weakly coupled Haldane chain.

The anisotropy energy gap in CaV_2O_4 has been previously estimated on the basis of NMR measurements [136]. By approximating the system by an array of weakly coupled $S = 1$ chains and performing linear spin wave theory the gap size was estimated to be $\Delta_{\text{NMR}} = 5.5 - 8.4$ meV, with the corresponding overall single ion anisotropy of $D \sim 0.086$ meV. This value for the energy gap is slightly larger than that observed with INS ($\Delta_1 = 4.47$ meV). However, inelastic neutron scattering is the most direct probe of magnetic excitations and as such it provides the most accurate way for measuring the energy gap in the excitation spectra. Based on the smaller gap size obtained by INS, it is no surprise that the average single ion anisotropy per vanadium site $D/2 = (D_1 + D_2)/2 = 0.075$ meV has a smaller value than the one derived from the NMR data.

Effects of spin wave broadening: A very remarkable result from spin wave analysis is the observed linewidth broadening of magnetic excitations, which is particularly pronounced at the higher energy part ($E > 25$ meV) of the spin wave spectrum. This broadening cannot be explained within the current spinwave model and in the following possible mechanisms will be discussed which can cause such an effect.

The main restriction of linear spin wave theory is that it only accounts for single magnon

processes, while multi-magnon processes as well as interactions between magnons are neglected. In particular, only those terms of the spin wave Hamiltonian are considered, which are bilinear in the magnon creation and annihilation operators, assuming that the effects of higher order terms are small. In collinear antiferromagnets, the first higher order term is one that is biquadratic in the boson operators and it causes a renormalization of the corresponding spin wave energies [169]. The situation becomes more complicated if the magnetic structure consists of canted spins (as it occurs in CaV_2O_4 between spins of different magnetic sites). In this case an additional cubic term appears in the spin Hamiltonian as the first correction to linear spin wave theory. This term originates from coupling between transverse (one-magnon) and longitudinal (two-magnon) fluctuations of the magnetic moment and gives rise to a renormalization of the spin wave spectra and to spin wave damping. The latter is due to magnon decay processes and gives rise to finite lifetime effects, e.g. spin wave broadening [170].

The effect of longitudinal fluctuations, e.g. fluctuations of the spins amplitude, becomes important if the size of the magnetic moment is reduced with respect to the full ordered moment. Since, in CaV_2O_4 the magnetic moment is $\approx 1\mu_B/V^{3+}$, which is only half of the size of the expected full moment $\langle\mu\rangle = gS\mu_B \approx 2\mu_B$, this issue has to be considered. The reduction of the ordered spin moment can be attributed to zero point quantum fluctuations, a phenomena that appears very often in systems with low dimensional structures, e.g. where intrachain coupling is much larger compared to interchain coupling. Prominent examples are the $S = 1/2$ chain compound KCuF_3 , with $\mu \approx 0.5\mu_B/\text{Cu}^{2+}$ [171] and the $S = 1$ chain compound CsNiCl_3 , with $\mu \approx 1.0\mu_B/\text{Ni}^{2+}$ [172]. In a fully magnetically ordered system, almost all longitudinal signal appears as elastic scattering and gives rise to magnetic Bragg peaks. However, in case of a reduced ordered moment, the integrated Bragg intensity of magnetic peaks is lowered and since the overall (Q - and energy-) integrated scattering intensity per spin is a constant ($S(S+1)$), spectral weight from longitudinal scattering has to be shifted into the inelastic part of the spectra. This longitudinal scattering can either give rise to an additional longitudinal mode, which appears above the transverse spin wave modes at the magnetic zone centre [50, 52], or as continuum scattering resulting from multi-magnon excitations¹¹ [51, 173].

Affleck *et al.* have studied longitudinal fluctuations in quasi-one-dimensional ($S = 1$) antiferromagnets based on Landau-Ginsburg model [174]. They predict the existence of a longitudinal mode for systems, which are close to a quantum critical point, e.g. where the system is in the 3D ordered state, but very close to being disordered by quantum fluctuations. Generally, the longitudinal mode has a finite decay rate into a pair of

¹¹Note that multi-magnon scattering appears in both, transverse and longitudinal channels.

transverse (Goldstone)-modes. The particular lifetime (and therefore the linewidth of the mode) depends on how close the system is to such a quantum critical point. The intensively studied spin-1 chain-compound CsNiCl_3 has a strongly reduced ordered moment (see above) and an interchain-to-intrachain coupling ratio of only about 2% and therefore was found to be very suitable to show a longitudinal mode. Inelastic polarized neutron scattering experiments indeed confirmed the predictions and revealed a longitudinal mode for CsNiCl_3 [52].

Concerning CaV_2O_4 , the Néel state is believed to be more stable than in CsNiCl_3 , mainly due to the presence of single ion anisotropy acting on (half of the) CaV_2O_4 zigzag chains. Nevertheless, the reduced moment indicates the existence of longitudinal fluctuations and the observed spin wave broadening might be a direct result of two-magnon decay processes. Additionally, the canting between spins of neighbouring chains provides a further mechanism of damping and as such contributes to the mode broadening.

At energies higher than the interchain dispersion maximum (≈ 30 meV), where one-dimensional quantum behaviour dominates the spectra, additional magnetic continuum scattering can appear as a result of multi-magnon excitations. In fact, the experiment performed on MAPS indicates some additional scattering at the antiferromagnetic zone centre above the upper spin wave branch, which might be due to multi-magnon excitations. However, the contamination with phonon scattering prevents clear statements about this observation and polarized neutron scattering experiments are required to separate magnetic and non magnetic signal and to identify longitudinal fluctuations.

Quantum fluctuations are not the only mechanism that can lead to a reduction of the spin moment. In systems with unquenched orbital angular momentum, spin-orbit coupling can play an important role, e.g. antiparallel coupling between orbital and spin angular momentum can lead to a significant reduction of the overall magnetic momentum. Recent DFT (density functional theory) calculations for the $S = 1$ compound ZnV_2O_4 revealed that spin-orbit coupling accounts for the significant moment reduction ($\sim 68\%$) found in this compound [175]. Generally, for t_{2g} -systems, which show a large crystal field splitting between t_{2g} and e_g -orbital states, the orbital angular momentum can be expressed by an effective value $\mathbf{L} = -\alpha\mathbf{L}'$, where $\alpha \approx 1$ is a constant [157]. The spin wave analysis of CaV_2O_4 revealed that spin-orbit coupling might be important for at least half of the magnetic sites of the system (chain 1), where the formation of complex orbital states $(d_{yz} \pm id_{xz})/\sqrt{2}$ leads to antiferromagnetic zigzag interactions. These complex orbital states generate an orbital angular momentum $L_z = -\alpha L'_z = \mp\alpha$, which points opposite to the spins, thus leading to a reduced total magnetic moment $(2 - \alpha)\mu_B \approx \mu_B$ [158].

Additionally, spin-orbit coupling can also have a strong effect on the magnetic excitation spectrum. In the case of strong λ , the spin and orbital momentum operators \mathbf{S} and \mathbf{L} are no longer good quantum numbers and a new theory based on the total angular momentum $\mathbf{J} = \mathbf{L}' + \mathbf{S}$ is required in order to derive the elementary excitations of the system. This has been done by Chern *et al.* for the V^{3+} -spinel compounds [176]. They found, that the mixing of orbital and pure spin excitations leads to a strong renormalization of the energy spectra, resulting in a bandwidth-reduction with respect to the spin only case. Even though, it is not clear, how SO-coupling would modify the particular excitation spectrum of CaV_2O_4 , the strong energy renormalization could be a possible explanation for the very flat-shaped mode observed at low energies along the Q_K -direction in CaV_2O_4 .

Further, it can be speculated that t_{2g} orbital fluctuations are another possible source for the observed spin-wave broadening. Preliminary DFT calculations for the low-temperature monoclinic phase of CaV_2O_4 have pointed out that the t_{2g} level structure is only marginally effected by the pseudo-tetragonal and pseudo-orthorhombic octahedral distortions [177]. It is therefore possible, that the t_{2g} -orbital occupation continuously changes as a function of time, causing a fluctuation of magnetic exchange interactions and consequently leading to broadening effects in the magnetic excitation spectra. However, up to now, those effects have never been studied theoretically.

In summary, the observed spin wave broadening in CaV_2O_4 has three possible sources. Firstly, additional terms in the spin Hamiltonian, not considered in the framework of the currently employed linear spin wave theory can lead to an energy renormalization of the spin wave spectra. In this case the broadening is just an artificial, which accounts for the lack of the missing terms.

Secondly, zero point quantum fluctuations, resulting in a reduction of the magnetic ordered moment give rise to the appearance of longitudinal signal at higher energies. Longitudinal excitations have a finite lifetime and consequently lead to mode broadening effects. A polarized neutron scattering experiment would shed light on this issue. Finally, the spin orbit coupling can be another source of magnetic moment reduction and moreover orbital fluctuations might provide another source for linewidth broadening.

6.6. Conclusions

The inelastic neutron scattering investigations of CaV_2O_4 reveal a complex spin wave spectrum, which is characterized by dominant magnetic excitations along the direction of the V^{3+} -zigzag chains, thus underlining the low-dimensional character of the material.

The excitations in the antiferromagnetically ordered phase are gapped as a consequence of single ion anisotropy. Spin wave analysis based on a 32 sublattice model helped to understand the peculiar mode structure and to assign the leading exchange interactions and anisotropy parameters. The best observed model is characterized by very different magnetic interactions along the zigzag-rungs of the two symmetry inequivalent V^{3+} -chains. These different interactions were interpreted in terms of different orbital ordering pattern, resulting in ferro-orbital order of complex orbitals for type 1 chains and antiferro-orbital order for type 2 chains.

The investigations were completed by a resolution study of selected IN20 scans and a strong linewidth broadening for excitations above ≈ 25 meV was detected. Various possible sources of broadening have been discussed, however, a final answer concerning this issue can not be given at the moment and additional experiments are necessary.

7. Conclusions and perspectives

In this thesis a detailed experimental study of two different types of low-dimensional quantum magnets has been presented.

The first part of the thesis (Chapter 4) focuses on the investigations of the spin dynamics of three Mn_6 -based single molecule magnets (SMMs). These magnetic molecules all possess the same magnetic core, but show slight differences in their ligand cages. Due to the fact that the magnetic (superexchange)-interactions between neighbouring Mn^{3+} -ions lie in the cross-over region from antiferromagnetic to ferromagnetic, those tiny structural differences have a significant effect on the magnetic properties of the molecules. As a result, two of the molecules have a $S = 12$ (high spin) ground state, while the third variant possesses a $S = 4$ (low spin) ground state. Furthermore, all three molecules show very different energy barriers for the reversal of the magnetization. Inelastic neutron scattering (INS) enabled the exploration of the low energy part of the magnetic excitation spectrum and (by comparing the findings to results from frequency domain magnetic resonance spectroscopy) all observed spin excitations could be accurately characterized. It was found, that a key feature of all three Mn_6 -SMMs is the presence of low lying excited S -states, which are nested within the (zero-field split) ground state multiplet and only with INS it was possible to unambiguously identify those states. The experimental findings allowed the parameter of the microscopic spin Hamiltonian to be determined and based on this, conclusions concerning the peculiar relaxation dynamics of these molecules could be drawn. It was found, that the energy barrier is strongly affected by the low lying S -multiplets, because those provide extra paths for the reversal of the magnetization and consequently lead to a lowering of the barrier. Generally it can be stated, that the Mn_6 -compounds represent a class of SMMs, for which the commonly encountered giant spin approximation (GSA) does not hold anymore. The GSA assumes a well isolated spin ground state, a situation that is certainly not given for the Mn_6 -clusters, where isotropic exchange interactions and crystal field effects have the same energy scale.

The fact, that all three investigated molecules possess different ground spin values S and single ion anisotropy parameters D enables new strategies to be discussed for increasing

the barrier height of SMMs. The experimental results confirmed recent theoretical findings, which pointed out, that a simultaneous increase of the total single ion anisotropy of the cluster and the total spin S , is not as fruitful approach to increase the barrier height, as the GSA result $U \approx |D|S^2$ would suggest, since both values are intrinsically coupled together [17, 36, 35].

In the particular case of the Mn_6 clusters, the strategy to tune the barrier height would be the following: One has to find suitable ligands that distort the Mn_6 cage in such a way, that the ferromagnetic superexchange coupling between the molecules increases. This would help to shift the parasitic excited S -states toward higher energies and thus prevent short-cuts for the magnetization reversal. Calculations have shown that in such a case the barrier height could reach values as high as $U \sim 105$ K [90, 89]. However, even this value is by far too small for industrial applications. Therefore, new routes should be considered, such as increasing the single ion anisotropy of the molecule. For example, this could be done by substituting the $3d$ -transition metal ions by $4f$ -elements, which generally have a large anisotropy and a large magnetic moment. First promising results concerning this route have been published already [178].

The second part of this thesis provides an in-depth study of the nuclear and magnetic properties of the quasi-one-dimensional spin-1 Heisenberg antiferromagnet CaV_2O_4 . The magnetism in CaV_2O_4 arises from the partially filled t_{2g} -orbitals of the V^{3+} -ions, which in addition give an orbital degree of freedom to the system. The material consists of (two symmetry inequivalent) weakly coupled double-chains of edge-sharing VO_6 -octahedra, where the particular octahedral staggering creates a zigzag-like arrangement of the vanadium ions. This in return gives rise to strong magnetic direct exchange interactions between nearest and next nearest neighbour vanadium ions and to geometrical frustration. Furthermore, the zigzag motif also establishes between the chains, such that interchain interactions (even though they are weak) are frustrated as well. The nuclear structure analysis (Chapter 5.1) revealed that the material undergoes a structural phase-transition from orthorhombic to monoclinic at $T_c \approx 147$ K, accompanied by a lifting of both the frustration and the orbital degeneracy. The resulting preferred exchange paths lead to antiferromagnetic long range order at $T_N \approx 71$ K. It was the main purposes of this thesis to understand this complex interplay of lattice, spin and orbital degree of freedom in CaV_2O_4 and to investigate the mechanisms that are responsible for the phase-transitions. A combined refinement of neutron and synchrotron diffraction data enabled the detailed investigation of distortions among the VO_6 -octahedra, which in turn allowed conclusions on the electronic structure of the system to be drawn. It was found, that at high temper-

atures the octahedra are compressed, partially lifting the degeneracy of the t_{2g} -orbitals and give rise to strong antiferromagnetic leg-interactions. In contrast, the interactions along the zigzag-paths are significantly weaker; a result, which was confirmed by the theoretical analysis of high temperature dc-susceptibility data (Chapter 5.2). Below T_c , the degree of octahedral distortion increases and significant differences in the octahedral environments of the two inequivalent vanadium sites have been observed. These differences manifest in a canting of the spins in the magnetically ordered phase of CaV_2O_4 . The magnetic structure has been solved by means of single crystal neutron diffraction (Chapter 5.3), which revealed a strongly reduced value of the ordered magnetic moment per V^{3+} -ions.

The experimental findings at low temperatures have been discussed in terms of orbital ordering and three possible ordering scenarios have been proposed by theory, in agreement with the magnetic structure [158]. In order to identify a unique pattern for each vanadium chain, a detailed study of the magnetic excitation spectrum of CaV_2O_4 was necessary (Chapter 6). The corresponding INS measurements clearly probed the one-dimensional character of the system, showing strong spin wave excitations along the chain direction and a much weaker dispersion perpendicular to the chains. Furthermore, the data revealed the existence of an anisotropy gap below T_N . The observed spectra was analysed by means of linear spin wave theory and the leading intra- and inter-chain interactions could be extracted. It was found that the two inequivalent vanadium zigzag-chains of CaV_2O_4 both have strong antiferromagnetic leg-interactions, but differ significantly in their zigzag-rung interactions, which are frustrated antiferromagnetic in one case and frustrated ferromagnetic in the other case. These different interactions were interpreted in terms of different orbital ordering patterns, resulting in a ferro-orbital order for type 1 chains and in a antiferro-orbital order for type 2 chains. However, the determined orbital pattern indicate that the nuclear phase transition has (at least for one type of chains) no significant influence on the particular orbital structure. This raises the question whether orbital ordering in CaV_2O_4 is the primary effect that causes the structural transition or if it just arises accidentally as a consequence of another symmetry breaking mechanism. Preliminary density functional theory results seem to support the latter conjecture [177], suggesting that the primary mechanism that drives the phase-transition is the lifting of intrachain frustration accompanied by the onset of strong one-dimensional magnetic correlations along the V^{3+} -chains.

Finally, the analysis of the spin wave spectra revealed a significant line broadening for the high energy spin waves. Various scenarios can lead to such broadening effects, including quantum-fluctuations, unresolved mode splitting or multi-magnon interactions.

Even though, the observed reduced moment value seems to support the picture of low-dimensional quantum fluctuations, a final answer concerning this issue cannot be given so far, thus providing a starting point for future investigations. In fact, additional experiments using polarized inelastic neutron scattering are already planned. This technique is not only suited to separate magnetic signal from non-magnetic background, but also to probe the character of the magnetic excitations (transverse or longitudinal).

Possible future experimental work on CaV_2O_4 should also include the study of magnetic excitations above the magnetic phase-transition. In this region, the magnetic excitations are purely one-dimensional and characteristic features of the $S = 1$ antiferromagnetic chain, such as the Haldane spin gap, should emerge. The simple Haldane chain has a gap of $\Delta \approx 0.41J$. With the intra-chain coupling determined for CaV_2O_4 , this would suggest a gap in the region $8 \leq \Delta_{\text{CaV}_2\text{O}_4} \leq 12$ meV. However, the presence of frustration and anisotropy will alter this value significantly and also new exotic magnetic phases have been predicted from theory, e.g. chiral phases [56].

Concerning the issue of orbital ordering in CaV_2O_4 , a final answer could be given by using resonant x-ray scattering. Due to its ability to separately measure the spin and orbital contributions to the magnetic cross section this technique is perfectly suited to study orbital ordering phenomena. However, the fact that CaV_2O_4 consists of two inequivalent chains, with possibly different orbital order, will complicate such an experiment.

From the theoretical point of view, an important improvement of the current spin-wave model would be given by including relativistic spin-orbit coupling into the calculations. The importance of spin-orbit coupling for CaV_2O_4 is indicated by the observed single ion anisotropy that stabilizes the Néel order. Additionally, the spin wave analysis revealed that for CaV_2O_4 type 1 chains the t_{2g} -orbitals remain partially degenerate and thus in the presence of finite spin-orbit coupling the system could gain energy by forming complex orbitals. Calculations of the spin-wave excitations for vanadium-spinel compounds revealed, that the mixing of orbital and pure spin excitations leads to a strong renormalization of the energy spectra, resulting in a bandwidth-reduction with respect to the spin only case [176]. Therefore, the extended model might be able to account for the small discrepancies between the INS data and the conventional spin wave model at low energies.

A. Exact diagonalization

The static magnetic susceptibility is a thermodynamic quantity that contains essential information about the exchange interactions between magnetic ions in a system. To extract this information from the measured data two basic things are required. First of all, a model is needed, which guarantees an adequate description of the system under investigation and secondly this model has to be solved on either an analytical or a numerical basis. In most cases of condensed matter physics the enormous number of interacting particles ($O(N) \sim 10^{23}$) makes it impossible to obtain an exact solution for the given model and one is reliant on approximations. Such approximations have to be chosen in such a way, that they allow the properties of interest of the model to be accessed, without significantly changing the underlying physics of it.

For the investigation of low-dimensional systems, such as small clusters of interacting particles (see Chapter 4) or one-dimensional spin chains (Chapter 5), the method of exact diagonalization (ED) has become a very powerful tool. The idea of this method is already fully described by its name, viz. it provides numerically exact results for a finite lattice system by direct diagonalization of the matrix representation of the system's Hamiltonian in an appropriate many-particle basis [179].

The static properties of a quantum mechanical problem can be in general expressed by the time-independent Schrödinger equation:

$$\mathcal{H}|\Psi\rangle = E|\Psi\rangle. \quad (\text{A.1})$$

In this equation \mathcal{H} is the model Hamiltonian of the system, E represents the eigenvalues and $|\Psi\rangle$ the eigenstates of it. Since, we are interested in magnetic interactions between localized spins, an appropriate Hamiltonian is given by the Heisenberg model

$$\mathcal{H} = \sum_{ij} J_{ij} \mathbf{S}_i \mathbf{S}_j. \quad (\text{A.2})$$

The idea is now to rewrite $|\Psi\rangle$ as a combination of adequate basis states and then obtain the matrix elements of \mathcal{H} in that basis. For spin systems a suitable basis is given by the eigenstates of $\{S_i^z, i = 1, \dots, N\}$, where S_i^z is the z component of the spin operator

at site i and z is the quantization axis. The $\hat{\mathcal{H}}$ matrix can finally be diagonalized using standard routines implemented in libraries such as LAPACK [180].

The main disadvantage of the ED method is, that the dimension of the $\hat{\mathcal{H}}$ matrix grows exponentially with the system size N , being $(2S+1)^N$, where S is the spin value. Similar to the matrix dimension, the memory requirements and the CPU time for diagonalizing the matrix increase, so that even with the fastest computers available today, one is restricted to a small number of system sites. The ED method will therefore be only appropriate for a given problem, if the finite system under investigation gives an adequate approximation of the real system ($N \rightarrow \infty$).

In order to be able to calculate largest possible system sizes it is also helpful to take advantage of the symmetries of a given system, because the dimension of the matrix to be diagonalized is then significantly reduced. Examples of symmetries are e.g. translation symmetry, which can be obtained by introducing periodic boundary conditions and further the conservation of certain quantum numbers, like the total spin S_z .

Once the eigenvalue problem for a given model is solved, the calculation of the thermodynamic expectation values can be performed using the energy representation of the partition function for L sites

$$Z_L = \text{tr}(e^{-\beta\mathcal{H}}) = \sum_n e^{-\beta E_n}, \quad (\text{A.3})$$

with $\beta = 1/k_B T$ and where the sum runs over all eigenvalues E_n of the system. From expression A.3 one can calculate the thermodynamic expectation value of a quantity O using

$$\langle O \rangle = \frac{\text{tr}(O e^{-\beta\mathcal{H}})}{Z_L}. \quad (\text{A.4})$$

Following this procedure, it is possible to obtain an expression for the static susceptibility in zero field (see e.g. [181]):

$$\chi = \frac{1}{L} \left. \frac{\partial \langle M \rangle}{\partial H} \right|_{H \rightarrow 0} = \frac{\beta}{L} \frac{\text{tr}[(S_{\text{tot}}^z)^2 e^{-\beta\mathcal{H}}]}{Z_L}. \quad (\text{A.5})$$

Here $\langle M \rangle/L$ is the magnetization of a spin chain with L sites and S_{tot}^z denotes the z value of the total spin.

Formula A.5 is the one used by the program `fulldiag_evaluate`, which is part of the ALPS software package and which was used in Section 5.2 to calculate the temperature dependent susceptibility.

B. Additional details about the nuclear structure of CaV_2O_4

The appendix provides a collection of additional results from nuclear diffraction measurements of CaV_2O_4 powder and single crystals.

B.1. $T = 160\text{K}$ synchrotron data

In addition to the data sets measured at $T = 10\text{ K}$ and $T = 300\text{ K}$, powder diffraction measurements using synchrotron radiation were also performed at $T = 160\text{ K}$. The refined powder pattern as well as the weighted difference plot are shown in Fig. B.1 and the corresponding atomic coordinates and isotropic temperature factors are listed in Tab. B.1. The crystal space group was found to be the same as for room-temperature phase ($Pnam$) and no contribution of the low temperature monoclinic phase were found. As an example, Fig. B.1 displays a selected part of the powder pattern showing all three measured spectra. The only difference between the $T = 300\text{ K}$ and $T = 160\text{ K}$ data is the slight shift of the (131)-Bragg reflection. This is due to the slightly different lattice parameters, which are listed in Tab. B.2.

$Pnam$	x/a	y/b	z/c	B(\AA^2)
Ca	0.7560(3)	0.6548(2)	0.25000	1.10(5)
V1	0.4317(2)	0.6115(2)	0.25000	0.06(2)
V2	0.4192(2)	0.1051(1)	0.25000	0.06(2)
O1	0.2097(6)	0.1597(5)	0.25000	0.46(6)
O2	0.1157(5)	0.4728(5)	0.25000	0.46(6)
O3	0.5194(7)	0.7769(5)	0.25000	0.46(6)
O4	0.4195(5)	0.4270(5)	0.25000	0.46(6)

Table B.1.: Atomic coordinates of CaV_2O_4 in orthorhombic space group $Pnam$ as obtained from the nuclear structure refinement using synchrotron data at $T = 160\text{ K}$. The z coordinate is at fix position $z = 1/4$.

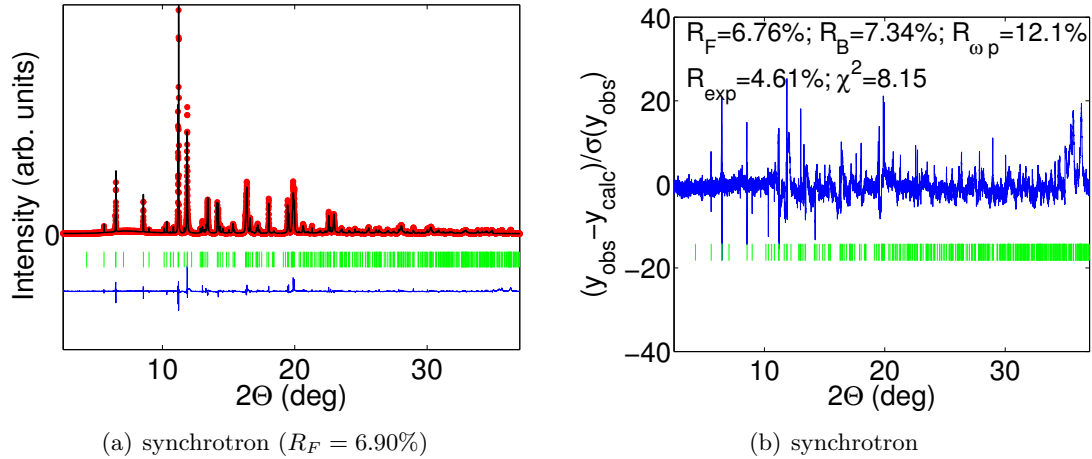


Figure B.1.: (left) Powder diffraction pattern of CaV_2O_4 measured with synchrotron radiation at $T = 160$ K. The red dots indicate the measured data, the black line indicates the calculated data, the blue line represents the difference of both and the green bar indicate the (hkl) positions. (right) Weighted difference plot for the fit of the corresponding figures on the left side. The inset contains the fit agreement factors.

T	a(Å)	b(Å)	c(Å)	α	V(Å ³)
300 K	9.20800(5)	10.67866(5)	3.00596(2)	90.0	295.573(3)
160 K	9.19717(7)	10.67626(7)	2.99980(3)	90.0	294.554(4)
10K	9.19568(6)	10.68070(6)	2.99748(3)	90.755(1)	294.376(4)

Table B.2.: Lattice vectors of CaV_2O_4 for three different temperatures as obtained from the nuclear structure refinement using Synchrotron data. The $T = 300$ K and 160 K data were refined in space group $Pnam$ and the $T = 10$ K data in $P2_1/n11$. $\beta = \gamma = 90^\circ$

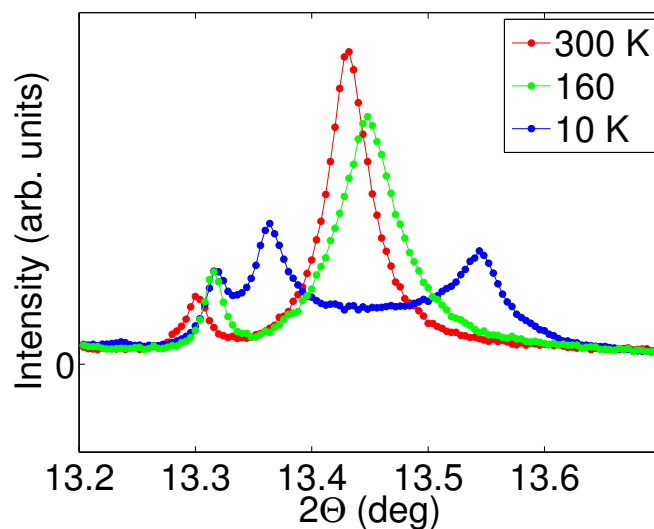


Figure B.2.: Selected part of the synchrotron powder pattern at $T = 10, 160$ and 300 K. The part shows the (131) reflection.

B.2. High temperature single crystal diffraction data

Displacement parameters, either isotropic or anisotropic, describe the mean displacement of an atom around its average position within the crystal. The reasons for the displacement are internal disorder, lattice defects and lattice vibrations. While for the powder data only the isotropic parameter, corresponding to the width of a spherical Gaussian could be refined, the single crystal neutron diffraction allowed an accurate determination of the whole displacement ellipsoids. Figure B.3 displays the displacement ellipsoids in CaV_2O_4 . While the Vanadium and Calcium ions are almost homogeneously moving around the mean position, the oxygen ions have a slightly larger component of the ellipsoid perpendicular to the cations. This indicates that they thermally vibrate between them.

Table B.3.: Anisotropic displacement factors of CaV_2O_4 at room temperature obtained with single crystal neutron diffraction. The displacement parameters U_{ij} are in the form $\exp[-2\pi^2(U_{11}h^2a^{*2} + \dots + 2U_{13}hla^*c^*)]$. For symmetry reasons the values U_{13} and U_{23} of all the atoms are equal to zero in the orthorhombic structure. Due to the weak scattering power of vanadium the isotropic parameter ($B_{is} = 8\pi U_{is}$) was taken from the X-ray synchrotron results and kept fix during the refinement. In the last column on the right, the refined occupancies are displayed.

Pnam $U_{ij}(100\text{\AA}^3)$	U_{11}	U_{22}	U_{33}	U_{12}	occ
Ca	0.53(2)	0.63(2)	0.54(2)	0.01(2)	0.992(2)
V1	0.77				1.13(3)
V2	0.77				1.13(3)
O1	0.38(2)	0.69(2)	0.51(2)	-0.01(1)	1.004(2)
O2	0.37(2)	0.45(2)	0.49(2)	-0.01(1)	1.002(2)
O3	0.60(2)	0.50(2)	0.50(2)	-0.01(1)	1.002(2)
O4	0.44(2)	0.37(2)	0.50(2)	-0.00(1)	1.001(2)

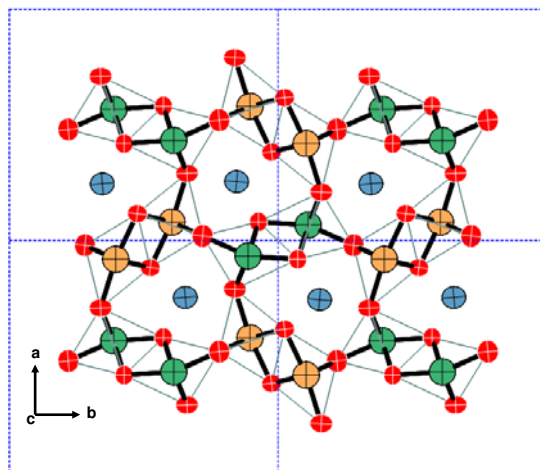


Figure B.3.: Anisotropic displacement ellipsoids at $T = 300$ K. Colour code: red - oxygen, green and orange - vanadium, blue -calcium.

C. Linear spin wave theory for the CaV_2O_4 lattice

This appendix refers to Chapter 6 and gives an outline of the linear spin wave derivation of the magnon dispersion relations and the spin-spin correlation functions for the CaV_2O_4 lattice. First, a simplified four sublattice model will be introduced and solved analytically, while after that some details of the full 32 sublattice model will be presented.

C.1. The four sublattice case

The general Hamiltonian expressing a system of zigzag chains with frustrated interchain coupling (Fig. C.1) can be written as follows:

$$\mathcal{H} = \mathcal{H}_{leg} + \mathcal{H}_{zz} + \mathcal{H}_{int} + \mathcal{H}_{ani} \quad (\text{C.1})$$

The different terms describe the interaction between spins along the legs of the zigzag chain, along its zigzag (zz) rungs, between the chains (inter ladder) and the single ion

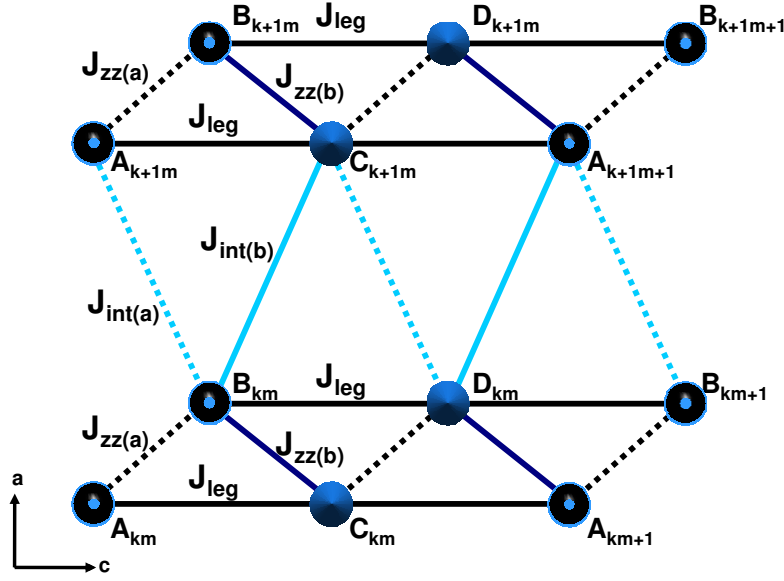


Figure C.1.: Magnetic unit cell of a system of coupled zigzag chains.

anisotropy, respectively. The individual terms read:

$$\mathcal{H}_{leg} = J_{leg} \sum_{k,m} \left[S_{k,m}^A S_{k,m}^C + S_{k,m}^B S_{k,m}^D + S_{k,m}^C S_{k,m+1}^A + S_{k,m}^D S_{k,m+1}^A \right] \quad (\text{C.2})$$

$$\begin{aligned} \mathcal{H}_{zz} = & J_{zz(a)} \sum_{k,m} \left(S_{k,m}^A S_{k,m}^B + S_{k,m}^C S_{k,m}^D \right) + \\ & + J_{zz(b)} \sum_{k,m} \left(S_{k,m}^B S_{k,m}^C + S_{k,m}^D S_{k,m+1}^A \right) \end{aligned} \quad (\text{C.3})$$

$$\begin{aligned} \mathcal{H}_{int} = & J_{int(a)} \sum_{k,m} \left(S_{k+1,m}^A S_{k,m}^B + S_{k+1,m}^C S_{k,m}^D \right) + \\ & + J_{int(b)} \sum_{k,m} \left(S_{k,m}^B S_{k+1,m}^C + S_{k,m}^D S_{k+1,m+1}^A \right) \end{aligned} \quad (\text{C.4})$$

$$\mathcal{H}_{ani} = -D \sum_{k,m} \left[\left((S_{k,m}^A)^y \right)^2 + \left((S_{k,m}^B)^y \right)^2 + \left((S_{k,m}^C)^y \right)^2 + \left((S_{k,m}^D)^y \right)^2 \right] \quad (\text{C.5})$$

Here the coupling constants $J_{zz(b)}$, $J_{int(b)}$ and J_{leg} have positive values (antiferromagnetic coupling), while $J_{zz(a)}$ and $J_{int(a)}$ are negative (ferromagnetic coupling). The indices k, m run over all the unit cell in two dimensions (unit cell parameter a and c), where

the position of a spin in cell (k,m) can be written as:

$$\mathbf{R}_{km}^\alpha = \begin{pmatrix} x_\alpha \\ z_\alpha \end{pmatrix} + \begin{pmatrix} ka \\ 2cm \end{pmatrix}; \quad \alpha = A, B, C, D \quad (\text{C.6})$$

Next the spin operators included in the Hamiltonian have to be transformed into Bose operators by using the Holstein-Primakoff transformation in the spin wave approximation [44]. The spins at sites A and B point parallel to the crystallographic b -axis, while spins at sites C and D point antiparallel to b . Therefore the transformation has the following form:

sublattice A :

$$(S_{k,m}^A)^+ = \sqrt{2S}a_{k,m}; \quad (S_{k,m}^B)^+ = \sqrt{2S}b_{k,m} \quad (\text{C.7})$$

$$(S_{k,m}^A)^- = \sqrt{2S}a_{k,m}^+; \quad (S_{k,m}^B)^- = \sqrt{2S}b_{k,m}^+ \quad (\text{C.8})$$

$$(S_{k,m}^A)^y = S - a_{k,m}^+ a_{k,m}; \quad (S_{k,m}^B)^y = S - b_{k,m}^+ b_{k,m} \quad (\text{C.9})$$

sublattice B :

sublattice C :

$$(S_{k,m}^C)^+ = \sqrt{2S}c_{k,m}^+; \quad (S_{k,m}^D)^+ = \sqrt{2S}d_{k,m}^+ \quad (\text{C.10})$$

$$(S_{k,m}^C)^- = \sqrt{2S}c_{k,m}; \quad (S_{k,m}^D)^- = \sqrt{2S}d_{k,m} \quad (\text{C.11})$$

$$(S_{k,m}^C)^y = -(S - c_{k,m}^+ c_{k,m}); \quad (S_{k,m}^D)^y = -(S - d_{k,m}^+ d_{k,m}) \quad (\text{C.12})$$

sublattice D :

This leads to the following Hamiltonian for the linear approximation (only bilinear terms are considered):

$$\begin{aligned} \mathcal{H}_{leg} = SJ_{leg} \sum_{k,m} & \left[(a_{k,m}c_{k,m} + a_{k,m}^+ c_{k,m}^+ + a_{k,m}^+ a_{k,m} + c_{k,m}^+ c_{k,m}) + \right. \\ & (b_{k,m}d_{k,m} + b_{k,m}^+ d_{k,m}^+ + b_{k,m}^+ b_{k,m} + d_{k,m}^+ d_{k,m}) + \\ & (c_{k,m}^+ a_{k,m+1}^+ + c_{k,m} a_{k,m+1} + c_{k,m}^+ c_{k,m} + a_{k,m+1}^+ a_{k,m+1}) + \\ & \left. (d_{k,m}^+ b_{k,m+1}^+ + d_{k,m} b_{k,m+1} + d_{k,m}^+ d_{k,m} + b_{k,m+1}^+ b_{k,m+1}) \right] \quad (\text{C.13}) \end{aligned}$$

$$\begin{aligned}
\mathcal{H}_{zz} = & SJ_{zz(a)} \sum_{k,m} \left[(a_{k,m} b_{k,m}^+ + a_{k,m}^+ b_{k,m} - a_{k,m}^+ a_{k,m} - b_{k,m}^+ b_{k,m}) + \right. \\
& \left. (c_{k,m}^+ d_{k,m} + c_{k,m} d_{k,m}^+ + c_{k,m}^+ c_{k,m} + d_{k,m}^+ d_{k,m}) \right] + \\
& SJ_{zz(b)} \sum_{k,m} \left[(b_{k,m} c_{k,m} + b_{k,m}^+ c_{k,m}^+ + b_{k,m}^+ b_{k,m} + c_{k,m}^+ c_{k,m}) + \right. \\
& \left. (d_{k,m}^+ a_{k,m+1}^+ + d_{k,m} a_{k,m+1} + d_{k,m}^+ d_{k,m} + a_{k,m+1}^+ a_{k,m+1}) \right] \quad (\text{C.14})
\end{aligned}$$

$$\begin{aligned}
\mathcal{H}_{int} = & SJ_{int(a)} \sum_{k,m} \left[(a_{k+1,m} b_{k,m}^+ + a_{k+1,m}^+ b_{k,m} - a_{k+1,m}^+ a_{k+1,m} - b_{k,m}^+ b_{k,m}) + \right. \\
& \left. (c_{k+1,m}^+ d_{k,m} + c_{k+1,m} d_{k,m}^+ + c_{k+1,m}^+ c_{k+1,m} + d_{k,m}^+ d_{k,m}) \right] + \\
& SJ_{int(b)} \sum_{k,m} \left[(b_{k,m} c_{k+1,m} + b_{k,m}^+ c_{k+1,m}^+ + b_{k,m}^+ b_{k,m} + c_{k+1,m}^+ c_{k+1,m}) + \right. \\
& \left. (d_{k,m}^+ a_{k+1,m+1}^+ + d_{k,m} a_{k+1,m+1} + d_{k,m}^+ d_{k,m} + a_{k+1,m+1}^+ a_{k+1,m+1}) \right] \quad (\text{C.15})
\end{aligned}$$

$$\mathcal{H}_{ani} = 2DS \sum_{k,m} a_{k,m}^+ a_{k,m} + b_{k,m}^+ b_{k,m} + c_{k,m}^+ c_{k,m} + d_{k,m}^+ d_{k,m} \quad (\text{C.16})$$

In the next step, the Hamiltonian has to be transformed into wave numbers, where the following Fourier transform for the creation and annihilation operators is used.

$$a_{k,m}^+ = \frac{1}{\sqrt{N}} \sum_Q e^{-iQR_{k,m}^a} a_Q^+; \quad a_{k,m} = \frac{1}{\sqrt{N}} \sum_Q e^{iQR_{k,m}^a} a_Q \quad (\text{C.17})$$

$$b_{k,m}^+ = \frac{1}{\sqrt{N}} \sum_Q e^{-iQR_{k,m}^b} b_Q^+; \quad b_{k,m} = \frac{1}{\sqrt{N}} \sum_Q e^{iQR_{k,m}^b} b_Q \quad (\text{C.18})$$

$$c_{k,m}^+ = \frac{1}{\sqrt{N}} \sum_Q e^{iQR_{k,m}^c} c_Q^+; \quad c_{k,m} = \frac{1}{\sqrt{N}} \sum_Q e^{-iQR_{k,m}^c} c_Q \quad (\text{C.19})$$

$$d_{k,m}^+ = \frac{1}{\sqrt{N}} \sum_Q e^{iQR_{k,m}^d} d_Q^+; \quad d_{k,m} = \frac{1}{\sqrt{N}} \sum_Q e^{-iQR_{k,m}^d} d_Q \quad (\text{C.20})$$

Using (C.17)-(C.20), the Hamiltonian \mathcal{H} can be rewritten. As an example this is shown for the first part of \mathcal{H}_{leg} :

$$\begin{aligned} \mathcal{H}_{leg}^1 &= S J_{leg} \sum_{k,m} (a_{k,m} c_{k,m} + a_{k,m}^+ c_{k,m}^+ + a_{k,m}^+ a_{k,m} + c_{k,m}^+ c_{k,m}) \\ &= S J_{leg} \sum_{k,m} \frac{1}{N} \sum_{Q,K} \left[e^{iQR_{k,m}^a} e^{-iKR_{k,m}^c} a_Q c_K + e^{-iQR_{k,m}^a} e^{iKR_{k,m}^c} a_Q^+ c_K^+ \right. \\ &\quad \left. + e^{-iQR_{k,m}^a} e^{iKR_{k,m}^c} a_Q^+ a_K + e^{iQR_{k,m}^a} e^{-iKR_{k,m}^c} c_Q^+ c_K \right] \end{aligned} \quad (C.21)$$

$$\begin{aligned} &= S J_{leg} \sum_{k,m} \frac{1}{N} \sum_{Q,K} \left[e^{-iR_{k,m}^a (K-Q)} e^{-iK(R_{k,m}^c - R_{k,m}^a)} a_Q c_K + \right. \\ &\quad e^{-iR_{k,m}^a (Q-K)} e^{iK(R_{k,m}^c - R_{k,m}^a)} a_Q^+ c_K^+ + e^{-iR_{k,m}^a (Q-K)} a_Q^+ a_K + \\ &\quad \left. e^{-iR_{k,m}^c (K-Q)} c_Q^+ c_K \right] \end{aligned} \quad (C.22)$$

$$= S J_{leg} \sum_{k,m} \sum_Q \left[e^{-iQ(R_{k,m}^c - R_{k,m}^a)} a_Q c_Q + e^{iQ(R_{k,m}^c - R_{k,m}^a)} a_Q^+ c_Q^+ + a_Q^+ a_Q + c_Q^+ c_Q \right] \quad (C.23)$$

Here $R_{k,m}^c - R_{k,m}^a$ stands for the distance between the spins at sites A_{km} and C_{km} . This can be simplified to:

$$R_{k,m}^c - R_{k,m}^a = \begin{pmatrix} x_c + ka \\ z_c + m2c \end{pmatrix} - \begin{pmatrix} x_a + ka \\ z_a + m2c \end{pmatrix} = \begin{pmatrix} 0 \\ c \end{pmatrix} \quad (C.24)$$

In the above expression x and z are the atomic coordinates of the particular site and a and c are the unit cell parameter. Therefore one gets:

$$\mathcal{H}_{leg}^1 = S J_{leg} \sum_{k,m} \sum_Q \left[e^{-iQ_c c} a_Q c_Q + e^{iQ_c c} a_Q^+ c_Q^+ + a_Q^+ a_Q + c_Q^+ c_Q \right] \quad (C.25)$$

The transformation of the residual parts of the Hamiltonian follows a similar procedure and the final Hamiltonian in wave-number representation is given by:

$$\begin{aligned} \mathcal{H}_{leg} &= 2S J_{leg} \sum_Q \left[\cos(Q_c c) (a_Q c_Q + a_Q^+ c_Q^+ + b_Q d_Q + b_Q^+ d_Q^+) + \right. \\ &\quad \left. + a_Q^+ a_Q + b_Q^+ b_Q + c_Q^+ c_Q + d_Q^+ d_Q \right] \end{aligned} \quad (C.26)$$

$$\begin{aligned}
\mathcal{H}_{zz} = & SJ_{zz(a)} \sum_Q \left[e^{-i[Q_a(x_b-x_a)+Q_c(z_b-z_a)]} a_Q b_Q^\dagger + e^{i[Q_a(x_b-x_a)+Q_c(z_b-z_a)]} a_Q^\dagger b_Q \right. \\
& + e^{-i[Q_a(x_b-x_a)+Q_c(z_b-z_a)]} c_Q^\dagger d_Q + e^{i[Q_a(x_b-x_a)+Q_c(z_b-z_a)]} c_Q d_Q^\dagger \\
& \left. - a_Q^\dagger a_Q - b_Q^\dagger b_Q - c_Q^\dagger c_Q - d_Q^\dagger d_Q \right] \\
+ & SJ_{zz(b)} \sum_Q \left[e^{-i[Q_a(x_a-x_b)+Q_c(z_a-z_b+c)]} b_Q c_Q + e^{i[Q_a(x_a-x_b)+Q_c(z_a-z_b+c)]} b_Q^\dagger c_Q^\dagger \right. \\
& + e^{-i[Q_a(x_a-x_b)+Q_c(z_a-z_b+c)]} d_Q^\dagger a_Q^\dagger + e^{i[Q_a(x_a-x_b)+Q_c(z_a-z_b+c)]} d_Q a_Q \\
& \left. + a_Q^\dagger a_Q + b_Q^\dagger b_Q + c_Q^\dagger c_Q + d_Q^\dagger d_Q \right] \tag{C.27}
\end{aligned}$$

$$\begin{aligned}
\mathcal{H}_{int} = & SJ_{int(a)} \sum_Q \left[e^{-i[Q_a(x_b-x_a-a)+Q_c(z_b-z_a)]} a_Q b_Q^\dagger + e^{i[Q_a(x_b-x_a-a)+Q_c(z_b-z_a)]} a_Q^\dagger b_Q \right. \\
& + e^{-i[Q_a(x_b-x_a-a)+Q_c(z_b-z_a)]} c_Q^\dagger d_Q + e^{i[Q_a(x_b-x_a-a)+Q_c(z_b-z_a)]} c_Q d_Q^\dagger \\
& \left. - a_Q^\dagger a_Q - b_Q^\dagger b_Q - c_Q^\dagger c_Q - d_Q^\dagger d_Q \right] \\
+ & SJ_{int(b)} \sum_Q \left[e^{-i[Q_a(x_a-x_b+a)+Q_c(z_a-z_b+c)]} b_Q c_Q + e^{i[Q_a(x_a-x_b+a)+Q_c(z_a-z_b+c)]} b_Q^\dagger c_Q^\dagger \right. \\
& + e^{-i[Q_a(x_a-x_b+a)+Q_c(z_a-z_b+c)]} d_Q^\dagger a_Q^\dagger + e^{i[Q_a(x_a-x_b+a)+Q_c(z_a-z_b+c)]} d_Q a_Q \\
& \left. + a_Q^\dagger a_Q + b_Q^\dagger b_Q + c_Q^\dagger c_Q + d_Q^\dagger d_Q \right] \tag{C.28}
\end{aligned}$$

$$\mathcal{H}_{ani} = 2DS \sum_Q \left[a_Q^\dagger a_Q + b_Q^\dagger b_Q + c_Q^\dagger c_Q + d_Q^\dagger d_Q \right] \tag{C.29}$$

The full (transformed) Hamiltonian can be written in matrix form [162]:

$$\mathcal{H} = \sum_Q X^\dagger H X + E_0 \tag{C.30}$$

E_0 denotes the ground state energy. Further X is a column vector containing a set of creation and annihilation operators, X^\dagger is its transposed hermitian adjoint and H is a

four-by-four matrix.

$$X = \begin{pmatrix} a_Q \\ b_Q \\ c_Q^+ \\ d_Q^+ \end{pmatrix}; \quad X^\dagger = (a_Q^+, b_Q^+, c_Q, d_Q) \quad (\text{C.31})$$

$$H = \begin{pmatrix} A_Q & B_Q & C_Q & D_{-Q} \\ B_{-Q} & A_Q & D_Q & C_Q \\ C_Q & D_{-Q} & A_Q & B_Q \\ D_Q & C_Q & B_{-Q} & A_Q \end{pmatrix} \quad (\text{C.32})$$

with:

$$A_Q = S \left(2J_{\text{leg}} - J_{zz(a)} + J_{zz(b)} - J_{\text{int}(a)} + J_{\text{int}(b)} + 2D \right) \quad (\text{C.33})$$

$$B_Q = S \left(J_{zz(a)} e^{i(Q_a(x_b - x_a) + Q_c(z_b - z_a))} + J_{\text{int}(a)} e^{i(Q_a(x_b - x_a - b) + Q_c(z_b - z_a))} \right) \quad (\text{C.34})$$

$$C_Q = 2S J_{\text{leg}} \cos(Q_c c) \quad (\text{C.35})$$

$$D_Q = S \left(J_{zz(b)} e^{i(Q_a(x_a - x_b) + Q_c(z_a - z_b + c))} + J_{\text{int}(b)} e^{i(Q_a(x_a - x_b + b) + Q_c(z_a - z_b + c))} \right) \quad (\text{C.36})$$

To find the spin wave excitations of the system it has to be taken into account that the operators in X and X^\dagger have to fulfill the commutation relations for Bose operators. Those relations can be summarized in a matrix g .

$$g = [X, X^\dagger] = \begin{pmatrix} 1 & 0 & 0 & 0 \\ 0 & 1 & 0 & 0 \\ 0 & 0 & -1 & 0 \\ 0 & 0 & 0 & -1 \end{pmatrix} \quad (\text{C.37})$$

Further, it can be shown, that the Eigenvalues of the matrix gH are the excitation energies of the system under investigation [162]. One has to solve:

$$\det(gH - \lambda I) = 0; \quad (\text{C.38})$$

This leads to the following dispersion relation:

$$\lambda_{1-4} = \pm \sqrt{\frac{A_Q^2 - C_Q^2 + B_Q B_{-Q} - D_Q D_{-Q} \pm \sqrt{4B_Q B_{-Q} A_Q^2 - 4B_Q C_Q D_Q A_Q}}{-4B_{-Q} C_Q D_{-Q} A_Q + B_Q^2 D_Q^2 + B_{-Q}^2 D_{-Q}^2 + 4C_Q^2 D_Q D_{-Q} - 2B_Q B_{-Q} D_Q D_{-Q}}} \quad (\text{C.39})$$

Following White *et al.* [162], one has to identify the real excitation energies of the system by using the expression:

$$\lambda_i = g'_{ii} \Omega_{ii} \quad (\text{C.40})$$

Here g' is the commutator matrix for the new basis operators. Since the new operators have to fulfill the same commutator relations for Bose operators than the initial operators, it holds that $g = g'$. Therefore the excitation energies of the system can be identified. One get:

$$\Omega_{11} = \lambda_1; \quad \Omega_{22} = \lambda_2; \quad \Omega_{33} = -\lambda_3 = \Omega_{11}; \quad \Omega_{44} = -\lambda_4 = \Omega_{22} \quad (\text{C.41})$$

One finally ends up with two spin wave excitation branches:

$$\Omega_{1,2} = \sqrt{\frac{A_Q^2 - C_Q^2 + B_Q B_{-Q} - D_Q D_{-Q} \pm \sqrt{4B_Q B_{-Q} A_Q^2 - 4B_Q C_Q D_Q A_Q}}{-4B_{-Q} C_Q D_{-Q} A_Q + B_Q^2 D_Q^2 + B_{-Q}^2 D_{-Q}^2 + 4C_Q^2 D_Q D_{-Q} - 2B_Q B_{-Q} D_Q D_{-Q}}} \quad (\text{C.42})$$

One can simplify parts of these expressions by performing some straight forward algebra:

$$B_Q B_{-Q} = \left(J_{zz(a)}^2 + J_{\text{int}(a)}^2 + 2J_{zz(a)} J_{\text{int}(a)} \cos(Q_a a) \right) \quad (\text{C.43})$$

$$D_Q D_{-Q} = \left(J_{zz(b)}^2 + J_{\text{int}(b)}^2 + 2J_{zz(b)} J_{\text{int}(b)} \cos(Q_a a) \right) \quad (\text{C.44})$$

$$4C_Q A_Q (B_Q D_Q + B_{-Q} D_{-Q}) = 8C_Q A_Q (J_{zz(a)} J_{zz(b)} \cos(Q_c c) + J_{zz(a)} J_{\text{int}(b)} \cos(Q_a a + Q_c c) + J_{\text{int}(a)} J_{zz(b)} \cos(Q_a a - Q_c c) + J_{\text{int}(a)} J_{\text{int}(b)} \cos(Q_c c)) \quad (\text{C.45})$$

$$\begin{aligned}
B_Q^2 D_Q^2 + B_{-Q}^2 D_{-Q}^2 &= 2 \left(J_{zz(a)}^2 J_{zz(b)}^2 \cos(2Q_c c) + J_{\text{int}(a)}^2 J_{zz(b)}^2 \cos(2(Q_c c - Q_a a)) + \right. \\
&2 J_{zz(a)} J_{\text{int}(a)} J_{zz(b)}^2 \cos(Q_c c - Q_a a) + J_{zz(a)}^2 J_{\text{int}(b)}^2 \cos(2(Q_a a + Q_c c)) + \\
&2 J_{zz(b)} J_{zz(a)}^2 J_{\text{int}(b)} \cos(Q_a a + 2Q_c c) + J_{\text{int}(a)}^2 J_{\text{int}(b)}^2 \cos(2Q_c c) + \\
&4 J_{\text{int}(b)} J_{zz(a)} J_{zz(b)} J_{\text{int}(a)} \cos(2Q_c c) + 2 J_{zz(b)} J_{\text{int}(a)}^2 J_{\text{int}(b)} \cos(2Q_c c - Q_a a) + \\
&\left. 2 J_{zz(a)} J_{\text{int}(b)}^2 J_{\text{int}(a)} \cos(Q_a a + 2Q_c c) \right)
\end{aligned} \tag{C.46}$$

The next step is to calculate the Eigenvectors of the system, which represent its normal modes. Further, it has to be guaranteed, that the new operators also fulfill the Bose commutator relations. This is given, if the following normalization condition is considered:

$$g = SgS^+; \quad \text{which can be also written as: } I = gS^+gS \tag{C.47}$$

The corresponding Eigenvector matrix reads:

$$S = \begin{pmatrix} \frac{W(\Omega_1)}{N_1} & \frac{W(\Omega_2)}{N_2} & \frac{W(-\Omega_1)}{N_3} & \frac{W(-\Omega_2)}{N_4} \\ \frac{X(\Omega_1)}{N_1} & \frac{X(\Omega_2)}{N_2} & \frac{X(-\Omega_1)}{N_3} & \frac{X(-\Omega_2)}{N_4} \\ \frac{Y(\Omega_1)}{N_1} & \frac{Z(\Omega_2)}{N_2} & \frac{Y(-\Omega_1)}{N_3} & \frac{Y(-\Omega_2)}{N_4} \\ \frac{Z(\Omega_1)}{N_1} & \frac{Z(\Omega_2)}{N_2} & \frac{Z(-\Omega_1)}{N_3} & \frac{Z(-\Omega_2)}{N_4} \end{pmatrix} \tag{C.48}$$

Here N_α is the normalization constant and W, X, Y, Z are functions of Ω :

$$\begin{aligned}
W(\Omega) &= -A^3 - \Omega A^2 + (C_Q^2 + \Omega^2)A + \Omega^3 - B_Q C_Q D_Q + C_Q^2 \Omega + \\
&+ D_Q(A + \Omega)D_{-Q} + B_{-Q}(B_Q(A - \Omega) - C_Q D_{-Q})
\end{aligned} \tag{C.49}$$

$$X(\Omega) = D_Q(B_Q D_Q - 2C_Q(A + \Omega)) + B_{-Q}(C_Q^2 + (A + \Omega)^2 - B_Q B_{-Q}) \tag{C.50}$$

$$Y(\Omega) = CA^2 - B_Q D_Q A + B_Q D_Q \Omega - C_Q(C_Q^2 + \Omega^2) + \tag{C.51}$$

$$+ C_Q D_Q D_{-Q} + B_{-Q}(B_Q C_Q - (A + \Omega)D_{-Q}) \tag{C.52}$$

$$Z(\Omega) = D_{-Q} B_{-Q}^2 - 2AC_Q B_{-Q} + D_Q(A^2 + C_Q^2 - \Omega^2 - D_Q D_{-Q}) \tag{C.53}$$

Using the normalisation condition (C.47) we can derive the value for the prefactor N_α :

$$|N_1| = N(\Omega_1) = \sqrt{||W1(\Omega_1)|^2 + |X1(\Omega_1)|^2 - |Y1(\Omega_1)|^2 - |Z1(\Omega_1)|^2|} \quad (\text{C.54})$$

$$|N_2| = N(\Omega_2) = \sqrt{||W2(\Omega_2)|^2 + |X2(\Omega_2)|^2 - |Y2(\Omega_2)|^2 - |Z2(\Omega_2)|^2|} \quad (\text{C.55})$$

$$|N_3| = N(-\Omega_1) = \sqrt{|-|W3(-\Omega_1)|^2 - |X3(-\Omega_1)|^2 + |Y3(-\Omega_1)|^2 + |Z3(-\Omega_1)|^2|}$$

$$|N_4| = N(-\Omega_2) = \sqrt{|-|W4(-\Omega_2)|^2 - |X4(-\Omega_2)|^2 + |Y4(-\Omega_2)|^2 + |Z4(-\Omega_2)|^2|} \quad (\text{C.56})$$

Once the normal modes of the system are known, one can calculate the spin-spin correlation functions. These correlation functions are directly accessible in an inelastic neutron scattering experiment and have the following form:

$$S^{xx}(\mathbf{Q}, \Omega) = \sum_{\lambda} |\langle \lambda | S^x(\mathbf{Q}) | 0 \rangle|^2 \delta(\Omega - \Omega_{\lambda}), \quad (\text{C.57})$$

where the superscript xx denotes that the spin-spin correlations are along the x -direction and the sum runs over the normal spin-wave excited states $|\lambda\rangle$ of energy Ω_{λ} above the ground-state. The ground-state is denoted by $|0\rangle$.

In the antiferromagnetically ordered state spin fluctuations only occur in transverse direction. Assuming that the spin direction is along S_y (as it is approximately the case for CaV_2O_4), one gets spin-spin correlations along S_x and S_z . Using symmetry arguments one can show that these correlations are equal ($S^{xx} = S^{zz}$).

Similar to the ladder operators, one can rewrite the x - and z - components of the spin operator in terms of Bose creation and annihilation operators:

$$S_{k,m}^x = \sqrt{\frac{S}{2}} (a_{k,m} + a_{k,m}^+) \quad (\text{C.58})$$

$$S_{k,m}^z = -i\sqrt{\frac{S}{2}} (a_{k,m} - a_{k,m}^+) \quad (\text{C.59})$$

In the further text it will be only concentrated on the S_x value (S_z can be determined in an analogue way). In case of a four sublattice system one gets the following Fourier

transformed spin operators:

$$\begin{aligned}
S^x(\mathbf{Q}) &= \frac{1}{\sqrt{N}} \sum_{k,m} (S_{k,m}^a)^x e^{i\mathbf{Q}\mathbf{R}_{km}^a} + (S_{k,m}^b)^x e^{i\mathbf{Q}\mathbf{R}_{km}^b} + (S_{k,m}^c)^x e^{i\mathbf{Q}\mathbf{R}_{km}^c} + (S_{k,m}^d)^x e^{i\mathbf{Q}\mathbf{R}_{km}^d} \\
&= \sqrt{\frac{S}{2}} (a_{-\mathbf{Q}} + a_{\mathbf{Q}}^+ + b_{-\mathbf{Q}} + b_{\mathbf{Q}}^+ + c_{\mathbf{Q}} + c_{-\mathbf{Q}}^+ + d_{\mathbf{Q}} + d_{-\mathbf{Q}}^+)
\end{aligned} \tag{C.60}$$

The next step is to rewrite the new creation and annihilation operators in term of the original Bose operators, which can be obtained by applying the Eigenvector matrix (C.48) on them:

$$\begin{pmatrix} a_{\mathbf{Q}} \\ b_{\mathbf{Q}} \\ c_{\mathbf{Q}}^+ \\ d_{\mathbf{Q}}^+ \end{pmatrix} = S \begin{pmatrix} \alpha_{\mathbf{Q}} \\ \beta_{\mathbf{Q}} \\ \gamma_{\mathbf{Q}}^+ \\ \delta_{\mathbf{Q}}^+ \end{pmatrix} \tag{C.61}$$

Bearing in mind the well known properties of ladder operators:

$$\alpha_{\mathbf{Q}}^+ |n\rangle = \sqrt{n_{\mathbf{Q}}^{\alpha} + 1} |n+1\rangle \tag{C.62}$$

$$\alpha_{\mathbf{Q}} |n\rangle = \sqrt{n_{\mathbf{Q}}^{\alpha}} |n-1\rangle, \tag{C.63}$$

where $n_{\mathbf{Q}}^{\alpha}$ denotes the expectation value of the number operator $\hat{n}_{\mathbf{Q}}^{\alpha} = \alpha_{\mathbf{Q}}^+ \alpha_{\mathbf{Q}}$, which in thermal average leads to the well known Bose occupation factor:

$$\langle n_{\mathbf{Q}}^{\alpha} \rangle = \frac{1}{e^{\Omega_{\mathbf{Q}}^{\alpha}/k_B T} - 1}. \tag{C.64}$$

Further, it follows from (C.63) that: $\alpha_{\mathbf{Q}} |0\rangle = 0$. In summary, this leads to the following result for the spin-spin correlation function along x (assuming $T = 0$):

$$\begin{aligned}
S^{xx}(\mathbf{Q}, \Omega) &= \left[\left| \frac{W(\Omega_1) + X(\Omega_1) + Y(\Omega_1) + Z(\Omega_1)}{N(\Omega_1)} \right|^2 \delta(\Omega - \Omega_1) + \right. \\
&+ \left| \frac{W(\Omega_2) + X(\Omega_2) + Y(\Omega_2) + Z(\Omega_2)}{N(\Omega_2)} \right|^2 \delta(\Omega - \Omega_2) + \\
&+ \left| \frac{W(-\Omega_1) + X(-\Omega_1) + Y(-\Omega_1) + Z(-\Omega_1)}{N(-\Omega_1)} \right|^2 \delta(\Omega - \Omega_1) + \\
&+ \left. \left| \frac{W(-\Omega_2) + X(-\Omega_2) + Y(-\Omega_2) + Z(-\Omega_2)}{N(-\Omega_2)} \right|^2 \delta(\Omega - \Omega_2) \right]
\end{aligned} \tag{C.65}$$

It has to be mentioned that $\Omega_{1,2} = \Omega_{1,2}(\mathbf{Q})$ is a function which is symmetric in \mathbf{Q} , which means that $\Omega_{1,2}(\mathbf{Q}) = \Omega_{1,2}(-\mathbf{Q})$. This relation was used in (C.65).

Finally, in order to compare the theory to the actual measured data, one has to calculate the differential magnetic cross section for the system under investigations. Applying Eq. (3.17) to the particular case of CaV_2O_4 one gets:

$$\left(\frac{d^2\sigma}{d\Omega dE_f} \right)_{\text{CaV}_2\text{O}_4} = C \frac{k_f}{k_i} f(\mathbf{Q})^2 \exp(-2W(\mathbf{Q}, T)) \left(1 + \frac{Q_y^2}{Q^2}\right) S^{xx}(\mathbf{Q}, \Omega). \quad (\text{C.66})$$

In the above expression C is a global constant which can be adjusted to the experimental data and further it was assumed that the spins point along the y -direction and ($S^{xx}(\mathbf{Q}, \Omega) = S^{zz}(\mathbf{Q}, \Omega)$).

C.2. The 32 sublattice case

The full spin Hamiltonian, which contains all relevant exchange interactions between the spin within the full magnetic unit cell of CaV_2O_4 (see Eq. 6.4(a)) has been introduced in Sec. 6.3 and is given by:

$$\mathcal{H} = \mathcal{H}_{\text{chain}_1} + \mathcal{H}_{\text{chain}_2} + \mathcal{H}_{\text{inter}} + \mathcal{H}_{\text{ani}}. \quad (\text{C.67})$$

In the following all terms of the spin Hamiltonian will be listed explicitly, where for convenience they were sorted according to their particular exchange constants. To do so, the Hamiltonian was subdivided in a different fashion than the one given in (C.67), being:

$$\begin{aligned} \mathcal{H} = & \mathcal{H}_{zz(a)}^1 + \mathcal{H}_{zz(b)}^1 + \mathcal{H}_{\text{leg}}^1 + \mathcal{H}_{zz(a)}^2 + \mathcal{H}_{zz(b)}^2 + \mathcal{H}_{\text{leg}}^2 \\ & + \mathcal{H}_{\text{int}(a)}^a + \mathcal{H}_{\text{int}(b)}^a + \mathcal{H}_{\text{int}(a)}^b + \mathcal{H}_{\text{int}(b)}^b + \mathcal{H}_{\text{ani}}, \end{aligned} \quad (\text{C.68})$$

where the particular terms are defined as:

$$\begin{aligned} \mathcal{H}_{J_{zz}^1(a)} &= J_{zz}^1(a) \sum_{klm} \left(\mathbf{S}_{A_{klm}}^\alpha \mathbf{S}_{B_{klm}}^\beta + \mathbf{S}_{C_{klm}}^\alpha \mathbf{S}_{D_{klm}}^\alpha + \mathbf{S}_{G_{klm}}^\beta \mathbf{S}_{F_{klm}}^\beta + \mathbf{S}_{E_{klm+1}}^\beta \mathbf{S}_{H_{klm}}^\beta \right. \\ &\quad \left. + \mathbf{S}_{A_{klm}}^\gamma \mathbf{S}_{B_{klm}}^\gamma + \mathbf{S}_{C_{klm}}^\gamma \mathbf{S}_{D_{klm}}^\gamma + \mathbf{S}_{G_{klm}}^\delta \mathbf{S}_{F_{klm}}^\delta + \mathbf{S}_{E_{klm+1}}^\delta \mathbf{S}_{H_{klm}}^\delta \right) \quad (\text{C.69}) \end{aligned}$$

$$\begin{aligned} \mathcal{H}_{J_{zz}^1(b)} &= J_{zz}^1(b) \sum_{klm} \left(\mathbf{S}_{B_{klm}}^\alpha \mathbf{S}_{C_{klm}}^\alpha + \mathbf{S}_{D_{klm}}^\alpha \mathbf{S}_{A_{klm+1}}^\alpha + \mathbf{S}_{E_{klm}}^\beta \mathbf{S}_{F_{klm}}^\beta + \mathbf{S}_{G_{klm}}^\beta \mathbf{S}_{H_{klm}}^\beta \right. \\ &\quad \left. + \mathbf{S}_{B_{klm}}^\gamma \mathbf{S}_{C_{klm}}^\gamma + \mathbf{S}_{D_{klm}}^\gamma \mathbf{S}_{A_{klm+1}}^\gamma + \mathbf{S}_{E_{klm}}^\delta \mathbf{S}_{F_{klm}}^\delta + \mathbf{S}_{G_{klm}}^\delta \mathbf{S}_{H_{klm}}^\delta \right) \quad (\text{C.70}) \end{aligned}$$

$$\begin{aligned} \mathcal{H}_{J_{\text{leg}}^1} &= J_{\text{leg}}^1 \sum_{klm} \left(\mathbf{S}_{A_{klm}}^\alpha \mathbf{S}_{C_{klm}}^\alpha + \mathbf{S}_{C_{klm}}^\alpha \mathbf{S}_{A_{klm+1}}^\alpha + \mathbf{S}_{B_{klm}}^\beta \mathbf{S}_{D_{klm}}^\alpha + \mathbf{S}_{D_{klm}}^\alpha \mathbf{S}_{B_{klm+1}}^\beta \right. \\ &\quad + \mathbf{S}_{E_{klm}}^\beta \mathbf{S}_{G_{klm}}^\beta + \mathbf{S}_{G_{klm}}^\beta \mathbf{S}_{E_{klm+1}}^\beta + \mathbf{S}_{F_{klm}}^\beta \mathbf{S}_{H_{klm}}^\beta + \mathbf{S}_{H_{klm}}^\beta \mathbf{S}_{F_{klm+1}}^\beta \\ &\quad + \mathbf{S}_{A_{klm}}^\gamma \mathbf{S}_{C_{klm}}^\gamma + \mathbf{S}_{C_{klm}}^\gamma \mathbf{S}_{A_{klm+1}}^\gamma + \mathbf{S}_{B_{klm}}^\gamma \mathbf{S}_{D_{klm}}^\gamma + \mathbf{S}_{D_{klm}}^\gamma \mathbf{S}_{B_{klm+1}}^\gamma \\ &\quad \left. + \mathbf{S}_{E_{klm}}^\delta \mathbf{S}_{G_{klm}}^\delta + \mathbf{S}_{G_{klm}}^\delta \mathbf{S}_{E_{klm+1}}^\delta + \mathbf{S}_{F_{klm}}^\delta \mathbf{S}_{H_{klm}}^\delta + \mathbf{S}_{H_{klm}}^\delta \mathbf{S}_{F_{klm+1}}^\delta \right) \quad (\text{C.71}) \end{aligned}$$

$$\begin{aligned} \mathcal{H}_{J_{zz}^2(a)} &= J_{zz}^2(a) \sum_{klm} \left(\mathbf{S}_{E_{klm}}^\alpha \mathbf{S}_{F_{klm}}^\alpha + \mathbf{S}_{G_{klm}}^\alpha \mathbf{S}_{H_{klm}}^\alpha + \mathbf{S}_{B_{klm}}^\beta \mathbf{S}_{C_{klm}}^\beta + \mathbf{S}_{D_{klm}}^\beta \mathbf{S}_{A_{klm+1}}^\beta \right. \\ &\quad \left. + \mathbf{S}_{E_{klm}}^\gamma \mathbf{S}_{F_{klm}}^\gamma + \mathbf{S}_{G_{klm}}^\gamma \mathbf{S}_{H_{klm}}^\gamma + \mathbf{S}_{B_{klm}}^\delta \mathbf{S}_{C_{klm}}^\delta + \mathbf{S}_{D_{klm}}^\delta \mathbf{S}_{A_{klm+1}}^\delta \right) \quad (\text{C.72}) \end{aligned}$$

$$\begin{aligned} \mathcal{H}_{J_{zz}^2(b)} &= J_{zz}^2(b) \sum_{klm} \left(\mathbf{S}_{G_{klm}}^\alpha \mathbf{S}_{F_{klm}}^\alpha + \mathbf{S}_{E_{klm+1}}^\alpha \mathbf{S}_{H_{klm}}^\alpha + \mathbf{S}_{A_{klm}}^\beta \mathbf{S}_{B_{klm}}^\beta + \mathbf{S}_{C_{klm}}^\beta \mathbf{S}_{D_{klm}}^\beta \right. \\ &\quad \left. + \mathbf{S}_{G_{klm}}^\gamma \mathbf{S}_{F_{klm}}^\gamma + \mathbf{S}_{E_{klm+1}}^\gamma \mathbf{S}_{H_{klm}}^\gamma + \mathbf{S}_{A_{klm}}^\delta \mathbf{S}_{B_{klm}}^\delta + \mathbf{S}_{C_{klm}}^\delta \mathbf{S}_{D_{klm}}^\delta \right) \quad (\text{C.73}) \end{aligned}$$

$$\begin{aligned} \mathcal{H}_{J_{\text{leg}}^2} &= J_{\text{leg}}^2 \sum_{klm} \left(\mathbf{S}_{E_{klm}}^\alpha \mathbf{S}_{G_{klm}}^\alpha + \mathbf{S}_{G_{klm}}^\alpha \mathbf{S}_{E_{klm+1}}^\alpha + \mathbf{S}_{F_{klm}}^\alpha \mathbf{S}_{H_{klm}}^\alpha + \mathbf{S}_{H_{klm}}^\alpha \mathbf{S}_{F_{klm+1}}^\alpha \right. \\ &\quad + \mathbf{S}_{A_{klm}}^\beta \mathbf{S}_{C_{klm}}^\beta + \mathbf{S}_{C_{klm}}^\beta \mathbf{S}_{A_{klm+1}}^\beta + \mathbf{S}_{B_{klm}}^\beta \mathbf{S}_{D_{klm}}^\beta + \mathbf{S}_{D_{klm}}^\beta \mathbf{S}_{B_{klm+1}}^\beta \\ &\quad + \mathbf{S}_{E_{klm}}^\gamma \mathbf{S}_{G_{klm}}^\gamma + \mathbf{S}_{G_{klm}}^\gamma \mathbf{S}_{E_{klm+1}}^\gamma + \mathbf{S}_{F_{klm}}^\gamma \mathbf{S}_{H_{klm}}^\gamma + \mathbf{S}_{H_{klm}}^\gamma \mathbf{S}_{F_{klm+1}}^\gamma \\ &\quad \left. + \mathbf{S}_{A_{klm}}^\delta \mathbf{S}_{C_{klm}}^\delta + \mathbf{S}_{C_{klm}}^\delta \mathbf{S}_{A_{klm+1}}^\delta + \mathbf{S}_{B_{klm}}^\delta \mathbf{S}_{D_{klm}}^\delta + \mathbf{S}_{D_{klm}}^\delta \mathbf{S}_{B_{klm+1}}^\delta \right) \quad (\text{C.74}) \end{aligned}$$

$$\begin{aligned}
\mathcal{H}_{\text{int(a)}}^{J^a} = & J_{\text{int(a)}}^a \sum_{klm} \left(\mathcal{S}_{B_{klm}}^\alpha \mathcal{S}_{E_{klm}}^\alpha + \mathcal{S}_{D_{klm}}^\alpha \mathcal{S}_{G_{klm}}^\alpha + \mathcal{S}_{F_{klm}}^\alpha \mathcal{S}_{A_{k+1lm}}^\alpha + \mathcal{S}_{H_{klm}}^\alpha \mathcal{S}_{C_{k+1lm}}^\alpha \right. \\
& + \mathcal{S}_{B_{klm}}^\beta \mathcal{S}_{G_{klm}}^\beta + \mathcal{S}_{D_{klm}}^\beta \mathcal{S}_{E_{klm+1}}^\beta + \mathcal{S}_{F_{klm}}^\beta \mathcal{S}_{C_{k+1lm}}^\beta + \mathcal{S}_{H_{klm}}^\beta \mathcal{S}_{A_{k+1lm+1}}^\beta \\
& + \mathcal{S}_{B_{klm}}^\gamma \mathcal{S}_{E_{klm}}^\gamma + \mathcal{S}_{D_{klm}}^\gamma \mathcal{S}_{G_{klm}}^\gamma + \mathcal{S}_{F_{klm}}^\gamma \mathcal{S}_{A_{k+1lm}}^\gamma + \mathcal{S}_{H_{klm}}^\gamma \mathcal{S}_{C_{k+1lm}}^\gamma \\
& \left. + \mathcal{S}_{B_{klm}}^\delta \mathcal{S}_{G_{klm}}^\delta + \mathcal{S}_{D_{klm}}^\delta \mathcal{S}_{E_{klm+1}}^\delta + \mathcal{S}_{F_{klm}}^\delta \mathcal{S}_{C_{k+1lm}}^\delta + \mathcal{S}_{H_{klm}}^\delta \mathcal{S}_{A_{k+1lm+1}}^\delta \right) \quad (\text{C.75})
\end{aligned}$$

$$\begin{aligned}
\mathcal{H}_{\text{int(b)}}^{J^a} = & J_{\text{int(b)}}^a \sum_{klm} \left(\mathcal{S}_{B_{klm}}^\alpha \mathcal{S}_{G_{klm}}^\alpha + \mathcal{S}_{D_{klm}}^\alpha \mathcal{S}_{E_{klm+1}}^\alpha + \mathcal{S}_{F_{klm}}^\alpha \mathcal{S}_{C_{k+1lm}}^\alpha + \mathcal{S}_{H_{klm}}^\alpha \mathcal{S}_{A_{k+1lm+1}}^\alpha \right. \\
& + \mathcal{S}_{B_{klm}}^\beta \mathcal{S}_{E_{klm}}^\beta + \mathcal{S}_{D_{klm}}^\beta \mathcal{S}_{G_{klm}}^\beta + \mathcal{S}_{F_{klm}}^\beta \mathcal{S}_{A_{k+1lm}}^\beta + \mathcal{S}_{H_{klm}}^\beta \mathcal{S}_{C_{k+1lm}}^\beta \\
& + \mathcal{S}_{B_{klm}}^\gamma \mathcal{S}_{G_{klm}}^\gamma + \mathcal{S}_{D_{klm}}^\gamma \mathcal{S}_{E_{klm+1}}^\gamma + \mathcal{S}_{F_{klm}}^\gamma \mathcal{S}_{C_{k+1lm}}^\gamma + \mathcal{S}_{H_{klm}}^\gamma \mathcal{S}_{A_{k+1lm+1}}^\gamma \\
& \left. + \mathcal{S}_{B_{klm}}^\delta \mathcal{S}_{E_{klm}}^\delta + \mathcal{S}_{D_{klm}}^\delta \mathcal{S}_{G_{klm+1}}^\delta + \mathcal{S}_{F_{klm}}^\delta \mathcal{S}_{A_{k+1lm}}^\delta + \mathcal{S}_{H_{klm}}^\delta \mathcal{S}_{C_{k+1lm}}^\delta \right) \quad (\text{C.76})
\end{aligned}$$

$$\begin{aligned}
\mathcal{H}_{\text{int(a)}}^{J^b} = & J_{\text{int(a)}}^b \sum_{klm} \left(\mathcal{S}_{A_{klm}}^\alpha \mathcal{S}_{B_{klm}}^\beta + \mathcal{S}_{C_{klm}}^\alpha \mathcal{S}_{D_{klm}}^\beta + \mathcal{S}_{A_{klm}}^\beta \mathcal{S}_{B_{klm}}^\gamma + \mathcal{S}_{C_{klm}}^\beta \mathcal{S}_{D_{klm}}^\gamma \right. \\
& + \mathcal{S}_{A_{klm}}^\gamma \mathcal{S}_{B_{klm}}^\delta + \mathcal{S}_{C_{klm}}^\gamma \mathcal{S}_{D_{klm}}^\delta + \mathcal{S}_{A_{klm}}^\delta \mathcal{S}_{B_{kl+1m}}^\alpha + \mathcal{S}_{C_{klm}}^\delta \mathcal{S}_{D_{kl+1m}}^\alpha \\
& + \mathcal{S}_{F_{klm}}^\alpha \mathcal{S}_{G_{klm}}^\beta + \mathcal{S}_{H_{klm}}^\alpha \mathcal{S}_{E_{klm+1}}^\beta + \mathcal{S}_{F_{klm}}^\beta \mathcal{S}_{G_{klm}}^\gamma + \mathcal{S}_{H_{klm}}^\beta \mathcal{S}_{E_{klm+1}}^\gamma \\
& \left. + \mathcal{S}_{F_{klm}}^\gamma \mathcal{S}_{G_{klm}}^\delta + \mathcal{S}_{H_{klm}}^\gamma \mathcal{S}_{E_{klm+1}}^\delta + \mathcal{S}_{F_{klm}}^\delta \mathcal{S}_{G_{kl+1m}}^\alpha + \mathcal{S}_{H_{klm}}^\delta \mathcal{S}_{E_{kl+1m+1}}^\alpha \right) \quad (\text{C.77})
\end{aligned}$$

$$\begin{aligned}
\mathcal{H}_{\text{int(b)}}^{J^b} = & J_{\text{int(b)}}^b \sum_{klm} \left(\mathcal{S}_{C_{klm}}^\alpha \mathcal{S}_{B_{klm}}^\beta + \mathcal{S}_{A_{klm+1}}^\alpha \mathcal{S}_{D_{klm}}^\beta + \mathcal{S}_{C_{klm}}^\beta \mathcal{S}_{B_{klm}}^\gamma + \mathcal{S}_{A_{klm+1}}^\beta \mathcal{S}_{D_{klm}}^\gamma \right. \\
& + \mathcal{S}_{C_{klm}}^\gamma \mathcal{S}_{B_{klm}}^\delta + \mathcal{S}_{A_{klm+1}}^\gamma \mathcal{S}_{D_{klm}}^\delta + \mathcal{S}_{C_{klm}}^\delta \mathcal{S}_{B_{kl+1m}}^\alpha + \mathcal{S}_{A_{klm+1}}^\delta \mathcal{S}_{D_{kl+1m}}^\alpha \\
& + \mathcal{S}_{F_{klm}}^\alpha \mathcal{S}_{E_{klm}}^\beta + \mathcal{S}_{H_{klm}}^\alpha \mathcal{S}_{G_{klm}}^\beta + \mathcal{S}_{F_{klm}}^\beta \mathcal{S}_{E_{klm}}^\gamma + \mathcal{S}_{H_{klm}}^\beta \mathcal{S}_{G_{klm}}^\gamma \\
& \left. + \mathcal{S}_{F_{klm}}^\gamma \mathcal{S}_{E_{klm}}^\delta + \mathcal{S}_{H_{klm}}^\gamma \mathcal{S}_{G_{klm}}^\delta + \mathcal{S}_{F_{klm}}^\delta \mathcal{S}_{E_{kl+1m}}^\alpha + \mathcal{S}_{H_{klm}}^\delta \mathcal{S}_{G_{kl+1m}}^\alpha \right) \quad (\text{C.78})
\end{aligned}$$

$$\mathcal{H}_{\text{ani}} = - \sum_{i=1,2} D_i \sum_{klm} \sum_{j=1}^{16} (S_{jklm}^y)^2 \quad (\text{C.79})$$

The spin operators in Hamiltonian C.68 can be transformed into magnon creation and annihilation operators, by applying Holstein-Primakoff transformation. The resulting Hamiltonian can be written in matrix form as has been shown in Sec. 6.3.

Next, the matrix elements of the 32×32 magnon-Hamiltonian matrix will be listed. According to (6.15), the matrix is defined as:

$$H = \begin{pmatrix} A^1(Q) & B(Q) & 0 & D^*(Q) \\ B^*(Q) & A^2(Q) & D(Q) & 0 \\ 0 & D^*(Q) & A^1(Q) & B(Q) \\ D(Q) & 0 & B^*(Q) & A^2(Q) \end{pmatrix}, \quad (\text{C.80})$$

and the particular elements are:

for $p = 1 - 4$ and $q = 5 - 8$:

$$A_{pp}^1 = A_{qq}^2 = S(2J_{\text{leg}}^1 - J_{\text{zz}(a)}^1 + J_{\text{zz}(b)}^1 - J_{\text{int}(a)}^a + J_{\text{int}(b)}^a - J_{\text{int}(a)}^b + J_{\text{int}(b)}^b + 2D_1), \quad (\text{C.81})$$

for $p = 5 - 8$ and $q = 1 - 4$:

$$A_{pp}^1 = A_{qq}^2 = S(2J_{\text{leg}}^2 - J_{\text{zz}(a)}^2 + J_{\text{zz}(b)}^2 - J_{\text{int}(a)}^a + J_{\text{int}(b)}^a - J_{\text{int}(a)}^b + J_{\text{int}(b)}^b + 2D_2) \quad (\text{C.82})$$

$$A_{21}^1(Q) = A_{43}^1(Q) = SJ_{\text{zz}(a)}^1 e^{2\pi i[h(x_{b\alpha} - x_{a\alpha}) + k(y_{b\alpha} - y_{a\alpha}) + l(z_{b\alpha} - z_{a\alpha})]} \quad (\text{C.83})$$

$$A_{31}^1(Q) = A_{42}^1(Q) = 2SJ_{\text{leg}}^1 \cos(2\pi l) \quad (\text{C.84})$$

$$A_{32}^1(Q) = A_{14}^1(Q) = SJ_{\text{zz}(b)}^1 e^{2\pi i[h(x_{a\alpha} - x_{b\alpha}) + k(y_{a\alpha} - y_{b\alpha}) + l(z_{a\alpha} - z_{b\alpha} + 1)]} \quad (\text{C.85})$$

$$A_{52}^1(Q) = A_{74}^1(Q) = SJ_{\text{int}(a)}^a e^{2\pi i[h(x_{e\alpha} - x_{b\alpha}) + k(y_{e\alpha} - y_{b\alpha}) + l(z_{e\alpha} - z_{b\alpha})]} \quad (\text{C.86})$$

$$A_{72}^1(Q) = A_{54}^1(Q) = SJ_{\text{int}(b)}^a e^{2\pi i[h(x_{e\alpha} - x_{b\alpha}) + k(y_{e\alpha} - y_{b\alpha}) + l(z_{e\alpha} - z_{b\alpha} + 1)]} \quad (\text{C.87})$$

$$A_{65}^1(Q) = A_{87}^1(Q) = SJ_{\text{zz}(a)}^2 e^{2\pi i[h(x_{f\alpha} - x_{e\alpha}) + k(y_{f\alpha} - y_{e\alpha}) + l(z_{f\alpha} - z_{e\alpha})]} \quad (\text{C.88})$$

$$A_{75}^1(Q) = A_{86}^1(Q) = 2SJ_{\text{leg}}^2 \cos(2\pi l) \quad (\text{C.89})$$

$$A_{85}^1(Q) = A_{67}^1(Q) = SJ_{\text{zz}(b)}^2 e^{2\pi i[h(x_{f\alpha} - x_{e\alpha}) + k(y_{f\alpha} - y_{e\alpha}) + l(z_{f\alpha} - z_{e\alpha} - 1)]} \quad (\text{C.90})$$

$$A_{16}^1(Q) = A_{38}^1(Q) = SJ_{\text{int}(a)}^a e^{2\pi i[h(x_{a\alpha} - x_{f\alpha} + 1) + k(y_{a\alpha} - y_{f\alpha}) + l(z_{a\alpha} - z_{f\alpha})]} \quad (\text{C.91})$$

$$A_{36}^1(Q) = A_{18}^1(Q) = SJ_{\text{int}(b)}^a e^{2\pi i[h(x_{a\alpha} - x_{f\alpha} + 1) + k(y_{a\alpha} - y_{f\alpha}) + l(z_{a\alpha} - z_{f\alpha} + 1)]} \quad (\text{C.92})$$

$$A_{ij}^1(\mathbf{Q}) = (A_{ji}^1)^*(\mathbf{Q}) \quad (\text{C.93})$$

$$A_{21}^2(\mathbf{Q}) = A_{43}^2(\mathbf{Q}) = SJ_{zz(b)}^2 e^{2\pi i[h(x_{b\beta} - x_{a\beta}) + k(y_{b\beta} - y_{a\beta}) + l(z_{b\beta} - z_{a\beta})]} \quad (\text{C.94})$$

$$A_{31}^2(\mathbf{Q}) = A_{42}^2(\mathbf{Q}) = 2SJ_{\text{leg}}^2 \cos(2\pi l) \quad (\text{C.95})$$

$$A_{32}^2(\mathbf{Q}) = A_{14}^2(\mathbf{Q}) = SJ_{zz(a)}^2 e^{2\pi i[h(x_{a\beta} - x_{b\beta}) + k(y_{a\beta} - y_{b\beta}) + l(z_{a\beta} - z_{b\beta} + 1)]} \quad (\text{C.96})$$

$$A_{52}^2(\mathbf{Q}) = A_{74}^2(\mathbf{Q}) = SJ_{\text{int}(b)}^a e^{2\pi i[h(x_{e\beta} - x_{b\beta}) + k(y_{e\beta} - y_{b\beta}) + l(z_{e\beta} - z_{b\beta})]} \quad (\text{C.97})$$

$$A_{72}^2(\mathbf{Q}) = A_{54}^2(\mathbf{Q}) = SJ_{\text{int}(a)}^a e^{2\pi i[h(x_{e\beta} - x_{b\beta}) + k(y_{e\beta} - y_{b\beta}) + l(z_{e\beta} - z_{b\beta} + 1)]} \quad (\text{C.98})$$

$$A_{65}^2(\mathbf{Q}) = A_{87}^2(\mathbf{Q}) = SJ_{zz(b)}^1 e^{2\pi i[h(x_{f\beta} - x_{e\beta}) + k(y_{f\beta} - y_{e\beta}) + l(z_{f\beta} - z_{e\beta})]} \quad (\text{C.99})$$

$$A_{75}^2(\mathbf{Q}) = A_{86}^2(\mathbf{Q}) = 2SJ_{\text{leg}}^1 \cos(2\pi l) \quad (\text{C.100})$$

$$A_{85}^2(\mathbf{Q}) = A_{67}^2(\mathbf{Q}) = SJ_{zz(a)}^1 e^{2\pi i[h(x_{f\beta} - x_{e\beta}) + k(y_{f\beta} - y_{e\beta}) + l(z_{f\beta} - z_{e\beta} - 1)]} \quad (\text{C.101})$$

$$A_{16}^2(\mathbf{Q}) = A_{38}^2(\mathbf{Q}) = SJ_{\text{int}(b)}^a e^{2\pi i[h(x_{a\beta} - x_{f\beta} + 1) + k(y_{a\beta} - y_{f\beta}) + l(z_{a\beta} - z_{f\beta})]} \quad (\text{C.102})$$

$$A_{36}^2(\mathbf{Q}) = A_{18}^2(\mathbf{Q}) = SJ_{\text{int}(a)}^a e^{2\pi i[h(x_{a\beta} - x_{f\beta} + 1) + k(y_{a\beta} - y_{f\beta}) + l(z_{a\beta} - z_{f\beta} + 1)]} \quad (\text{C.103})$$

$$A_{ij}^2(\mathbf{Q}) = (A_{ji}^2)^*(\mathbf{Q}) \quad (\text{C.104})$$

$$B_{21}(\mathbf{Q}) = B_{43}(\mathbf{Q}) = SJ_{\text{int}(a)}^b e^{2\pi i[h(x_{b\beta} - x_{a\alpha}) + k(y_{b\beta} - y_{a\alpha}) + l(z_{b\beta} - z_{a\alpha})]} \quad (\text{C.105})$$

$$B_{41}(\mathbf{Q}) = B_{23}(\mathbf{Q}) = SJ_{\text{int}(b)}^b e^{2\pi i[h(x_{b\beta} - x_{a\alpha}) + k(y_{b\beta} - y_{a\alpha}) + l(z_{b\beta} - z_{a\alpha} - 1)]} \quad (\text{C.106})$$

$$B_{56}(\mathbf{Q}) = B_{78}(\mathbf{Q}) = SJ_{\text{int}(b)}^b e^{2\pi i[h(x_{e\beta} - x_{f\alpha}) + k(y_{e\beta} - y_{f\alpha}) + l(z_{e\beta} - z_{f\alpha})]} \quad (\text{C.107})$$

$$B_{76}(\mathbf{Q}) = B_{58}(\mathbf{Q}) = SJ_{\text{int}(a)}^b e^{2\pi i[h(x_{e\beta} - x_{f\alpha}) + k(y_{e\beta} - y_{f\alpha}) + l(z_{e\beta} - z_{f\alpha} + 1)]} \quad (\text{C.108})$$

$$D_{21}(\mathbf{Q}) = D_{43}(\mathbf{Q}) = SJ_{\text{int}(a)}^b e^{2\pi i[h(x_{b\alpha} - x_{a\beta}) + k(y_{b\alpha} - y_{a\beta} + 1) + l(z_{b\alpha} - z_{a\beta})]} \quad (\text{C.109})$$

$$D_{41}(\mathbf{Q}) = D_{23}(\mathbf{Q}) = SJ_{\text{int}(b)}^b e^{2\pi i[h(x_{b\alpha} - x_{a\beta}) + k(y_{b\alpha} - y_{a\beta} + 1) + l(z_{b\alpha} - z_{a\beta} - 1)]} \quad (\text{C.110})$$

$$D_{56}(\mathbf{Q}) = D_{78}(\mathbf{Q}) = SJ_{\text{int}(b)}^b e^{2\pi i[h(x_{e\alpha} - x_{f\beta}) + k(y_{e\alpha} - y_{f\beta} + 1) + l(z_{e\alpha} - z_{f\beta})]} \quad (\text{C.111})$$

$$D_{76}(\mathbf{Q}) = D_{58}(\mathbf{Q}) = SJ_{\text{int}(a)}^b e^{2\pi i[h(x_{e\alpha} - x_{f\beta}) + k(y_{e\alpha} - y_{f\beta} + 1) + l(z_{e\alpha} - z_{f\beta} + 1)]} \quad (\text{C.112})$$

The Eigenvalues of the matrix $\mathbf{g}H$ are the 32 spin wave modes of the system under investigation. The matrix \mathbf{g} has been introduced in Sec. C.1 and accounts for the fact, that the magnon operators have to fulfil the fundamental commutator relations for bosons. In the particular case discussed here, \mathbf{g} is a 32×32 diagonal matrix and is given

by:

$$g = [X, X^\dagger] = \begin{pmatrix} \mathbf{g}_1 & 0 & 0 & 0 \\ 0 & \mathbf{g}_2 & 0 & 0 \\ 0 & 0 & -\mathbf{g}_1 & 0 \\ 0 & 0 & 0 & -\mathbf{g}_2 \end{pmatrix}, \quad (\text{C.113})$$

with:

$$\mathbf{g}_1 = \begin{pmatrix} 1 & 0 & 0 & 0 & 0 & 0 & 0 & 0 \\ 0 & 1 & 0 & 0 & 0 & 0 & 0 & 0 \\ 0 & 0 & -1 & 0 & 0 & 0 & 0 & 0 \\ 0 & 0 & 0 & -1 & 0 & 0 & 0 & 0 \\ 0 & 0 & 0 & 0 & 1 & 0 & 0 & 0 \\ 0 & 0 & 0 & 0 & 0 & 1 & 0 & 0 \\ 0 & 0 & 0 & 0 & 0 & 0 & -1 & 0 \\ 0 & 0 & 0 & 0 & 0 & 0 & 0 & -1 \end{pmatrix} \quad (\text{C.114})$$

$$\mathbf{g}_2 = \begin{pmatrix} -1 & 0 & 0 & 0 & 0 & 0 & 0 & 0 \\ 0 & 1 & 0 & 0 & 0 & 0 & 0 & 0 \\ 0 & 0 & 1 & 0 & 0 & 0 & 0 & 0 \\ 0 & 0 & 0 & -1 & 0 & 0 & 0 & 0 \\ 0 & 0 & 0 & 0 & -1 & 0 & 0 & 0 \\ 0 & 0 & 0 & 0 & 0 & 1 & 0 & 0 \\ 0 & 0 & 0 & 0 & 0 & 0 & 1 & 0 \\ 0 & 0 & 0 & 0 & 0 & 0 & 0 & -1 \end{pmatrix} \quad (\text{C.115})$$

And the row vector X^\dagger consists of the Fourier transformed magnon operators, which were defined in (6.6-6.9):

$$X^\dagger = (\hat{\alpha}^\dagger(\mathbf{Q}), \hat{\beta}^\dagger(\mathbf{Q}), \hat{\gamma}(\mathbf{Q}), \hat{\delta}(\mathbf{Q})) \quad (\text{C.116})$$

The Eigenvalues of matrix $(\mathbf{g}H)$ were calculated numerically and after applying (C.40) one finally ends up with 16 double-degenerated spin wave modes that define the full excitation spectrum of CaV_2O_4 . In addition, also the corresponding Eigenvectors could be calculated and following exactly the same procedure as described in Sec. C.1, it was possible to obtain the spin-spin correlation functions and therefore the partially

magnetic cross section (C.66), which has been also observed experimentally by means of INS. It is interesting to mention, that the corresponding calculations reveal that half of the determined spin wave modes do not show any intensity. This is due to the fact, that for the calculations presented here a magnetic unit cell has been chosen, which is twice as large as the primitive unit cell of CaV_2O_4 .

D. Neutron scattering instruments

This appendix provides descriptions of selected neutron scattering instruments that have been used for the work presented in this thesis. Further information about neutron instrumentation is given in Sec. 3.

D.1. IN5

The time-of-flight spectrometer IN5 is located at the H16 cold guide at ILL, France. Its direct geometry allows to study low-energy transfer processes as a function of momentum transfer. The general instrumental set-up is depicted in Fig. D.1. IN5 employs six counter rotating disc choppers, enabling a flexible choice of wavelengths (1.8 Å-20 Å) and chopper speed and thus allowing to chose the optimal configuration needed for the experiment (e.g. energy- and momentum-range, resolution and neutron flux at sample position). The six choppers rotate in phase to each other with a velocity of 2000-17000 rpm. The first chopper pair creates the time structure necessary for a TOF experiment by producing a pulse of polyenergetic neutrons. The second chopper pair is used to prevent frame overlap and contaminant higher order harmonics [182]. Finally, the last chopper pair prior to the detectors monochromatizes the beam.

On its way to the sample, the neutron beam gets focussed by an approximately tapered neutron guide, compressing the source beam from 200 mm × 30 mm down to 50 mm × 15 mm. The secondary spectrometer (from sample to detector bank) consists of an evacuated sample box, providing space for various sample environments, such as an orange cryostat and a cryomagnet. Finally, the detector bank is built up of 3 × 259 ³He detector tubes, covering an angular range from $-11.5^\circ \leq 2\theta \leq 140^\circ$.

D.2. IN6

IN6 is another TOF spectrometer installed at the cold neutron source at ILL, France. The instrument is designed for quasielastic and inelastic scattering for incident wavelengths in the range 4 to 6 Å [182]. A draft of the spectrometer is shown in Fig. D.2.

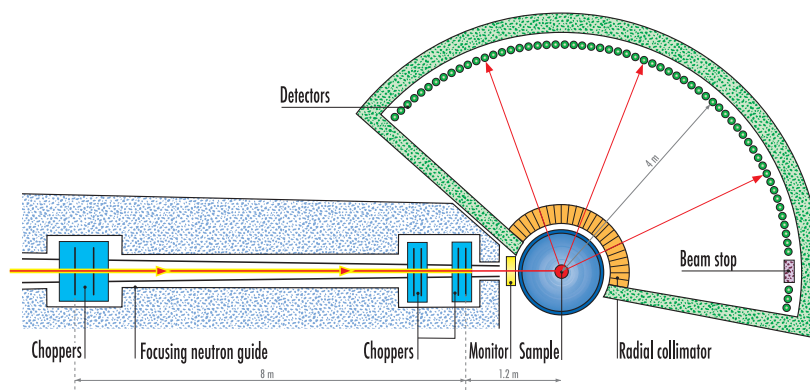


Figure D.1.: Layout of the IN5 spectrometer (picture taken from [182], copyright (2008) by ILL).

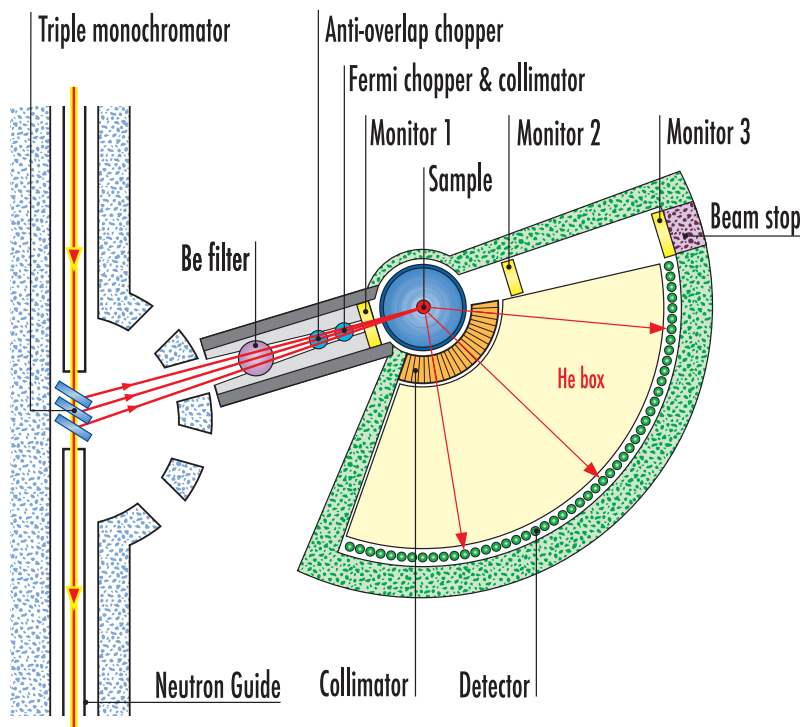


Figure D.2.: Layout of the IN6 spectrometer (picture taken from [182], copyright (2008) by ILL).

The incident white beam is reflected by a monochromator selecting neutrons with a fixed wavelength λ (and thus with a fixed incident energy E_i). In order to minimize interference with subsequent instruments, only four wavelength are available from the

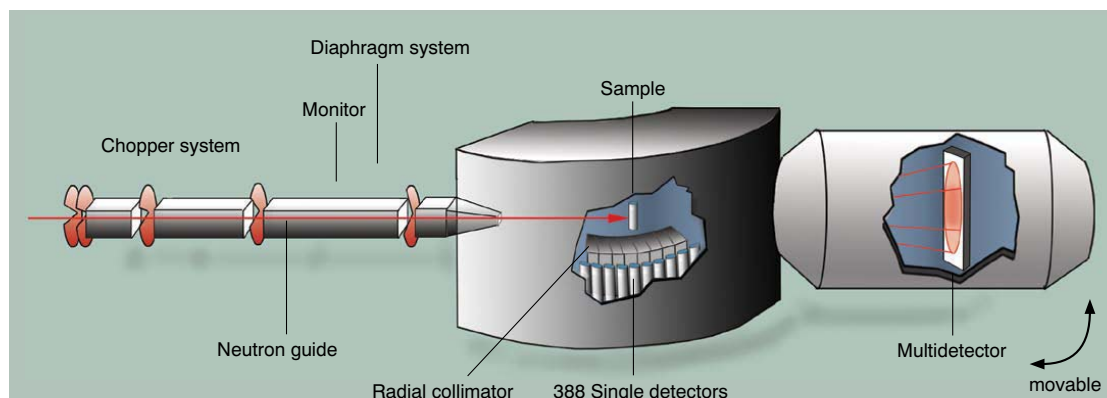


Figure D.3.: Layout of the NEAT TOF spectrometer (picture taken from [64]).

monochromator (4.1, 4.6, 5.1 and 5.9 Å). Second order contributions in λ are removed by a beryllium-filter cooled to nitrogen temperature.

Time focusing condition is achieved by a Fermi chopper, which is located very close to the sample area. For high resolution measurements, when the Fermi chopper rotates faster than 7500 rpm, an additional suppressor chopper placed in front of the Fermi chopper prevents frame-overlap by taking out every second neutron pulse.

The sample area is designed to provide space for cryogenic sample environment. Further it is equipped with an oscillating collimator which prevents parasitic reflections (e.g. from the walls of the cryostat). Finally, the large detector bank consisting of 337 ^3He tube detectors covers an angular range between 10° and 115° .

D.3. NEAT, V3

NEAT is a TOF disc chopper spectrometer located at the cold neutron source of the BERII reactor at HZB, Berlin [64]. Its design is very similar to that of IN5 and a draft is depicted in Fig. D.3. The instrument consists of seven individual disc choppers. After the neutrons are emitted from the reactor source a pair of counter rotating disc choppers produces ‘white’ pulses of neutrons. In the next step a single disc chopper creates a first crude monochromatization of the neutron pulses followed by another pair of counter rotating choppers which are used to reduce the pulse rate if necessary. This prevents frame overlap. Finally, another pair of counter rotating choppers selects neutrons within a small time frame, thus acting as NEAT’s main monochromator. All choppers are phased with respect to each other and the disc speed can be set between 2000 and 20000 rpm giving wavelengths from 1 Å to 16 Å.

The neutrons scattered by the sample are recorded with 388 ^3He area single counter detectors, covering scattering angles from 13.35° to 136.5° . For high resolution inelastic measurements and small angle scattering experiment, NEAT provides an additional 1 m^2 area ^3He position sensitive detector consisting of 64×64 detector elements.

D.4. MAPS

Figure (D.4) displays the MAPS (MultiArray Position Sensitive) spectrometer located at the ISIS spallation source, Didcot, UK. The neutrons produced in the spallation process are first moderated by inelastic scattering in water at room temperature before they are guided to the MAPS instrument. The spallation process creates polychromatic pulses of neutrons, which are then monochromatized using two different chopper devices. First, a background chopper is positioned along the beam path. This chopper rotates with the frequency of the proton pulse (50 Hz) and is phased such that it closes the beam path when the proton beam hits the target. By doing so, it prevents epithermal neutrons from entering the detector bank as well as frame overlap effects. Second, a Fermi chopper is placed after the background chopper, selecting a fixed incident neutron energy E_i . This chopper is also phased with respect to the proton pulse and capable of rotating at frequencies between 50 and 600 Hz, thus determining the energy resolution and the flux at the sample position.

The core of the MAPS instrument is its huge array of position sensitive ^3He -detectors, covering approximately an area of 16 m^2 with 147,456 individual pixel elements. The detector array is positioned at a six meter distance from the sample position.

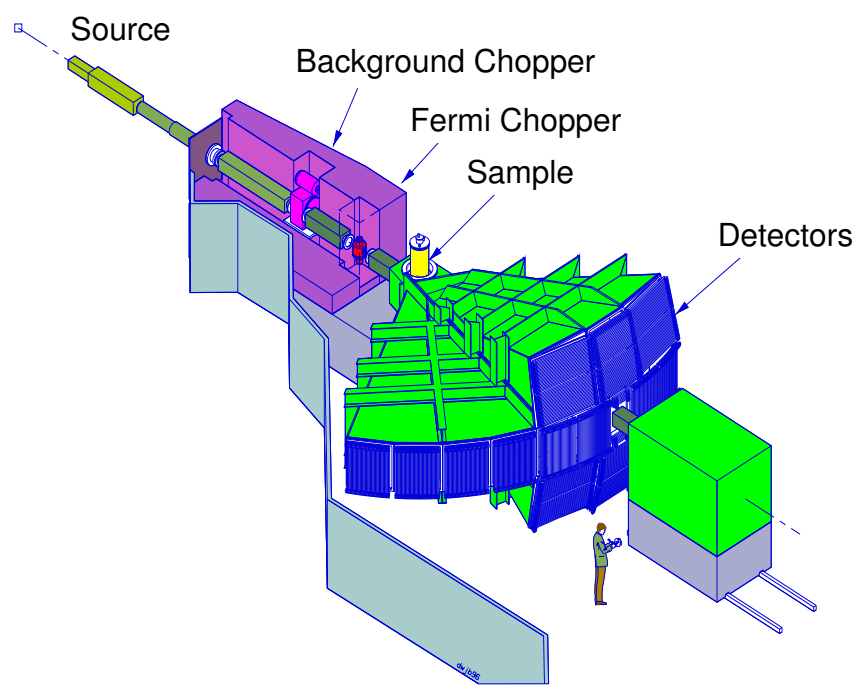


Figure D.4.: Layout of the MAPS TOF spectrometer [183].

Bibliography

- [1] C. J. Milios, A. Vinslava, W. Wernsdorfer, S. Moggach, S. Parsons, S. P. Perlepes, G. Christou, and E. K. Brechin, *J. Am. Chem. Soc.* **129**, 2754 (2007).
- [2] S. Blundell, *Magnetism in Condensed Matter*, Oxford University Press, New York (2001).
- [3] J. Kanamori, *J. Phys. Chem. Solids* **10**, 87 (1959).
- [4] H. A. Jahn and E. Teller, *Proc. R. Soc. A* **161**, 220 (1937).
- [5] P. A. M. Dirac, *Proc. Roy. Soc A* **123**, 714 (1929).
- [6] W. A. Harrison, *Electronic structure and the properties of solids*, Dover Publications, Inc., New York (1989).
- [7] P. W. Anderson, *Phys. Rev.* **79**, 350 (1950).
- [8] P. Fazekas, *Lecture Notes on Electron Correlation and Magnetism, Vol. 5*, World Scientific, Singapore (2003).
- [9] J. B. Goodenough, *Phys. Rev.* **117**, 1442 (1960).
- [10] J. B. Goodenough, *Magnetism and the Chemical Bond*, Interscience-Wiley, New York (1963).
- [11] A. M. Oles, P. Horsch, L. F. Feiner, and G. Khaliullin, *Phys. Rev. Lett.* **96**, 147205 (2006).
- [12] R. Sessoli, D. Gatteschi, A. Caneschi, and M. A. Novak, *Nature* **365**, 141 (1993).
- [13] L. Thomas, F. Lioni, R. Ballou, D. Gatteschi, R. Sessoli, and B. Barbara, *Nature* **383**, 145 (1996).
- [14] W. Wernsdorfer and R. Sessoli, *Science* **284**, 133 (1999).

- [15] D. Gatteschi, R. Sessoli, and J. Villain, *Molecular Nanomagnets*, Oxford University Press, Oxford (2006).
- [16] D. Gatteschi and R. Sessoli, *Angew. Chem. Int. Ed.* **42**, 268 (2003).
- [17] R. Sessoli, *Inorganica Chimica Acta* **361**, 3356 (2008).
- [18] G. Christou, D. Gatteschi, D. N. Hendrickson, and R. Sessoli, *MRS Bulletin* **25**, 66 (2000).
- [19] A. Caneschi, D. Gatteschi, C. Sangregorio, R. Sessoli, L. Sorace, A. Cornia, N. A. Novak, C. Paulsen, and W. Wernsdorfer, *J. Magn. Magn. Mater.* **200**, 182–201 (1999).
- [20] T. Guidi, *Spin excitations and magnetic properties of molecular nanomagnets*, PhD thesis, Università Politecnica della Marche, (2004).
- [21] J. Villain, F. Hartmanboutron, R. Sessoli, and A. Rettori, *Euro. Phys. Lett.* **27**, 159 (1994).
- [22] J. R. Friedman, M. P. Sarachik, J. Tejada, and R. Ziolo, *Phys. Rev. Lett.* **76**, 3830 (1996).
- [23] C. Sangregorio, T. Ohm, C. Paulsen, R. Sessoli, and D. Gatteschi, *Phys. Rev. Lett.* **78**, 4645 (1997).
- [24] A. L. Barra, P. Debrunner, D. Gatteschi, C. E. Schulz, and R. Sessoli, *Europhys. Lett.* **35**, 133 (1996).
- [25] A. Caneschi, T. Ohm, C. Paulsen, D. Rovai, C. Sangregorio, and R. Sessoli, *J. Magn. Magn. Mater.* **177-181**, 1330–1336 (1998).
- [26] P. Ghigna, A. Campana, A. Lascialfari, A. Caneschi, D. Gatteschi, A. Tagliaferri, and F. Borgatti, *Phys. Rev. B* **64**, 132413 (2001).
- [27] W. Wernsdorfer, T. C. Stamatatos, and G. Christou, *Phys. Rev. Lett.* **101**, 237204 (2008).
- [28] O. Kahn, *Molecular Magnetism*, VCH Publishers, New York (1993).
- [29] A. Abragam and Bleaney B., *Electron paramagnetic resonance of transition metal ions*, Clarendon Press Oxford, Oxford (1970).

- [30] E. Livioti, S. Carretta, and G. Amoretti, *J. Chem. Phys.* **117**, 3361 (2002).
- [31] A. Bencini and D. Gatteschi, *Electron Paramagnetic Resonance of Exchange Coupled Clusters*, Springer, Berlin (1990).
- [32] S. Carretta, *Microscopic interactions and quantum effects in magnetic molecules*, PhD thesis, Università degli studi di Parma dipartimento di fisica, (2005).
- [33] S. Carretta, E. Livioti, N. Magnani, P. Santini, and G. Amoretti, *Phys. Rev. Lett.* **92**, 207205 (2004).
- [34] A. Wilson, J. Lawrence, E.C. Yang, M. Nakano, D. N. Hendrickson, and S. Hill, *Phys. Rev. B* **74**, 140403(R) (2006).
- [35] E. Ruiz, J. Cirera, J. Cano, S. Alvarez, C. Loose, and J. Kortus, *Chem. Comm.* pages 52–54 (2008).
- [36] O. Waldmann, *Inorg. Chem.* **46**, 10035 (2007).
- [37] J. Cirera, E. Ruiz, S. Alvarez, F. Neese, and J. Kortus, *Chem. Eur. J.* **15**, 4078–4087 (2009).
- [38] A. M. Ako, I. J. Hewitt, V. Mereacre, R. Clerac, W. Wernsdorfer, C. E. Anson, and A. K. Powell, *Angew. Chem. Int. Ed* **45**, 4926 (2006).
- [39] N. E. Chakov, S.-C.Lee, A. G. Harter, P. L. Kuhns, A. P. Reyes, S. O. Hill, N. S. Dalal, W. Wernsdorfer, K. Abboud, and G. Christou, *J. Am. Chem. Soc.* **128**, 6975–6989 (2006).
- [40] H. Bethe, *Z. Phys.* **71**, 205 (1931).
- [41] U. Schollwöck, J. Richter, D. J. J. Farnell, and R. F. Bishop, editors, *Quantum Magnetism, Lecture Notes in Physics* volume 645, Springer, Berlin (2004).
- [42] N. D. Mermin and H. Wagner, *Phys. Rev. Lett.* **17**, 1133 (1966).
- [43] T. Holstein and H. Primakoff, *Phys. Rev.* **58**, 1098 (1940).
- [44] W. Nolting and A. Ramakanth, *Quantum Theory of Magnetism*, Springer-Verlag, Berlin, Heidelberg (2009).
- [45] J. Goldstone, A. Salam, and S. Weinberg, *Phys. Rev.* **127**, 965–970 (2001).
- [46] J. d. Cloizeaux and J. J. Pearson, *Phys. Rev.* **128**, 2131 (1962).

- [47] S. Yamamoto and S. Miyashita, *Phys. Lett. A* **235**, 545 (1997).
- [48] F. D. M. Haldane, *Phys. Rev. Lett.* **67**, 937–940 (1991).
- [49] F. D. M. Haldane, *Phys. Rev. Lett.* **50**, 1153 (1983).
- [50] B. Lake, D. A. Tennant, and S. E. Nagler, *Phys. Rev. Lett.* **85**, 832 (2000).
- [51] B. Lake, D. A. Tennant, and S. E. Nagler, *Phys. Rev. B* **71**, 134412 (2005).
- [52] E. Enderle, T. Tun, W. J. L. Buyers, and M. Steiner, *Phys. Rev. B* **59**, 4235 (1999).
- [53] H. J. Schulz, *Phys. Rev. Lett.* **77**, 2790 (1996).
- [54] W. J. L. Buyers, R. M. Morra, R. L. Armstrong, M. J. Hogan, P. Gerlach, and K. Hirakawa, *Phys. Rev. Lett.* **56**, 371 (1986).
- [55] A. P. Ramirez, *Annu. Rev. Mater. Sci.* **24**, 453–480 (1994).
- [56] T. Hikihara, *J. Phys. Soc. Jpn.* **71**, 319 (2002).
- [57] G. L. Squires, *Introduction to the theory of thermal neutron scattering*, Dover Publications, Inc., Mineola, New York (1996).
- [58] G. Shirane, S. M. Shapiro, and J. M. Tranquada, *Neutron scattering with a triple-axis spectrometer*, Cambridge University Press, Cambridge (2004).
- [59] T. Chatterji, editor, *Neutron scattering from magnetic materials*, Elsevier, Amsterdam (2006).
- [60] S. W. Lovesey, *Thermal neutron scattering from condensed matter, Vol.2*, Oxford University Press, Oxford (1984).
- [61] A. Furrer, J. Mesot, and T. Strässer, *Neutron scattering in condensed matter physics*, World Scientific, Singapore (2009).
- [62] <http://serc.carleton.edu/details/images/8400.html> (last visit: March 2010).
- [63] C. Giacovazzo, H. L. Monaco, G. Artioli, D. Viterbo, G. Ferraris, G. Gilli, G. Zanotti, and M. Catti, *Fundamentals of Crystallography*, Oxford University Press, Oxford (2002).
- [64] M. Tovar and H. A. Graf, editors, *Neutron Scattering Instrumentation at the Research Reactor BER II*, Helmholtz-Zentrum Berlin, Berlin (2007).

- [65] D. A. Keen, M. J. Guttman, and C. W. Wilson, *J. Appl. Crystallogr.* **39**, 714–722 (2006).
- [66] W. Massa, *Crystal Structure Determination*, Springer-Verlag, Berlin (2004).
- [67] R. E. Dinnebier and S. J. Billinge, editors, *Powder Diffraction: Theory and Practice*, RSC Publishing, Cambridge (2008).
- [68] <http://www.pns.anl.gov/instruments/sepd/subsepd/> (last visit: March 2010).
- [69] H. M. Rietveld, *J. Appl. Crystallogr.* **2**, 65 (1969).
- [70] R. A. Young, editor, *The Rietveld Method*, Oxford University Press, Oxford (1993).
- [71] P. Thompson, D. E. Cox, and J. B. Hastings, *J. Appl. Cryst.* **20**, 79–83 (1987).
- [72] Stephens P. W., *J. Appl. Crystallogr.* **32**, 281–289 (1999).
- [73] A. Clearfield, J. Reibenspies, and N. Bhuvanesh, editors, *Principles and Applications of Powder Diffraction*, Wiley-Blackwell, Oxford (2008).
- [74] M. J. Cooper and R. Nathans, *Acta Crystallogr., Sect. A* **29**, 160–169 (1967).
- [75] M. Popovici, *Acta Crystallogra. Sect. A* **31**, 507 (1975).
- [76] <http://www.ill.eu/instruments-support/computing-for-science/cs-software/all-software/matlab-ill/rescal-for-matlab/> (last visit: March 2010).
- [77] C. G. Windsor, *Pulsed neutron scattering*, Taylor & Francis, London (1981).
- [78] B. E. Warren, *X-ray diffraction*, Dover Publications, Mineola (1990).
- [79] <http://www.esrf.eu/UsersAndScience/Experiments/CRG/BM01> (last visit: Jan 2010).
- [80] http://www.esrf.eu/UsersAndScience/Experiments/CRG/BM01/shepherds/SNBL_BLRPreport.pdf (last visit: July 2010).
- [81] J. A. Osborn, *Phys. Rev.* **67**, 351–357 (1945).
- [82] *PPMS VSM Option User Manual*, Quantum Design, San Diego (2004).
- [83] C. J. Milios, A. Vinslava, P. A. Wood, S. Parsons, W. Wernsdorfer, G. Christou, S. P. Perlepes, and E. K. Brechin, *J. Am. Chem. Soc.* **129**, 8 (2006).

- [84] C. J. Milios, A. Vinslava, W. Wernsdorfer, A. Prescimone, P. A. Wood, S. Parsons, S. P. Perlepes, G. Christou, and E. K. Brechin, *J. Am. Chem. Soc.* **129**, 6547 (2007).
- [85] R. Inglis, L. F. Jones, C. J. Milios, S. Datta, A. Collins, S. Parsons, W. Wernsdorfer, S. Hill, S. P. Perlepes, S. Piligkos, and E. K. Brechin, *Dalton Trans.* **18**, 3403 (2009).
- [86] C. J. Milios, S. Piligkos, and E. K. Brechin, *Dalton Trans.* **14**, 1809–1817 (2008).
- [87] C. J. Milios, R. Inglis, A. Vinslava, R. Bagai, W. Wernsdorfer, S. Parsons, S. P. Perlepes, G. Christou, and E. K. Brechin, *J. Am. Chem. Soc.* **129**, 12505 (2007).
- [88] C. J. Milios, C. P. Raptopoulou, A. Terzis, F. Lloret, R. Vicente, S. P. Perlepes, and A. Escuer, *Angew. Chem., Int. Ed.* **43**, 210 (2004).
- [89] O. Pieper, T. Guidi, S. Carretta, J. van Slageren, F. El Hallak, B. Lake, P. Santini, G. Amoretti, H. Mutka, M. Koza, M. Russina, A. Schnegg, C. J. Milios, E. K. Brechin, A. Julià, and J. Tejada, *Phys. Rev. B* **81**, 174420 (2010).
- [90] S. Carretta, T. Guidi, P. Santini, G. Amoretti, O. Pieper, J. van Slageren, F. El Hallak, W. Wernsdorfer, H. Mutka, M. Russina, C. J. Milios, and E. K. Brechin, *Phys. Rev. Lett.* **100**, 157203 (2008).
- [91] A. Sieber, C. Boskovic, R. Bircher, O. Waldmann, S.T. Ochsenein, G. Chabousant, H.U. Güdel, N. Kirchner, J. van Slageren, W. Wernsdorfer, A. Neels, H. Stoeckli-Evans, S. Janssen, F. Juranyi, and H. Mutka, *Inorg. Chem.* **44**(12), 4315–4325 (2005).
- [92] S. Piligkos, G. Rajaraman, M. Soler, N. Kirchner, J. van Slageren, R. Bircher, S. Parsons, H.-U. Güdel, J. Kortus, W. Wernsdorfer, G. Christou, and E.K. Brechin, *J. Am. Chem. Soc.* **127**, 5572–5580 (2005).
- [93] O. Waldmann and H. U. Güdel, *Phys. Rev. B* **72**, 094422 (2005).
- [94] http://www.magmanet-eu.net/index.php?/article_10627/modelling_magnetism.html (Last visit: March 2010).
- [95] A. F. Albuquerque, F. Alet, P. Corboz, P. Dayal, A. Feiguin, S. Fuchs, L. Gamper, E. Gull, S. Guertler, A. Honecker, R. Igarashi, M. Koerner, A. Kozhevnikov, A. Laeuchli, S. R. Manmana, M. Matsumoto, I. P. McCulloch, F. Michel, R. M.

- Noack, G. Pawlowski, L. Pollet, T. Pruschke, U. Schollwoeck, S. Todo, S. Trebst, M. Troyer, P. Werner, S. Wessel, and ALPS Collaboration, *J. Magn. Magn. Mater.* **310**, 1187–1193 (2007).
- [96] J. J. Borrás-Almenar, J. M. Clemente-Juan, E. Coronado, and B. S. Tsukerblat, *J. Comput. Chem.* **22**, 985 (2001).
- [97] S. Carretta, P. Santini, G. Amoretti, M. Affronte, A. Candini, A. Ghirri, I. S. Tidmarsh, R. H. Laye, R. Shaw, and E. J. L. McInnes, *Phys. Rev. Lett.* **97**, 207201 (2006).
- [98] A. Furrer and H. U. Güdel, *Phys. Rev. Lett.* **39**, 657 (1977).
- [99] O. Waldmann, *Phys. Rev. B* **68**, 174406 (2003).
- [100] S.M.J. Aubin, Z. Sun, H.J. Eppley, E.M. Rumberger, I.A. Guzei, K. Folting, P.K. Gantzel, A.L. Rheingold, G. Christou, and D.N. Hendrickson, *Inorg. Chem.* **40**, 2127 (2001).
- [101] J. van Slageren, P. Rosa, A. Caneschi, R. Sessoli, H. Casellas, Y. V. Rakitin, L. Cianchi, F. D. Giallo, G. Spina, A. Bino, A. L. Barra, T. Guidi, S. Carretta, and R. Caciuffo, *Phys. Rev. B* **73**, 014422 (2006).
- [102] I. Mirebeau, M. Hennion, H. Casalta, H. Andres, H.U. Güdel, A.V. Irodova, and A. Caneschi, *Phys. Rev. Lett.* **83**, 628–631 (1999).
- [103] P. L. Feng, C. Koo, J. J. Henderson, M. Nakano, S. Hill, E. del Barco, and D. N. Hendrickson, *Inorganic Chemistry* **47**, 8610–8612 (2008).
- [104] S. Bahr, C. J. Milios, L. F. Jones, E. K. Brechin, V. Mosser, and W. Wernsdorfer, *New J. Chem.* **33**, 1231–1236 (2009).
- [105] E. Cremades, J. Cano, E. Ruiz, G. Rajaraman, C. J. Milios, and E. K. Brechin, *Inorg. Chem.* **48**, 8012–8019 (2009).
- [106] A. Furrer and H. U. Güdel, *J. Magn. Magn. Mater.* **14**, 256 (1979).
- [107] S. Piligkos, J. Bendix, H. Weihe, C. J. Milios, and E. K. Brechin, *Dalton Trans.* **17**, 2277–2284 (2008).
- [108] C. M. Ramsey, E. Del Barco, S. Hill, S. J. Shah, C. C. Beedle, and D. N. Hendrickson, *Nature Phys.* **4**, 277–281 (2008).

- [109] C. I. Yang, W. Wernsdorfer, G.-H. Lee, and H.-L. Tsai, *J. Am. Chem. Soc.* **129**, 456 (2007).
- [110] M. Soler, W. Wernsdorfer, Z. M. Sun, J. C. Huffman, D. N. Hendrickson, and G. Christou, *Chem. Comm.* **21**, 2672 (2003).
- [111] S. Carretta, T. Guidi, P. Santini, G. Amoretti, O. Pieper, B. Lake, J. van Slageren, F. El Hallak, W. Wernsdorfer, H. Mutka, M. Russina, C. J. Milios, and E. K. Brechin, *Polyhedron* **28**, 1940–1944 (2009).
- [112] S. Datta, E. Bolin, R. Inglis, C. J. Milios, E. K. Brechin, and S. Hill, *Polyhedron* **28**, 1788–1791 (2009).
- [113] E. F. Bertaut, P. Blum, and G. Magnano, *C.R. Hebd. Seances Acad. Sci.* **241**, 757 (1955).
- [114] P. M. Hill, H. S. Peiser, and J. R. Rait, *Acta Cryst.* **9**, 981–986 (1956).
- [115] K. Yamaura, Q. Huang, M. Moldovan, D. P. Young, A. Sato, Y. Baba, T. Nagai, Y. Matsui, and E. Takayama-Muromachi, *Chem. Mater.* **17**, 359–365 (2005).
- [116] T. Irifune, K. Fujino, and E. Ohtani, *Nature* **349**, 409–411 (1991).
- [117] K. Yamaura, Q. Huang, L. Zhang, K. Takada, Y. Baba, T. Nagai, Y. Matsui, K. Kosuda, and E. Takayama-Muromachi, *J. Am. Chem. Soc.* **128**, 9448–9456 (2006).
- [118] K. Ohgushi, H. Gotou, T. Yagi, and Y. Ueda, *J. Phys. Soc. Jpn.* **75**, 023707 (2006).
- [119] A. Niazi, S. L. Budko, D. L. Schlagel, J. Q. Yan, T. A. Lograsso, A. Kreyssig, S. Das, S. Nandi, A. I. Goldman, A. Honecker, R. W. McCallum, M. Reehuis, O. Pieper, B. Lake, and D. C. Johnston, *Phys. Rev. B* **79**, 104432 (2009).
- [120] J. Q. Yan, M. Reehuis, O. Pieper, B. Lake, A. Daoud-Aladine, Y. Mudryk, V. Pecharsky, A. Kreyssig, S. Das, A. Niazi, D. C. Johnston, P. Pattison, E. Herman, Y. Ren, J. Fieramosca, and R. J. McQueeney, unpublished (2009).
- [121] A. P. Holm, V. K. Pecharsky, K. A. Gschneidner Jr., R. Rink, and M. Jirmanus, *Rev. Sci. Instrum.* **75**, 1081 (2004).
- [122] J. Rodriguez-Carvajal, *Physica B* **192**, 55–69 (1993).
- [123] P. Rozier, A. Ratuszna, and J. Galy, *Z. Anorg. Allg. Chem.* **628**, 1236–1242 (2002).

- [124] H. Falcón, J. A. Alonso, M. T. Casais, M. J. Martinez-Lope, and J. Sánchez-Benitez, *J. Solid State Chem.* **177**, 3099 (2004).
- [125] M. Reehuis, C. Ulrich, P. Pattison, B. Ouladdiaf, M. C. Rheinstadter, M. Ohl, L. P. Regnault, M. Miyasaka, Y. Tokura, and B. Keimer, *Phys. Rev. B* **73**, 094440 (2006).
- [126] D. B. Rogers, R. J. Arnott, A. Wold, and J. B. Goodenough, *J. Phys. Chem. Solids* **24**, 347–360 (1976).
- [127] M. Onoda and J. Hasegawa, *J. Phys. Condens. Matter* **15**, L95–L102 (2003).
- [128] M. Reehuis, A. Krimmel, Büttgen, A. Loidl, and A. Prokofiev, *Eur. Phys. J. B* **35**, 311–316 (2003).
- [129] K. Yamaura, M. Arai, A. Sato, A. B. Karki, D. P. Young, R. Movshovich, S. Okamoto, D. Mandrus, and E. Takayama-Muromachi, *Phys. Rev. Lett.* **99**, 196601 (2007).
- [130] I. D. Brown, *Chem. Soc. Rev.* **7**, 359 (1977).
- [131] J. A. Alonso, Martinez-Lope M. J., Casais M. T., and Fernaández-Diaz M. T., *Inorg. Chem.* **39**, 917–923 (2000).
- [132] I. D. Brown, *The chemical bond in inorganic chemistry - the bond valence model*, Oxford University Press, Oxford (2002).
- [133] A. Salinas-Sanchez, J. L. Carcia-Muñoz, J. Rodriguez-Carvajal, R. Saez-Puche, and J. L. Martinez, *J. Sol. Stat. Chem.* **100**, 201–211 (1992).
- [134] H. F. Pen, J. van den Brink, D. I. Khomskii, and G. A. Sawatzky, *Phys. Rev. Lett.* **78**, 1323 (1997).
- [135] H. Kikuchi, M. Chiba, and T. Kubo, *Can. J. Phys.* **79**, 1551–1555 (2001).
- [136] X. Zong, B. J. Suh, A. Niazi, J. Q. Yan, D. L. Schlagel, T. A. Lograsso, and D. C. Johnston, *Phys. Rev. B* **77**, 014412 (2008).
- [137] O. Pieper, B. Lake, A. Daoud-Aladine, M. Reehuis, K. Prokeš, B. Klemke, K. Kiefer, J. Q. Yan, A. Niazi, D. C. Johnston, and A. Honecker, *Phys. Rev. B* **79**, 180409 (2009).

- [138] M. Onoda, I. Hiroyoshi, Y. Amako, and H. Nagasawa, *Phys. Rev. B* **56**, 3760 (1997).
- [139] E.D. Jones, *Phys. Rev.* **137**, A 978 (1964).
- [140] E. König and G. König, edited by K.-H. Hellwege and A.M. Hellwege, *Landolt-Börnstein, New Series pages Group II, Vol.12* (Springer-Verlag, Berlin), Chap.1 (1984).
- [141] www.mathworks.com/access/helpdesk/help/techdoc/ref/interp2.html (last visit: March 2010).
- [142] J. Villian, *Ann. Isr. Phys. Soc.* **2**, 565 (1977).
- [143] D. Bloch, *J. Phys. Chem. Solids* **27**, 881 (1966).
- [144] D. Coombes, T. Xiang, and G. A. Gehring, *J. Phys. Condens. Matter* **10**, L159 (1998).
- [145] E. F. Bertaut and N. van Nhung, *C.R. Hebd. Seances Acad. Sci. B* **264**, 1416 (1967).
- [146] J.M. Hastings, L.M. Corliss, W. Kunnmann and S. La Placa, *J. Phys. Chem. Solids* **28**, 1089–1092 (1967).
- [147] J. Sugiyama, Y. Ikedo, T. Goko, E. J. Ansaldo, J. H. Brewer, P. L. Russo, K. H. Chow, and H. Sakurai, *Phys. Rev. B* **78**, 224406 (2008).
- [148] P. Müller, R. Herbst-Irmer, Spek A. L., Schneider T. R., and Sawaya M. R., *Crystal structure refinement*, Oxford University Press, Oxford (2006).
- [149] E. F. Bertaut, *Acta Crystallogr., Sect. A* **24**, 217 (1968).
- [150] A. Authier, editor, *International tables for crystallography, Vol. D, Physical properties of crystals*, Kluwer academic publisher, Dordrecht (2003).
- [151] <http://www.ill.eu/sites/fullprof/php/programsfa7c.html?pagina=GBasireps> (last visit: March 2010).
- [152] F. Damay, C. Martin, V. Hardy, A. Maignan, G. André, K. Knight, S. R. Giblin, and L. C. Chapon, *Phys. Rev. B* **81**, 214405 (2010).
- [153] C. Wilkinson and H. W. Khamis, *J. Appl. Crystallogr.* **21**, 471–478 (1988).

-
- [154] S. Kirkpatrick, C. D. Gelatt Jr., and M. P. Vecchi, *Science* **220**, 671–680 (1983).
- [155] B. J. Kim, Hosub Jin, S. J. Moon, J. Y. Kim, B. G. Park, C. S. Leem, Jaejun Yu, T. W. Noh, C. Kim, S. J. Oh, J. H. Park, V. Durairaj, G. Cao, and E. Rotenberg, *Phys. Rev. Lett.* **101**, 076402 (2008).
- [156] G. Jackeli and Khaliullin G., *Phys. Rev. Lett.* **349**, 017205 (2009).
- [157] O. Tchernyshyov, *Phys. Rev. Lett.* **93**, 157206 (2004).
- [158] G. Chern and N. Perkins, *Phys. Rev. B* **80**, 220405(R) (2009).
- [159] D. Allen and D. Senechal, *Phys. Rev. B* **61**, 12134 (2000).
- [160] H. Fukushima, H. Kikuchi, M. Chiba, Y. Fujii, Y. Yamamoto, and H. Hori, *Prog. Theor. Phys. Suppl.* **145**, 72 (2002).
- [161] H. Sakurai, *Phys. Rev. B* **78**, 094410 (2008).
- [162] R. M. White, M. Sparks, and I. Ortenburger, *Phys. Rev.* **139**, A450 (1965).
- [163] D. A. Tennant, D. F. McMorrow, S. E. Nagler, R. A. Cowley, and B. Fåk, *J. Phys.: Condens. Matter* **6**, 10341 (1994).
- [164] S. Fulton, S. E. Nagler, L. M. N. Needham, and B. M. Wanklyn, *J. Phys. Condens. Matter* **6**, 6667 (1994).
- [165] S. Di Matteo, G. Jackeli, and N. B. Perkins, *Phys. Rev. B* **72**, 020408 (2005).
- [166] N. B. Perkins, Private Communications.
- [167] K. Takubo, J. Y. Son, T. Mizokawa, H. Ueda, M. Isobe, Y. Matsushita, and Y. Ueda, *Phys. Rev. B* **74**(15) (2006).
- [168] T Mizokawa and A Fujimori, *Phys. Rev. B* **54**, 5368–5380 (1996).
- [169] T. Oguchi, *Phys. Rev.* **117**, 117 (1960).
- [170] A. L. Chernyshev and M. E. Zhitomirsky, *Phys. Rev. B* **79**, 144416 (2009).
- [171] M. T. Hutchings, E. J. Samuelsen, G. Shirane, and K. Hirakawa, *Phys. Rev.* **188**, 919–923 (1969).
- [172] W. B. Yelon and D. E. Cox, *Phys. Rev. B* **7**, 2024 (1972).

-
- [173] I. A. Zaliznyak, S.-H. Lee, and Petrov S. V., Phys. Rev. Lett. **87**, 017202 (2001).
- [174] I. Affleck and G. F. Wellman, Phys. Rev. B **46**, 8934 (1992).
- [175] T. Maitra and Valentí, Phys. Rev. Lett. **99**, 126401 (2007).
- [176] G. Chern and N. Perkins, Phys. Rev. B **80**, 180409(R) (2009).
- [177] V. Eyert, private communications.
- [178] C. Aronica, G. Pilet, G. Chastanet, W. Wernsdorfer, J.F. Jacquot, and D. Luneau, Angew. Chem., Int. Ed. **45**, 4659 (2006).
- [179] R. M. Noack and Manmana S. R., arxiv:cond-mat/0510321v1 (2005).
- [180] E. Anderson, Z. Bai, C. Bischof, L. S. Blackford, J. Demmel, J. Du Croz, A. Greenbaum, S. Hammarling, A. McKenney, and D. Sorensen, *LAPACK Users' Guide, Third Edition*, SIAM, Philadelphia (1999).
- [181] A. Honecker and A. Läuchli, Phys. Rev. B **63**, 174407 (2001).
- [182] G. Cicognani, editor, *The Yellow Book*, Institut Laue-Langevin, Grenoble (2008).
- [183] T. G. Perring, A. D. Taylor, R. Osborn, D. McK Paul, A. T. Boothroyd, and G. Aeppli, Proc. ICANS XII, RAL report 94-025 pages 1–60 (1994).

List of Publications

Parts of the work presented in this thesis have been published in scientific journals.

- *Photoinduced ferromagnetism in diluted magnetic semiconductors*, O. Pieper, Diploma thesis (2006)
- *The role of excited S multiplets in the magnetic relaxation of the high anisotropy barrier Mn6 Single Molecule Magnet*, T. Guidi, O. Pieper, B. Lake, S. Carretta, P. Santini, G. Amoretti, J. Van Slageren, M. Russina, A. Buchsteiner, C.J. Milios, E.K. Brechin, BENS Annual report 2006, Highlight
- *Breakdown of the Giant Spin model in the magnetic relaxation of the Mn6 nanomagnets*, S. Carretta, T. Guidi, P. Santini, G. Amoretti, O. Pieper, B. Lake, J. van Slageren, F. El Hallak, W. Wernsdorfer, H. Mutka, M. Russina, C.J. Milios and E. K. Brechin, Phys. Rev. Lett. **100**, 157203 (2008)
- *Spin canting and orbital driven change of exchange pathways in the quasi one-dimensional chain material CaV₂O₄*, O. Pieper, B. Lake, A. Daoud-Aladine, M. Reehuis, K. Prokes, B. Klemke, K. Kiefer, A. Niazi, J. Q. Yan and D. C. Johnston, A. Honecker, BENS Annual report 2008, Highlight
- *Neutron spectroscopy and magnetic relaxation of the Mn6 nanomagnets*, S. Carretta, T. Guidi, P. Santini, G. Amoretti, O. Pieper, B. Lake, J. van Slageren, F. El Hallak, W. Wernsdorfer, H. Mutka, M. Russina, C.J. Milios and E. K. Brechin, Polyhedron **28**, 1940-1944 (2009)
- *Magnetic structure and interactions of the quasi-one-dimensional antiferromagnet CaV₂O₄*, O. Pieper, B. Lake, A. Daoud-Aladine, M. Reehuis, K. Prokes, B. Klemke, K. Kiefer, A. Niazi, J. Q. Yan and D. C. Johnston, A. Honecker, Phys. Rev B, **79**, 180409(R) (2009)

- *Single Crystal Growth, Crystallography, Magnetic Susceptibility, Heat Capacity, and Thermal Expansion of the Antiferromagnetic $S = 1$ Chain Compound CaV_2O_4* , A. Niazi, S. L. Budko, D. L. Schlage, T. A. Lograsso, J. Q. Yan, A. Honecker, R. W. McCallum, M. Reehuis, O. Pieper, B. Lake and D. C. Johnston, Phys. Rev B, **79**, 104492 (2009)
- *Inelastic neutron scattering and frequency domain magnetic resonance studies of $S=1/2$ and $S=4$ Mn^{2+} single-molecule magnets*, O. Pieper, T. Guidi, S. Carretta, J. van Slageren, F. El Hallak, B. Lake, P. Santini, G. Amoretti, H. Mutka, M. Koza, M. Russina, A. Schnegg, C.J. Milios, E.K. Brechin, A. Julia and J. Tejada, Phys. Rev B, **81**, 174420 (2010)
- *Neutron scattering investigations of zero- and one-dimensional quantum magnets*, O. Pieper, P.hD. thesis (2010)

Eidesstattliche Versicherung

Hiermit versichere ich an Eides Statt, dass ich meine Dissertation mit dem Titel:

“Neutron Scattering Investigations of Zero- and One-dimensional Quantum Magnets”

selbstständig verfasst habe. Alle benutzten Hilfsmittel und Quellen sind in der Arbeit aufgeführt.

Berlin, den 12.03.2010

Oliver Pieper